UNIVERSITY *of*
TASMANIA
AUSTRALIA

School of Physical Sciences

6.7 GHz Maser Astrometry with the Australian Long Baseline Array

Vasaant $^{S}/_{O}$ Krishnan

January 2016

Supervisors:
Prof. Simon P. Ellingsen
Dr. Shari L. Breen

Submitted in fulfilment of the requirements for the Degree of
Doctor of Philosophy

Declaration of Originality

This thesis contains no material which has been accepted for a degree or diploma by the University or any other institution, except by way of background information and duly acknowledged in the thesis, and to the best of my knowledge and belief no material previously published or written by another person except where due acknowledgement is made in the text of the thesis, nor does the thesis contain any material that infringes copyright.

Signed: _____

Date: 30th March 2016

Authority of Access

The publishers of the papers comprising Chapters 3 and 7 hold the copyright for that content, and access to the material should be sought from the respective journals. The remaining non–published content of the thesis may be made available for loan and limited copying and communication in accordance with the Copyright Act 1968.

Signed: _____

Date: 30th March 2016

Statement of Co–authorship

The following people and institutions contributed to the publication of work undertaken as part of this thesis:

Candidate	**V. Krishnan**	**University of Tasmania,** **CSIRO Astronomy & Space Science**
Co–author 1	S. P. Ellingsen	University of Tasmania
Co–author 2	S. L. Breen	CSIRO Astronomy & Space Science
Co–author 3	M. A Voronkov	CSIRO Astronomy & Space Science
Co–author 4	M. J. Reid	Harvard–Smithsonian Center for Astrophysics
Co–author 5	A. Brunthaler	Max–Plank–Institut für Radioastronomie
Co–author 6	A. Sanna	Max–Plank–Institut für Radioastronomie
Co–author 7	J. McCallum	University of Tasmania
Co–author 8	C. Reynolds	Curtin University
Co–author 9	H. E. Bignall	Curtin University
Co–author 10	C. J. Phillips	CSIRO Astronomy & Space Science
Co–author 11	R. Dodson	University of Western Australia
Co–author 12	M. Rioja	University of Western Australia, Observatorio Astronómico Nacional
Co–author 13	J. L. Caswell	CSIRO Astronomy & Space Science
Co–author 14	X. Chen	Shanghai Astronomical Observatory
Co–author 15	J. R. Dawson	Macquarie Research Centre in Astronomy, CSIRO Astronomy & Space Science
Co–author 16	K. Fujisawa	Yamaguchi University
Co–author 17	S. Goedhart	Hartebeesthoek Radio Astronomical Observatory, SKA South Africa
Co–author 18	J. A. Green	Jodrell Bank Observatory, CSIRO Astronomy & Space Science
Co–author 19	K. Hachisuka	Shanghai Astronomical Observatory, Yamaguchi University
Co–author 20	M. Honma	Mizusawa VLBI Observatory
Co–author 21	K. Menten	Max–Plank–Institut für Radioastronomie
Co–author 22	Z. Q. Shen	Shanghai Astronomical Observatory
Co–author 23	A. J. Walsh	Curtin University
Co–author 24	Y. Xu	Purple Mountain Observatory
Co–author 25	B. Zhang	Shanghai Astronomical Observatory
Co–author 26	X. W. Zheng	Nanjing University

Paper 1: ***The first high-resolution observations of 19.9–GHz methanol masers.***
Located in Chapter 3.

The candidate was responsible for the data reduction and analysis, and was the primary author of the manuscript. Co–author 1 was responsible for the idea, its formalisation and development and also wrote the introduction. Co–authors 1 and 2 were the primary contributors to the material in Section 3.3.2, and co–author 3 produced Figure 3.16. Co–author 3 assisted with the observations as well as with providing feedback to refine the manuscript for publication.

Paper 2: ***First Parallax Measurements Towards a 6.7 GHz Methanol Maser with the Australian Long Baseline Array - Distance to G 339.884−1.259.***
Located in Chapter 7.

The candidate was responsible for the data reduction and analysis, and was the primary author of the manuscript. Co–authors 1, 4 and 5 were responsible for the idea, its formalisation and development. The candidate as well as co–authors 1, 10 and 15 assisted with the VLBI observations, and co–authors 8 and 9 correlated the data from the various observatories. Co–author 4 was responsible for the analysis in Section 7.1.2 and produced Figure 7.3. Co–authors 11 and 12 were the primary contributors to the material in Section 7.3.2. Co–authors 4 – 26 assisted with providing feedback to refine the manuscript for publication.

We the undersigned agree with the above stated "proportion of work undertaken" for each of the above published (or submitted) peer–reviewed manuscripts contributing to this thesis:

Signed: _____

Prof. Simon P. Ellingsen
Supervisor
School of Physical Sciences
University of Tasmania

Date: 23/12/15

Prof. John M. Dickey
Head of School
School of Physical Sciences
University of Tasmania

23/12/15

Acknowledgements

I would like to thank my supervisors Prof. Simon Ellingsen and Dr. Shari Breen for their invaluable support during the course of my study. The guidance which you have provided me has formed the bedrock for my professional advancement over the last four years, as well as for the years to come. Through my supervision team, I am fortunate to have been handed the opportunity to be at the forefront of an international project, having developed close ties with the experts in the fields of radio interferometry and astrometry.

It was a pleasure to have had Courtney Brown, David Horsley and Paul Stack as my closest colleagues, whom I have known for the entire duration of my time away from home. We have shared a common experience, beginning as undergraduate students who progressed to office mates as we pursued our doctorates. It is a fitting end to this chapter of our lives that we are all now at the cusp of commencing our individual careers after 9 years of academic fellowship.

Andrew, Amanda and Margaretta, you have made me feel at home even though all which was familiar to me had been left thousands of kilometers away. Some of my happiest times in Australia have been spent in your company and in *The Kiwi*.

To my family and friends of new and old, though I am not able to single you out individually at this moment, your presence has been essential in keeping me in balance. This has especially been the case during the final months of 2015, while I was concurrently completing this dissertation, orchestrating wedding ceremonies in Singapore and Australia, and planning a move overseas to embark on married and working life. To Appa, Amma and Hannah, a special Thank You for your patience and tirelessness in providing stability, care and vital support during these demanding, demanding years.

Contents

List of Figures

List of Tables

Chapter 1

Introduction

Astrometry is the science of measuring the positions of astronomical objects in the sky, and as such forms a practical bedrock for astrophysics in general. This is because it is only when a source's position is unambiguously known, can it be observed while it transits across the sky or be detected at different wavelengths. One of the first discoveries as a result of astrometry was in differentiating between the planets in our Solar System and the stars in the Milky Way. Early astronomers would have noted the arcminute/day rate of *proper motion* of the nearby planets with respect to the distant celestial objects fixed in the sky with the passage of time. With the advancement of telescopes the arcsecond/year proper motions for the fastest moving nearby stars was resolved as well.

In comparing comets or asteroid size objects of a few kilometres, to galaxies spanning hundreds of thousands of light–years, it becomes apparent that the absolute size of astronomical objects extends across dimensions spanning many orders of magnitude. Despite this, the distances to these objects render many of them regardless of size to be minuscule pinpoints, when viewed from the Earth. The accuracy with which an object's position can be known is governed by the diffraction limit $\theta_d \approx \lambda/D$ of the observing system and improvements in astrometric resolution have led to astronomical discoveries including Earth's precession, stellar aberration, atmospheric refraction, particle jets from black holes, the rate of expansion of planetary nebulae, detailed structure of circumstellar disks and outflows from protostars, high–energy jets from quasars and the orbits of exoplanets around distant stars. The focus of this thesis is on the impact of accurate astrometry to measure trigonometric stellar parallaxes (from now on *parallax*) towards masers in high–mass star formation regions (HMSFRs) in the Milky Way galaxy using the Australian Long Baseline Array (LBA).

1.1 Overview of distance in the Milky Way

Distance measurement is fundamental to astronomy and governs our ability to estimate important properties, such as luminosity ($L \propto D^2$) and mass ($L \propto M^a$, where $3 < a < 4$ for main sequence stars) of astronomical objects. An uncertainty in distance will naturally propagate into other quantities and reduce the effectiveness with which we are able to verify our theories of the observable Universe. No one method of distance measurement is valid across the entire field of astronomy because of the immense range of scales involved. Instead, as-

tronomers are reliant upon a *distance ladder* system, where overlapping regions employed by adjacent techniques are used to calibrate the subsequent rung. As a result, the astronomical distance scale beyond the boundaries of the Milky Way galaxy is entirely dependant on the precision with which we can measure absolute parallax distances to calibrator sources within our Galaxy (Melis et al. 2014; Sowell et al. 2007; Reid 1999; Webb 1999).

The next assumption in the distance ladder scheme is that Cepheid variables, RR Lyrae variables, planetary nebulae, type Ia supernovae and other suitable calibrators emit radiation at specific luminosities based on sound theories of their physical characteristics. In comparing such a calibrator source within the Milky Way to an extragalactic target the diminished brightness can be attributed to a corresponding increase in distance (e.g. Benedict et al. 2007; Riess et al. 2004). This is provided that appropriate corrections are made for the intervening absorption, reddening and scattering. Important parameters in the study of cosmology, such as the Hubble constant (H_0) therefore depend directly on the accuracy with which we can measure parallax distances within the Milky Way itself. The following is an overview of the key techniques employed to measure distances within our Galaxy.

1.1.1 Parallax

Parallax remains as the most direct and accurate method to determine distances to objects beyond our Solar System. This technique is dependant on the change in perspective of foreground sources against distant background ones as the Earth orbits the Sun. It was with the advent of a new class of powerful telescopes that Friedrich Wilhelm Bessel was successfully able to measure the changes in the relative astrometric positions between 61 Cygni and a background star in 1838. From his measurements, Bessel determined the parallax of 61 Cygni to be $\pi = 0.314''$, and this triumph provided the ultimate evidence in support for the Heliocentric model of the Solar System. The additional outcome of Bessel's observation was to extract the distance from π, placing 61 Cygni at a distance of $\frac{1}{\pi} = 3.185$ pc from the Sun.

Unlike most other distance measurement techniques, such as the use of a Galactic rotation model, or *standard candles* where the distances to objects with known luminosities can be determined from their observed brightness, parallax distance is considered to be the gold standard in astrophysics. It is a model independent technique, making it robust to systematic errors which the other procedures are liable to. For example, Xu et al. (2006) found a discrepancy of a factor of 2 between the parallax and kinematic distances in the HMSFR W3(OH) due to the peculiar velocity of the source. Accurate parallax distances to objects in our Galaxy are needed to minimize the propagation of such errors along subsequent rungs in the distance ladder scheme.

One constraint is that the size of parallax angles which can be measured in practice are limited. The maximum baseline which is subtended by Earth's motion around the Sun sets a natural bound to the apparent change in position of foreground objects. The three recent high–profile parallax experiments are the High Precision Parallax Collecting Satellite (Hipparcos; Perryman et al. 1995), the Bar and Spiral Structure Legacy (BeSSeL; Reid et al. 2014, 2009a) and Gaia (launched in 2013; Perryman et al. 2001) surveys. The Hipparcos mission was conducted between 1989 – 1993 with the satellite having a measurement accuracy of 1 mas to about 120,000 stars, and to 2.5 million stars to a lesser accuracy. Gaia is a follow–

up mission and is expected to collect parallax data to ∼1 billion stars to typical accuracies of 10 μas (for stars over the range G = 3 − 12 mag), which corresponds to an accuracy of ∼10% at 10 kpc. In contrast to these satellite–based optical surveys, BeSSeL is in the radio regime and has made parallax measurements to an excess of 100 masers in HMSFRs to typical accuracies of 10 μas well. This is significant as radio waves are not affected by interstellar extinction which will limit the number and distance of sources for which Gaia can measure parallaxes close to the Galactic Plane. The current technological limit for accuracy in parallax measurements is ∼5 μas, corresponding to an accuracy of 5% at 10 kpc (Reid & Honma 2014).

1.1.2 Kinematic distance

The kinematic distance to sources in the Galactic Plane (typically up to 20 kpc) can be determined from a model which describes the rotational speed of the disk for a given Galactic radius (i.e. $\Theta(R)$). Common models assume constant rotation of the disk (which may include a term for non–linearity; Reid et al. 2014), empirically determined functions of radius (Clemens 1985), power–law parameterization (Brand & Blitz 1993) or a universal rotation curve which can include terms for an exponential disk and Galactic halo (Persic et al. 1996). The distance to an object can then be calculated from measuring the local standard of rest velocity (v_{lsr}) to it. Kinematic distances assume that the Doppler shifts in the observed spectrum are entirely due to the rotation of the source by virtue of its position in the Galactic Plane.

This technique is notorious for introducing a distance ambiguity which is intrinsic to the geometric properties of the model. The ambiguity arises for sources which are found in the region enclosed by the circular orbit of the Sun about the Galactic Centre. Each measured radial velocity corresponds to two valid distances, on either side of the object's circular orbit, and equidistant from the tangent point as shown in Figure 1.1. Only sources that lie on the tangent point are immune to this effect.

Extensive catalogues of Galactic sources with known kinematic distances continue to be an indispensable resource for astronomers researching molecular cloud clumps (Roman-Duval et al. 2009), HMSFRs (Green & McClure-Griffiths 2011; Caswell et al. 2010) and Galactic structure (Clemens 1985), with the ambiguity being resolved with HI absorption against HII continuum (Jones et al. 2013; Jones & Dickey 2012; Busfield et al. 2006), HI Self–absorption (HISA; Green & McClure-Griffiths 2011; Roman-Duval et al. 2009) or statistical techniques which place constrains on distance probabilities to resolve the ambiguity (e.g. Ellsworth-Bowers et al. 2013). Significant errors are introduced into the distance when there are large peculiar motions, broad spectral line profiles and uncertainties in the model parameters, frequently resulting in uncertainties in distance estimates of 50% or greater.

1.1.3 Hertzsprung–Russell diagrams

Hertzsprung–Russell (HR) diagrams are plots of the absolute magnitude luminosities of stars versus their spectral type or colour. These diagrams show clearly that stars of different luminosities are not randomly distributed with spectral type but instead fall into distinct

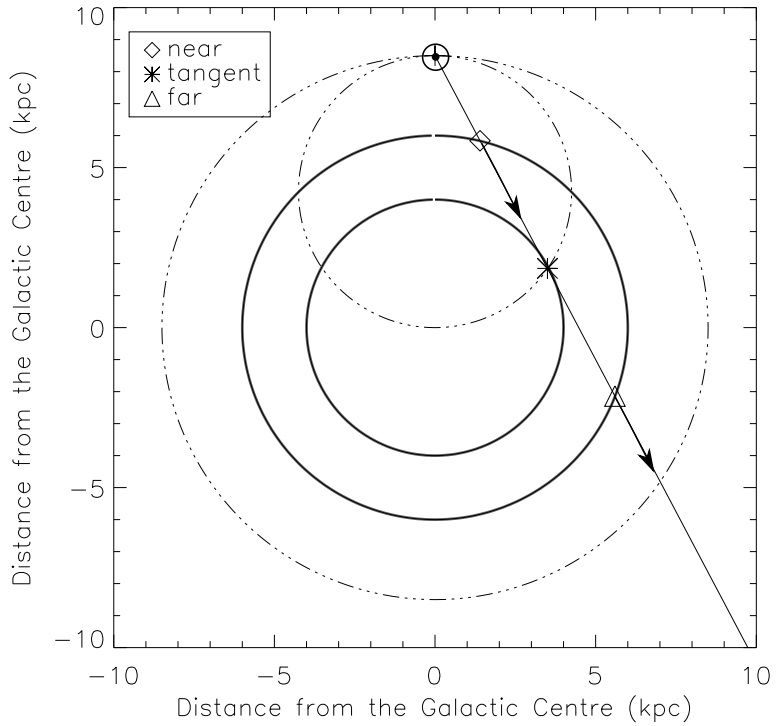

Figure 1.1: An illustration of the kinematic distance ambiguity adopted from Urquhart et al. (2012). The large dashed circle marks the solar orbit around the Galactic Centre with the Sun at $(0\,, 8.5)$ kpc. The arrows describe the line–of–sight radial velocities corresponding to *near* and *far* distances for a particular orbit. Only the tangent point velocity can be unambiguously determined. The locus of the available tangent points is shown by the small dashed–dotted circle.

regions based on their physical properties (see Figure 1.2). Since this discovery, stars have been classified into the white–dwarf, main sequence, giant, sub–giant and other groups based on their location in the HR diagram (Sowell et al. 2007; Perryman et al. 1995). HR diagrams provide basic data for astronomers seeking to understand the structure and evolution of stars and stellar clusters (Siegel et al. 2002), and also provide a means to determine the distances to stellar clusters in what is known as *photometric parallax*. If the stellar classification is known (e.g. main sequence), its luminosity (L) can be determined from the location of the star on the HR diagram by virtue of its observed colour and apparent brightness (F) while accounting for extinction. The distance (D) is then determined using a simple relation

$$F = \frac{L}{4\pi D^2}$$

The distances to M29 (Straižys et al. 2014), the Pleiades (An et al. 2007b; Percival et al. 2005) as well as the Large Magellanic Cloud (LMC; An et al. 2007a) have been determined using this method. The distances to stellar clusters in the LMC are especially important as variable stars and supernovae in this nearby dwarf galaxy act as important rungs in the cosmic distance ladder system.

In order for this technique to be effective, there is a need for the stars in a particular cluster to be well sampled so that the source in question can be identified as belonging to a particular family. Errors are introduced as a result of extinction and reddening in the interstellar medium (ISM), and the determined relative luminosity uncertainties from HR diagrams are typically $\sim$0.2 – 0.3 mag, corresponding to an accuracy of 10% at 10 kpc. Chen et al. (2015) report that they can be as great as $0.5 - 1.0$ mag which is unacceptable for distance measurement.

1.1.4 Variable stars

Variable stars are evolved main sequence stars which are in transit through an instability strip in the HR diagram. They are not in gravitational and hydrostatic equilibrium, which causes them to swell and contract resulting a period–luminosity (PL) relation which can be used for distance calibration if well constrained.

Cepheid and RR Lyrae variables were amongst the first type of variable stars which were discovered and will be the focus here due to their usefulness in the Galactic distance scale. There is an ever increasing classification of variable stars especially as sub–categories are discovered within established families. Examples of these include Beta Cephei, Delta Scuti, Mira variables, SX Phoenicis and Wolf-Rayet varieties. The assumption that Cepheid and RR Lyrae variable stars which were once thought to pulsate at well calibrated luminosities are continuously being challenged and refined (e.g. McNamara & Barnes 2014; Pejcha & Kochanek 2012; Sandage & Tammann 2006; Tanvir et al. 2005; Pritzl et al. 2001).

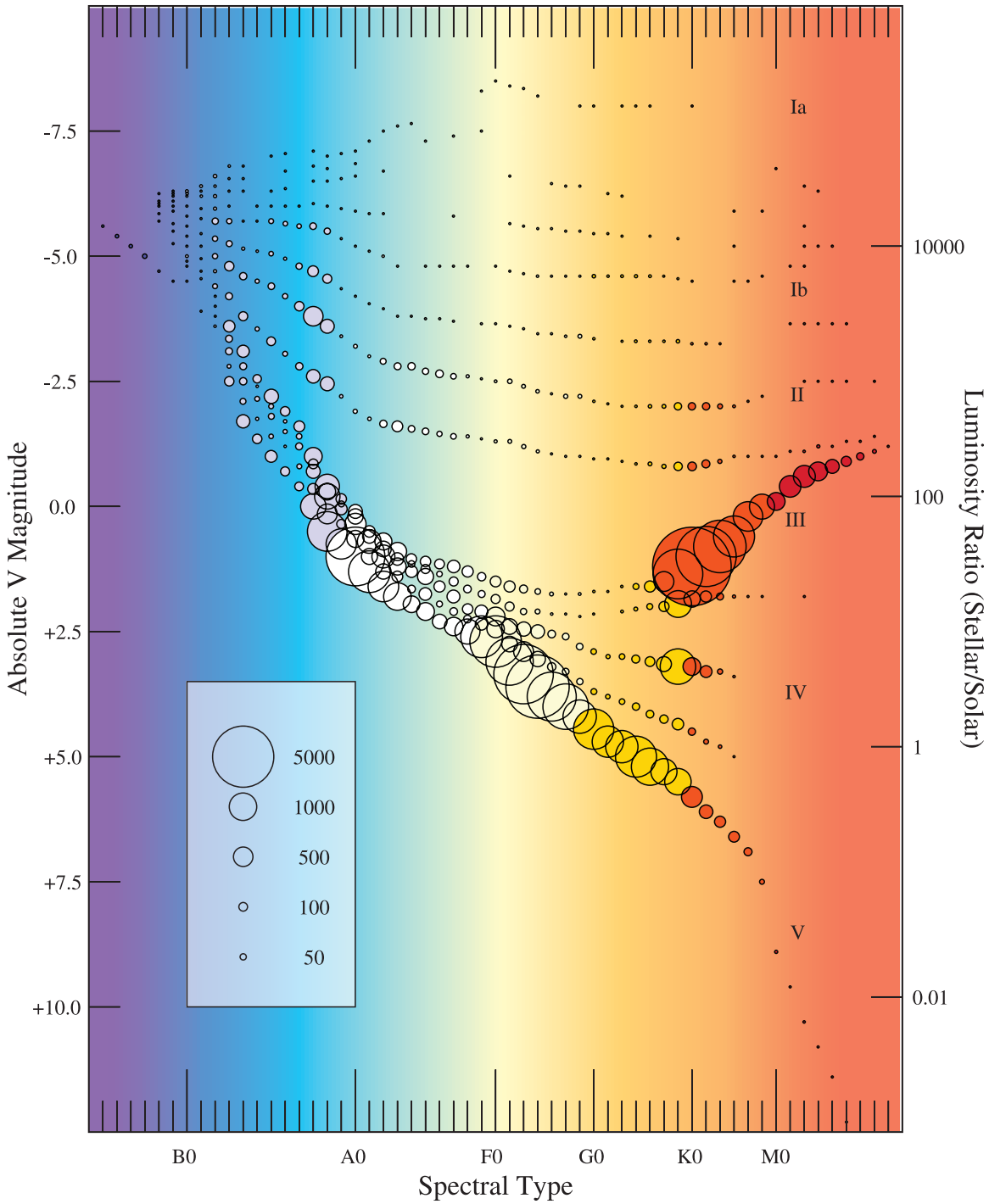

Figure 1.2: A HR diagram containing 113,286 stars from Sowell et al. (2007). Each circle represents the number of stars per spectral type and luminosity class.

Cepheid variables

Cepheid variables are massive stars (>8 $M_{\odot}$) first classified by Leavitt & Pickering (1912), and are in transit through the instability strip of the HR diagram. They shine with an apparent magnitude of $M_v \approx -4$ (for a Cepheid of $P \approx 10$ days), and with brightness variations of $M_v \sim 1$. Distances to Cepheid variables are determined from the well–behaved PL relation which governs their energy output (Chiosi et al. 1993). Cepheid variables are famous for providing the first direct evidence that the Milky Way is not the only galaxy in the Universe, when Hubble (1925) used them to determine the distance to M31, Andromeda.

Cepheid variables are relatively young stars and are therefore found in abundance in spiral galaxies. Over 200 distances to Cepheid variables have been calibrated using parallax data from *Hipparcos* (Di Benedetto 2002) as well as through searches towards Galactic Cepheids (e.g. Chen et al. 2015), and the Hubble space telescope (e.g. Riess et al. 2014; Benedict et al. 2007) to ∼0.04 mag which corresponds to a 5% uncertainty at 10 kpc. These characteristics make Cepheid variables an indispensable tool in measuring distances to nearby Galaxies. However, the ability to resolve individual Cepheid variables is constrained to ∼30 Mpc with even the most advanced instruments such as *Hubble* (Freedman et al. 2001). Current investigations are being undertaken on the use of ultralong–period Cepheids for distances greater than 100 Mpc (Fiorentino et al. 2012; Bird et al. 2009). However significant improvement in the calibration techniques are required before this becomes viable, as exemplified by the current error of 0.76 mag to M31 using these (Ngeow et al. 2015). Accomplishing this feat is of importance to the distance ladder for calibration of type Ia supernovae outside the 30 Mpc range of current Cepheids.

RR Lyrae variables

RR Lyrae stars are core helium–burning stars which are found within the instability strip in the horizontal–branch region of the HR diagram (Cacciari 2013; Cassisi et al. 2004). Like the Cepheids, their light–curves follow a PL relation which allows them to be used as standard candles. RR Lyrae stars are relatively low mass and less luminous than Cepheid variables, and so are commonly used to map the structure of the Milky Way rather than for distance measurements to external galaxies (Navarrete et al. 2015; Cacciari 2013; Cacciari et al. 2005; Layden et al. 1996). They are typically $>10^9$ yr old Population II stars (e.g. Marconi et al. 2001), and belong to systems which do not contain Cepheid variables (e.g. Amigo et al. 2013; Cohen et al. 2011; Clement et al. 2001). There are presently more than 2000 known RR Lyrae in Milky Way Galactic globular clusters (Dambis et al. 2013; Clement et al. 2001) with periods ranging between 0.2 – 0.9 days (Skarka 2014). RR Lyrae stars have been used to measure distances to the Small and Large Magellanic clouds (Deb & Singh 2010; Clementini et al. 2002), nearby dwarf galaxies (Greco et al. 2009; Poretti et al. 2008; Greco et al. 2007) and numerous globular clusters within the Milky Way (e.g. Navarrete et al. 2015; Braga et al. 2015; Jurcsik et al. 2014; Kunder et al. 2013). The distances obtained from the PL relationship are consistent with trigonometric parallaxes to ∼10% (Marconi et al. 2005), and recent results have shown that a precision to better than 0.1 mag corresponding to errors better than 2 – 3% may be possible in some cases (e.g. Braga et al. 2015).

1.2 Parallaxes distances to HMSFRs

The parallax distances which are introduced in Section 1.1.1 form the fundamental rung of the astronomical distance ladder system. The focus of this thesis will be on using the Very Long Baseline Interferometry (VLBI) technique to make accurate astrometric measurements of 6.7 GHz methanol masers in the Milky Way galaxy. Once (at least) 4 epochs of observations have been obtained, the faint parallax signature and proper motion of the masers is determined from the measured positions.

The class II 6.7 GHz methanol masers (see Section 2.1) are also closely associated ($\sim$0.1 pc) with HMSFRs that are deeply embedded in dense molecular clouds forming the spiral arms of the Milky Way galaxy. Therefore the parallax distances to these sources are used to characterise the detailed structure of the Galactic arms (Brunthaler et al. 2011). Thus far, all the parallax distances to HMSFRs in the Milky Way have been obtained from Northern Hemisphere VLBI instruments. However, for the purposes of accurate astrometry, a large portion of the Galaxy is beyond the reach of the Northern Hemisphere telescopes (Honma et al. 2008).

In this thesis, I explore how the inaugural Southern Hemisphere observations are providing data to the Northern Hemisphere Bar and Spiral Structure Legacy (BeSSeL) survey, to determine the shape and dynamical properties of the Galaxy. Chapters 2 and 3 provide an overview of the interstellar masers which are the focus of our observations, and Chapter 4 introduces the HMSFRs which they are associated with. In Chapter 5, I introduce the phase–referenced and tropospheric calibration techniques which we employed for our observations, before proceeding to data reduction in Chapter 6. I present the inaugural results from the Southern Hemisphere 6.7 GHz methanol maser parallax program in Chapters 7 and 8, before providing a summary of my findings in Chapter 9.

Chapter 2

Interstellar Masers

The spectrum which is obtained from astronomical sources has been pivotal in advancing our understanding of the chemical, dynamical and thermal structure of these objects. This is because the particles within the sources emit or absorb radiation at particular energy levels, manifesting at specific locations in their observed spectrum, thus allowing them to be identified and compared with known elements on Earth. In maser emission, molecules are pumped to an energetically excited state through stimulation and return to a ground (or more stable) state by releasing photons at specific wavelengths. Such an emitted photon might be reabsorbed by a neighbouring ground state molecule, which is then energized to an excited state until it too undergoes spontaneous emission. This process of absorption and emission is repeated, resulting in a chain reaction in the molecular environment. If the conditions in the medium are favourable (e.g Cragg et al. 2002, 1992; Elitzur 1976; Cook 1968) the emission of photons can be amplified via a collimation process into coherent beams known as masers.

Astrophysical masers are prominent, point–like radio sources, which are associated with interstellar and stellar sources, as well as with galactic nuclei, comets and planets. A detailed survey of all masing sources and their associated molecules and transitions is therefore beyond the scope of a single review, and the focus of this thesis will be on interstellar masers associated with HMSF. Masing activity in HMSF occurs within relatively dense conditions, with a highly luminous source to provide the pumping energy. The maser molecules themselves are in the immediate region surrounding the protostellar source, and are hence referred to as *interstellar* masers (Reid & Moran 1981). Research into maser emission associated with HMSFRs has been focused on the class II methanol masers characterised by the 6.7 and 12.2 GHz transitions, class I methanol masers in the 44 GHz transition, water masers at 22 GHz and OH masers at 1.6 GHz. Where there has been an overlap of these, comparative studies of HMSF masing regions (Forster & Caswell 1999, 1989; Caswell 1997; Caswell et al. 1995a) suggests that the maser spots (except class I methanol and water masers) are usually contained within a region of 30 mpc ($\sim$6200 AU), corresponding to an angular diameter of about $1''$ at typical distances of 6 kpc to HMSFRs in our Galaxy (Breen et al. 2010a; Caswell 1997; Forster & Caswell 1989). The study of masers has shed light on the HMSF process by characterising circumstellar disks, bipolar outflows, magnetic fields and internal motions; and are beginning to provide a rudimentary timeline for classifying the evolutionary stage of young high–mass stars.

2.1 Methanol

The methanol emission of masers is a common and well–studied species, initially detected by Barrett et al. (1971). The methanol molecule has a rich radio and millimetre wavelength spectrum, and more than 30 transitions have been observed to exhibit maser emission (Müller et al. 2004) which are grouped into class I and class II varieties (Menten 1991a; Batrla et al. 1987). The two classes distinguish the masers by virtue of the different pumping mechanisms which produce the emission. Class I sources are believed to be collisionally excited, whereas class II masers undergo radiative excitation from infrared photons. Due to the different conditions which give rise to their spectra, class I masers are associated with the distant parts of the outflows (Voronkov et al. 2006; Cyganowski et al. 2009) or other shocks (Voronkov et al. 2010b) in HMSFRs, and class II masers are associated close to the young star at distances of $\sim 10^3$ AU (e.g. Ellingsen 2006; Minier et al. 2001, 2000).

Class II

The 6.7 and 12.2 GHz class II methanol masers are two of the strongest and best studied transitions of astrophysical maser emission. Even though it has been shown that the physical conditions responsible for both transitions are similar (Cragg et al. 2005), and that they are closely associated (Moscadelli et al. 2002; Minier et al. 2002; Norris et al. 1993), the 12.2 GHz masers form a complete subset of the 6.7 GHz emission with the former aligning in velocity to either the primary or one of the secondary features of the latter (Breen et al. 2012b; Caswell et al. 1995b).

Class II methanol masers are pumped by radiative excitation of the methanol molecule (Sutton et al. 2001), and Cragg et al. (2002, 2005) show that the physical conditions giving rise to these masers are quite similar. The 6.7 and 12.2 GHz class II masers are thought to require warm temperatures of $\sim$150 K within clouds of densities $10^6 - 10^7$ cm^{-3}, typical of HMSFRs. The 6.7 GHz masers almost always have higher flux densities and broader velocity ranges than the 12.2 GHz transition (Breen et al. 2011), and $\sim$55% of 6.7 GHz do not exhibit corresponding 12.2 GHz emission (Breen et al. 2014, 2012b,a), it is thought that the physical conditions in these masing regions must be close to the point of onset or termination of the 12.2 GHz masers. The 6.7 GHz maser is an important transition for astronomers, as it is exclusively observed towards HMSFRs (Breen et al. 2013).

Methanol masers are typically known to trace the evolutionary stage of HMSF lasting between $10^3 - 10^4$ years (Kurtz et al. 2000). Evidence suggests that they are observed during the final period of the hot molecular core stage (see Section 4.2) of the young stellar object (de Villiers et al. 2015; van der Tak et al. 2000) and they are therefore often seen prior to any OH maser emission or the onset of HII regions (Beuther et al. 2002; Caswell 2001; Phillips et al. 1998a; Walsh et al. 1998). Breen et al. (2011, 2010b) show that the luminosity of 6.7 and 12.2 GHz masers increases for more evolved young stellar objects, and correspond to regions which exhibit OH maser emission or cm–wavelength continuum emission. Generally, only one or two 6.7 or 12.2 GHz maser sites are observed in a given HMSFR, and the masers are distributed on scales an order of magnitude smaller than the class I masers (0.1 pc as opposed to 1 pc; Menten 1991b).

Norris et al. (1993) proposed that strong 6.7 GHz methanol masers showed preferential spatial and velocity distribution along lines or arcs, indicating that they may be associated with shock fronts, jets, or edge–on circumstellar disks. The circumstellar disk hypothesis has been further supported by Moscadelli et al. (2011); Pestalozzi et al. (2004), however te Lintel Hekkert et al. (1992) show that masers in collimated outflows can also display the observed spatial and velocity gradients. Minier et al. (2000) present a case where the linear distribution of masers can result from the layer between the ionization and shock fronts surrounding an HII region (with no requirement for a velocity gradient) and Bartkiewicz et al. (2014) model the 6.7 GHz methanol maser ring in G 23.657−0.127 as an outflow or/and an interaction zone between the outflow and accretion disk. While the results from Bartkiewicz et al. (2014); Minier et al. (2000); Walsh et al. (1998) provide evidence against the masers tracing circumstellar disks, the linear spatial and velocity gradients observed in class II masers continue to be in contrast to the energetic outflows which contain class I methanol, water and OH maser emission. The spectra of methanol masers have small velocity ranges with a median 6 km s^{-1} (Caswell et al. 2014, 2009) and which fall within 3 km s^{-1} of the systemic velocity of their associated molecular cloud (Szymczak et al. 2007). The v_{lsr} of methanol maser emission is therefore used to provide reliable kinematic distances to the associated HMSFRs (e.g. Green & McClure-Griffiths 2011). Unlike water and OH masers, class II methanol masers can be stable over timescales spanning decades, (Ellingsen et al. 2007; Caswell et al. 1995a).

The class II methanol masers have been extensively catalogued in the methanol multibeam (MMB) survey at 6.7 GHz spanning Galactic Longitudes 345° – 6° (Caswell et al. 2010), 6° – 20° (Green et al. 2010), 330° – 345° (Caswell et al. 2011c), 186° – 330° (Green et al. 2012b) and 20° – 60° (Breen et al. 2015), and at 12.2 GHz spanning Longitudes 330° – 10° (Breen et al. 2012b), 186° – 330° (Breen et al. 2012a), 10° – 20° (Breen et al. 2014).

Examples of rare class II methanol maser transitions include transitions at 19.9, 37.7, 104.1, 107.0, 156.6, 216.9 GHz and are thought to signpost unusual sources (e.g. Ellingsen et al. 2012; Caswell et al. 2000), exceptional physical conditions in the associated region (e.g. Caswell et al. 2000; Val'tts et al. 1995) or a relatively brief evolutionary phase in the HMSF process (e.g. Krishnan et al. 2013; Ellingsen et al. 2003).

The stability of the 6.7 and 12.2 GHz methanol maser emission and their ubiquitous association with HMSFRs have made these the prime targets for parallax distance measurements in the BeSSeL survey (see Section 4.4.2).

Class I

These masers are known to result from the collisionally excited methanol molecule which reside in the shocks from outflows (Voronkov et al. 2010a), cloud–cloud interactions (Mehringer & Snyder 1996) or expanding HII regions (Fish & Reid 2006) of HMSFRs. Studies show that the pumping mechanisms responsible for class I and class II masers are competitive (Voronkov et al. 2005; Voronkov 1999; Cragg et al. 1992), with strong radiation from nearby infrared sources quenching class I masers and strengthening class II maser emission, explaining why the two varieties are observed in different locations. Class I methanol masers have also been observed toward lower–mass young stars (Kalenskii et al. 2010) and supernova remnants

(Pihlström et al. 2014). More than 20 transitions can produce class I masers, with more than half in the 25 – 30 GHz range (Voronkov et al. 2006; Müller et al. 2004). The most well studied of these are at the 44 and 95 GHz transitions. However, observations have also been made of the 23.4, 25.0, 36.2, 84 GHz as well as rare 9.9 and 104 GHz transitions.

Several authors have observed high detection rates of class I methanol masers associated with shock traced Extended Green Objects (EGOs; e.g. Chen et al. 2011, 2009; Cyganowski et al. 2009). These *green fuzzies* catalogued by Cyganowski et al. (2008) appear to be associated with infrared dark clouds (see Section 4.1) containing deeply embedded young massive stars. De Buizer & Vacca (2010) showed that EGOs exhibit high flux in the 4.5 μm band. This is significant as the band interval from 4 to 5 μm contains some prominent spectral lines from molecular hydrogen (H_2) and carbon monoxide (CO), commonly seen in outflow emission associated with protostars accreting material from the surrounding cloud (e.g. Plunkett et al. 2015; Teixeira et al. 2012).

Research into methanol masers has been dominated by class II objects with ∼1000 sources catalogued in the MMB surveys. In comparison, only ∼400 class I masers are known from single dish (e.g Jordan et al. 2015; Chen et al. 2011; Fontani et al. 2010; Ellingsen et al. 2005; Val'tts et al. 2000; Slysh et al. 1994; Haschick et al. 1990) and high–resolution surveys (e.g. Voronkov et al. 2014; Cyganowski et al. 2009; Kurtz et al. 2004). VLBI observations of class I masers have only recently been successfully made by Matsumoto et al. (2014).

The HMSF evolutionary phase linking class I and class II masers is not well constrained. Breen et al. (2010b); Ellingsen et al. (2007) place class I sources as the earliest detectable maser type on their evolutionary diagram. However, it is shown that these masers can outlast the class II, 6.7 GHz emission, and to overlap with OH masers observations (known to trace the later evolutionary stages; Voronkov et al. 2012, and references therein). Thus it is possible that class I masers are observed more than once during the HMSF process (Cyganowski et al. 2012; Chen et al. 2011).

2.2 Water

Cheung et al. (1969) made the first observations of water masers which are now regarded as one of the best indicators of low– and HMSFRs (e.g. Lyo et al. 2014). They are more populous and stronger than the OH and methanol varieties (Walsh et al. 2011), with W49N having an isotropic luminosity of 0.1 $L_\odot$ (Walker et al. 1982). Breen et al. (2010a) find that 79% out of 202 OH star formation maser sites show coincident water maser emission. In addition to HMSFRs, water masers are associated with a variety of astronomical objects including Active Galactic Nuclei (AGNs; Zhu et al. 2011), the envelopes of Asymptotic Giant Branch (AGB) stars (Dodson et al. 2014; Walsh et al. 2009), late M–type stars (Lekht et al. 2005), planetary nebulae (Miranda et al. 2001), Mira variables (Hinkle & Barnes 1979) and even in comets (Cosmovici et al. 2014). Water masers were also observed when Shoemaker–Levy 9 collided with Jupiter (Cosmovici et al. 1996), and this has spurred on the search for water masers in exoplanets (Cosmovici et al. 2010; Minier & Lineweaver 2006). Research into water masers in HMSFRs has primarily been focused on the 22 GHz line.

Water masers are collisionally pumped, and are observed towards molecular regions with

high gas densities $10^7 - 10^9$ cm^{-3} and temperatures of ∼400 K (Hollenbach et al. 2013; Elitzur et al. 1989). These conditions are consistent with the inner parts of circumstellar disks (Torrelles et al. 1998), high–velocity bipolar outflows perpendicular to circumstellar disks (Torrelles et al. 1998; Hofner & Churchwell 1996) and bow shocks, at distances of ∼10 – 10^3 AU from the central source (e.g. Sanna et al. 2012; Trinidad et al. 2003; Torrelles et al. 2003). The conditions required for water maser emission to be observed is similar to that of methanol maser emission, except that methanol masers require lower gas temperatures, and are quenched at gas densities of $>10^8$ cm^{-3} (Cragg et al. 2005, 2002).

Water masers are more variable compared to OH and methanol masers (Colom et al. 2015; Caswell & Breen 2010; Felli et al. 2007), with the most steady features found to occur at velocities close to that of the associated molecular cloud (Felli et al. 2007; Brand et al. 2003) and in the most luminous sources (Brand 2008). The 22 GHz transition has been observed to vary dramatically in amplitude on monthly timescales (Engels et al. 1999) and Breen et al. (2010a) find few common features in their maser observations spread over 2 decades. This echos the results from Batchelor et al. (1980) who show that only slightly more than half of the water maser features observed in one epoch were found to be present during an earlier or later observation. The reason for this variability has been attributed to turbulence in the masing region which results in fluctuations in the pumping action, density, path length, temperature or shock fronts (Sullivan 1971). Caswell & Breen (2010); Breen et al. (2010a) show that the variability in the spectra has little effect on the position of the masers at arcsecond accuracy.

Unlike methanol and OH masers, water masers display velocity features which deviate from the systemic velocity by several hundreds of km s^{-1} (e.g. Titmarsh et al. 2013; Walsh et al. 2011, 2009). Walsh et al. (2011) report that this occurrence of maser sites with high–velocity features is relatively rare, with only 10% of the 540 sources spanning velocity ranges >50 km s^{-1} with the highest at 351.3 km s^{-1}. However, this percentage is likely to be higher, as the observations were made from low sensitivity single dish observations. The relatively high–velocities can be attributed to these masers tracing energetic outflows, in contrast to 6.7 GHz methanol masers which are never associated with outflows (Caswell et al. 1995b). Like methanol masers, water masers are also present at the early stages of star formation, prior to the onset of OH maser emission (Breen et al. 2010a).

Dust clumps are embedded within the molecular clouds from which stars are born (Gómez et al. 2014), and Breen & Ellingsen (2011) show that 128 out of the 294, 1.2 mm dust clumps exhibited water maser emission, further demonstrating a correspondence between maser and dust clump peak emission. Water masers are shown to be associated with the bigger, more massive young stellar objects with higher peak and integrated flux densities (Titmarsh et al. 2014; Breen & Ellingsen 2011) and the most luminous water masers were preferentially detected towards regions which exhibit 6.7 GHz methanol emission and 8 GHz radio continuum. The collective observations of Titmarsh et al. (2014); Breen & Ellingsen (2011); Breen et al. (2010a) show that water masers can be present at an even earlier evolutionary stage than the methanol masers and outlast them to a period when OH masers and HII regions form. However, pending further research, the duration of water maser emission remains one of the greatest uncertainties in the maser evolutionary sequence of HMSF.

Surveys of water masers have been less comprehensive than methanol masers. This has been partly due to the variable nature of the emission (Caswell et al. 2011a; Caswell & Breen 2010). Early targeted water maser searches in the Southern Hemisphere have been conducted with Parkes (Caswell et al. 1989, 1983), with more recent searches by Caswell et al. (2011a); Caswell & Breen (2010); Breen et al. (2007) covering small regions of the Galactic Plane or have focused on HMSFRs based on IRAS colours (Sunada et al. 2007) or other maser species (e.g. Titmarsh et al. 2014). Walsh et al. (2014, 2011) conducted an untargeted search for water masers in the H_2O Southern Galactic Plane Survey (HOPS) survey between $290° < \ell < 360°$, $0° < \ell < 30°$ and $0.5° < b < -0.5°$, with an RMS between 1 and 2 Jy. Out of the 631 maser sites observed, Walsh et al. (2014) classify 433 as associated with star formation, 121 with evolved stars and 77 as unknown sources. In the Northern Hemisphere, Brand (2008); Felli et al. (2007); Valdettaro et al. (2002) have conducted decade–long observations of water masers towards more than 40 HMSFRs in order to summarize the general properties of water maser emission and draw conclusions between the various emission parameters (e.g. periodicity, flux density, v_{lsr}). A preliminary analysis of the results is presented in Brand et al. (2003) who demonstrate that for far–infrared (FIR) luminosity sources of $>10^4$ $L_\odot$, the water maser emission is more structured and extended in the velocity range. Brand et al. (2003) show that there is some evidence for periodicity in the maser emission of $\sim$5.5 years for several of their sources and up to $\sim$8 years in L1204–A. The periodicity is interpreted to be as a result of cyclic variations in the wind/jets from the central source responsible for the water maser emission.

There are currently no definitive studies to categorize the association of water masers with low– or high–mass star formation, however Walsh et al. (2014) argue that at least 40% of water masers are associated with HMSF based on their association (up to $4''$) with class II methanol masers. Results from HOPS suggests that water masers associated with evolved stars tend to have more maser spectral components than those associated with star formation.

Bright rimmed clouds (BRCs) are observed at mm wavelengths towards star formation regions where the photon ionized gas collides with the neutral surrounding gas (e.g Paron et al. 2015). Valdettaro et al. (2005) found only 3 water maser detections from 44 BRC in Sugitani et al. (1991), and propose a model to suggest that BRCs are associated with predominantly young low–mass stars. If this relationship is further verified, then water maser emission associated with BRCs can be preferentially attributed to low–mass star formation regions.

VLBI astrometric measurements of water masers have also been used to determine parallax distances to the spiral arms of our Galaxy as part of the BeSSeL survey (Asaki et al. 2014; Kusuno et al. 2013; Asaki et al. 2010; Hachisuka et al. 2006).

2.3 OH

The first detection of an astrophysical maser was of the 1665 MHz transition by Weaver et al. (1965). The emission was confirmed to be an OH maser by (Moran et al. 1978), who made VLBI observations of the HMSFR in W3(OH), and concluded that the brightness temperatures of the individual components was too high to be thermal in nature. OH masers have since been observed towards supernova remnants (Brogan et al. 2013), comets (Galt

1998), AGB stars (Gonidakis et al. 2014) and megamaser sources (Migenes et al. 2011). Current research into OH masers emission associated with HMSFRs is mainly focused on the strongest lines at 1665 and 1667 MHz, though weaker transitions have been observed at 1612, 1720, 4765, 6030, 6035, 13441 MHz.

OH masers are commonly believed to be found in the compressed zone just outside the expanding HII region associated with young stellar objects (Cook 1968). They are radiatively and collisionally pumped in warm molecular clouds of $100 - 200$ K with gas densities of $10^3 - 10^5$ cm^{-3} and column densities of $10^5 - 10^9$ cm^{-3} (Cragg et al. 2002; Pavlakis & Kylafis 2000). The common transitions at 1665 and 1667 MHz are coincident to $\sim 1''$ Caswell (1998), and can be found in a region within $10^2 - 10^3$ AU from the central star (e.g. Colom et al. 2015; Argon et al. 2000).

OH masers in HMSFRs show variability of up to a factor of two in the relative amplitudes of the individual peaks over a period of years (e.g. Colom et al. 2015; Fujisawa et al. 2014; Green et al. 2012a). However sources with stable spectra have also been observed over the course of decades (Caswell 1998). Caswell et al. (2014, 2013) argue that OH masers associated with HMSFRs can be split into two varieties based on the spread of the spectrum around the median velocity of the emission. In their sample, the first group of 101 sources show a spread of 8.3 km s^{-1} (similar to methanol maser emission) and the second group of 15 sources show a spread of >25 km s^{-1} (similar to water maser emission). The first variety arises in the late stage of the maser evolution scheme where the expansion is driven by an enclosed HII region, resulting in blue and red shifted OH maser emission from either side of the bubble. The second variety appear to be from collimated outflows which are the driving force of water masers, showing the preferentially blue shifted maser emission which are observed with water masers as well (Caswell & Phillips 2008). Caswell et al. (2014) explain that more observations are required before a statistical catalogue of the blue shifted OH masers is available to examine any preference of blue shifted OH maser emission (e.g. Caswell et al. 2011a; Caswell & Phillips 2008).

The OH molecule is paramagnetic and hence exhibits Zeeman splitting when exposed to a magnetic field. This effect has been well documented in over 400 sites of HMSF by (Caswell et al. 2014, 2013; Fish et al. 2003; Argon et al. 2000). A field of strength $\sim 10^{-3}$ G will split the OH emission into left and right circular polarization components, greater than a line's width (Elitzur 1992). The splitting is proportional to the magnetic field allowing it to be probed directly. Magnetic fields of a few mG are common in star formation regions (Green et al. 2015; Fish et al. 2003; Caswell 2003, 1998) but fields of up to 40 mG have been observed (Fish & Reid 2007), along with polarity reversals and fluctuations (Caswell et al. 2011b). It is argued that periodic field reversals can be attributed to the masers arising in a torus (Wang et al. 2012; Hutawarakorn & Cohen 2005, 2003) or due to the changes in curvature of an expanding shell shocked by an HII region (Stark et al. 2007; Bourke et al. 2001). These observations suggest that magnetic fields are preserved even after a stellar collapse, meaning they can be useful in the study of large scale Galactic field patterns (Green et al. 2012b; Caswell et al. 2011c,b; Fish & Reid 2007).

Caswell (1997); Forster & Caswell (1989) find that OH masers are preferentially associated with a later phase of HMSF than water and methanol masers. This is clearly demonstrated

by Forster & Caswell (2000) who show that 15 out of 29 OH maser sites had an associated HII region, and made further arguments that the remaining 14 water maser sources were associated with HMSFRs in the pre–main sequence contraction phase. From their observations of the association of OH masers with MIR sources, Qiao et al. (2014) suggest that the stellar mass range associated with OH masers can extend to higher masses than that for methanol masers, or that the OH masers trace a later evolutionary phase than methanol masers because of the higher dust temperatures. Caswell et al. (2014) show that 82.4% of the OH masers are associated with methanol masers. However this high statistic was from a targeted survey towards methanol masers and so the authors maintain that the actual coincidence of both masers will be much lower and similar to detection statistics in Caswell (1998, 1997, 1996) should a blind survey be conducted. The remaining 17.6% of sources in Caswell et al. (2014) with no methanol maser emission are thought to be at a more evolved stage, and sensitive continuum measurements towards these will be required to test this hypothesis. Breen et al. (2010a) report a similarly high coincidence between OH and water maser emission of 79%, despite a difference in the pumping mechanisms which drives the different varieties of masers.

Catalogues of Galactic OH maser sources in comparison with methanol and water masers have also been made (Caswell 1998), showing that methanol and water masers are associated with ∼80% of OH maser sites. However, studies to examine the proportion of water and methanol maser sites that do not show OH emission has not been well constrained. A full polarization survey of known OH masers has been made by Caswell et al. (2014, 2013) in the Galactic range $240^\circ < \ell < 41^\circ$ and through the Galactic Centre.

2.4 Summary

Astrophysical masers are bright sources of radio emission associated with HMSFRs. Studies of their spectral characteristics have provided insight into the chemical, dynamical and thermal nature of young high–mass stars. The three common forms of maser emission which are explored in this chapter are limited to the methanol, water and OH varieties.

Methanol masers are classified into class I and II sources which are produced by different pumping mechanisms. Class I masers result from collisional excitation of the methanol molecule in the shocks from outflows, from cloud–to–cloud interactions or expanding HII regions at distances of ∼1 pc from the central source. Class II masers are radiatively excited from infrared photons and are found at distances of $\sim 10^3$ AU from the central source. Strong radiation which intensifies class II maser emission has been shown to quench class I masers. The 6.7 GHz methanol transition is an important and reliable identifier of HMSFRs, with both 6.7 and 12.2 GHz masers being prime targets in the search for circumstellar disks around massive young stellar sources. Class II methanol masers are thought to be associated with the final period of the HMC phase of HMSF, and are stable over timescales spanning decades.

Water masers are colllisionally pumped and observed towards regions in the inner parts of circumstellar disks, bipolar outflow regions and bow shocks at distances of $\sim 10 - 10^3$ AU from the central source. Their spectra can span several hundreds of km s^{-1} and are changeable over timescales of months. This variability has been attributed to turbulence in the masing region resulting from fluctuations in the pumping action, density, path length, temperature

or shock fronts. While water masers are associated with dust clumps of the earliest stages of HMSF, they are also known to outlast the methanol maser phase after the onset of HII regions.

The radiatively and collisionally pumped OH masers are found in the compressed zone just outside the expanding HII region $\sim 10 - 10^3$ AU from the central source. Their association with HII regions make them good traces of HMSFRs at the latter stages of formation. Caswell et al. (2014, 2013) categorize OH masers into two varieties based on the spread of spectrum around the median velocity. One class arises when the expanding HII region results in blue and red shifted OH maser emission from either side of the bubble. The other class appears to be from collimated outflows which give rise to water masers. The paramagnetic OH molecule exhibits Zeeman splitting proportional to the strength of the surrounding magnetic field. Observations of periodic field reversals have been used to hypothesize the existence of a torus around the central object or due to changes in curvature of an expanding HII region.

Research into astrophysical masers have help to characterise the HMSF process which will be introduced in the following chapter.

Chapter 3

The First High-Resolution Observations of 19.9 GHz Methanol Masers

As described in Chapter 2, methanol, water and OH molecules commonly show maser emission towards young HMSFRs. Amongst these, methanol has the richest spectrum in the radio and millimetre regime and shows the largest number (in excess of 30) of different maser transitions. The methanol maser transitions are empirically classified into two classes (Menten 1991a; Batrla et al. 1987). The class I maser transitions are collisionally pumped and are associated either with molecular outflows (Voronkov et al. 2006; Cyganowski et al. 2009), or other shocks (Voronkov et al. 2010b) within $\sim$1 pc of a young high–mass star (Kurtz et al. 2004). The best studied class I methanol masers are the 44.1 GHz (e.g. Cyganowski et al. 2009) and the 95.1 GHz (e.g. Chen et al. 2011) transitions. The class II methanol masers are found close to very young high–mass stars (e.g. Ellingsen 2006) and are often associated with ground–state OH masers (Caswell et al. 1995b) and water masers (Szymczak et al. 2005). The best studied class II methanol maser transitions are the 6.7 and 12.2 GHz. To date more than 900 class II methanol maser regions have been identified in the Galaxy, with a sensitive, complete survey of the Southern sky recently completed in the 6.7 GHz transition (Caswell et al. 2010, 2011c; Green et al. 2010, 2012b). In this chapter we focus solely upon class II methanol masers, of which a total of 18 different transitions, or transition groups have been identified to date (see Ellingsen et al. 2012, and references therein).

In total twenty–nine methanol maser sites have been searched for the class II 19.9 GHz methanol masers (Wilson et al. 1985; Menten & Batrla 1989; Ellingsen et al. 2004), resulting in nine detections. The search undertaken by Ellingsen et al. (2004) using the Tidbinbilla 70 m antenna was significantly more sensitive than most searches for rare, weak methanol maser transitions, and resulted in the detection of a number of sources with peak flux density less than 0.5 Jy. Ellingsen et al. (2004) also found that the 19.9 GHz methanol masers appeared to be preferentially associated with class II maser sites with an ultracompact (UC) HII region (see Section 4.3) and 6035 MHz OH masers. Seven of the nine known 19.9 GHz methanol maser sources are visible from the Southern Hemisphere, the two exceptions are W3(OH) and NGC7538.

The presence of an interstellar maser in a region signposts the presence of physical conditions capable of producing population inversion for that transition (e.g. Cragg et al. 2005). However, the intensity of the observed maser emission depends (non–linearly) on a number of factors, many of which are poorly constrained observationally, and so inferring the specific physical conditions in the maser region from observations of its intensity is in general not possible. Where comparative observations have been made of the 6.7 and 12.2 GHz methanol masers they show that emission at the same velocity is spatially coincident on scales of tens of milliarcseconds, or less (Menten et al. 1992; Norris et al. 1993; Minier et al. 2000). If there are multiple maser transitions observed from the same molecule and in the same general vicinity (sub–arcsecond scales), theoretical models are much better constrained as they are then required to reproduce both the presence of the different maser transitions, as well as the observed intensity ratio.

Multi–transition modelling using methanol masers has been undertaken in just a few sources which show emission in a larger number of transitions. Examples of such sources include W3(OH) (Sutton et al. 2001), NGC6334F and G 345.01 + 1.79 (Cragg et al. 2001). These studies used some low angular resolution (single–dish) data, and assume that where emission is observed at the same velocity it originates from the same region, in terms of spatial location and dimensions. The first of these assumptions is likely to be correct, as it has been explicitly demonstrated for the two strongest and most common class II methanol maser transitions. The second assumption: that the maser "spot" size is the same at all frequencies is not likely to be correct, as differences have been shown in studies of spatially coincident 6.7 and 12.2 GHz emission (Minier et al. 2002), however, in the absence of milliarcsecond–scale observations of all the transitions, it is the simplest one to make. The multi–transitional modelling of Sutton et al. (2001) and Cragg et al. (2001) find conditions in the masing region consistent with those expected in young, HMSFRs, with gas temperatures of around 30 K, dust temperatures of around 175 K and densities of 10^6 cm^{-3}.

While the assumption that emission from the different class II methanol maser transitions at the same velocity are spatially coincident seems to be generally true for 6.7 and 12.2 GHz methanol masers, high resolution studies of the less common class II masers are needed to determine if this property extends to other class II transitions. Here we present the first high–resolution observations of the 19.9 GHz methanol maser transition, which will allow us to determine the degree to which its emission is coincident with that observed in the 6.7 GHz (and 12.2 GHz) methanol maser transitions in the same regions.

3.1 Observations and data reduction

We have used the ATCA in the 6A configuration (baselines ranging from 337 to 5939m) to conduct high resolution 19.9 GHz observations towards nine Southern class II methanol maser sites. The sample includes the seven sources detected in the 19.9 GHz transition by Ellingsen et al. (2004) and two additional sources (G 309.921+0.479 & G 330.953−0.182) which were detected in later Tidbinbilla observations (unpublished). For each source we also observed the 6.7 GHz transition, and all measurements were made during a single session in 2005 March 27 (see Table 3.1 for details). The 19.9 GHz ($2_1 - 3_0$E) transition observations typically consisted

of either six or seven 5–minute scans on each target source over a range of hour angles. In some cases up to nine 5–minute observations were undertaken and the total time onsource for each target is given in Table 3.1. Each target–source observation was both preceded and followed by a 90–second scan on a phase calibrator, offset on the sky by between 2 – 12 degrees. For NGC6334F, observations were also made of the 23.1 GHz ($9_2-10_1\mathrm{A}^+$) transition of methanol. NGC6334F was considered for the observations at 23.1 GHz as it is the only source with known emission at this frequency which can be observed by the ATCA (Cragg et al. 2004). A total of six 5–minute scans of this source were made at 23.1 GHz, again over a range of hour angles and in between phase calibrator scans. These 23.1 GHz observations were undertaken after each 19.9 GHz scan of NGC6334F. The 6.7 GHz ($5_1 - 6_0A^+$) transition observations consisted of a total of three (or more) 90–second scans over a range of hour angles, preceded and followed by 90–second observations of the same phase calibrators as used in the 19.9 GHz observations. Table 3.1 gives the pointing centre for the observations, the total time on source for each transition and the name of the phase calibrator. Observations of the different maser transitions were interleaved to minimise the potential sources of error, in the absolute position of measurements at two different frequencies. A discussion of the observed difference in the absolute position of the different maser transitions is presented in Section 3.2.

PKS B1253−055 was observed as the bandpass calibrator for the 19.9 and 23.1 GHz observations. Primary flux density calibration is relative to PKS B1934−638 which was also used as the bandpass calibrator for the 6.7 GHz observations. The assumed flux densities for PKS B1934−638 were 3.92 Jy, 0.93 Jy and 0.80 Jy for the 6.7, 19.9 and 23.1 GHz transitions respectively and based on ATNF MIRIAD's built–in flux scale (Sault 2003; Reynolds 1994). The absolute flux density calibration is expected to be accurate to better than 10 percent.

The correlator was set to record 1024 spectral channels for both parallel– and cross–polarization products across a 4–MHz bandwidth for all frequencies. This corresponds to a velocity coverage of 179.8, 60.1 and 51.9 km s^{-1}, and channel separations of 0.176, 0.058 and 0.051 km s^{-1} at 6.7, 19.9 and 23.1 GHz respectively. With uniform weighting of the auto-correlation function, this corresponds to velocity resolutions of 0.211, 0.070 and 0.061 km s^{-1}.

Data reduction was performed using the MIRIAD package using the built–in model to correct for the differential opacity between the source and calibrators due to their slightly different elevations. Channels associated with line emission were deconvolved, and the spectra of the masers extracted (shown in Figure 3.1 and with details in Table 3.3). These were then imaged to determine the spatial distribution of the emission (Figures 3.2 to 3.9). The line–free spectral channels were averaged together before imaging to investigate the continuum emission associated with each of the maser targets (Figures 3.10 to 3.15 and Table 3.2.2). We adopted rest frequencies of 6.6685192(8), 19.9673961(2) and 23.1210242(5) GHz (numbers in brackets indicate the magnitude of uncertainty in the last digit) for the three observed methanol maser transitions (Müller et al. 2004). The uncertainty in the velocity scale due to the accuracy to which the rest frequencies have been determined are 0.036, 0.003 and 0.007 km s^{-1}, at 6.7, 19.9 and 23.1 GHz respectively (i.e. much less than the spectral resolution in each case). The synthesised beam size for the observations were approximately 0.6×0.4 arcsec^2 for sources at 19.9 and 23.1 GHz and 2.2×1.6 arcsec^2 for those at 6.7 GHz.

Table 3.1: Observation details. Target positions are based on the 6.7 GHz positions from Caswell et al. (1995c,a). The phase calibrator for NGC6334F at the 23.1 GHz observation was 1759−39.

Source Name	**RA (J2000)**	**Dec (J2000)**	**Observation Duration (mins)**			**Phase Calibrator**
	h m s	$^\circ$ $\prime$ $\prime\prime$	**19.9 GHz**	**6.7 GHz**	**23.1 GHz**	
G 309.921+0.479	13 50 41.77	−61 35 10.1	45	7		1352−63
G 323.740−0.263	15 31 45.45	−56 30 50.1	40	7		1511−55
G 328.808+0.633	15 55 48.45	−52 43 06.6	35	7		1511−55
G 330.953−0.182	16 09 52.83	−51 54 57.6	35	7		1613−586
G 339.884−1.259	16 52 04.66	−46 08 34.2	30	6		1646−50
G 345.003−0.223	17 05 10.89	−41 29 06.2	35	5		1729−37
G 345.010+1.792	16 56 47.58	−40 14 25.8	35	5		1729−37
NGC6334F	17 20 53.37	−35 47 01.2	30	3	30	1729−37
G 353.410−0.360	17 30 26.18	−34 41 45.6	34	4		1759−39

The absolute position of each maser transition was determined by imaging the velocity channel corresponding to the strongest emission at 19.9 GHz. We then fitted a 2D Gaussian, with the same dimensions as the synthesised beam, to the emission in the deconvolved image to determine the absolute position of the peak maser emission associated with the source. Once the absolute position of each maser source had been determined, we self–calibrated the strongest emission channel for the brighter sources and then applied these solutions to all other spectral channels for that source. The resulting improvement can be seen from comparison of the RMS noise of the image frames between those sources which have and have not been self–calibrated (Table 3.3). The RMS noise in the image of an individual spectral channel at 19.9 GHz if self–calibration was performed is typically <10 mJy/beam. The 19.9 GHz maser emission in G 328.808+0.633 and G 345.003−0.224 was too weak for reliable self–calibration and the associated image RMS for these sources is approximately a factor of 5 times greater. The RMS itself was measured from a square box of ∼10 arcsec^2 in a deconvolved image frame which was free from any maser emission and away from the pointing centre. Either one or two iterations of self–calibration (phase then amplitude), was undertaken using a one minute solution interval, using the clean components as the initial model. The use of self–calibration enabled us to more accurately investigate the relative distribution of the maser features within an individual source.

3.2 Results

The spectra of all observed 6.7, 19.9 and 23.1 GHz methanol masers (presented in Figure 3.1) have been extracted from regions of the image cube approximately the size of the synthesised beam (0.6″ at 19.9 and 23.1 GHz, and 2.0″ at 6.7 GHz), centred at the location of the strongest emission in the cube. In general, the 19.9 GHz methanol masers contrast with the 6.7 GHz masers which are much stronger (peak flux density >100 Jy) and cover a much

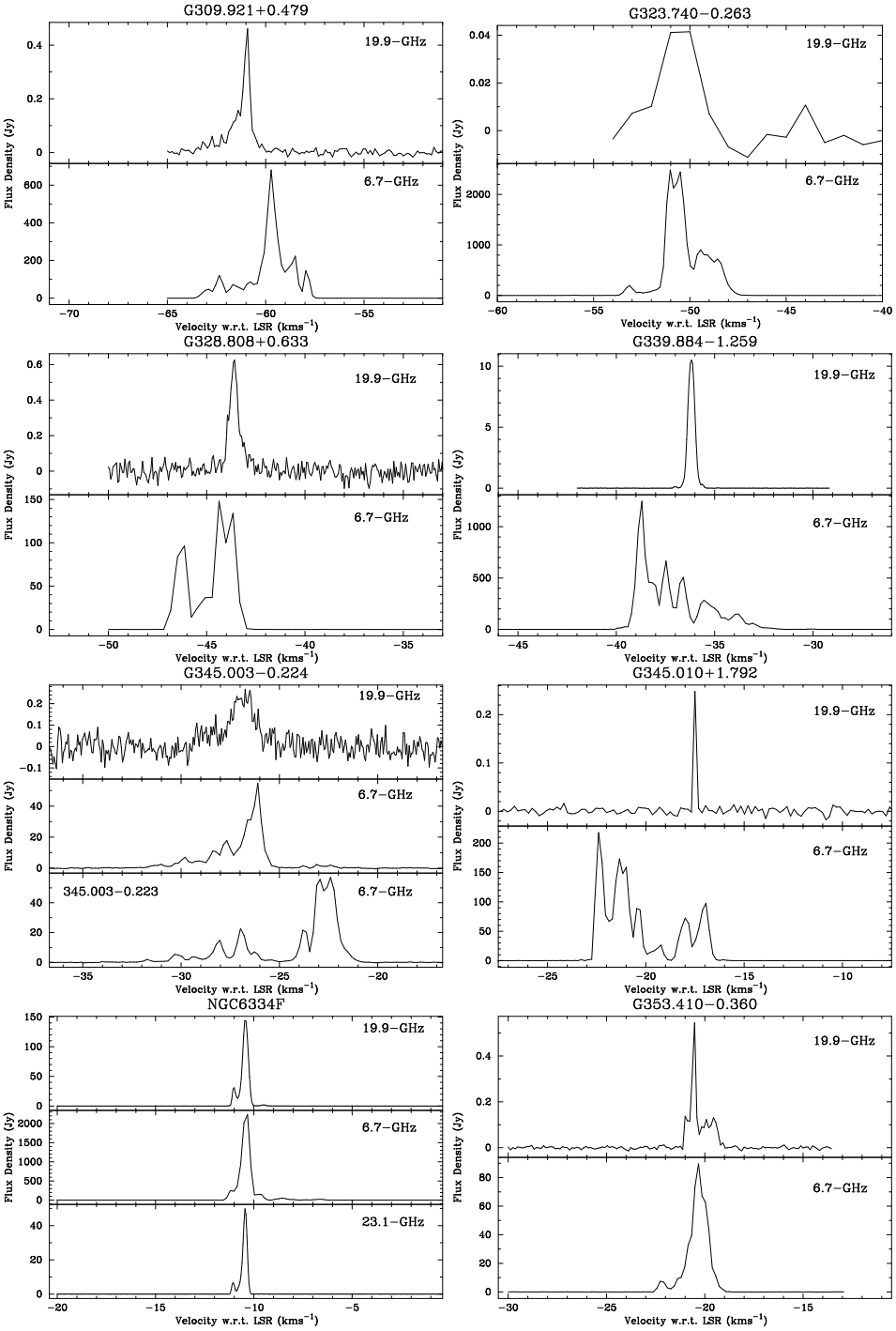

Figure 3.1: Spectra of the 19.9, 6.7 and 23.1 GHz methanol masers extracted from ATCA image cubes. G 345.003−0.224 is presented in conjunction with G 345.003−0.223 to show the extent of the maser emission overlap. See Section 3.2.1 for detailed comments on each source.

larger velocity range. These 19.9 GHz methanol masers are in many cases weak (<1 Jy) and often only have a single spectral feature. A detailed comparison between the spectra at both frequencies is made in Section 3.2.1 on a source–by–source basis.

Table 3.2 lists the thermal velocities and angular separation of the centroid of NH_3 (Purcell et al. 2012) and CS(2–1) (Bronfman et al. 1996) thermal emission associated with the observed methanol masers. The only exception is G 345.010+1.792, which was not observed in either of those studies. However, Ellingsen et al. (2012) measured a thermal velocity of -12.8 km s^{-1} at 216.9 GHz for this source, compared to peak maser v_{lsr} at -17.5 km s^{-1} at 19.9 GHz and -22.4 km s^{-1} at 6.7 GHz (Table 3.3). The peak velocity of the methanol maser emission at 19.9 and 6.7 GHz in this study are within 5 km s^{-1} of the thermal velocities of the cloud in all cases but for G 339.884−1.259, where the difference is of magnitude 7.2 km s^{-1}. This is consistent with studies undertaken by Xu et al. (2009); Pandian et al. (2009), and shows that the maser peak velocity is a good indicator of the systemic velocities of the regions. Pandian et al. (2009) showed that the median v_{lsr} of the maser is usually close to the systemic velocities of the regions and so we present these in Table 3.2 for the 6.7 GHz emission.

Source Name	NH_3 Centroid Velocity (km s^{-1})	NH_3 Separation ($''$)	CS(2–1) Centroid Velocity (km s^{-1})	CS(2–1) Separation ($''$)	19.9 GHz Peak velocity (km s^{-1})	6.7 GHz Peak velocity (km s^{-1})	6.7 GHz Median velocity (km s^{-1})
G 309.921+0.479	−57.7	26.2	−58.4	2.0	−60.9	−59.7	−60.8
G 323.740−0.263	−50.5	50.4	−49.5	31.1	−50.0	−51.0	−60.0
G 328.808+0.633	–	–	−42.3	3.7	−43.6	−44.4	−45.1
G 339.884−1.259	–	–	−31.6	14.1	−36.2	−38.7	−35.0
G 345.003−0.224	−28.2	9.9	−22.2	18.1	−26.5	−26.1	−26.9
NGC6334F	–	–	−6.9	17.2	−10.5	−10.3	−9.0
G 353.410−0.360	−17.8	45.6	−16.7	33.4	−20.5	−20.3	−20.8

Table 3.2: A comparison between the 6.7 and 19.9 GHz methanol maser peak velocity and the velocity centroids of the NH_3 (Purcell et al. 2012) and CS(2–1) (Bronfman et al. 1996) emission associated with the same star formation region. The separation columns show the proximity of the centroid of the NH_3 or CS cloud to the absolute position of the peak of the 19.9 GHz maser as presented in Table 3.3. Purcell et al. (2012) report emission from the ammonia NH_3 (1,1) transition for G 309.921+0.479 and G 323.740−0.263, and the NH_3 (2,2) transition for G 345.003−0.224 and G 353.410−0.360.

The (unpublished) Tidbinbilla detection of G 330.953−0.182 was marginal and the current ATCA observations detected no emission at 19.9 GHz towards G 330.953−0.182 above a limit of 90 mJy which corresponds to 3 times the RMS noise. For the remaining sources we were able to detect maser emission in one or more individual spectral channels (velocity width 0.070 km s^{-1}), the only exception was G 323.740−0.263, for which it was necessary to average four spectral channels to obtain sufficient signal–to–noise to detect 19.9 GHz emission. Spectral averaging was also employed for G 345.010+1.792, and even though self–calibration was not employed in imaging either of these sources, the RMS in the image frames was measured to be <10 mJy as a result of averaging.

We have compared our ATCA spectra to those of Ellingsen et al. (2004, observations made October–November 2003 with the Tidbinbilla 70 m antenna), and find that the 19.9 GHz spectra have in general changed very little in the 16 month time interval between the two sets of observations. The only exception is again G 323.740−0.263, which is weaker by a factor of 4 in the current observations. Where changes are observed, they are discussed in more detail, on a source–by–source basis in Section 3.2.1.

We examined the intensity of the strongest maser emission for each source as a function of baseline length and found it to be consistent with the masers being unresolved for a 6 km baseline, implying that the actual angular size of the 19.9 GHz emission is less than 0.6″ (the approximate dimensions of the synthesised beam). A small decrease in flux density was observed, but this appears to be due to slight decorrelation on the longest baselines, rather than source structure. If we assume that the emission for all sources and all transitions was unresolved we are able to use the peak flux density and the synthesised beam size to calculate a lower limit on the brightness temperature of the emission in each case (see last column in Table 3.3). With the exception of G 323.740−0.263, the brightness temperature exceeds ∼3000 K for each of the sources.

One of the primary aims of these observations was to determine if the methanol maser emission at 6.7 and 19.9 GHz is spatially coincident. Our aim is to deduce the characteristics of the physical environment surrounding the masers, as the conditions surrounding the young high–mass star must be conducive for both transitions to co–exist. Similar analysis has previously been undertaken by Cragg et al. (2005); Moscadelli et al. (2002); Cragg et al. (2002); Minier et al. (2002); Norris et al. (1993). This was achieved by first identifying the single 6.7 GHz spectral channel with velocity closest to that of the 19.9 GHz methanol maser peak velocity, and measuring the difference in the absolute position between the two frequencies at those identified velocities. We then undertook the same measurement between the position of the emission in all other spectral channels at 6.7 GHz, with the same position of the peak maser emission at 19.9 GHz. Our findings showed that for all sources the minimum difference in position occurs for the 6.7 GHz velocity channel most closely corresponding to the velocity at the 19.9 GHz maser peak. This difference was measured to be between 0.1 – 0.35″, with the angular and corresponding linear offsets summarised in Table 3.4 and the third last column of the 19.9 GHz masers' rows of Table 3.3. A detailed analysis of positional coincidence between the primary and any secondary maser components between the two transitions is presented in Section 3.2.1.

The mean offset in absolute position between the 19.9 and 6.7 GHz methanol maser

emission at the same velocity was calculated to be 0.2″. We compared this to the absolute positions that were determined for the spectral channel containing the 6.7 GHz methanol maser peak emission with those reported in the MMB survey. We find the RMS difference between the positions of the same 6.7 GHz methanol masers observed at different epochs (with the same instrument) to be 0.4″. The absolute positions of the 6.7 GHz masers in Green et al. (2010, 2012b); Caswell et al. (2010) were determined from frames with the peak flux emission for each source. The formal errors reported in the fitting process for the positions of the masers are ∼0.03″, however, this is likely to be an underestimate of the uncertainty in absolute positions due to the accuracy of the calibration which will dominate any contribution due to fitting Gaussian profiles to the maser images. A comparison of the v_{lsr} of the peak of the spectra of the 6.7 GHz masers, between the MMB survey and this study, shows that identified peaks are always similar to ≤0.5 km s^{-1}. This means that positional measurements between the different sets of observations were with respect to the same spectral feature. The 0.4″ RMS result between the positional differences between the different sets of 6.7 GHz observations corresponds to the expected positional accuracy for ATCA observations made in good weather, with unresolved phase calibrators (Caswell 1997). We attribute the closer correspondence between our 19.9 and 6.7 GHz measurements made on the same day, and that between our 6.7 GHz positions compared to Green et al. (2010, 2012b); Caswell et al. (2010) to the observation strategy (interleaved observations of the two transitions using the same phase calibrators). We were able to test this assertion through the use of additional phase calibrators which were observed for G 328.808+0.633, G 339.884−1.259 and NGC6334F at 6.7 and 19.9 GHz. For each of these additional calibrators, the channels containing continuum emission were averaged, CLEANed and imaged, using the primary phase calibrators (Table 3.1), while following standard reduction procedures. The absolute positions of the additional calibrators were then determined using a 2D Gaussian fit, and the RMS between these at 6.7 and 19.9 GHz was better than 0.2″.

Our observations also show that six of the eight 19.9 GHz methanol masers are projected against radio continuum with a peak flux density in excess of 100 mJy at 20 GHz, and we present the details in Section 3.2.2.

	Source Name	RA (J2000)	Dec (J2000)	Peak	Velocity	V_{Low}	V_{High}	Offset	RMS	$T_B \times 10^3$
		h m s	$^\circ$ $'$ $''$	(Jy)		(km s^{-1})		($''$)	(mJy)	(K)
19.9 GHz										
	G 309.921+0.479	13 50 41.78	−61 35 10.8	0.46	−60.9	−61.9	−60.4	0.17	8	5.4
	G 323.740−0.263	15 31 45.39	−56 30 50.5	0.04	−50.0	−52.0	−50.0	0.25	7	0.5
	G 328.808+0.633	15 55 48.45	−52 43 06.8	0.63	−43.6	−44.0	−43.1	0.29	40	7.3
	G 339.884−1.259	16 52 04.60	−46 08 34.1	10.5	−36.2	−37.1	−35.5	0.23	9	122.
	G 345.003−0.224	17 05 11.21	−41 29 07.0	0.26	−26.5	−27.3	−26.4	0.10	40	3.0
	G 345.010+1.792	16 56 47.53	−40 14 25.8	0.25	−17.5	−17.7	−17.3	0.34	7	2.9
	NGC6334F	17 20 53.36	−35 47 01.5	144.	−10.5	−11.4	−8.7	0.10	20	1870.
	G 353.410−0.360	17 30 26.17	−34 41 45.6	0.55	−20.5	−21.1	−19.3	0.10	6	6.3
23.1 GHz										
	NGC6334F	17 20 53.35	−35 47 01.8	50.0	−10.5	−11.2	−10.2	0.23	30	
6.7 GHz										
	G 309.921+0.479	13 50 41.76	−61 35 10.7	681.	−59.7	−64.1	−57.6	0.52	30	
	G 323.740−0.263	15 31 45.42	−56 30 50.5	2490.	−51.0	−55.1	−46.8	0.47	40	
	G 328.808+0.633	15 55 48.42	−52 43 06.7	148.	−44.4	−46.8	−43.3	0.29	30	
	G 330.953−0.182	16 09 52.35	−51 54 57.2	5.7	−87.7	−88.9	−87.3	0.44	60	
	G 339.884−1.259	16 52 04.69	−46 08 34.5	1250.	−38.7	−40.3	−29.6	0.36	40	
	G 345.003−0.224	17 05 11.21	−41 29 06.9	54.7	−26.1	−31.6	−22.2	0.22	200	
	G 345.010+1.792	16 56 47.56	−40 14 25.8	218.	−22.4	−22.9	−16.6	0.23	40	
	NGC6334F	17 20 53.36	−35 47 01.6	2230.	−10.3	−11.4	−6.5	0.42	1000	
	G 353.410−0.360	17 30 26.17	−34 41 45.7	89.6	−20.3	−22.4	−19.1	0.16	50	

Table 3.3: A summary of the 19.9, 6.7 and 23.1 GHz methanol maser characteristics. All velocities are given with respect to the v_{lsr}. V_{Low} and V_{High} give the velocity range for which maser emission is observed for each source above 5 times the RMS. The offset for the 6.7 GHz observations is a comparison of the coordinates of the peak of the emission determined from the current observations, and those reported by Green et al. (2010, 2012b); Caswell et al. (2010). The offset listed for the 19.9 and 23.1 GHz masers is the difference with respect to the 6.7 GHz emission from the current observations at the velocity of 19.9 GHz maser peak. The final column gives a lower limit to the brightness temperature of the sources observed at 19.9 GHz, calculated from the peak flux density assuming an upper limit to the angular size of the source of $0.62''$ (typical synthesised beam dimension).

Table 3.4: Estimates of the separation between individual maser components identified at 6.7 and 19.9 GHz. The values presented in the 19.9 GHz and 6.7 GHz columns represent the maximum separation between the maser components (where there is more than a single component) for that transition in arcseconds and milliparsecs. The offsets have been taken from Table 3.3 and describe the difference in absolute position between the peak emission at 19.9 GHz and the emission at the corresponding velocity at 6.7 GHz. Distances have been adopted from Green & McClure-Griffiths (2011)[1]; Caswell et al. (2011b)[2]; Ellingsen et al. (1996a)[3]. The two maser components at 23.1 GHz for NGC6334F are separated by 0.1″ with an offset of 0.23″ from the position of the 19.9 GHz peak.

Source Name	**19.9 GHz**		**6.7 GHz**		**Offset**		**Distance**
	(″)	**(mpc)**	(″)	**(mpc)**	(″)	**(mpc)**	**(kpc)**
G 309.921+0.479	0.2	2.3	0.8	9.3	0.17	2.0	4.8[1]
G 323.740−0.263	–	–	0.2	1.4	0.25	1.7	2.8[1]
G 328.808+0.633	0.2	1.3	0.5	3.2	0.29	1.8	2.6[1]
G 339.884−1.259	0.1	0.6	0.8	5.0	0.23	1.4	2.6[1]
G 345.003−0.224	–	–	1.0	6.5	0.10	0.7	2.7[1]
G 345.010+1.792	–	–	0.2	1.0	0.34	0.6	2.0[1]
NGC6334F	0.2	0.8	4.0	16.	0.10	0.4	1.7[3]
G 353.410−0.360	0.1	1.1	0.1	1.1	0.10	1.1	4.5[2]

3.2.1 Relative positions

The high spectral resolution of the 19.9 and 23.1 GHz observations means that around 5 channels cover the width of a single maser spectral feature. We also find that the 19.9 and 23.1 GHz emission mostly consists of 2 or 3 maser components. In contrast, despite the coarser spectral resolution at 6.7 GHz, we typically identified twice as many maser components for this transition.

All of the 6.7 GHz methanol masers observed in this project have previously been imaged with the ATCA either by Norris et al. (1993), Ellingsen et al. (1996a), Phillips et al. (1998a), Walsh et al. (1998) or Caswell (1997). Their observations were more sensitive than those undertaken here, as we spent the majority of observing time on the weaker 19.9 GHz maser emission. The correlator configuration was also selected to be optimal for the 19.9 GHz observations, and the main purpose for determining the distribution of the 6.7 GHz emission here is to enable a direct single epoch comparison with the 19.9 GHz masers, without any uncertainty regarding temporal variability.

We infer that the regions responsible for the maser emission from the two transitions are coincident to within the accuracy of these observations (approximately 0.2″), as described in Section 3.2. This is also comparable to the typical size of class II methanol maser clusters (Caswell 1997). Table 3.4 summarises the distances and separation associated with the masers and their constituent components as identified in Figures 3.2 to 3.9. The detailed morphology of the maser components for each source is discussed further in Section 3.2.1.

Comments on individual sources

Figures 3.2 to 3.9 show the individual masers components which were identified from the spectral image cubes of the 6.7, 19.9 and 23.1 GHz observations. The spectral channels with weaker maser emission in the image cubes had lower signal–to–noise and correspondingly higher uncertainty in position. In these cases, it was important to distinguish between real maser emission and residual noise in the image. We therefore used a flux density weighted algorithm to group the relevant frames with associated emission into individual maser components, thus ensuring that positional and velocity information from the strongest masers are accurately represented. Our 6.7 GHz results indicate the efficacy of this technique, as they can be directly compared with previous observations of the same sources which were made with higher spectral resolution and sensitivity (thus representing superior data on the number and relative distribution of these masers). In cases where there was only a single 19.9 GHz maser component which was identifiable, we only show the more complex 6.7 GHz maser morphology and present details of the 19.9 GHz maser in the figure caption. The size of the data markers are proportional to the flux densities of the maser components, and the error bars show the mean formal uncertainty of the spectral channels which have been averaged to give the position of the particular maser. The origin in each panel is the location of the peak spectral emission channel for that transition. The small deviations of the reference maser from the origin are the result of the flux–weighting process, which moves this peak off–centre when combined with emission at slightly offset positions. In the overlay panels, the origin is with respect to the peak 19.9 GHz maser emission and the data markers have not been scaled with flux density due to the very different intensities of the two transitions.

In the following sections dedicated to each individual source, we also discuss the spectra of the 19.9 GHz masers obtained in our observations (Figure 3.1) compared to those observed by Ellingsen et al. (2004). The absolute flux density calibration is estimated to be better than 10 percent for the Ellingsen et al. observations, with uncertainty in velocity being better than 0.1 km s^{-1}. We have optimised the panel sizes in Figures 3.2 to 3.9 to best display the distribution of maser emission for each source, so they are typically different for the different transitions (although always with a one–to–one aspect ratio).

G 309.921+0.479

This is the only source in the current study which was not observed by Ellingsen et al. (2004). It was detected in (to date unpublished) additional 19.9 GHz observations made with the Tidbinbilla 70m antenna, and these observations confirm that detection. The current ATCA observations show a 19.9 GHz methanol maser with a peak flux density of 0.46 Jy, at a velocity of −60.9 km s^{-1}. In comparison the 6.7 GHz transition has its strongest emission at a velocity of −59.7 km s^{-1}, and a weaker peak with a flux density of 86.7 Jy at essentially the same velocity (−60.8 km s^{-1}) as the 19.9 GHz maser (Figure 3.1).

Figure 3.2 shows two 19.9 GHz maser components with an approximately East–West orientation and a separation of $<0.2''$. The spatial distribution of the 6.7 GHz masers lies roughly North–South, with maximum separation of $0.8''$, similar to that observed by Phillips et al. (1998a). The right–hand plot in Figure 3.2 shows that when the 19.9 GHz component at

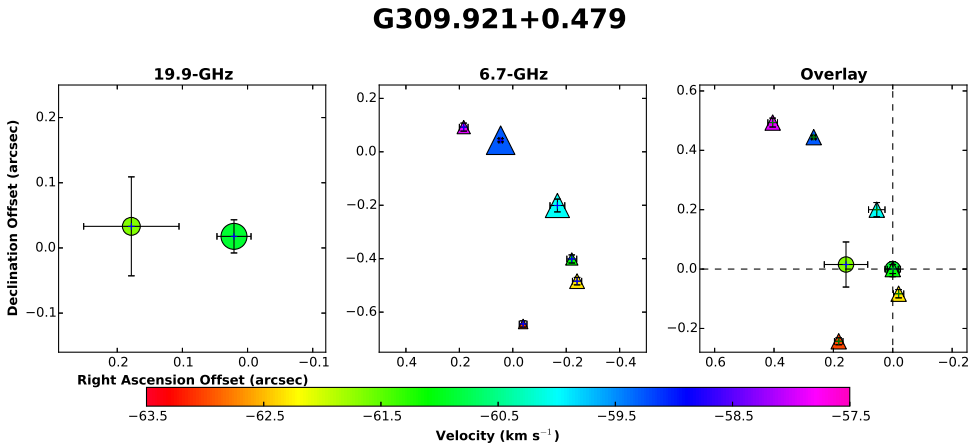

Figure 3.2: Spatial distribution of the methanol maser components at 19.9 and 6.7 GHz. The 19.9 GHz components are at velocities of −61.7 and −60.9 km s^{-1} with an East–West orientation and the velocity increasing from East to West. The 6.7 GHz emission has a curved profile. The spread of the components is mostly in the North–South direction and are spatially consistent with that observed by Phillips et al. (1998a). The components have velocities of −63.0, −62.3, −61.1, −60.0, −59.3 and −57.9 km s^{-1} increasing from South to North. There is no evidence for spatial or velocity correlation between the masers at the two transitions.

−60.9 km s^{-1} and the 6.7 GHz component at −61.1 km s^{-1} are aligned, there is no evidence for spatial or velocity correlation between the remaining components.

G 323.740−0.263

Ellingsen et al. (2004) reported a peak flux density of 0.15 Jy at −51.4 km s^{-1} for this source, the marginal detection being approximately 3 times the RMS noise level in their spectrum. The current observations (undertaken approximately a year and a half later) detected only very weak 19.9 GHz emission of 40 mJy, with an RMS of 7 mJy in the spectrally averaged (velocity resolution ∼1 km s^{-1}) image cube. The initial detection by Ellingsen et al. (2004) of 19.9 GHz methanol emission in this source was with a relatively broad line width (3.1 km s^{-1}), possibly indicative of quasi–thermal emission, however, the large fractional change in flux density suggests that at least some of the emission must be from a maser, as we would not expect to see significant changes in thermal emission on such short timescales. Figure 3.1 shows that the major peaks of the 6.7 GHz spectrum, with flux density ∼2500 Jy at −50.5 and −51.0 km s^{-1} coincide with the 19.9 GHz peak at this velocity resolution. Figure 3.3 shows the spatial distribution of the 6.7 GHz methanol maser emission, which agrees with the earlier images of Norris et al. (1993) and Walsh et al. (2002). The morphology is curved with North–South and East–West separations of ∼0.2″.

G 328.808+0.633

The 19.9 GHz methanol maser emission has a peak flux density of 0.63 Jy at −43.6 km s^{-1}. Figure 3.1 shows that the 6.7 GHz methanol maser has its second strongest peak (flux density

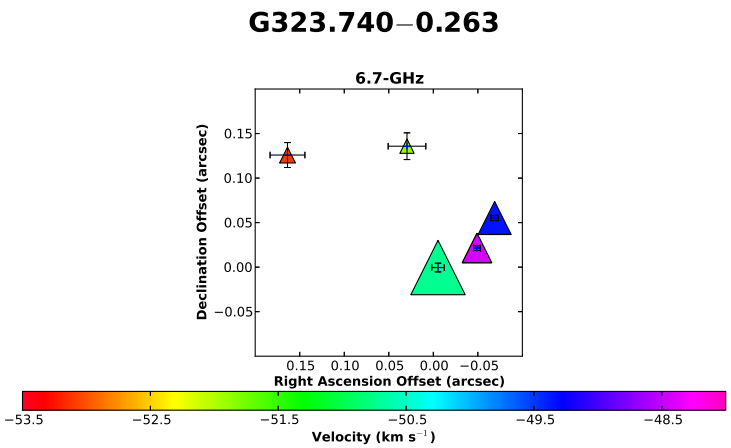

Figure 3.3: The maser components at 6.7 GHz have a spatial distribution which is consistent with Norris et al. (1993); Walsh et al. (2002). Velocity components were detected at −53.1, −51.9, −50.7, −49.3 and −48.4 km s^{-1} spanning 0.15″ and 0.2″ along the North–South and East–West axes respectively. The magnitude of the line of sight velocity generally increases from East to West, with the exception of the −48.4 km s^{-1} feature. Only a single 19.9 GHz maser component was identified at a velocity of −50.5 km s^{-1}and aligned with the −50.7 km s^{-1} component at 6.7 GHz.

of 134 Jy) at essentially the same velocity (−43.7 km s^{-1}). Ellingsen et al. (2004) reported a peak flux density of 0.79 Jy at −43.7 km s^{-1}, with a FWHM of 0.9 km s^{-1} for the 19.9 GHz methanol maser. The current observations show the 19.9 GHz emission covering the same velocity range as the Tidbinbilla observations, with some evidence for weak, spectrally blended maser components on either side of the main peak. From our image cubes we are able to identify two maser components in the 19.9 GHz emission (Figure 3.4). These are at velocities of −43.2 and −43.6 km s^{-1} and are separated by 0.2″, offset approximately North–South. This is quite different to the spatial distribution observed in the 6.7 GHz maser emission which shows elongation predominantly in the East–West direction, with a total angular separation of 0.5″ between the component at −43.8 km s^{-1} and those at −44.4 and −46.3 km s^{-1}, consistent with Norris et al. (1993). The right–hand panel in Figure 3.4 shows that when the 19.9 and 6.7 GHz components at −43.6 km s^{-1} and −43.8 km s^{-1} are aligned, there is no appreciable coincidence between the other components in terms of position or velocity. The North–South separation between the maser components at 19.9 GHz and 6.7 GHz is similar, however, the velocity increases for the 19.9 GHz components but decreases for the 6.7 GHz masers, suggesting that any correlation is unlikely.

G 339.884−1.259

This is the second strongest 19.9 GHz methanol maser in our observed sample, with a peak flux density of 10.5 Jy at a velocity of −36.2 km s^{-1}. This source also shows two additional weaker spectral features on either side of the strongest emission. The 6.7 GHz methanol masers cover a large velocity range with at least six peaks resolved with our coarse spectral resolution; the strongest having a flux density of 1250 Jy at a velocity of −38.6 km s^{-1}. The closest velocity 6.7 GHz maser component to the 19.9 GHz peak has a flux density of ∼500 Jy

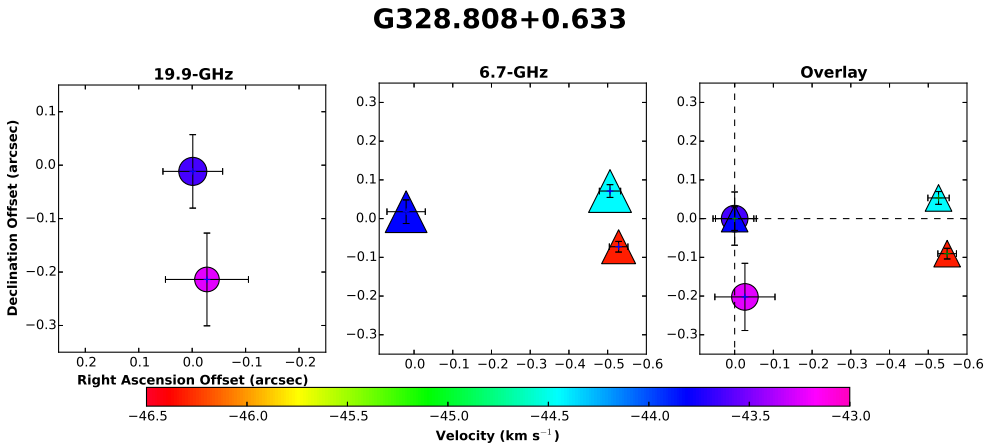

Figure 3.4: Two 19.9 GHz methanol maser components were identified from the image cubes, at velocities of −43.2 and −43.6 km s^{-1}. The 6.7 GHz maser shows a predominantly East–West elongation of 0.5″ and are observed at velocities of −43.8 km s^{-1} and −44.4, −46.3 km s^{-1}. We find no evidence for spatial or velocity correlation between the other 6.7 and 19.9 GHz components when we align the 19.9 GHz peak with the 6.7 GHz component with closest associated velocity.

at a velocity of −36.7 km s^{-1} (Figure 3.1). Ellingsen et al. (2004) report a 19.9 GHz peak flux density of 9.8 Jy at −36.2 km s^{-1} with FWHM of 0.4 km s^{-1}, consistent with the current observations. Looking at the relative distribution of maser components in the two transitions (Figure 3.5), the 19.9 GHz emission traces a linear morphology in the North–West direction with an extent of <0.1″ along either axis. The orientation is similar to that observed at 6.7 GHz (Norris et al. 1993), however, the 6.7 GHz methanol masers span a linear separation of 0.8″ and there is no spatial or velocity coincidence between the two transitions.

G 345.003−0.224

The 19.9 GHz methanol maser has a single peak, with a flux density of 0.26 Jy at a velocity of −26.5 km s^{-1} (Figure 3.1). The 6.7 GHz maser spectrum shows many more peaks with the strongest having a flux density of 54.7 Jy at velocity −26.1 km s^{-1}, and evidence for blending with a secondary peak which is unresolved at our velocity resolution. This lies at the high–velocity extreme of the 19.9 GHz methanol maser velocity range. Caswell et al. (2010) show a spectrum where two peaks at 6.7 GHz are resolved at −26 and −27 km s^{-1}, meaning the 19.9 GHz maser peak lies between the two. Ellingsen et al. (2004) detected 19.9 GHz emission with a peak flux density of 0.22 Jy at a velocity of −27.4 kms (FWHM of 3.4 km s^{-1}). Ellingsen et al. (2004) reported the 19.9 GHz emission as being associated with G 345.003−0.223, whereas our high spatial resolution ATCA observations show that the 19.9 GHz masers are associated with the nearby 6.7 GHz methanol maser G 345.003−0.224 which is separated from G 345.003−0.223 by 3.5″. Caswell et al. (2010) report “no significant overlap” in the velocity range of these two neighbouring sources. Figure 3.1 shows that there is noticable overlap in some of the weaker emission in the velocity range between −29.8 and −22.8 km s^{-1}, and is consistent with Caswell (1997); Walsh et al. (1998). The differences in these studies between the level of overlap is not explored in detail here, but can perhaps

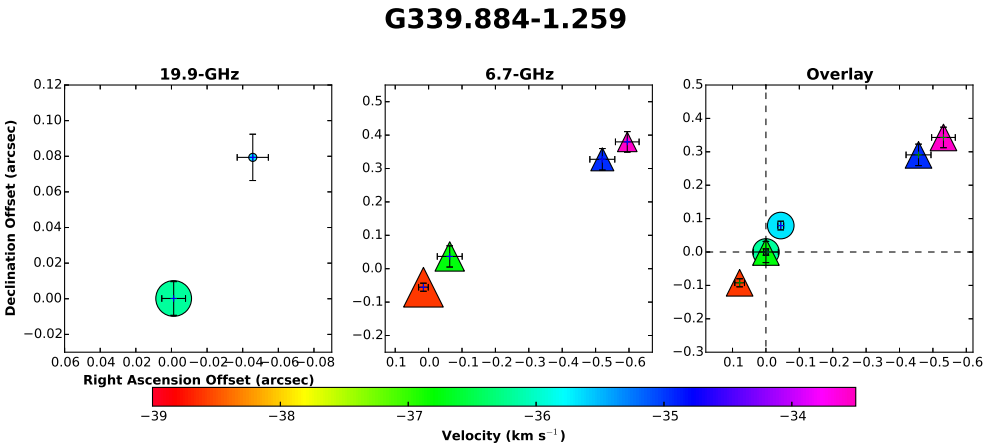

Figure 3.5: Two 19.9 GHz methanol maser components were identified with velocities of −36.2 and −35.7 km s^{-1}. Four 6.7 GHz methanol maser components at velocities of −38.6, −36.7, −34.9 and −33.6 km s^{-1} were observed. Both transitions show a similar position angle for the maser distributions, and have velocity increasing in the same sense from East to West. However, no spatial or velocity correlation is evident.

be attributed to changes in the morphology in the spectra, as a result of the range of epochs over which this source was observed.

Five maser components were identified from the 6.7 GHz image cubes of G 345.003−0.224. The components have velocities ranging between −22.8 and −31.1 km s^{-1}, and are shown in the left panel in Figure 3.6. The spread is predominantly in a North–South direction, spanning 1.0″, with less scatter (∼0.5″) East–West. G 345.003−0.223 is shown in the centre panel in Figure 3.6 with components ranging between −22.6 and −30.2 km s^{-1}. These components have a complex distribution spanning a range of ∼0.5″ East–West. The spatial and kinematic distribution of the 6.7 GHz methanol maser emission for both sources are consistent with those presented in Caswell (1997). The sources are separated by 3.5″ along an East–West axis as shown in the right panel of Figure 3.6.

G 345.010+1.792

Ellingsen et al. (2004) detected a 19.9 GHz methanol maser with peak flux density of 0.21 Jy at a velocity of −17.6 km s^{-1} (FWHM of 1.5 km s^{-1}). The current ATCA observations show this maser to have a similar peak flux density of 0.25 Jy at −17.5 km s^{-1}. The spectrum in Figure 3.1 shows the velocity width of the maser feature to be less than 1 km s^{-1}. The 6.7 GHz spectrum has at least six spectral peaks with the strongest having a flux density of 218 Jy at −22.4 km s^{-1}. The 19.9 GHz methanol maser has a velocity which lies between two secondary 6.7 GHz maser peaks, with flux densities of 72.4 and 97.7 Jy and velocities of −18.0 and −16.9 km s^{-1}, respectively. G 345.010+1.79 has been detected in a larger number of different class II methanol maser transitions than any other source, including some that have only been detected in this source (Ellingsen et al. 2012), however, in general the rare, weak maser transitions are at velocities close to −22 km s^{-1}(the 19.9 GHz transition being the only exception). The individual 6.7 GHz maser components identified from the image cubes

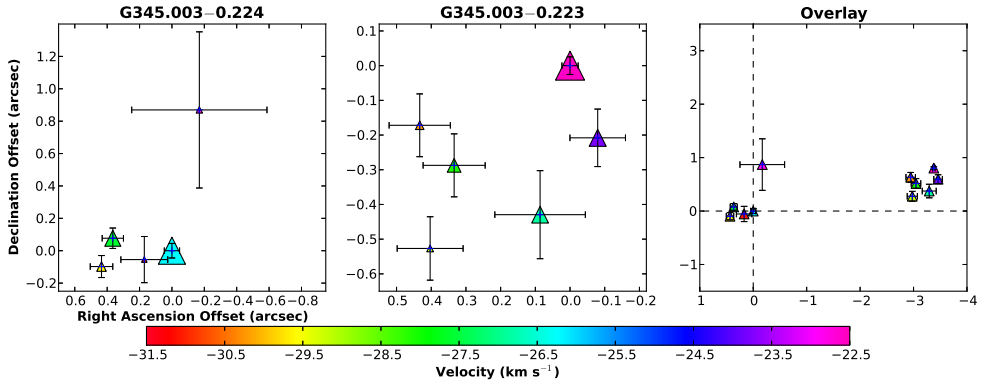

Figure 3.6: 6.7 GHz methanol masers associated with G 345.003−0.224 (left cluster) range between v_{lsr} of −22.8 and −31.1 km s^{-1}, and G 345.003−0.223 (right cluster) range between −22.6 and −30.2 km s^{-1}. In both sources, the v_{lsr} increases from East to West except for the −31.1 km s^{-1} (weakest) feature associated with G 345.003−0.224. The overlay panel shows that the two sources have a separation of 3.5″ along an approximately East–West direction. The single 19.9 GHz methanol maser at −26.9 km s^{-1} was identified to be associated with G 345.003−0.224. It aligns closest to the −26.2 km s^{-1} 6.7 GHz component associated with this source.

are distributed into two distinct groups in Figure 3.7. The observed distribution is consistent with that shown by Norris et al. (1993), covering an angular range of 0.2″ East–West and a North–South spread of <0.1″.

NGC6334F

This is the strongest of the 19.9 GHz methanol masers observed in the current ATCA observations. The spectra of the 6.7, 19.9 and 23.1 GHz methanol masers are similar in their general structure, and individual peaks align closely in velocity (Figure 3.1). The 19.9 GHz methanol maser has a peak flux density of 144 Jy at −10.5 km s^{-1}, similar to that observed by Ellingsen et al. (2004) who report a peak flux density of 146 Jy at −10.4 km s^{-1} and FWHM of 0.3 km s^{-1}. At 23.1 GHz the peak flux density (50.0 Jy) occurs at −10.5 km s^{-1}, while the 6.7 GHz maser peak (2230 Jy) occurs at a velocity of −10.3 km s^{-1}. Figure 3.8 shows the 6.7 GHz methanol maser emission, with maximum separation of 4.0″ between the components along a North–West elongation, consistent with Ellingsen et al. (1996a). The 19.9 GHz maser components have an East–West separation of <0.2″ and a North–South separation of 0.1″. The bottom right panel of Figure 3.8 shows the region where the velocity components at all three transitions are close in proximity. The two maser components at 23.1 GHz (−10.5 and −11.1 km s^{-1}) are separated by 0.1″ along the North–South axis, and align to within 0.1″ (and 0.1 km s^{-1} in velocity) with two of the three 19.9 GHz maser components (which are at velocities of −9.6, −10.5 and −11.0 km s^{-1}). The distribution of the 6.7 GHz emission is less certain due to the lower spatial resolution, although there is evidence for alignment between the 6.7 GHz masers and the 19.9 GHz component at −9.6 km s^{-1}, to within less than 0.1″. Overall NGC6334F appears to be the most likely candidate for co–spatial emission

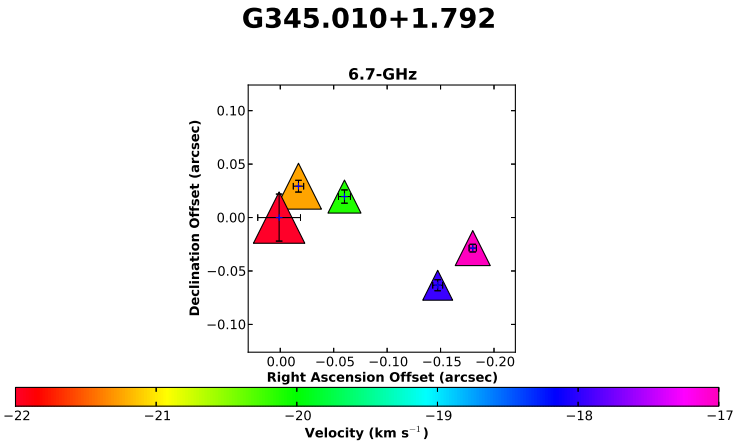

Figure 3.7: A total of 5 maser components were identified from the velocity cube of the 6.7 GHz observations. These have velocities of −17.0, −17.9, −20.1, −21.2 and −22.3 km s^{-1}, with increasing v_{lsr} from East to West. A single maser is identified at 19.9 GHz at a velocity of −17.5 km s^{-1}and aligned with the −17.9 km s^{-1} component at 6.7 GHz.

of the 19.9 GHz methanol masers with other class II transitions, especially given the similar spectra, however, VLBI observations are required to determine if spatially coincidence exists on milliarcsecond scales.

G 353.410−0.360

We detect 19.9 GHz methanol maser emission with a peak flux density of 0.55 Jy at a velocity of −20.5 km s^{-1} in this source (Figure 3.1). Ellingsen et al. (2004) measured the 19.9 GHz maser to have a peak flux density of 0.33 Jy at velocity −20.5 km s^{-1} with a FWHM of 1.8 km s^{-1}. Our ATCA observations show secondary peaks on either side of the strongest emission which are likely why the Tidbinbilla observations required a relatively broad Gaussian component to fit the emission. At 6.7 GHz, G 353.410−0.360 has two maser peaks detected at the spectral resolution of our ATCA observations (there is some indication of additional weaker emission at velocities similar to the strongest peak). The 6.7 GHz peak flux density is 89.6 Jy, at a velocity of −20.3 km s^{-1}. Two maser components were identified in the 19.9 GHz image cubes at velocities of −19.7 and −20.6 km s^{-1} (Figure 3.9). The 6.7 GHz components have velocities of −20.3 and −21.2 km s^{-1} and emission in both transitions shows a similar position angle and separation of <0.1″. The 6.7 GHz maser emission shows a distribution like that observed by Phillips et al. (1998a). When the 19.9 and 6.7 GHz components at similar velocities are assumed coincident there is no evidence for spatial and velocity alignment of the other components (see right–hand panel of Figure 3.9).

3.2.2 Continuum

Ellingsen et al. (2004) noted that 19.9 GHz methanol masers are generally associated with 6.7 GHz methanol masers where the emission is projected against strong (greater than 100 mJy at 8.5 GHz) HII continuum emission. Six of the eight 19.9 GHz methanol masers

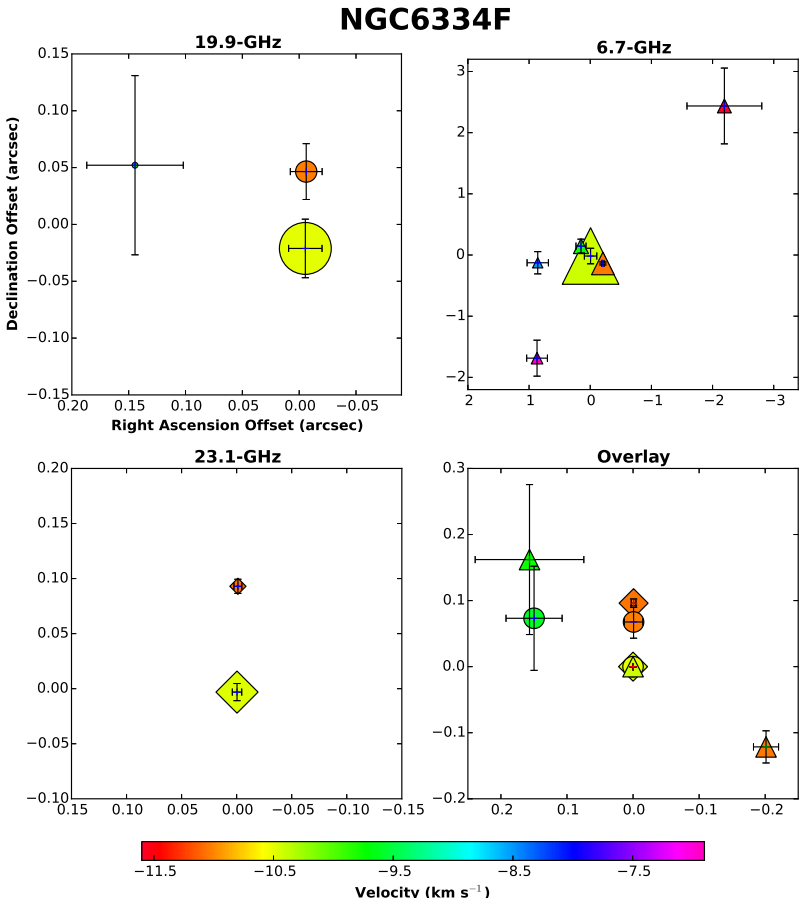

Figure 3.8: There are three maser components observed at 19.9 GHz at velocities of −9.6, −10.5 and −11.0 km s^{-1}. The two components at 23.1 GHz have velocities of −10.5 and −11.1 km s^{-1}. The bottom right–hand panel shows the primary maser cluster with components at 23.1 GHz aligning with corresponding 19.9 GHz emission to within 0.1″. The 6.7 GHz masers have velocities ranging between −11.6 and −6.9 km s^{-1}. There is possibly an alignment between the −9.6 km s^{-1} maser at 19.9 GHz and −9.8 km s^{-1} maser at 6.7 GHz as seen in the bottom right panel.

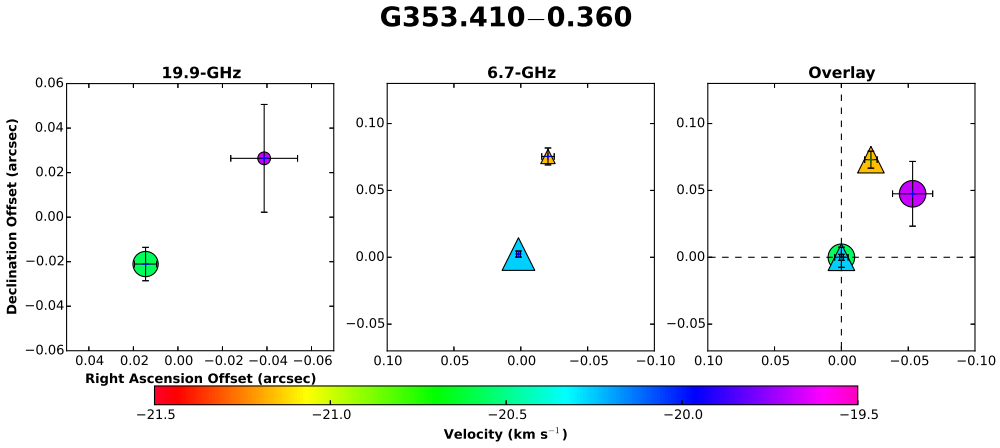

Figure 3.9: The 19.9 GHz methanol maser emission has two components at velocities of −19.7 and −20.6 km s^{-1}. Our observations also show two maser components at 6.7 GHz at velocities of −20.3 and −21.2 km s^{-1}. No evidence for detailed spatial or velocity coincidence is apparent.

we observed are projected against radio continuum emission from an UC HII region (see Section 3.3.1 and Figures 3.10 to 3.15). This is in contrast to the majority of known 6.7 GHz methanol masers which are not associated with radio continuum emission stronger than a few mJy (Phillips et al. 1998a; Walsh et al. 1998; Minier et al. 2001; Bartkiewicz et al. 2009; Pandian et al. 2010; Cyganowski et al. 2011). The six HII regions all have integrated flux density at 20 GHz stronger than approximately 80 mJy. The 19.9 GHz methanol masers for which we did not detect radio continuum emission were G 323.740−0.263 and G 339.884−1.259. Sensitive ATCA observations by Ellingsen et al. (1996a) detected an HII region with an integrated flux density of 6.14 mJy at 8.6 GHz towards G 339.884−1.259 (and also in Ellingsen et al. (2005)). The spectral index of all the observed HII regions is less than 0.5 and even for a spectral index of unity, the expected 20 GHz integrated flux density for G 339.884−1.259 is significantly less than the upper limit set by the current observations. Sensitive observations of G 323.740−0.263 at 8.6 GHz by Walsh et al. (2002) failed to detect an HII region associated with this source above 0.2 mJy, and in the light of this our non–detection at 20 GHz is expected for observations at the current sensitivity.

The properties of the 20 GHz radio continuum emission for the detections are summarised in Table 3.2.2, and in the captions of Figures 3.10 to 3.15. In these figures, circles, triangles and diamonds represent 19.9, 6.7 and 23.1 GHz masers respectively. The 20 GHz continuum observations have an approximate synthesised beam size of $\sim$0.5″, compared to a 6.7 GHz beam of $\sim$2″. Integrated fluxes were determined based on boxes which were similar in size to the HII regions to mitigate effects due to different beam sizes between 6.7 and 19.9 GHz observations. The RMS for the peak and integrated fluxes were measured from a square box of $\sim$10 arcsec^2 in a region of the deconvolved image which was free from any continuum emission. These were $\leq$20 mJy for the peak flux density and $\leq$40 mJy for the integrated flux density at 19.9 and 6.7 GHz. Detailed studies of these ultracompact HII regions at 3.5 cm have been previously undertaken by Ellingsen et al. (1996a); Walsh et al. (1998); Phillips et al. (1998a).

Source Name	Flux Density				Spectral Index
	19.9 GHz		6.7 GHz		
	Peak (mJy)	Integrated (Jy)	Peak (mJy)	Integrated (Jy)	α
G 309.921+0.479	197 ±3	872 ±7	380 ±5	480 ±10	0.5
G 323.740−0.263		<45		<55	
G 328.808+0.633	110 ±20	870 ±40	356 ±7	1410 ±10	−0.4
G 339.884−1.259		<45		<35	
G 345.003−0.224	180 ±10	290 ±20	162 ±5	200 ±10	0.3
G 345.010+1.792	182 ±3	345 ±6	179 ±5	230 ±10	0.4
NGC6334F	220 ±10	2030 ±20	830 ±20	2320 ±40	−0.1
G 353.410−0.360	84 ±4	349 ±8	271 ±8	490 ±20	−0.3

Table 3.5: Properties of the radio continuum emission associated with 19.9 GHz methanol masers. The upper limit for sources without any detected continuum in the image is 5 times the RMS noise. The spectral indices, are based on a 2–point fit between the integrated flux densities at 19.9 and 6.7 GHz, and have errors of <0.1. The peak and integrated flux densities for NGC6334F for the 23.1 GHz observation are (390±30) and (1900±60) mJy.

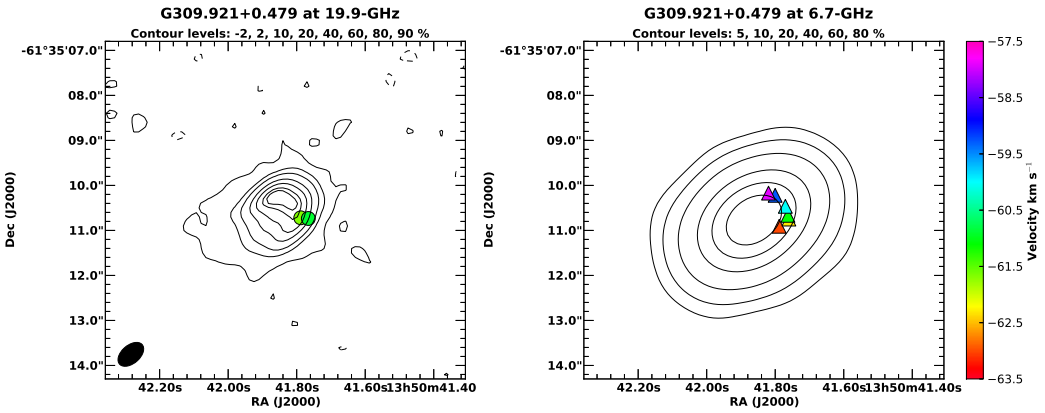

Figure 3.10: The 20 GHz continuum shows a cometary HII region with the methanol maser emission (-61.7 and -60.9 km s^{-1}) projected against the South–West edge. At 6.7 GHz the radio continuum emission is unresolved. The beam size at this frequency is $2.1\times1.4''$.

3.3 Discussion

Our observations have made the first high spatial resolution investigation of the 19.9 GHz methanol maser transition. Many of these sources are quite weak at 19.9 GHz with peak flux densities often <1 Jy. This is in contrast to the 6.7 GHz methanol masers in the same regions. The 19.9 GHz methanol masers typically have simple spectra with 1 or 2 identifiable components. The maser emission at 19.9 GHz is spatially coincident with 6.7 GHz maser emission to within approximately $0.2''$, demonstrating that the two transitions arise from the same star formation site. However, unlike comparisons of the relative distribution of 6.7 and 12.2 GHz methanol masers (e.g. Menten et al. 1992; Norris et al. 1993; Minier et al. 2000) there is little or no evidence for close correlation in the morphology of the 19.9 and 6.7 GHz masers. The small number of maser features at 19.9 GHz and the difference in the spatial and velocity resolution between the 19.9 and 6.7 GHz observations makes such comparisons difficult. However, our results suggest that unlike the 12.2 GHz transition, the 19.9 GHz transition would not, in most sources, have a close correspondence (10's of milliarcsecond scale) with the 6.7 GHz methanol masers in the same region.

Figure 3.1 shows that the peak velocity of the 19.9 GHz maser aligns with the strongest emission in the 6.7 GHz maser spectrum for at most three sources (G 323.740−0.263, NGC6334F & G 353.410−0.360). For some of the remaining sources (e.g. G 328.808+0.633) the 19.9 GHz peak aligns with a secondary 6.7 GHz component. For other sources (e.g. G 339.884−1.259 & G 345.010+1.792) there is no corresponding component in the 6.7 GHz emission identifiable from the spectrum. Breen et al. (2011) found 80 percent of 12.2 GHz methanol masers show their strongest emission at the same velocity as the 6.7 GHz maser peak, while Ellingsen

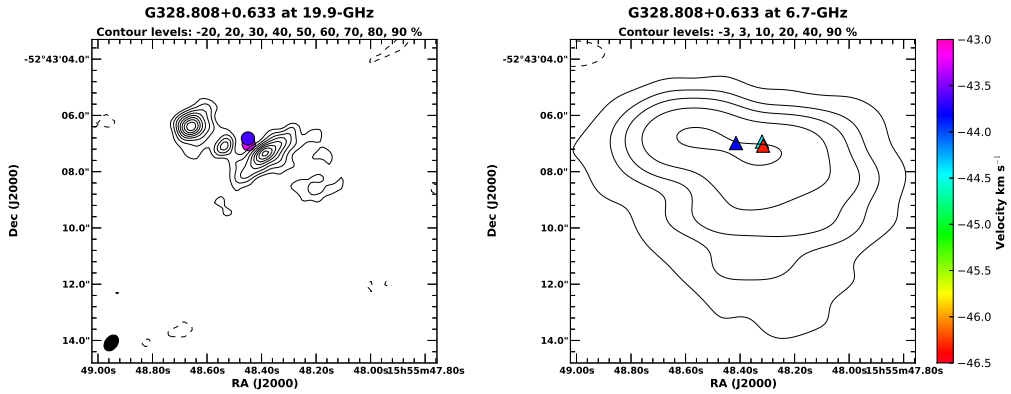

Figure 3.11: The radio continuum at 20 GHz shows three compact components aligned roughly East–West. The masers at −43.2 and −43.6 km s^{-1} are not projected against radio continuum emission at this frequency, however, they do lie in regions where extended emission is observed at lower frequencies (e.g. the current 6.7 GHz observations and Ellingsen et al. (2005)). The beam size at 6.7 GHz is 2.5×1.5″.

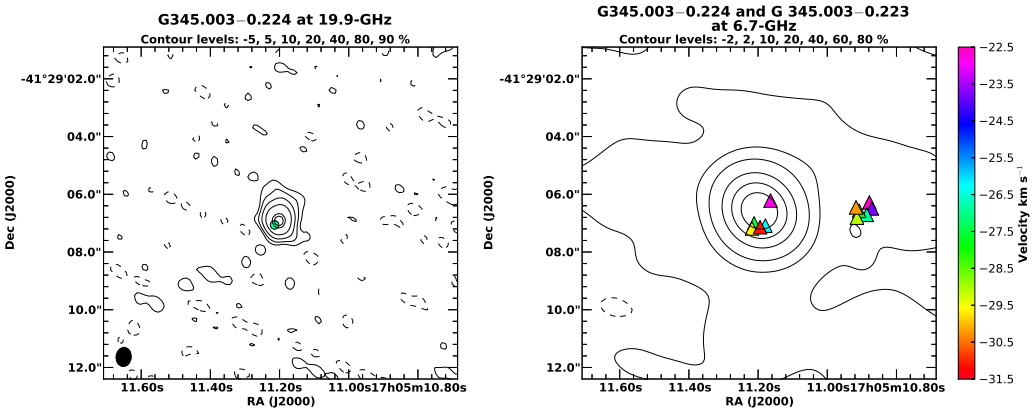

Figure 3.12: The single maser component at 19.9 GHz (−26.9 km s^{-1}) is closely associated with radio continuum emission at this frequency. This is slightly resolved with a 0.5 arc second beam. At 6.7 GHz, the two distinct groups of masers are associated with G 345.003−0.224 (left cluster and closely associated with radio continuum) and G 345.003−0.223 (right cluster and offset to the West of radio continuum). The beam size at 6.7 GHz is 2.1×1.9″.

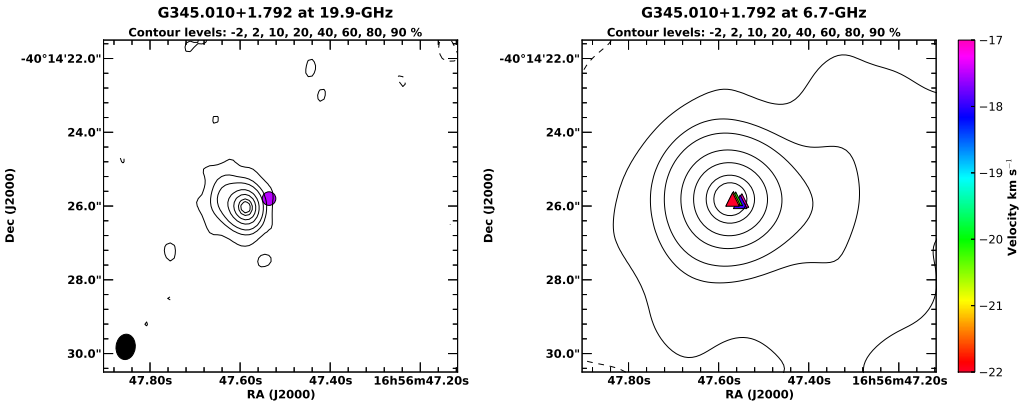

Figure 3.13: At 19.9 GHz, the single maser at -17.5 km s^{-1} is slightly West of the continuum peak, which has slightly asymmetric profile, with the extended emission on the opposite side of the HII region to the masers. The beam size at 6.7 GHz is $2.1\times1.9''$.

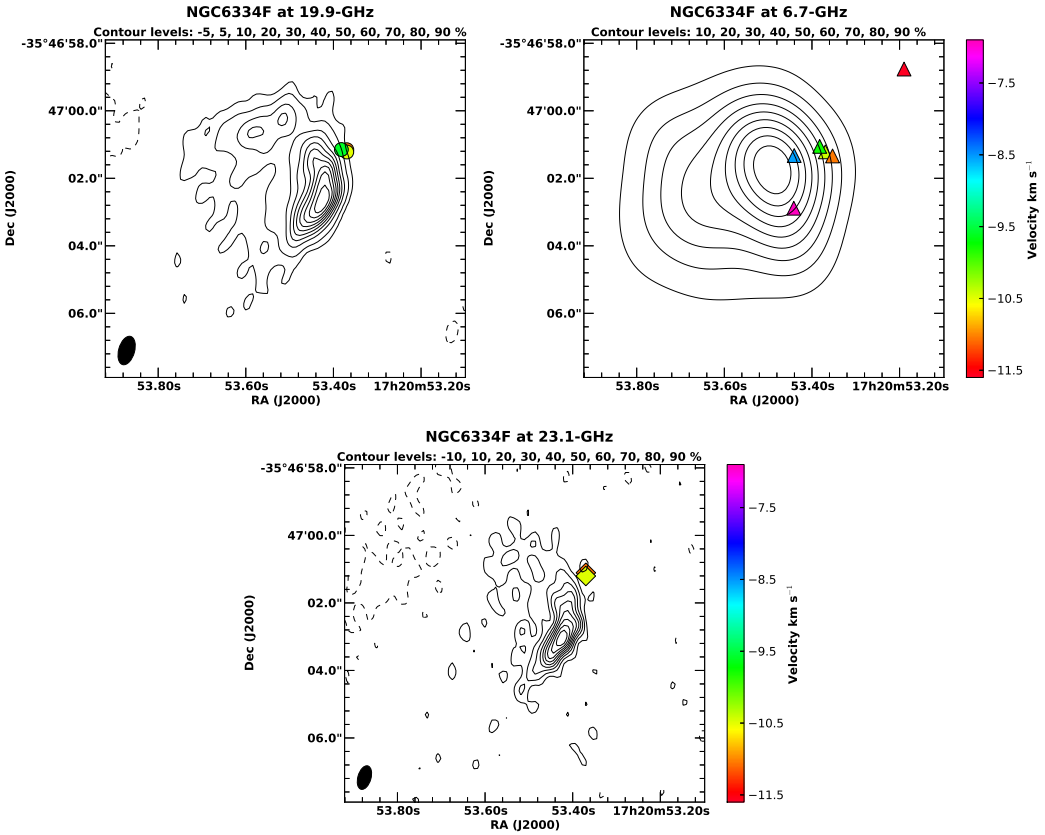

Figure 3.14: The HII region is cometary, with the 19.9 GHz maser emission at -9.6, -10.5 and -11.0 km s^{-1} observed towards the leading edge. At 6.7 GHz, additional maser clusters are observed both North–West and to the South of the cluster associated with the 19.9 and 23.1 GHz transitions. The beam size at 6.7 GHz is $2.5\times2.0''$.

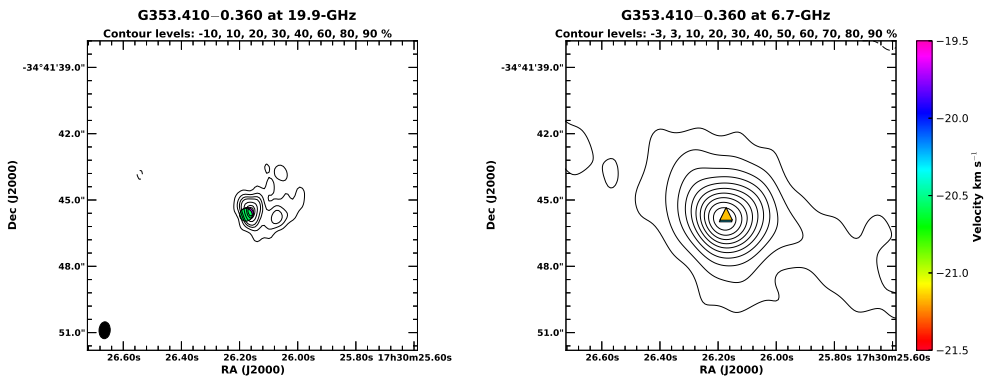

Figure 3.15: The radio continuum emission for this source at 20 GHz has a cometary morphology with the masers at -19.7 and -20.6 km s^{-1}. They are projected against the leading edge of the HII region. The masers at 6.7 GHz are also projected against the (unresolved) HII continuum at this frequency. The beam size at 6.7 GHz is $2.4\times1.8''$.

et al. (2013) found 37.7 GHz methanol masers to have the same peak velocity as the associated 12.2 GHz methanol masers in more than 50 percent of sources. A close correspondence between the velocity of different transitions makes close spatial coincidence more likely and in contrast, it is unlikely for different maser transitions to be coincident if they have different line of sight velocities. In this context, the lack of close spatial coincidence between 19.9 GHz methanol masers and the associated 6.7 GHz masers is not surprising, as the 19.9 GHz masers frequently have the velocity of their peak emission offset from that observed for the stronger transitions.

Multi–transition modelling, such as that undertaken by Sutton et al. (2001) and Cragg et al. (2001) is based on the assumption that the different maser transitions are co–spatial. Clearly the evidence for the 19.9 GHz methanol masers suggests this is not likely to be the case for the majority of sources. The degree to which the 19.9 GHz methanol masers are spatially coincident with other class II maser transitions can only be rigorously determined through phase–referenced very long baseline interferometry experiments of the various transitions. We would expect such observations to show that the 19.9 GHz methanol maser emission generally arises in different locations within the larger class II maser cluster from the stronger, more common transitions. Ellingsen et al. (2004) found that 19.9 GHz methanol masers prefer lower gas and dust temperatures and higher densities than those sources which are not detected in this transition (e.g 19.9 GHz methanol masers prefer gas temperatures $T_k \sim 50$ K, dust temperature $T_d \sim 175$ K, density $n_H \sim 10^7$ cm^{-3}). Given our results it would appear to be better not to include 19.9 GHz methanol masers in multi–transition models in sources where there is not a close alignment in velocity between the different transitions.

3.3.1 Association with UCHII regions

Ellingsen et al. (1996a); Phillips et al. (1998a); Walsh et al. (1998) and others have shown that some 6.7 GHz methanol masers have an associated HII region detectable at 8 GHz. The correlation between the observed 19.9 GHz methanol masers with strong radio continuum emission is indicative that these masers are associated with the later stages of the class II methanol

maser phase for young high–mass stars (Breen et al. 2010b). For most of the HII regions detected in our observations, previous observations with an angular resolution of around 2″ at 8.5 GHz showed them to be largely unresolved on these scales (Ellingsen et al. 2005). The current observations at 20 GHz, with a resolution approximately a factor of 4 higher confirm the hints of asymmetry in the lower frequency radio continuum observations, and show that in all sources the 19.9 GHz methanol masers are projected against, or very close to the steepest gradient in the radio continuum emission. Masers which are projected onto a HII region have their brightness temperature boosted by seed photons (Sobolev & Deguchi 1994). As a result, it is possible that 19.9 GHz masers are rare because they are low gain and only the sources which are projected against HII regions are detected.

The majority of the HII regions (5 of the 6 sources) have either a definite cometary morphology, or some indication of such a morphology. We take a cometary morphology to be one where there is an asymmetry in the intensity distribution with a well–defined axis consisting of closely spaced contours in the radio intensity on one side of a source and more diffuse emission on the opposite side. We assess that the 19.9 GHz continuum images of all of the sources except G 328.808+0.633 either clearly show, or indicate some signs of such morphology. In a large sample of HII regions Wood & Churchwell (1989b) found 20 percent of observed sources had a cometary morphology. Given the small sample size (and the subjective nature of morphological classification), we refrain from speculating whether 19.9 GHz methanol masers are preferentially associated with cometary HII regions. However, if a larger sample becomes available it may be a question worthy of further investigation.

The spectral index α of the radio continuum emission associated with each maser source was calculated using the integrated flux densities at 20.0 and 6.7 GHz (see Table 3.2.2). These are all $-0.5 < \alpha < 0.5$, confirming that the associated emission is thermal. The calculated value of $\alpha = -0.4$ for G 328.808+0.633 is likely to be due in part to the difference in spatial filtering between observations at different frequencies as seen in Figure 3.11. The measured spectral index suggests that the turnover between optically thick and optically thin free–free emission occurs at a frequency in between 7 and 20 GHz for these sources (Hoare et al. 2007).

3.3.2 Maser-based evolutionary schemes

The presence and absence of different maser transitions in different HMSFRs is indicative of differing physical conditions. Ellingsen et al. (2007) suggested that these differences could be used to characterise the evolutionary stage of HMSFRs which have associated masers, and the proposed maser–based evolutionary timeline was subsequently quantified by Breen et al. (2010b). In general, the strong, common maser transitions are most useful in such classifications, however, the rarer maser transitions must signpost regions with atypical conditions. This could be a star formation region with unusual properties, or perhaps more likely one which is in a relatively short–lived evolutionary phase. Recently Ellingsen et al. (2011, 2013) presented evidence that 37.7 GHz methanol masers are associated with star formation regions in the last few thousand years of the class II methanol maser phase, and called these masers the "Horsemen of the Apocalypse" for this phase. That the 19.9 GHz methanol masers do not in general appear to be cospatial with the more common class II methanol maser tran-

sitions at the milliarcsecond level does not diminish their utility for evolutionary studies, as these focus on the large–scale physical properties of the broader region (i.e. comparable to, or larger than the scale of the maser clusters), where the transitions do coincide.

Searches for the rarer, weaker class II methanol maser transitions have generally been targeted towards star formation regions which show strong emission at 6.7 and 12.2 GHz. The next most common class II methanol maser transition is the 107 GHz (3_1 – 4_0A^+) transition, which has been detected towards 25 of more than 175 sites searched (Val'tts et al. 1995, 1999; Caswell et al. 2000; Minier & Booth 2002). This sample of twenty five 107 GHz methanol masers has formed the basis of searches for the other rarer class II methanol maser transitions over the last decade (e.g. Ellingsen et al. 2003; Cragg et al. 2004) and the results for a dozen transitions have been tabulated by Ellingsen et al. (2011). The majority of the 107 GHz methanol maser sample are located in the Southern Hemisphere (22 sources), with the remaining three sources (W3(OH), Cep A and NGC7538) at high Northern declinations. The search for 19.9 GHz methanol masers by Ellingsen et al. (2004) targeted the 22 Southern 107 GHz methanol maser sites. Combining their results with data from the literature for the three Northern 107 GHz methanol masers Ellingsen et al. (2004) found that eight of the nine known 19.9 GHz methanol masers have an associated 6035 MHz excited–state OH maser (the exception being G 323.740−0.263). This association implies that 19.9 GHz masers trace a specific range of physical conditions, likely linked with a late evolutionary phase (Cragg et al. 2002). Breen et al. (2010b) showed that the luminosity of both 6.7 and 12.2 GHz methanol masers increases as the source evolves, and Ellingsen et al. (2011) showed that the sample of twenty five 107 GHz methanol masers typically have very high maser luminosities compared to the bulk of class II masers. Figure 3.16 plots the isotropic peak luminosity of the 6.7 and 12.2 GHz methanol masers towards all Southern 12.2 GHz methanol maser sources (Breen et al. 2012b; Breen & Ellingsen 2012), with all but one of the 107 GHz methanol maser sources lying to the right of the dashed line in this plot (Breen & Ellingsen 2012), which are the higher 6.7 GHz luminosity sources. There are no clear trends for the properties of the 107 GHz methanol masers with and without an associated 19.9 GHz methanol maser, unlike the 37.7 GHz methanol masers, which are only associated with the higher luminosity 12.2 GHz methanol masers from the 107 GHz sample (Ellingsen et al. 2011).

Ellingsen et al. (2011) used the Onsala and Mopra telescopes to search for 37.7 GHz methanol masers towards all twenty five 107 GHz methanol maser sources. There are twelve 37.7 GHz methanol masers associated with the sample of twenty five 107 GHz masers, compared to nine 19.9 GHz methanol masers associated with the same 107 GHz sample. Five of the 107 GHz sample exhibit both 19.9 and 37.7 GHz class II methanol masers (W3(OH), G 323.740−0.263, G 339.884−1.259, G 345.010+1.792 and NGC6334F). Of these five sources, four have an associated 6035 MHz OH maser (the exception being G 323.740−0.263) and four have a peak 6.7 GHz flux density in excess of 1500 Jy (the exception being G 345.010+1.792). These five sources include all the strong (peak flux density >1500 Jy) 6.7 GHz maser sources, with the exception of G 9.621+0.196. In contrast, for the seven 37.7 GHz methanol maser sources which are not associated with a 19.9 GHz methanol maser, two have an associated 6035 MHz OH maser and five do not.

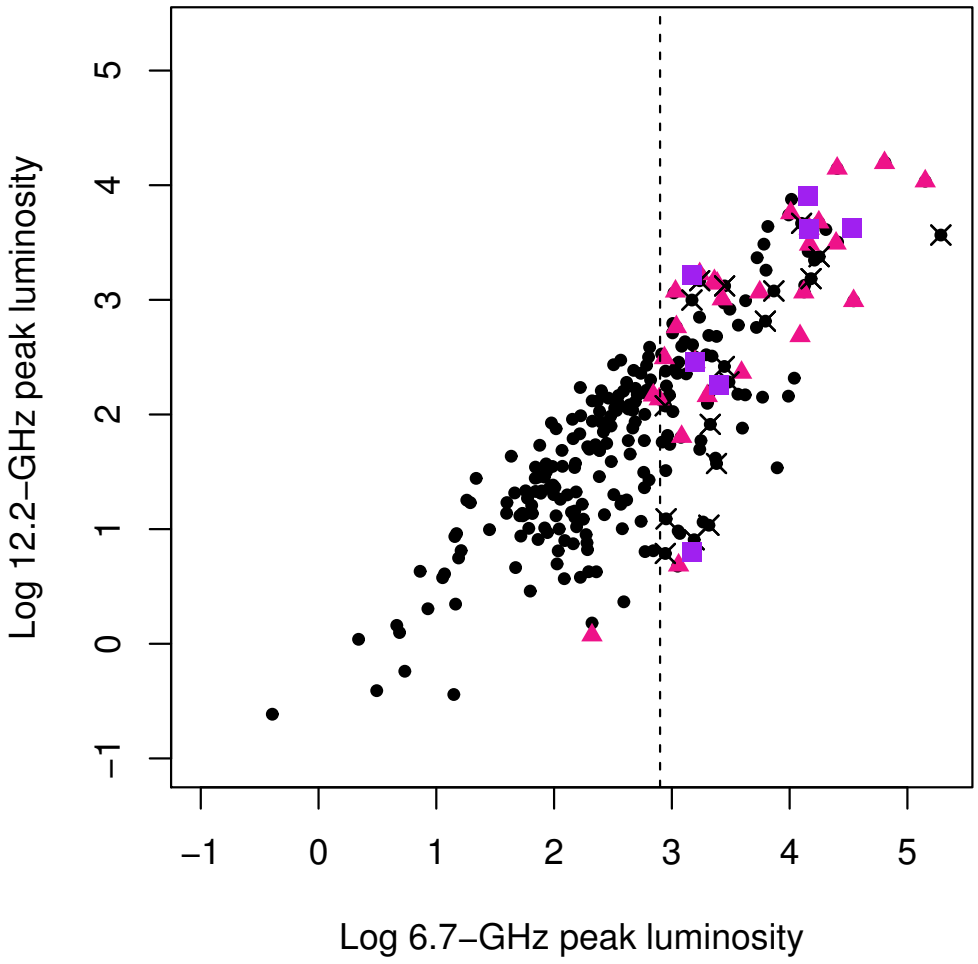

Figure 3.16: The isotropic peak luminosity of the 6.7 and 12.2 GHz methanol maser emission towards all 12.2 GHz methanol masers South of declination −20° (Breen et al. 2012b; Breen & Ellingsen 2012). The purple squares are sources with an associated 19.9 GHz methanol maser, the pink triangles are sources with an associated 107 GHz methanol maser (without an associated 19.9 GHz methanol maser). The dashed vertical line shows the 6.7 GHz peak luminosity cut off observed for 107 GHz methanol masers (Ellingsen et al. 2011). The black crosses indicate sources which have been searched for 107 GHz methanol maser emission, but were not detected.

Table 3.6: A comparison of the 6.7 GHz methanol maser to ground–state OH maser peak flux density ratio R for 107 GHz methanol maser sources with and without associated 19.9 GHz and 37.7 GHz masers.

Methanol Maser Transitions	**Methanol–favoured** ($R > 32$)	**Intermediate** ($8 < R < 32$)	**OH–favoured** ($R < 8$)	**Total**
37.7 GHz, no 19.9 GHz	3	4	0	7
37.7 GHz & 19.9 GHz	1	4	0	5
no 37.7 GHz, 19.9 GHz	0	2	2	4

Caswell (1997) suggested the ratio of the 6.7 GHz to 1665 MHz OH peak flux density (R) is indicative of the age of a star formation region, with "methanol–favoured" sources ($R > 32$) being younger than those which are "OH–favoured" ($R < 8$). Sixteen of the sample of twenty five 107 GHz methanol masers are associated with either or both of the 19.9 and 37.7 GHz transitions. Table 3.6 shows that there is a tendency for the 107 GHz methanol masers which have an associated 19.9 GHz methanol maser to have generally lower values of R, indicative of these being more evolved sources. Although the sample size here is small and there is significant scatter for the observed methanol–OH peak flux density ratio, this trend appears consistent with the tendency for 19.9 GHz methanol masers to have an associated 6035 MHz OH maser and 37.7 GHz methanol masers not to, suggesting that the former trace a more evolved young high–mass star than the latter.

Based on the above trends, we suggest that the greatest number of class II methanol maser transitions (including the 19.9 and 37.1 GHz transitions) are detectable close to the period when the 6.7 GHz masers reach their peak luminosity. Those sources where 37.7 GHz methanol masers are observed without an associated 19.9 GHz methanol maser likely precede the "peak luminosity" phase, while those with 19.9 GHz maser emission and no 37.7 GHz maser emission have evolved past "peak luminosity". However, in making comparisons between the 19.9 GHz methanol masers and the 37.7 GHz methanol masers, it is important to note that the 19.9 GHz maser search of Ellingsen et al. (2004) is a factor of 5 – 10 more sensitive than the searches that have been undertaken for 37.7 GHz methanol masers (or any of the other rare maser transitions). Hence, it is possible (but not likely, as 37.7 GHz masers are associated with only the most luminous 6.7 and 12.2 GHz methanol masers; Ellingsen et al. 2011) that the differences in sensitivity and small sample size may have indirectly introduced biases into the comparisons undertaken.

3.4 Conclusions

19.9 GHz methanol masers arise in HMSFRs which also have associated 6.7 and 12.2 GHz methanol masers. The 19.9 GHz methanol masers are coincident with the stronger, more common class II methanol maser transitions to within $0.2''$ in those sources where they are detected. Despite the similarity in the relative distribution of the 6.7 and 12.2 GHz methanol masers, both the velocity and spatial distribution of 19.9 GHz methanol masers suggests that they generally arise at different locations within the maser cluster.

Six of the eight sources are also associated with strong UC HII regions (>80 mJy at

20 GHz) with five out of these exhibiting a cometary type morphology. This close association with strong UC HII regions is in contrast to the majority of known 6.7 GHz methanol masers which are generally known not to be associated with radio continuum emission stronger than a few mJy.

We find that 19.9 GHz methanol masers are preferentially associated with OH masers with greater peak flux density (relative to the peak flux density of the 6.7 GHz methanol masers) than the 37.7 GHz methanol masers. Based on this relationship, while keeping in mind the small pool of 19.9 GHz masers in this study, we suggest that these masers likely trace more evolved HMSFRs than those sources with an associated 37.7 GHz methanol maser.

Chapter 4

High–Mass Star Formation

In the classical theory proposed by Shu (1977), it is assumed that star formation results from the collapse of an isothermal sphere of gas. However this model cannot be applied to high–mass (sources with >10 $M_{\odot}$, briefly summarized in Table 4.1) star formation (HMSF), as once hydrogen burning commences in the core (Keto 2003; Norberg & Maeder 2000; Bernasconi & Maeder 1996), the outward radiation pressure will halt any more material from accreting onto the protostar (Zinnecker & Yorke 2007; Stahler et al. 2000).

The time prior to ignition is measured as the Kelvin–Helmholtz timescale $t_{\rm KH} = \frac{GM_*^2}{RL}$ and for high–mass stars of >10 $M_{\odot}$, $t_{\rm KH} \lesssim 10^5$ yr (see dotted green graph in Figure 4.1) is shorter than the accretion time $t_{acc} \sim 10^6$ yr (e.g. Fedele et al. 2010). This results in nuclear burning during accretion, leading to outward radiation pressure and photoionisation which should halt the accretion of material (e.g. Kudritzki 2002; Larson & Starrfield 1971). There are currently several models which attempt to circumvent the accretion timescale problem in HMSF in order to explain the existence of high–mass stars:

1. McKee & Tan (2003) propose the existence of a *turbulent core* whereby massive molecular prestellar cores are temporarily supported against collapse (and therefore core fusion) by surrounding gas turbulence. During this phase where the core is unable to collapse, it undergoes accretion which accelerates with time.

2. In the *competitive accretion* model of clustered HMSF (Bonnell & Bate 2006), gas is funnelled to the cluster of protostars, resulting in a surge of accretion through the (Bondi & Hoyle 1944) mechanism.

3. Schmeja & Klessen (2004) describe a complex interaction between gravity and turbu-

Mass range ($M_{\odot}$)	**Designation**	**Spectral type**	
8 – 16	Early B	B3V to B0V	
16 – 32	Late O	O9V to O6V	
32 – 64	Early O	O5V to O2V	(Walborn et al. 2002)
64 – 128	O/WR	WNL–H	(Crowther 2007)

Table 4.1: Main–sequence massive star definition from Zinnecker & Yorke (2007).

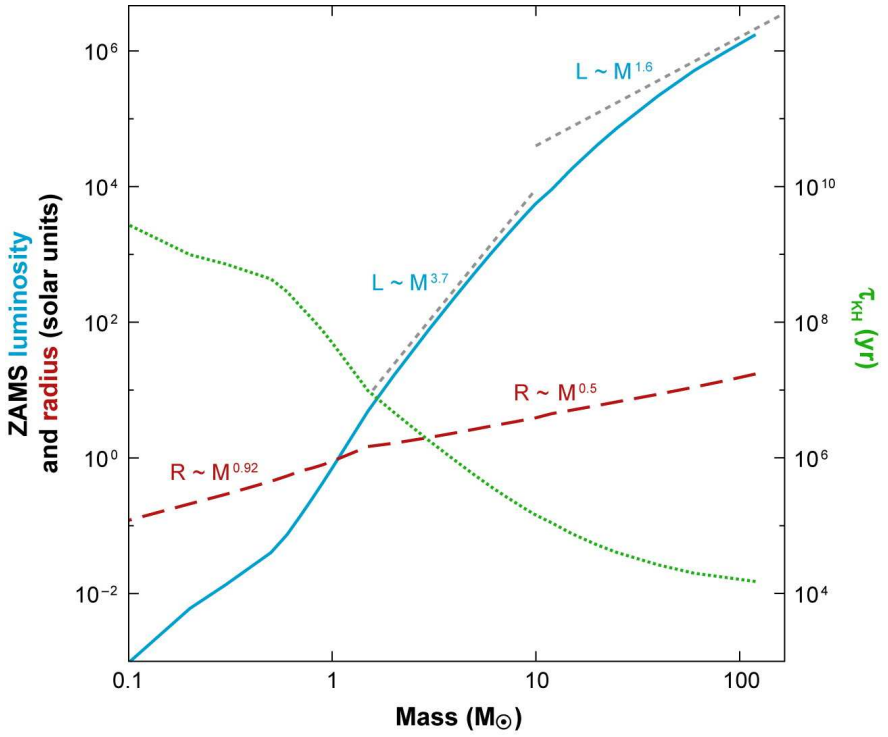

Zinnecker H, Yorke HW. 2007.
Annu. Rev. Astron. Astrophys. 45:481–563

Figure 4.1: Luminosity L, radius R and Kelvin–Helmholtz timescale $t_{\rm KH}$ models vs. mass M of zero–age main–sequence (ZAMS) high–mass stars from Zinnecker & Yorke (2007).

lence during *gravoturbulent fragmentation* which results in high accretion rates, due to large amounts of material in the molecular cloud, which trails off after the initial burst.

The examples given above rely on mechanisms which modulate the accretion rate as the protostar gains mass. The scenario examined by McKee & Tan (2003) and Bonnell & Bate (2006), where the accretion rate accelerates with time, seems to favor current observations (e.g. Davies et al. 2011).

The challenge in testing the theories of HMSF is that the young stellar objects are embedded in optically thick molecular clouds of H_2 column densities 10^{23} – 10^{24} cm^{-2}, making them observable only at mid–IR through to radio wavelengths (Churchwell 2002). Furthermore, high–resolution interferometric observations indicate that the star forming cores consist of small compact objects in crowded clusters, making it difficult to resolve individual features (e.g. Rathborne et al. 2009).

Comprehensive discussions about the HMSF process can be found in Zinnecker & Yorke (2007); McKee & Ostriker (2007); McKee & Tan (2003); Churchwell (2002); Garay & Lizano (1999) and an overview on the evolutionary stages in HMSF is provided in Urquhart et al. (2014b). Here we give a brief account of the most commonly studied phases of HMSF.

4.1 Infra–red dark clouds

High–mass stars form in clusters (Lee et al. 2013; de Wit et al. 2005; Lada & Lada 2003), and infra–red dark clouds (IRDCs) are thought to be the cold precursors of the warm (cluster–forming) molecular clumps and hot molecular cores (HMC) of these stars (e.g. Traficante et al. 2015; Rathborne et al. 2010). The IRDCs in the Milky Way galaxy range from regions where there is no sign of active star formation (e.g. Tackenberg et al. 2012), to where star formation has definitely commenced (e.g. Shipman et al. 2014; Sakai et al. 2013). This suggests that IRDCs are on the verge of where both low– and high–mass star formation is commencing, within giant molecular clouds (GMCs; Beuther et al. 2013b; Ragan et al. 2012). However, only the densest (and most opaque) clouds eventually collapse into high–mass stars (Kauffmann & Pillai 2010). IRDCs are found primarily in the Galactic Plane (Simon et al. 2006) and correspond to GMCs with high densities $>10^5$ cm^3; high column densities $\sim 10^{23} - 10^{25}$ cm^2; and low temperatures <25 K (Schneider et al. 2015; Carey et al. 2000; Egan et al. 1998). They are clustered together, with each cluster spanning $\sim$0.1 – 10 pc with a separation of $\sim$1 pc between adjacent clusters, and masses ranging from about $10 - 10^3$ $M_\odot$ (Battersby et al. 2014; Simon et al. 2006; Carey et al. 2000).

IRDCs were initially identified in the images from the Infrared Space Observatory (ISO; Perault et al. 1996). Since then, the Midcourse Space Experiment (MSX; Simon et al. 2004; Egan et al. 1998), the Galactic Legacy Infrared Mid–Plane Survey Extraordinaire (GLIMPSE; Benjamin et al. 2003), Spitzer (Peretto & Fuller 2009) and the Planck Consortium (Ade et al. 2014) have all sampled IRDCs in our Galaxy to within 10 kpc (Carey et al. 2000; Egan et al. 1998).

During this stage of HMSF, molecular observations of ^{12}CO, ^{13}CO (Schneider et al. 2015), H_2O (Shipman et al. 2014), $H^{13}CO^+$ and HCO^+ (Csengeri et al. 2011) show evidence for infalling material. The infall has been hypothesized to result primarily from external pressures or self–gravitation, or to a smaller extent from magnetic fields. Numerical simulations to determine the dominant driving factor indicates that supersonic turbulence in an isothermal gas without self–gravitation produces a log–normal probability density function (PDF) tail (Federrath et al. 2008). When self–gravitation is turned on, a power–law tail develops (Girichidis et al. 2014; Federrath & Klessen 2013; Kritsuk et al. 2011). By using this property, Schneider et al. (2015, 2013); Froebrich & Rowles (2010) argue that the observed infall can be attributed to self–gravitation.

IRDCs are rich in their molecular composition and analysis of their spectra have been used to determine evolutionary stages, constrain lifetimes and physical parameters such as ionization, temperature and density (Schneider et al. 2015; Gerner et al. 2015, 2014). The methanol, OH and water masers which are used to identify and characterize HMSF in Chapter 2 have also been observed towards IRDCs (e.g. Shipman et al. 2014; de Villiers et al. 2014; Ellingsen 2006).

4.2 Hot molecular cores within molecular clumps

The first observable manifestation of a high–mass protostar is the HMC (de Villiers et al. 2015; Rathborne et al. 2011; Purcell et al. 2006). HMCs trace the immediate environment surrounding a high–mass star that has already formed, and correspond to a stage considerably after the earliest cold, dense starless core IRDC phase described in Section 4.1. Many HMCs are embedded within IRDCs, and these may represent the earliest stages of HMC evolution (e.g. Rathborne et al. 2008, 2007). HMCs typically have dimensions of $\sim$0.01 – 0.1 pc; densities of $>10^5$ – 10^8 cm^{-3}; temperatures of >100 K; masses of $10 - 10^3$ $M_\odot$; luminosities of $>10^4$ $L_\odot$ and accrete material for $<10^5$ years (Choudhury et al. 2015; Beltrán et al. 2014; Beuther et al. 2013a; Viti 2005; Kurtz et al. 2000; Garay & Lizano 1999). They reside in clusters consisting of several fragmented cores separated by distances as small as 0.01 pc (e.g. Beltrán et al. 2014; Sánchez-Monge et al. 2014; Beuther et al. 2013a; Lee et al. 2013).

Hot molecular clumps form the surrounding environment of the centrally embedded HMCs, and are considered to be separate physical structures (Cesaroni 2005). Urquhart et al. (2013) present a sample of hot molecular clumps from the ATLASGAL and CORNISH surveys for Galactic Longitudes between $\ell = 10°$ and 60° and latitudes $|b| < 1°$. These clumps are typically 10 times larger and more massive than HMCs (e.g. Higuchi et al. 2014; Urquhart et al. 2013; Higuchi et al. 2013; Hofner et al. 2000), and are warmed by UV radiation from the embedded protostar, resulting in numerous line spectra from these sources (e.g. Beltrán et al. 2014; Calcutt et al. 2014; Rathborne et al. 2011).

Even though high–resolution observations of HMCs associated with G 29.960.02 and G 31.41+0.31 by Cesaroni et al. (1998) showed increasing temperatures towards the central core, there is still some debate as to whether HMCs are internally or externally heated (e.g. Cesaroni 2005; Kurtz et al. 2000). Recent Sub–millimetre Array (SMA) observations of 17 HMCs by Hernández-Hernández et al. (2014) give evidence for a centrally heated core and, along with an increase in density towards the central core (Zhang et al. 1998), are consistent with expectations for a collapsing source.

Regardless of the differences between the details of contraction as proposed by McKee & Tan (2003) and Bonnell et al. (2001, 1997), conservation of angular momentum will force rotating structures to form around HMCs during collapse. As a result, HMCs are prime candidates for the search of accretion disks and associated perpendicular outflows. The interstellar maser emission described in Chapter 2 is used to trace potential accretion disks (e.g. De Buizer et al. 2012; Moscadelli et al. 2011; Norris et al. 1998; Phillips et al. 1998a) and outflows (e.g. Plunkett et al. 2015; Teixeira et al. 2012; Ridge & Moore 2001) which are thought to be associated with HMCs. Observations by Longmore et al. (2006) and Minier et al. (2005) have also identified internally heated cores and driven outflows associated with methanol maser emission in HMCs. During the HMC phase, the protostellar source accretes mass at rates of $\sim 10^{-2}$ $M_\odot$ yr^{-1} (Lee et al. 2013; Beuther et al. 2013a; Osorio et al. 2009), which is high enough to prevent the development of an ionized region (introduced in Section 4.3). HMCs are therefore believed to precede the HII phase, and Kurtz et al. (2000) propose a minimum lifetime of $\sim 10^4$ years for the formation of a high–mass main–sequence star from HMCs.

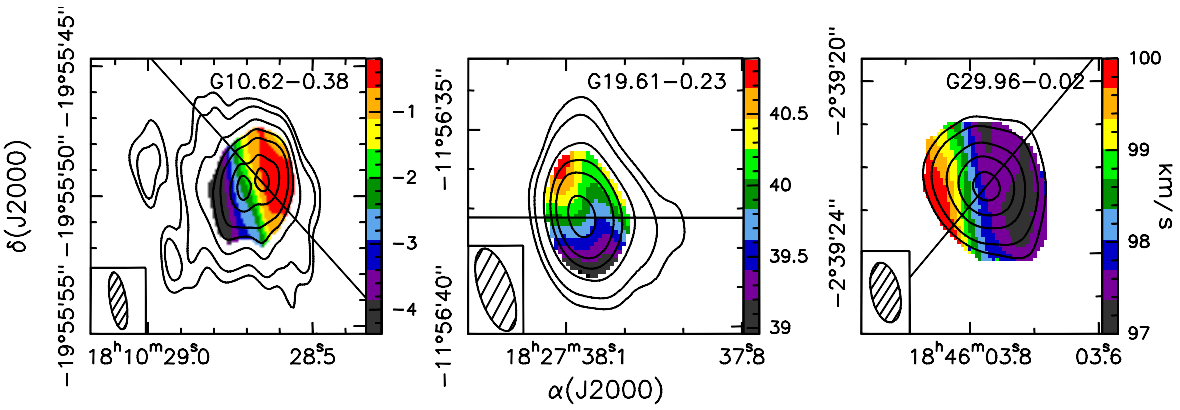

Figure 4.2: Beltrán et al. (2011) find clear velocity gradients in their v_{lsr} observations of CH_3CN (12–11) emission toward HMCs in the HMSFRs G 10.62−0.38, G 19.61−0.23, and G 29.96−0.02. The continuous straight lines spanning across the emission indicate the direction of the molecular outflow.

Rathborne et al. (2011) made observations of G 34.43+00.24 MM1 using the SMA and find velocity gradients (from 8 different molecular transitions), which could represent an accretion disk for an IRDC embedded HMC. Beltrán et al. (2011) also reveal clear velocity gradients from CH_3CN (12–11) observations toward G 10.62−0.38, G 19.61−0.23 and G 29.96−0.02, which are interpreted to be rotational toroids perpendicular to the observed outflows (see Figure 4.2). However, the inferred mass infall rates in G 19.61−0.23 and G 29.96−0.02 are two orders of magnitude greater than the accretion rates, suggesting that the material in the toroids is not infalling onto a single massive star (thought to be responsible for the outflow), but onto a cluster of protostars.

To further test the hypothesis of rotating disks perpendicular to outflows, Beltrán et al. (2014) made high–resolution (<0.5″) interferometric observations of G 35.03+0.35 with the Atacama Large Millimetre Array (ALMA) and found 6 cores (each separated by ∼0.02 pc) associated with this region. One of the cores shows a clear velocity gradient along the major axis, which is consistent with an edge–on Keplerian disk rotating about the axis of an outflow. The authors conclude from these results that at least B–type stars can form through a disk accretion process. Similarly, Sánchez-Monge et al. (2014) made observations of 6 HMCs within the G 35.20−0.74 N complex with ALMA. The cores are separated by ∼0.023 pc and the two densest (4 $M_\odot$ and 18 $M_\odot$) show velocity gradients consistent with Keplerian disks rotating about the central masses.

In spite of these clear examples, accretion in HMSF may not be universal nor straightforward process. For example, infalling material could be responsible for the observed Keplerian rotation signature instead (Beltrán et al. 2014). Beuther et al. (2013a) made 843 μm interferometric observations of NGC 7538 IRS1 and report at least 3 subcores within a radius of 0.01 pc. While this is consistent with Beltrán et al. (2014) and Sánchez-Monge et al. (2014) who also report multiple fragmented cores at these scales, Beuther et al. (2013a) were unable to detect Keplerian rotation signatures around the cores, and conclude that such disks are difficult to observe, possibly being detectable only at higher resolution during the earliest stages of HMSF.

Table 4.2: Comparing physical properties of HC– and UC HII regions from Murphy et al. (2010a).

Parameter		HC HII	UC HII
Size	(pc)	<0.05	<0.1
Density	(cm^{-3})	$\geq 10^5$	$\geq 10^4$
EM	(pc cm^{-6})	$\geq 10^8$	$\geq 10^7$
Recombination linewidth	(km s^{-1})	>40	$\leq$40

4.3 HII regions

HII regions are bubbles of hot ionized gas (10^4 K) around newly formed massive O or B stars on the main–sequence that are expanding into the colder (10^2 K) surrounding medium (e.g Kurtz et al. 1994; Wood & Churchwell 1989b). They are observed at radio, submillimeter and infrared wavelengths toward the recently formed ionizing star still deeply embedded in the molecular clump. HII regions are believed to mark the end (Churchwell 2002), or nearly the end (Cesaroni et al. 2015), of the rapid accretion phase of HMSF and correspond to the onset of the main sequence lifetime of the central star. Even though the HMCs introduced in Section 4.2 produce large UV photon outputs, these photons are absorbed by the infalling matter before the HII region has a chance to form (Walmsley 1995).

HII regions are typically categorized into hypercompact (HC) and ultracompact (UC) varieties. HC HII regions are thought to be associated with an earlier phase of the central object (e.g. Churchwell 2002) and display approximately linear continuum spectral energy distribution (SEDs) with frequency (i.e. $S_\nu \propto \nu^\alpha$ up to the 100 GHz range; e.g. Choi et al. 2012; Murphy et al. 2010a; Galván-Madrid et al. 2009). HC HII regions are small and dense regions (e.g. Zhang et al. 2014) which are thought to eventually evolve into UC HII regions as the ionized bubble expands. As such UC HII regions give an insight into HMSF within the last $\sim 10^5$ years (Mottram et al. 2011; Davies et al. 2011). A comparison between physical properties of HC– and UC HII regions is summarised in Table 4.2. As the UC HII bubble expands, it evolves into a compact radio HII region before settling as a diffuse optical HII source such as the famous Orion Nebula (e.g. Pon et al. 2014).

The first comprehensive studies of UC HII regions and their associations with HMSFRs were conducted by Wood & Churchwell (1989a,b). Wood & Churchwell (1989b) observed 75 HII regions using the Very Large Array (VLA) and classified the sources into 5 distinct morphologies: 43% of their sources were spherical or unresolved, 20% were cometary, 16% were core–halo, 4% shell, and the remaining 17% showed irregular or multiply peaked structures.

Current models predict that UC HII bubbles expand at the sound speed of ionized gas $c_i \approx 10$ km s^{-1}, thereby setting a theoretical lifetime of $\sim 10^4$ yr before the region becomes too diffuse for detection (Comeron & Torra 1996; Wood & Churchwell 1989a). In principle, this corresponds to less than 1% of an OB star's lifetime of $\sim 10^5 - 10^6$ years, and a similar detection rate between HII regions and OB stars was expected from survey results. However, Comeron & Torra (1996) and Wood & Churchwell (1989a) found that over 10% of the OB stars in the Galactic Plane were surrounded by UC HII regions, corresponding to lifetimes of $\sim 10^5$ years

instead.

There have been numerous theories which have been proposed to explain the lifetime problem. These include mass–loading (e.g. Lizano et al. 1996) or ram pressure (e.g. Hollenbach et al. 1994) of the stellar winds, champagne or bow shock models (e.g. Arthur & Hoare 2006) or the sources experiencing pressure–confinement or instabilities in the ionization shock fronts, thereby halting the expansion of the HII regions (e.g. Garcia-Segura & Franco 1996). Ellingsen et al. (2005) describe a scenario where a zone of diffuse ionized gas begins to form surrounding newly formed UC HII regions during a phase which could last for $\sim 10^5$ yr. As the diffuse region expands the compact region dissipates, leaving behind a classical HII region. In recent times, Peters et al. (2010) utilize the principle that HC– and UC HII regions are the ionized parts of the accreting high–mass star (Keto 2007). The high accretion rates ($\sim 10^{-2}$ $M_\odot$ yr^{-1}; see Section 4.2) involved in HMSF result in gravitational instability during collapse, leading to dense gas filaments being formed in the HII environment of the young massive star cluster. There will be periods when the strongest ionizing sources repeatedly pass through the dense gas filaments during their orbits. At such times, the filaments absorb the ionizing radiation and shield the rest of the HII region while recombination occurs. This would explain the discrepancy in the lifetime problem as the compact HII bubble will only expand when the ionizing source exits the dense filamentary gas regions.

HII regions have been the targets of several Galactic Plane surveys in light of their usefulness in identifying HMSFRs as well as for studies of spiral structure (e.g Brown et al. 2014; Bania et al. 2010; Haverkorn et al. 2006; Giveon et al. 2005; Araya et al. 2002; Lockman 1989; Caswell & Haynes 1987). Anderson et al. (2011) conduced a 9 GHz, sensitive search for HII regions of the Galaxy using the Green Bank Telescope (GBT) in the HII Region Discovery Survey (HRDS). At the sensitivity limit of 180 mJy, they show that 95% of their 448 target sources in the longitude $343^\circ \leq \ell \leq 67^\circ$ and latitude $|b| \leq 1^\circ$ show radio recombination lines (RRLs), thus demonstrating this to be an effective tool for identifying HII regions. They also find that nearly all GLIMPSE "bubble" sources are HII regions and that $\sim$50% of all Galactic HII regions have a "bubble" morphology at 8 μm. In a follow–up study, Anderson et al. (2014) used data from the Wide–Field Infrared Survey Explorer (WISE) satellite to compile over 8000 Galactic HII and candidate HII regions. Approximately 1500 sources from their sample have measured RRLs or Hα emission, thereby confirming them to be HII regions.

4.4 HMSFRs in the Milky Way galaxy

The massive stars described in this chapter are expected to affect their environments very soon after the stellar core has formed. For example, HMSF events regulate the formation of new stars (Steinbring 2014; Heckman et al. 2001), are the principal source of heavy elements in the Universe (Woosley et al. 2002) and alter the ISM through their energy and momentum outputs (Martínez-González et al. 2014; Kennicutt 2005) with massive outflows, expanding HII regions and supernova explosions. In spite of this dominant role in shaping the properties of galaxies, their structure and evolution, our understanding of their formation is incomplete. This is because massive stars are rare, distant from us, are formed whilst deeply embedded in

obscuring dense molecular clouds and are short–lived, thus making it improbable to detect key stages during their formation. The focus of the remainder of this thesis is on measuring the distances to HMSFRs in the Milky Way in order to characterise the structural and dynamical properties of the Galaxy.

4.4.1 The BeSSeL survey

In VLBI radioastronomy, information from an object is extracted by aligning radiation from the astronomical source, through unifying multiple radio telescopes spread over continental scales into a single array. The effective aperture size of this solitary virtual telescope now spans the separation between its numerous constituent instruments. Recent advancements in VLBI radio astronomical techniques have allowed astronomers to determine the relative astrometry between nearby sources to microarcsecond (μas) precision. This capability remains as the highest limit available to astronomers to accurately ascertain the positions of astronomical sources.

A decade ago, Honma et al. (2004) used the VLBI Exploration of Radio Astrometry (VERA) array to conduct high precision astrometry on the water maser pair W49N/OH43.8−0.1 and achieved an accuracy of 0.2 mas. This success demonstrated the feasibility of performing maser astrometry on Galactic scales, and subsequently several groups obtained parallax results to masers and their associated star formation regions (Honma et al. 2007; Hachisuka et al. 2006; Xu et al. 2006). Following this, Reid et al. (2009a); Moscadelli et al. (2009); Xu et al. (2009); Zhang et al. (2009); Brunthaler et al. (2009); Reid et al. (2009b); Sanna et al. (2009) started the BeSSeL survey (Brunthaler et al. 2011), which is a comprehensive Northern Hemisphere survey to measure accurate distances to HMSFRs and associated HII regions of the Milky Way galaxy using trigonometric parallax. This is being undertaken using the National Radio Astronomy Observatory's (NRAO) Very Long Baseline Array (VLBA) to measure position changes of methanol and water masers in the Galactic Plane, with respect to distant background quasars.

Phase–referencing (see Section 5.3) of a nearby background quasar to the maser emission and vice versa, combined with careful calibration of atmospheric effects (see Section 5.2), allows the change in the relative separation between the masers and quasars to be accurately measured. Repeat observations timed to maximise the measured amplitude of the parallax signature can in some cases measure the parallax to an accuracy of up to 10 μas and simultaneously determine the source proper motions to $\sim$1 μas yr^{-1} (Reid & Honma 2014). Thus far the combination of all astrometric VLBI observations (including the European VLBI Network (EVN); e.g. Reid & Honma 2014; Chibueze et al. 2014; Imai et al. 2013; Honma et al. 2012; Sakai et al. 2012; Rygl et al. 2010, 2008) has yielded more than 100 parallax and proper motion measurements for star forming regions across large portions of the Milky Way visible from the Northern Hemisphere.

Having determined the position at a reference epoch, the parallax and proper motion of the masers, the complete three–dimensional location and velocity vectors of these sources relative to the Sun can be found. These are currently being used to determine the spiral structure and rotation properties of the Milky Way.

4.4.2 Galactic structure & dynamics from BeSSeL

There is currently much ambiguity in our knowledge of the Milky Way's structure and orbital properties. No consensus exists as to the number of spiral arms, their positions, or rotational attributes (e.g. Urquhart et al. 2014a; Reid & Honma 2014; Purcell et al. 2011). Determining the Milky Way's structure has been listed as a primary objective for the Gaia mission, launched by the European Space Agency (ESA) in 2014. Even though Gaia aims to measure parallaxes of approximately 1 billion stars by 2022, the thick dust clouds which permeate the Galactic Plane and where much of the spiral structure exists, will be obscured from this advanced optical facility due to extinction of visible light. The VLBI observations of methanol (and water) maser targets from BeSSeL will complement the results from Gaia, as radio waves are able to penetrate the disk and central barred regions of the Galaxy allowing these sources to be detected through the Galactic Plane.

Spiral arm locations

The discovery of the 21 cm Hydrogen (HI) emission line brought with it the opportunity to characterise the shape of the Milky Way, as coherent arcs and loops in the longitude–velocity ($\ell - V$) plots hinted at its spiral structure (Westerhout 1957; Kerr et al. 1959). While Galactic HI was deemed to be an excellent atomic tracer, the H_2 molecule is symmetric and does not radiate in the radio range. Therefore astronomers rely on the Carbon monoxide (CO) molecule as a molecular tracer instead (Dame et al. 1987; Burton et al. 1975; Schwartz et al. 1973). Molecular gas clouds are an important tool in mapping out individual spiral arms (e.g. Dame & Thaddeus 2008), as they contain around 50% of the ISM mass within a small fraction of volume (e.g. Ade et al. 2014). While CO gas is regarded as a good spiral arm tracer, the $\ell - V$ diagrams give little information about the distances to individual arms or the extent of the separation between them.

In Reid et al. (2014), the authors present the latest results from over 100 trigonometric parallaxes and proper motions of masers associated with HMSFRs from the BeSSeL survey. The HMSFRs are assigned to spiral arms by association with CO and HI emission features. In doing so, any subjective judgments of spiral arm assignment based on parallax distances alone are avoided. The spiral arms are then modeled using a log–periodic spiral pattern in equation (4.1) for radius R from the Galactic Centre, with longitude β and pitch angle (which measures of the chirality of the spiral arm) ψ. The results from Reid et al. (2014) are summarized in Table 4.3 and described in Figure 4.3.

$$\ln\left(\frac{R}{R_{\rm ref}}\right) = -(\beta - \beta_{\rm ref})\tan\psi \tag{4.1}$$

Galactic dynamics

Using the complete three–dimensional location and velocity parameters (position $(\ell\,, b)$, parallax distance $\frac{1}{\pi}$, proper motion $(\mu_x\,,\ \mu_y)$ and Doppler shift) of $\gtrsim 100$ HMSFRs in the Milky

Arm	**N**	$\beta_{\mathbf{ref}}$ (°)	β **range** (°)	$R_{\mathbf{ref}}$ **(kpc)**	**Width (kpc)**	ψ (°)
Scutum	17	27.6	+3 to 101	5.0±0.1	0.17±0.02	19.8±2.6
Sagittarius	18	25.6	−2 to 68	6.6±0.1	0.26±0.02	6.9±1.6
Local	25	8.9	−8 to 27	8.4±0.1	0.33±0.01	12.8±2.7
Perseus	24	14.2	−21 to 88	9.9±0.1	0.38±0.01	9.4±1.4
Outer	6	18.6	−6 to 56	13.0±0.3	0.63±0.18	13.8±3.0

Table 4.3: Spiral arm characteristics from parallax measurements of HMSFRs in Reid et al. (2014) and described in Figure 4.3.

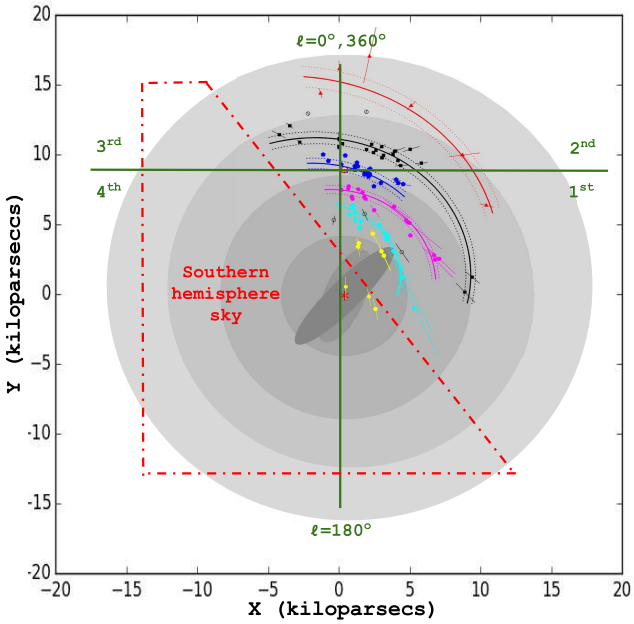

Figure 4.3: The Milky Way with spiral arms, adopted from Reid et al. (2014). The data are from trigonometric parallax measurements to HMSFRs using the VLBA, VERA and the EVN. The Galactic Centre is at $(0\,,0)$ and the Sun is at $(0\,,8.34)$. The inner Galaxy sources are described in yellow; the Scutum arm in cyan octagons; the Sagittarius arm in magenta hexagons the Local arm in blue pentagons; the Perseus arm in black squares and the Outer arm in red triangles. The open black circles are sources for which arm assignment was unclear. The data are concentrated in the 1$^{\text{st}}$ and 2$^{\text{nd}}$ quadrants, showing the need for Southern Hemisphere data as explained in Section 4.4.3.

Way, Reid et al. (2014, 2009b) construct a model of the Milky Way as a flat disk as described in equation (4.2). The circular disk velocity at a given radius $\Theta(R)$ is described as a function of the circular orbit of the Sun Θ_0 around the Galactic Centre, rate of change of orbital velocity with radius $\frac{d\,\Theta}{d\,R}$ and Solar distance from the Galactic Centre R_0. In this model, sources close to the Galactic Centre were excluded due to complications in their orbits resulting from the gravitational potential of the central bar(s).

$$\Theta(R) = \Theta_0 + \frac{d\,\Theta}{d\,R}(R - R_0) \tag{4.2}$$

A Bayesian fitting approach was used in conjunction with *a priori* values for the peculiar (deviations from circular) components of Solar motion, $U_\odot = 11.1 \pm 1.2$ km s^{-1} (radial inwards); $V_\odot = 15 \pm 10$ km s^{-1} (in the direction of Galactic rotation); $W_\odot = 7.2 \pm 1.1$ km s^{-1} (vertically upwards; Bovy et al. 2012; Schönrich et al. 2010; Reid et al. 2009b), and $\overline{U_s} = 3 \pm 10$ km s^{-1} and $\overline{V_s} - 3 \pm 10$ km s^{-1} (Reid et al. 2009b) for the average peculiar motions of HMSFRs.

Due to large uncertainties in $V_\odot$, $\overline{U_s}$ and $\overline{V_s}$, Reid et al. (2014) adopted a loose *prior* for $V_\odot$ which resulted in a chi–squared (χ^2) value of 224.9 for 232 degrees of freedom. They report a distance to the Galactic Centre of $R_0 = 8.3 \pm 0.16$ kpc, circular rotation speed of the spiral arms of $\Theta_0 = 240 \pm 8$ km s^{-1} and a flat rotation curve between radii of $\sim 5 - 16$ kpc from the Galactic Centre of $\frac{d\,\Theta}{d\,R} = 0.2 \pm 0.4$ km s^{-1} kpc^{-1}. The International Astronomical Union (IAU) recommended value for Θ_0 is 220 km s^{-1} (Kerr & Lynden-Bell 1986) and has not been updated for almost 30 years. The implications for an updated value for Θ_0 in Reid et al. (2014) means that the Milky Way is larger than has been assumed and has a more substantial dark matter halo.

4.4.3 Southern Hemisphere VLBI maser parallaxes

Astronomical sources at Southerly declinations achieve only low elevations in the Northern Hemisphere, if they rise at all. For the phase–referencing observations employed in the BeSSeL survey, the delay difference between the sources is sensitive to the zenith angle z and governed by equation (7.1). This relationship results in an increase in delay by a factor of 3 and 6.5 between zenith angle $z = 60°$ and 70° respectively (Fomalont 2013), and affects the astrometric accuracy of Northern Hemisphere VLBI instruments for Southern Hemisphere parallax measurements.

The sources with trigonometric parallax measurements compiled in Reid et al. (2014) predominantly lie within the Galactic Longitude range of $0° < l < 240°$. There are two sources within the 4$^{\text{th}}$ quadrant of the Galaxy, with the most Southerly of these at a declination of $-39°$. Therefore, the updated estimates for fundamental Galactic parameters such as Θ_0 and R_0 are based on data which are restricted to only a little over half the total Galactic Longitude range. In order to ensure that models of Galactic structure and rotation are reliable, they must be derived from a more uniformly sampled distribution including sources in the 3$^{\text{rd}}$ and 4$^{\text{th}}$ quadrants. The Pearson product–moment correlation coefficient (PPMCC) in Reid et al. (2014) between R_0 and Θ_0 in equation (4.2) is 0.46. This is significantly better

than the PPMCC of 0.87 from 18 sources reported in Reid et al. (2009b), but still indicates a strong level of dependence between Θ_0 and R_0 in modelling Galactic parameters from VLBI parallaxes which are concentrated towards Northern Hemisphere observations.

Distances to Southern maser sources and their associated HII regions have exclusively been determined via indirect methods, such as through kinematic distance estimates (e.g. Green & McClure-Griffiths 2011; Caswell et al. 2010, 1975). However, the issues which can produce significant errors in these techniques include potentially large peculiar motions, broad spectral line profiles and uncertainties in the model parameters. The LBA is the only VLBI instrument in the Southern Hemisphere and is currently involved in a program to provide parallax distances towards Southern HMSFRs in the 3$^{\rm rd}$ and 4$^{\rm th}$ quadrants of the Milky Way. The aim of this program is to determine the parallaxes to $\sim$30 Southern 6.7 GHz methanol maser sources, and the details of the observations and our first results will be presented in the following chapters.

Chapter 5

6.7 GHz Methanol Maser Observations

In the previous chapters I have briefly outlined the major stages of HMSF, the important role which masers play as probes of the concealed regions surrounding the immediate vicinity (10 – 10^3 AU) of young high–mass stars, how sub–milliarcsecond astrometry is required to measure trigonometric parallaxes that provide the most reliable distances to these regions, and how accurate distances to such regions are essential to place tight constrains on the physical properties these objects. The massive molecular (e.g. CO and HII) regions in which young high–mass objects are embedded in, are also excellent tracers of Galactic spiral arms, and the BeSSeL project has catalogued over 100 parallax distances to methanol masers associated with HMSFRs in the Milky Way galaxy; thereby allowing the latest structural and dynamical properties of our Galaxy to be determined. These parallaxes have been concentrated towards the 1^{st} and 2^{nd} quadrants of the Galaxy due to the technical challenges of performing sub–milliarcsecond astrometry at low declinations from the Northern Hemisphere (Honma et al. 2008). Being the only VLBI array in the Southern Hemisphere, the LBA is currently the only instrument which is available to accurately measure the positions of Southern HMSFRs in the 3^{rd} and 4^{th} quadrants of the Milky Way. VLBI phase–referenced observations using the LBA to determine parallaxes to Southern Hemisphere 6.7 GHz methanol masers began in 2008 March (LBA experiment code v255, epochs *a* to *x* inclusive). The details of the observations and results presented in this thesis are based on the epochs between 2012 and 2015 March (see Table 5.1). However, the procedures described here are broadly applicable to all observations since 2008 March.

The LBA is a heterogeneous interferometer with between 5 – 7 antennas available for the 6.7 GHz observations reported here (see Table 5.2.1). The antennas which observed for one or more epochs were the Australia Telescope Compact Array (ATCA), Ceduna, Hartebeesthoek (HartRAO), Hobart, Mopra, Parkes and Warkworth 30m (Wark30m). The ATCA is itself a connected six element interferometer which was operated in tied–array mode, and with the outputs from either four or five 22 metre antennas phased and combined. The Wark30m antenna is a recent addition to the LBA and only participated in the 2014 November and 2015 March epochs of observations. Baselines to the Wark30m antenna were not used in this thesis because of insufficient data and the importance of

using a similar array for all epochs in parallax measurements. The shortest baseline for the LBA lies between ATCA – Mopra (113 km) and the longest connects HartRAO – Wark30m (10,481 km). For the parallax results presented in Chapters 7 and 8, we were not able to use data from HartRAO (see Section 7.3.1 for details), leaving the longest baseline connecting Ceduna – Hobart (1,702 km).

5.1 Considerations for astrometry

As described in Fomalont (1995) the response $r(t)$ from a two–element interferometer has quasi–sinusoidal time behavior (fringes) given by

$$r(t) = A \cos \phi_T \tag{5.1}$$

where A is the amplitude of the fringe pattern and ϕ_T is the delay in total phase between the radio signals incident on each antenna element. The fringe amplitude is dependent on the receiver gain, attenuation, bandwidth of the received signal and is of secondary concern for astrometry. This is because the position information for a radio source is contained entirely within ϕ_T.

For observations at frequency ν this is given as

$$\phi_T = 2\pi\nu(\tau_g + \tau_n) + \phi_d + \phi_V \tag{5.2}$$

where τ_g is the geometric time delay between the radio signal incident on each antenna and τ_n is the non–dispersive time delay (defined explicitly as τ_{tropo} in equation (6.2)), which includes factors such as clock timing errors and tropospheric refraction. The delays from τ_g and τ_n do not affect the bandwidth of ν as the waveform propagates through the atmosphere, and the methods used to correct for them are detailed in Sections 6.2.5 and 6.3.4. The dispersive component given by ϕ_d is primarily an ionospheric effect and is corrected using techniques described in Section 6.2.1. The visibility phase ϕ_V is dependent on source structure, and the individual methanol maser components that we selected for the purposes of astrometry exhibit point–like structure at the milliarcsecond scale (see Figure 6.5), and we expect minimal contribution from this term to ϕ_T.

				AEST		UT		Participating
Epoch	**Year**	**Date**	**D.O.Y**	**Start**	**Stop**	**Start**	**Stop**	**stations**
v255q	2012	06 Mar	067	14:00	1/08:00	04:00	22:00	AT, CD, HO, MP, PA
v255r	2013	18 Mar	077	14:00	1/14:00	04:00	1/04:00	AT, CD, HH, HO, PA
v255s	2013	17 Jun	168	12:30	1/08:00	02:30	22:00	AT, CD, HH, HO, MP, PA
v255t	2013	14 Aug	226	04:00	1/04:00	18:00	1/18:00	AT, CD, HH, HO, MP, PA
v255u	2013	19 Nov	323	22:00	1/21:00	12:00	1/11:00	AT, CD, HO, MP, PA
v255v	2014	01 Mar	060	08:00	1/08:00	22:00	1/22:00	AT, CD, HH, HO, MP
v255w	2014	21 Nov	324	09:00	1/09:00	23:00	1/23:00	AT, CD, HH, HO, MP, WA
v255x	2015	27 Mar	086	12:00	1/12:00	02:00	1/02:00	AT, CD, HH, HO, MP, PA, WA

Table 5.1: Phase–referenced 6.7 GHz methanol maser observations between 2012 March and 2015 March. The participating stations are the Australia Telescope Compact Array (AT), Ceduna (CD), HartRao (HH), Hobart (HO), Mopra (MP), Parkes (PA) and Wark30m (WA).

In practice the total phase is approximated with the model phase by

$$\phi_T = \phi_M + \phi_R \tag{5.3}$$

and the objective of our interferometric observations and subsequent data reduction in Chapter 6, is to determine an accurate phase model ϕ_M as a function of time and direction, by reducing residuals in ϕ_R to a minimum. The strategies which we used to ensure that the relevant error terms are well constrained are based on the techniques outlined in Reid et al. (2009a), Reid & Brunthaler (2004) and Reid et al. (1999). The observations consisted of two distinct modes which will be explored in Sections 5.2 and 5.3. An example of the schedule from the 2014 November observations is summarized in Table 5.3.

5.2 ICRF mode

The correlator model does not account for tropospheric refraction and we compensated for this through the International Celestial Reference Frame (ICRF) calibration observations. An excess in $\tau_{\rm tropo}$ in equation (6.2) limits the relative positional accuracy between the 6.7 GHz methanol maser and quasar sources in Section 5.3, and is likely to be a significant source of systematic error for our 6.7 GHz phase–referenced observations (Reid et al. 2009a; Mioduszewski & Kogan 2009; Pradel et al. 2006). This excess can be determined by observing about ten calibrators spread over a range of azimuths and elevations (Mioduszewski & Kogan 2009) and applying the calibration technique in Section 6.2.5. We also used these observations to model the clock drift rate at the observatories.

5.2.1 Source selection

The source list was generated using the 2$^{\rm nd}$ realization of the ICRF catalogue by Ma et al. (2009). The sources from this catalog have well–determined positions (<1 mas) and are assumed to have point–like structure at high–resolution. Any residual delays for these ICRF sources with well known positions will therefore be dominated by a combination of ionospheric and tropospheric refraction (assuming that the antenna positions are also well known).

We used an algorithm to generate trial schedules from a random selection of sources with a minimum elevation of 12°. A least–squares fit was then performed to estimate the accuracy to which the selection of sources characterise $\tau_{\rm tropo}$ and clock offsets for all stations (see Section 7.3.1 for exceptions). We ran 1000 such trial schedules and chose the one which minimized the largest of the formal uncertainties in $\tau_{\rm tropo}$ among the stations for the ICRF observations.

		ATCA	Ceduna	HartRAO	Hobart	Mopra	Parkes	Wark30m
Diameter	(m)	22	30	26	26	22	64	30
SEFD	(Jy)	140	550	290	700	600	110	650
X position	(mm)	−4751639859.72	−3753442743.76	5085442784.75	−3950236740.25	−4682769058.50	−4554231943.79	−5115425600.00
		±14.62	±25.53	±0.87	±0.90	±14.91	±15.30	±80.00
Y		2791700356.70	3912709755.73	2668263489.55	2522347552.67	2802619042.17	2816758914.42	477880300.00
		±15.79	±25.06	±0.68	±0.85	±16.1 3	±9.64	±20.00
Z		−3200491113.39	−3348067527.18	−2768697010.08	−4311562533.71	−3291759338.37	−3454035789.13	3767042810.00
		±20.29	±26.32	±0.58	±0.74	±19.97	±11.93	±60.00
$\dot{X}$	(mm/yr)	−30.99	−39.95	−0.89	−38.40	−37.04	−32.71	−19.60
		±1.27	±2.22	±0.13	±0.13	±1.28	±0.92	±1.20
$\dot{Y}$		−4.58	0.55	18.86	8.46	−9.02	−3.31	−2.50
		±1.41	±2.13	±0.11	±0.12	±1.44	±0.60	±0.50
$\dot{Z}$		42.03	45.46	14.57	38.66	45.02	47.26	34.10
		±1.84	±2.37	±0.09	±0.11	±1.80	±0.74	±1.00

Table 5.2: Antenna parameters.The system equivalent flux density (SEFD) is for each antenna's 6.7 GHz receivers as listed in:
`www.atnf.csiro.au/vlbi/documentation/vlbi_antennas/index.html`
The ATCA is a 6 element connected interferometer with between four to five 22 m antennas phased–up for LBA observations. The phased array has an SEFD of 140 Jy. The antenna positions are from:
`http://astrogeo.org/vlbi/solutions/2009d/`
The station parameters for Wark30m are from Petrov et al. (2015).

AEST	Source
2300 – 2345	ICRF run 1
2345 – 0300	G339, G287, G291
0300 – 0345	ICRF run 2
0345 – 0700	G287, G316, G339
0700 – 0745	ICRF run 3
0745 – 1100	G316, G339
1100 – 1145	ICRF run 4
1145 – 1500	G291, G287
1500 – 1545	ICRF run 5
1545 – 1900	G291, G287, G316
1900 – 1945	ICRF run 6
1945 – 2215	G316
2215 – 2300	ICRF run 7

Table 5.3: A break–down of the 2014 November schedule. The ICRF mode observations (Section 5.2), are used to make calibration measurements for slow changes in the total tropospheric delay for each station and are interspersed at intervals of $3-4$ hours between the main mode phase–referenced maser observations (Section 5.3) for astrometry.

5.2.2 Set–up

The ICRF continuum observations were recorded across 4 IF bands spanning 390 MHz, which was as broad a frequency range as could be accommodated by the LBA. An important consideration is to spread the IFs across this range in a way which minimizes the ambiguity in finding the delay solution. In the ideal case, there needs to be both narrow and wide margins between consecutive IFs in order to rule out very large and small delays (see Figure 5.1). However, the heterogeneous nature of the array meant that with different receiver front ends, it was necessary to compromise the frequency setup so that it could be adopted at all antennas. The LBA Data Acquisition System (DAS) can record the observed signals onto two independent IF bands. The optimal frequency configuration which is able to accommodate these restrictions is to have 4×16 MHz bands, the first pair (LBA DAS IF 1 with RR polarization) with lower–band edges at 6300 and 6316 MHz and the second pair (LBA DAS IF 2 with LL polarization) with lower–band edges at 6642 and 6658 MHz.

5.2.3 Observations

We grouped the ICRF observations into 45 minute blocks with an interval of between 3–4 hours separating consecutive blocks (Mioduszewski & Kogan 2009). These were interspersed between the main mode maser observations as shown in Table 5.3, and between 12 and 18 sources ($\sim$2 minutes per source) were observed in each block.

5.3 Phase–referencing observations

Radio astrometry is broadly divided into two categories:

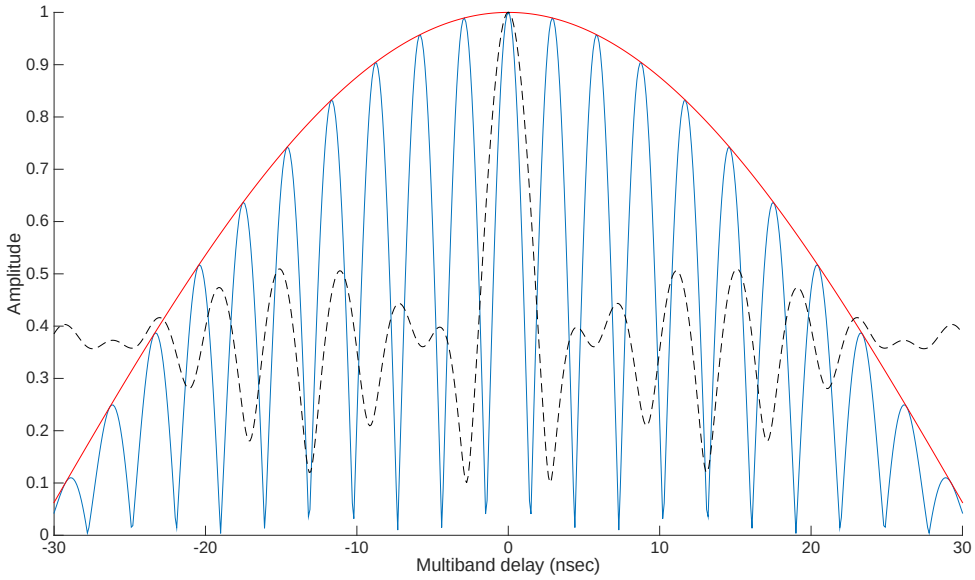

Figure 5.1: Examples of the expected multiband delay model from three different IF band configurations between 6300 and 6690 MHz with the LBA, assuming a bandwidth of 16 MHz. The dashed black line is an ideal case with a *Golomb ruler*[1] spacing of 6386, 6466, 6498, 6594, 6642 and 6658 MHz. In this example all secondary peaks adjacent to the central feature have significantly reduced relative amplitudes, allowing the multiband delays in Section 6.2.4 to be unambiguously determined. The blue line models the solution from the observational set–up in Section 5.2, with the first IF pair at 6300 and 6316 MHz and the second pair at 6642 and 6658 MHz. Secondary peaks are of comparable amplitude to the central peak and are separated by only ∼2.5 nsec. A likely scenario during the search for the multiband delay in this case is that, in addition to the central peak, additional solutions are incorporated from the secondary components as the delay. This confusion could explain the noise in the delay in Section 6.2.4 and Figure 6.2. The red line models the expected delay from the 6300 and 6316 MHz IF configuration which was eventually used for data reduction in Section 6.2.4.

[1]A set of points on an imaginary ruler such that no combination of two points are the same distance apart.

1. The narrow–field case of measuring relative positions of sources within several degrees
2. The wide–field case of measuring relative/absolute positions of sources

In both cases the atmospheric delay and turbulence from the wet/dry troposphere, the ionosphere and the structure of the target source(s) contribute to the positional error. The phase–referencing procedure is used to compensate for the short–term stochastic component caused by the turbulent atmosphere in the narrow–field case.

In many VLBI observations, data from the target source is used to characterise the *phase*, *delay* and *delay rate* errors (e.g. through fringe fitting in Section 6.2.3 or through self–calibration). The premise of phase–referencing is to eliminate these errors by using data from an external calibrator instead of the source itself. Beasley & Conway (1995) describe how the phase information from a *calibrator* source can be transferred to a *target* source if the pair are observed using a nodding technique with a short cycle time. Under this assumption, the calibrator source delay solutions will provide a good estimate of the target source delay, to allow integration of the target (and calibrator) data over frequency and time without a loss of coherence.

5.3.1 Source selection

Current maser parallax measurements made with the VLBA and VERA have primarily been towards either 12.2 GHz methanol masers or water masers. However, not all LBA antennas have receivers capable of observing at 12.2 GHz, and many of the LBA antennas have significantly poorer sensitivity at 22 GHz than they do at frequencies less than 10 GHz. Hence the 6.7 GHz class II methanol maser transition was considered to provide the best targets for parallax observation with the LBA. They have strong, stable and compact emission over the timescales required for parallax measurements and are well sampled from the Southern Hemisphere, with close to 1000 sources being documented in the MMB survey (Breen et al. 2015; Green et al. 2012b; Caswell et al. 2011c, 2010; Green et al. 2010) — a sensitive, unbiased search for 6.7 GHz methanol masers in the Southern Galactic Plane.

It can be assumed that the long–term residual tropospheric, ionospheric and astrometric parameters produce a quasi plane–parallel phase gradient (delay) over each antenna. In this case, the relative positional accuracy scales with the angular separation between sources, meaning that it is of fundamental importance that the quasar and maser are as closely spaced in the sky as possible (Beasley & Conway 1995). There currently exist numerous catalogues of compact radio sources with sub–milliarcsecond positional accuracies (Lambert 2014; Ma et al. 2009; Hirabayashi et al. 2000; Ma et al. 1998). However, these are predominantly from the Northern Hemisphere (see Figure 5.2 for an example), and there is a paucity of accurately positioned calibrators in regions South of $\delta = 30^{\circ}$, and close to the Galactic Plane (Petrov et al. 2011). The primary databases which were used in our search for background quasars were the Australia Telescope 20 GHz (AT20G; Hancock et al. 2011), Astrogeo (Petrov et al. 2011) and Australia Telescope Parkes–MIT–NRAO (ATPMN; McConnell et al. 2012) calibrator catalogues.

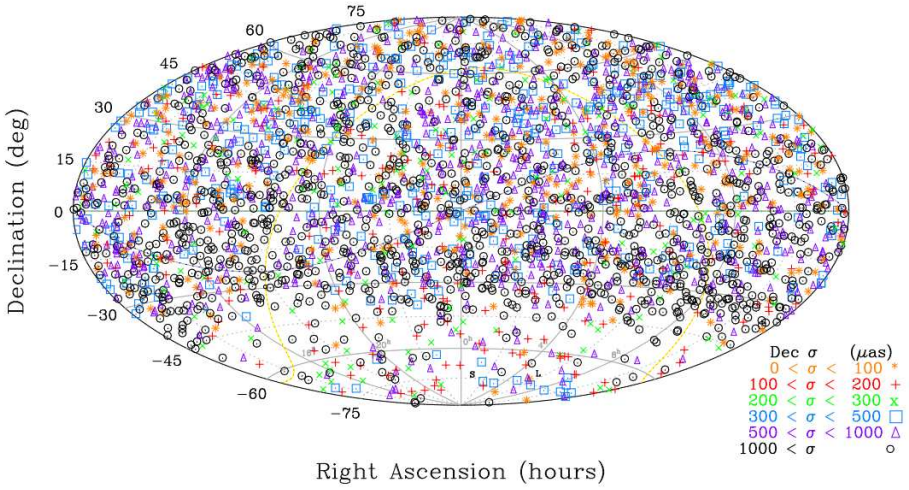

Figure 5.2: The distribution of calibrators in the ICRF2 catalogue consisting of 3414 sources. The figure is adopted from Malkin et al. (2015) and shows a paucity of data for the Southern Hemisphere.

5.3.2 Observations

Our 6.7 GHz maser astrometry observations involved alternating scans for 2 minutes on the maser with scans lasting 2 minutes on a nearby quasar to compensate for most of the short–term atmospheric distortions (e.g Reid et al. 1999; Fomalont 1995). In order for this technique to work in practice, the maser must be detectable above the RMS noise on each baseline over the 2 minute scan duration, and the switching timescale be <20% of 360° phase change for coherence to be maintained. For our phase–referenced observations, the LBA DAS system was set to record dual circular polarization for 2×16 MHz bands with lower–band edges at 6642 and 6658 MHz.

5.4 Correlation

The data were correlated with the DiFX correlator at Curtin University (Deller et al. 2011). As the maser emission covers only a small fraction of the 2×16 MHz of recorded bandwidth, it was not necessary to correlate the entire band. Hence for the maser data, a 2 MHz zoom–band was correlated with 2048 channels (1 MHz over 1024 channels for the 2014 March epoch), giving a spectral resolution of 0.977 kHz corresponding to a velocity separation of 0.055 km s^{-1}. For the observations of the background quasar the entire observed bandwidth was correlated. In the 2012 March and 2013 March epochs, 256 spectral channels were used per 16 MHz bandwidth, corresponding to a resolution of 62.5 kHz. In the remaining epochs, 32 spectral channels were used per 16 MHz bandwidth, corresponding to a resolution of 500 kHz. The ICRF data were correlated using the same spectral resolution as the background quasar observations in each epoch. The different parameters which were used for the correlation of the maser and quasar emission from the same band resulted in a complication during "manual" delay calibration which is detailed in Section 6.3.4.

5.5 Sources of errors

Radio calibrators (including the ICRF sources in Section 5.2) are not perfect point sources and consist of a compact core component of $\geq$20% of the source intensity within a 0.05 mas region (Horiuchi et al. 2004). They are also known to have variable intensity and structure over periods of days to years, which naturally lead to positional errors (e.g. Fomalont et al. 2010). Another source of error includes uncertainties with the astrometric parameters of the array (see Table 5.2.1), as well as offsets between the target and calibrator sources as described in Section 5.3.1.

In our 6.7 GHz phase–referencing observations, it is estimated that astrometric errors will be dominated by unmodeled atmospheric effects. These are introduced from residual plane–parallel troposphere and ionosphere delays above each antenna toward the source and primarily affect the image quality, not the the relative position of the emission (Mioduszewski & Kogan 2009). Further details on the effects of tropospheric and ionospheric errors on LBA maser astrometry are presented in Section 7.3.

Chapter 6

Data Reduction

I used the 31DEC13 version of the Astronomical Image Processing System (AIPS; Greisen 2003) for data reduction, based on the procedure described in Reid et al. (2009a). The same steps were employed across all epochs for consistency and standardisation of the procedures was maintained through the use of AIPS runfiles. An example of a complete set of runfiles which were used for the 2012 March epoch is given in Appendix A and a flowchart of the pipeline is presented in Figure 6.6. AIPS tasks and procedures will be distinguished with an * in the following text.

6.1 Loading and flagging

The task FITLD* was used to load the interferometric FITS files into AIPS. In each epoch, these consisted of the geodetic (ICRF), continuum (quasar) and spectral line (maser) modes. The combined data for each epoch of observation was typically ∼10 gigabytes. UVFLG* was then used to apply automatic flag files which were generated from each antenna during the observation for times when antennas were off–source or experiencing problems.

In some instances the automatic flag files from the antennas were imperfect and VPLOT* clearly revealed whenever a baseline pair was off–source, as the amplitudes were seen to drop to zero while the antennas were slewing. These time ranges were then identified and manually flagged using UVFLG*. In the case of the ICRF and quasar data, we verified the quality of the scans for each source by using VPLOT* to show the uncalibrated amplitudes vs. time for that source across all channels and IFs. The process was repeated for the maser data, except we first used POSSM* to identify a single channel corresponding to a peak in the spectrum before plotting the amplitudes for that channel. Scans containing sharp spikes or dips in amplitude were similarly identified and flagged as being indicative of poor data for the ICRF, quasar and maser datasets.

6.2 ICRF data calibration

We calibrated the geodetic mode ICRF observations prior to using the multiband delays from these observations to determine $\tau_{\rm tropo}$ and the non–dispersive clock delays (see Section 5.1) from equation (6.2). The LBA correlator at Curtin University uses a model for the tropo-

sphere which has been determined from seasonal models, estimates for the clocks as well as the coordinates of each antenna in the array (Brisken 2014; Deller et al. 2011). None of these are perfect and the residual errors affect the positional accuracy of the sources and the quality of the phase–referencing procedure. We calibrated the ICRF mode observations using the procedures in Sections 6.2.1 to 6.2.4 before obtaining the tropospheric delay and clock rate models in Section 6.2.5.

6.2.1 Ionospheric delay corrections

We ran VLBATECR* which automatically downloads the ionosphere map (IONEX) files containing measurements of the total electron content (TEC) in the Earth's ionosphere. The vertical TEC data are generated on an hourly and daily basis at the Jet Propulsion Labs (JPL), determined from up to 100 Global Positioning System (GPS) sites scattered around the planet, and modeled in a solar–geomagnetic reference frame on a spherical grid. An estimated position of a particular receiver is determined from measuring the time delay between a transmission between each satellite and the ground–based receiver. This delay ($\tau_{\rm iono}$) is a result of ionospheric disruptions via the presence of free electrons.

VLBATECR* accepts the IONEX format of ionospheric models and interpolates the temporal and spatial TEC corrections to the point at which the line–of–sight from each antenna to the source passes through the assumed nominal height of the ionosphere at an altitude of 450 km (e.g. Varney et al. 2011). Adopting such a procedure assumes that the ionosphere is infinitely thin and that the direction of the Sun remains fixed (due to the large day–night dependence), as the ionosphere is more constant in this reference frame, than one rotating with the Earth. VLBATECR* then derives and applies the corrections for the ionospheric Faraday rotation and dispersive delay from the TEC maps.

One caveat is that the TEC models suffer at Southern declinations due to a paucity of GPS receivers at these latitudes (Deller et al. 2009b). An estimate of the residual errors from the ionospheric corrections is covered in Section 7.3.2.

6.2.2 Earth Orientation Parameters

The United States Naval Observatory (USNO) provides the International Earth Rotation and Reference Systems Service (IERS) and determines the rotation of the Earth about its axis. The data products are compiled into the Earth Orientation Parameters[1] (EOPs) and are updated daily as new VLBI data become available. The EOPs provide a means to relate the International Terrestrial Reference System (ITRS) to the International Celestial Reference System (ICRS) as a function of time, in conjunction with existing precession–nutation models from McCarthy & Petit (2004). We obtained the latest EOPs and used CLCOR* to implement the corrections for the changing aspects between the ITRS and the ICRS.

[1] `http://gemini.gsfc.nasa.gov/solve_save/usno_finals.erp`

6.2.3 "Manual" delay calibration

Imperfections in the correlator delay τ will result in errors which are time and frequency ν dependent in phase $\phi(t, \nu) = \tau\nu$. To first order, this error is given by

$$\Delta\phi(t, \nu) = \phi_0 + \left(\frac{\partial\phi}{\partial\nu}\Delta\nu + \frac{\partial\phi}{\partial t}\Delta t\right) \tag{6.1}$$

where ϕ_0 is the phase error (in number of turns) at a reference time and frequency. Here $\frac{\partial\phi}{\partial\nu}$ is the *delay* and $\frac{\partial\phi}{\partial t}$ is the *rate* of the interferometer (Cotton 1995). As the phases for the calibrator source can have high residual delays (see Figure 6.1), we remove these using "manual" delay calibration to ensure the data can be averaged in frequency. The global fringe fitting process which was employed for delay calibration minimizes the difference between a model and the measured delay (and rate for phase–referencing in Section 6.3.5), by solving for station based parameters from all baselines (Schwab & Cotton 1983).

FRING* was used to perform "manual" delay calibration using a strong ICRF source with well known position (<1 mas) and a relatively short scan of ∼2 mins. A single value of delay is then determined for each antenna, polarization and IF band. A list of the ICRF sources which were used as the delay calibrator for each epoch are given in Table 6.1 and plots of the amplitude and phase from our 2013 August epoch of observations for the calibrator source 0013−005 before and after "manual" delay calibration are shown in Figure 6.1.

6.2.4 Multiband delays

In phase–reference observations, the unmodelled troposphere produces a systematic phase difference between the calibrator and target, which limits the target positional accuracy and image quality. However, the model errors can be sufficiently large that the measured phase of the all–sky calibrator observations in Section 5.2.3 span many turns and cannot be used to determine the troposphere delay. The phase ambiguity problem is solved by the measurement of a related term, the multiband (or group) delay (Mioduszewski & Kogan 2009).

In order to obtain the multiband delays for all the ICRF sources, we ran FRING* to extract a single delay across a combination of all the IF bands. During data reduction, we discoverd the multiband delay solutions obtained from 4×16 MHz IFs were significantly noisier than those obtained when only 2×16 MHz IFs were used (see Figure 6.2). Due to the technical limitations of using a heterogeneous array, the LBA setup was not able to accommodate a frequency configuration which minimized the ambiguity in finding accurate delays (see Section 5.2). As a result, the multiband delays for our observations were determined from a total bandwidth separation of only 32 MHz from IFs 1 & 2 instead of the intended 390 MHz over 4 IFs. This naturally led to a loss in the accuracy of the delay calibration, and affected our ability to model the tropospheric path length contribution as described by Figure 5.1. The possible reasons for this are explored in Section 7.3. I found that RMS noise of the multiband delay solutions from FRING* for the 2 IF set–up ranged between 0.01 – 0.5 nsec, with a mean of 0.1 nsec. This corresponds to path lengths of 10s of cm, and is consistent

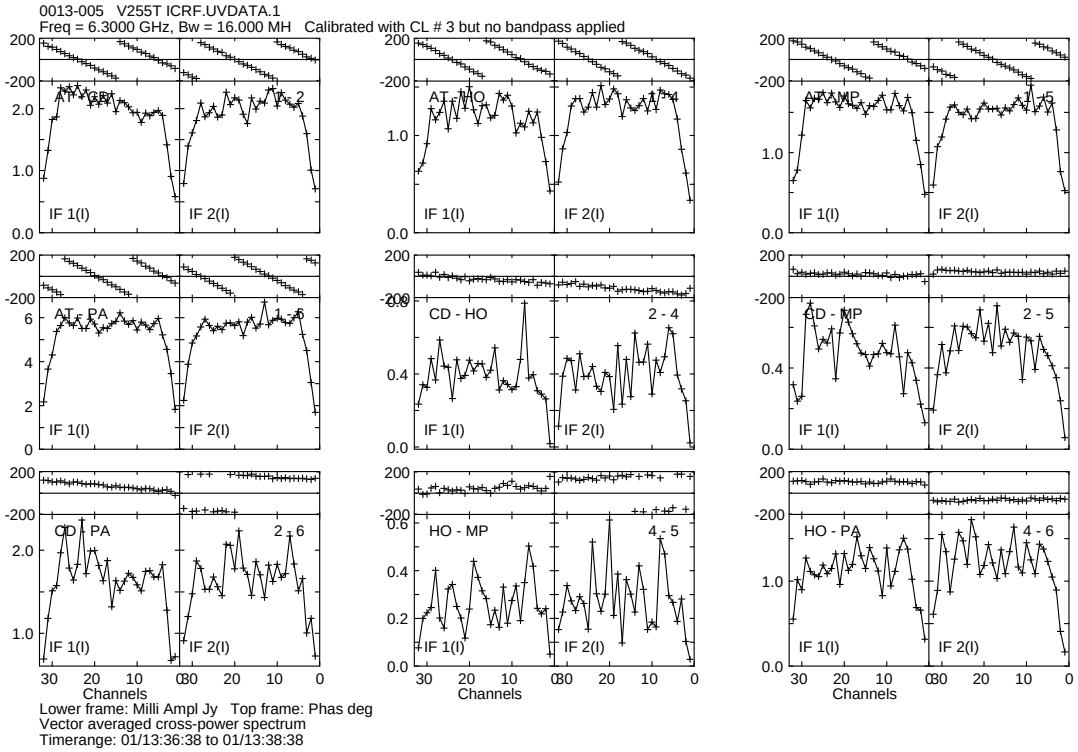

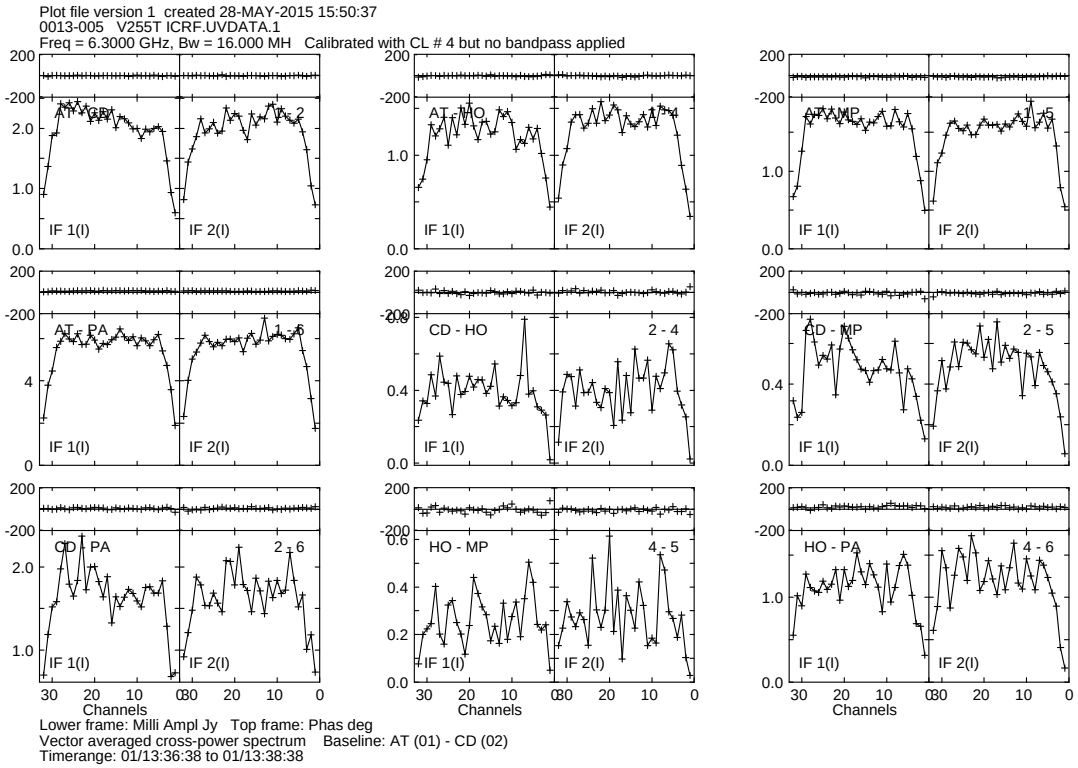

Figure 6.1: The change of phase with frequency, before "manual" delay calibration is applied to 0013−005 in 2013 August, shows rapid wrapping in some instances due to high residual delays post correlation (top). After calibration is applied, the phases are flat across all IFs and baselines (bottom).

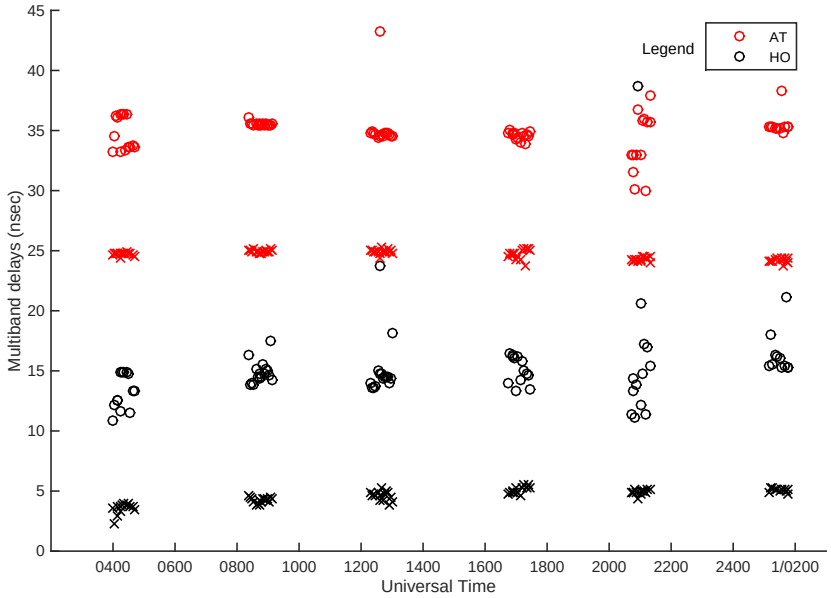

Figure 6.2: A sample of the multiband delays obtained from the ATCA (AT) and Hobart (HO) from the 2013 March epoch of ICRF observations. The delays for each station have been offset from each other on the y–axis for clarity. The circles represent delays from all 4 IFs of ICRF observations, and the the crosses represent the delays from IFs 1 and 2 only. The solutions from 2 IFs were found to exhibit less scatter and were therefore used to determine the tropospheric multiband delays in Section 6.2.4.

with the reported path length errors from the troposphere delay fit in Section 6.2.5.

6.2.5 Troposphere delay fitting

A least squares fit based on the approach in Reid et al. (2009a) was employed to model the zenith tropospheric delay (and delay–rate), as well as a clock offset (and clock drift rate) as given by equation (6.2). The model was based entirely on the multiband delays, as the fringe rates carried large uncertainties due to the short integration times per source. An iterative approach was used in the fitting process to account for defects in the data, where outliers relative to the previous solution were severely down–weighted. The uncertainty assigned to

Epoch	**Source name**	**RA (h m s)**	**Dec (° ′ ″)**	**Scan (min)**
2012 March	1349−439	13 52 56.54	−44 12 40.388	1:00
2013 March	0537−441	05 38 50.36	−44 05 08.939	1:00
2013 June	1302−102	13 05 33.02	−10 33 19.428	2:00
2013 August	0013−005	00 16 11.09	−00 15 12.445	2:00
2013 November	1929+226	19 31 24.92	+22 43 31.259	1:15
2014 March	0537−441	05 38 50.36	−44 05 08.939	4:00
2014 November	0537−441	05 38 50.36	−44 05 08.939	3:00

Table 6.1: Sources in each epoch which were used for “manual” delay calibration during the ICRF mode observations.

each delay or fringe rate after an iteration was increased by a factor of $e^{(r/4)^2}$, where r is the post–fit residual after each iteration, divided by the previous uncertainty. The sensitivity of the exponential term greatly down–weights residuals of more than 4σ, corresponding to <10% of the input data being down–weighted. The first iteration used an initial estimate of the multiband delay of 3 cm and a fringe rate of 0.003 Hz.

We then used the elevation of the source for each station, LST of the observation and the source zenith angle z to calculate the delay and fringe rate model for the entire set of baselines. The source elevation e (derived from z) is used to determine the wet mapping function $m(e, a, b, c)$, which is a ratio expression of the "line of sight" tropospheric delay $\tau_{\rm tropo}$ to the corresponding zenith delay τ_z (Niell 1996). We also substituted the Niell (1996) mapping function with a latitude specific Global Mapping Function (Boehm et al. 2006), and found the results between the two to be consistent within error margins. The parameters in equation (6.3) are based on a 30° latitude for all stations, where $a = 5.6795 \times 10^{-4}, b = 1.5139 \times 10^{-3}$ and $c = 4.6730 \times 10^{-2}$.

$$\tau_{\rm tropo} \quad = \quad \tau_z \; m(e, a, b, c) + \text{Clocks} \tag{6.2}$$

where

$$m(e, a, b, c) = \frac{\frac{1}{1+\frac{a}{1+\frac{b}{1+c}}}}{\frac{1}{\sin e+\frac{a}{\sin e+\frac{b}{\sin e+c}}}} \tag{6.3}$$

Table 6.2 shows that the typical zenith delays were ≤10 cm in magnitude. The errors were found to range between 10 – 100%, with large errors being attributed to an uncertainty in finding multiband delay solutions (see Section 6.2.4). Zenith delay corrections which had significant errors, or which were unreasonably large (e.g. >15 cm) were discarded. In such cases, we studied the preceding and proceeding zenith delay corrections and used an intermediate value or applied a 0 cm solution instead. In addition to computing the atmospheric path length, the linear clock drift rate (see Figure 6.3) of the H–maser with time for each antenna was determined from the multiband delays from FRING*.

The zenith delays and clock drift rates were written into an ASCII file to be applied to the phase–referencing data with CLCOR* in Section 6.3.1.

6.3 Phase–referenced data calibration

6.3.1 Initial preparations

We used CLCOR* to remove phase contributions resulting from the parallactic angle, which forms between the great circle passing through the source–zenith and the hour circle (the great circle through the source–celestial poles). We then applied the tropospheric path length and clock drift corrections from Section 6.2.5 and the EOPs as in Section 6.2.2. Ionospheric delay

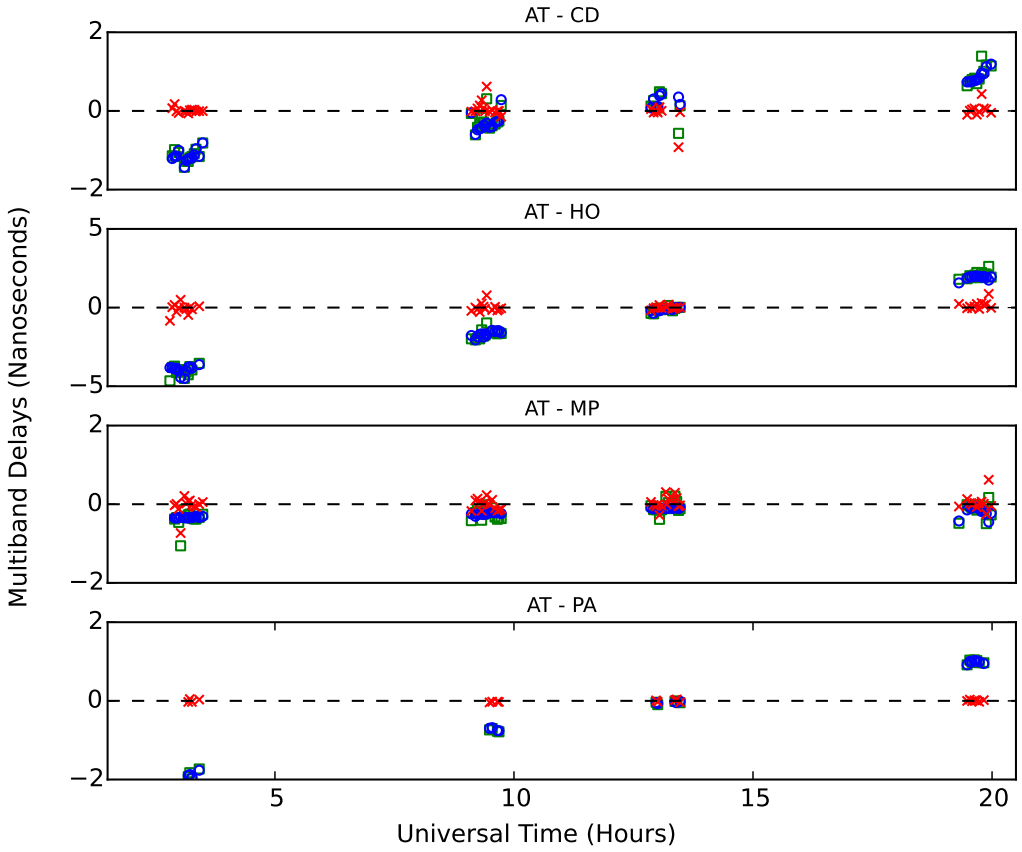

Figure 6.3: A sample of the multiband delay solutions from Ceduna (CD), Hobart (HO), Mopra (MP) and Parkes (PA) with respect to the ATCA (AT), determined from the ICRF mode observations in 2013 June. The (green) squares, (blue) circles and (red) crosses represent the data, model and residuals between the two.

Antenna code	**Day**	**Hour**	**Minute**	**Second**	**Zenith delay (cm)**	**Clock delay (cm)**	**Derivative of zenith delay ($\times 10^{-14}$ sec / sec)**	**Derivative of clock delay ($\times 10^{-14}$ sec / sec)**
1	1	3	21	44.4	−7.755	0.000	0.00000	0.00000
2	1	3	21	44.4	5.912	16.941	0.00000	−1.19286
4	1	3	21	44.4	−9.142	−108.861	0.00000	9.12370
5	1	3	21	44.4	6.036	96.612	0.00000	−8.34096
1	1	7	24	23.8	−4.561	0.000	0.00000	0.00000
2	1	7	24	23.8	−2.585	11.734	0.00000	−1.19286
4	1	7	24	23.8	−1.564	−69.038	0.00000	9.12370
5	1	7	24	23.8	4.617	60.206	0.00000	−8.34096
1	1	11	25	50.6	−2.082	0.000	0.00000	0.00000
2	1	11	25	50.6	−6.564	6.554	0.00000	−1.19286
4	1	11	25	50.6	0.021	−29.413	0.00000	9.12370
5	1	11	25	50.6	0.823	23.981	0.00000	−8.34096
1	1	15	26	5.0	3.260	0.000	0.00000	0.00000
2	1	15	26	5.0	0.043	1.399	0.00000	−1.19286
4	1	15	26	5.0	−2.792	10.013	0.00000	9.12370
5	1	15	26	5.0	−4.563	−12.064	0.00000	−8.34096
1	1	19	25	35.6	0.023	0.000	0.00000	0.00000
2	1	19	25	35.6	0.194	−3.740	0.00000	−1.19286
4	1	19	25	35.6	5.816	49.320	0.00000	9.12370
5	1	19	25	35.6	0.820	−47.998	0.00000	−8.34096

Table 6.2: ATMOS.FITS from the 2014 November epoch for ATCA (1), Ceduna (2), Hobart (4) and Parkes (5).

corrections in Section 6.2.1 were also applied to the maser and quasar datasets. Any updates (see Section 6.3.7) to the maser coordinates are also applied using CLCOR* in this step.

6.3.2 Doppler corrections

The 6.7 GHz maser spectral emission experiences Doppler effects which manifest as a spectral frequency shift. This is mainly due to Earth's rotation, the heliocentric motion specific to each epoch and the use of fixed local oscillators at each station. These effects are not accounted for at the correlator and will result in a slow drift of the spectral line over the band, thereby compromising the spectral resolution. We used SETJY* to specify the local standard of rest frequency for the 6.7 GHz maser, $\nu_{\rm ref} = 6668519200$ Hz (Müller et al. 2004), and CVEL* was used to make the correction by multiplying the delay functions by $e^{i2\pi\Delta\nu\tau}$. Here $\Delta\nu$ is the desired frequency shift and if calculated correctly will hold the spectrum steady in a given velocity for the duration of the observations (Reid 1995).

6.3.3 Amplitude calibration

We used ACCOR* to correct the amplitude of the data for imperfect sampler statistics at recording, and also for incorrect amplitude scaling at the correlator which was a problem in some versions of the DiFX software (Deller et al. 2011) used for correlation. Following this we used CLCOR* to input the square–root of the system equivalent flux density (SEFD) for each antenna (see Table 5.2.1). This applies a polynomial correction for the antenna voltage gain as a function of the zenith angle, which we approximated to the first order as being a constant. We then extracted a single autocorrelation scan of the maser spectrum from the most sensitive single antenna (typically Parkes) using SPLIT* and used ACFIT* to scale the spectra at all observing stations to this template based on the nominal SEFD of the antennas. The resultant amplitude gains as a function of time were then smoothed using SNSMO* and applied to the quasar and maser datasets using CLCAL*.

6.3.4 "Manual" delay calibration

We applied "manual" delay calibration to correct phase slopes ($\frac{\partial\phi}{\partial\nu}$ in equation (6.1)) across frequency bands. We used 1 – 2 minute scans on the quasar for delay calibration to correct the initial residual clock and instrumental error from correlation (see Section 6.2.3). As the observations typically spanned 24 hours, we calibrated the delays at ∼5 hour intervals, during each phase–reference mode between ICRF observations (see Table 5.3). Each delay solution was applied, using CLCAL*, to the specific time range for which it was valid.

The quasar datasets were not correlated with the same spectral resolution as the maser (see Section 5.3) and there was a need to account for this by modifying the delay solutions transferred to the zoom–band maser data. This crucial step was required in order to prevent the introduction of spurious R–L polarization phase differences (resulting in destructive interference upon averaging) into the maser delay solutions, and the efficacy of this procedure (see the following paragraph) is demonstrated by the similarity in the phase solutions between the different polarizations in Figure 6.4. Similar phase transfer issues between datasets with

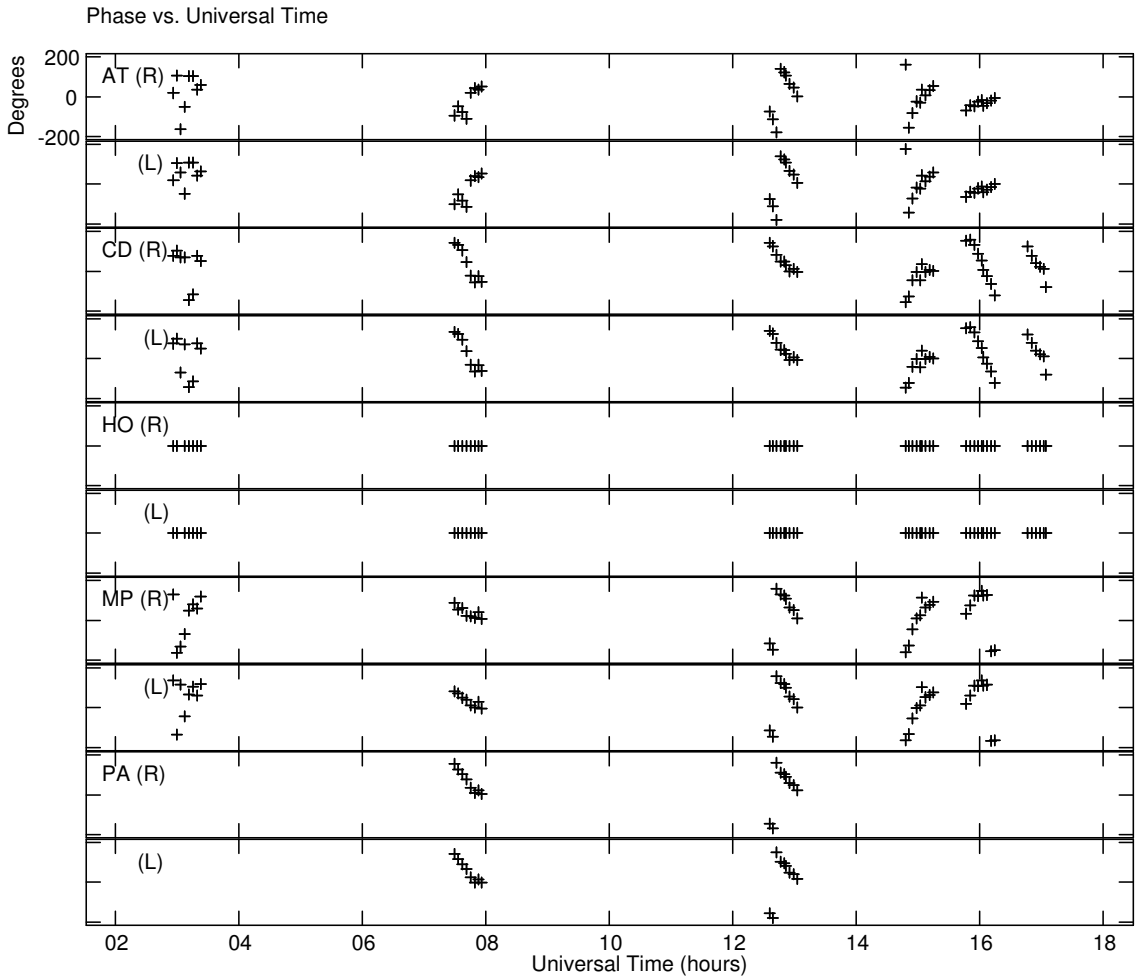

Figure 6.4: Phase solutions in each polarization from ATCA (AT), Ceduna (CD), Hobart (HO), Mopra (MP) and Parkes (PA) in the 2013 August session after fringe fitting (with reference to Hobart 26m) on the -35.6 km s^{-1} feature in G 339.884−1.259.

differing frequency properties have previously been resolved using comparable methods (e.g. Dodson et al. 2014; Rioja et al. 2008).

Delay calibration for maser data

We used FRING* to determine the visibility phases and group delay from an individual scan on the delay calibrator taken from the continuum mode data. It is assumed that the delay τ calculated by FRING* is a constant across the IF band and can be used to determine a phase correction $\Delta\phi$ for a frequency channel with width $\Delta\nu$ and with respect to the lower–band edge given by

$$\Delta\phi = \tau\Delta\nu \tag{6.4}$$

The 2 MHz maser zoom–band is a sub-band of the IF used to determine the manual delay, but it has a different lower band–edge (offset by B_{off}) from the continuum data and a

different spectral channel width $\delta\nu$. To apply the appropriate phase correction to the maser reference channel it was necessary to edit the frequency (FQ) table in AIPS so that the spectral channel width $\delta\nu'$ times the channel number σ_{pr} corresponds to the frequency of the maser phase–reference channel ν_{pr}, referenced to the lower band-edge of the continuum mode data given by

$$\nu_{pr} = B_{off} + \sigma_{pr}\delta\nu = \sigma_{pr}\delta\nu' \quad (6.5)$$

$$\delta\nu' = \frac{B_{off}}{\sigma_{pr}} + \delta\nu \quad (6.6)$$

It was also necessary to edit the total bandwidth parameter in the FQ table for the maser data so that it matched the bandwidth of the continuum mode data. We made a copy of the maser dataset using UVCOP* and replaced the *channel width* and *total bandwidth* parameters in the FQ table using TABED*.

This step can be avoided if the delay calibrator scans are correlated for both continuum and zoom mode configurations and it is recommended that this be the general procedure in future LBA observations. Equivalent solutions for $\Delta\phi$ and τ can be obtained for both datasets if an identical time range is used in FRING*.

An alternative approach would be to correlate the continuum data into several channels such that one of these corresponds exactly to the band coverage of the zoom mode maser data. The multiband group delay solutions obtained from the continuum mode data could then be used to find the phase solution in the channel corresponding to the zoom band. This solution could then be directly transferred to the maser data.

6.3.5 Fringe–rate calibration and phase–referencing

We examined the cross correlation spectra to find the spectral features which showed the smallest relative flux density variations across all baselines for the duration of the observations. This was taken to be an indication that it was an unresolved point source which would enable an accurate position determination. Peaks which exhibit substantial variability across individual baselines suggest that emission is not point–like on milliarcsecond scales, or that there is a blend of emission from different locations. We then used FRING* to determine the fringe rate ($\frac{\partial\phi}{\partial t}$ in equation (6.1)) on the chosen maser spectral channel associated with this feature before transferring the solutions to the quasar. A solution interval of 4 minutes was used as a balance between achieving good signal–to–noise, by increasing the amount of data in the solution, and for maintaining coherence in phase. The solutions (example in Figure 6.4) were then copied and applied to the quasar dataset to complete the phase–referencing procedure.

6.3.6 Astrometry

We averaged all channels in the quasar dataset and then imaged the emission using a Gaussian beam. The beam size was $\sim 5 \times 4$ mas and images of a typical maser channel that was used for phase–referencing as well as a typical quasar are shown in Figure 6.5. We located the

centroid position of the quasar by fitting a 2D Gaussian to the deconvolved quasar emission using the task JMFIT*. The offset of the emission peak from the centre of the image field was recorded for all epochs. An example of the offset positions between a maser and quasar over 5 epochs is given in Table 7.2.

6.3.7 Position shift

The errors in source positions are assumed to be $\sim 0.4''$ for the maser MMB coordinates, which is poor for milliarcsecond astrometry, and as good as ~ 2 mas for the quasar coordinates (see *Source selection* in Section 5.3 for details). Therefore, when applying the solutions from the phase–referencing feature in the maser to the quasar in Section 6.3.5, we can assume that any offset of the quasar image from the centre of the field is due to the offset of the phase–referenced position with respect to the true maser position. We iteratively corrected the maser coordinates in the AIPS source table using CLCOR*, prior to applying the procedures in Section 6.3.1. We then erased/reset all calibration (CL), solution (SN) and source (SU) tables, re–processed and imaged the phase–referenced data until there was no further improvement in the quasar position from the image centre in a chosen epoch of observations. The position corrections for the maser from the first epoch was then applied to all other epochs in Section 6.3.1. This is required because accurate coordinates for the maser source are critical for successful phase–referencing (Beasley & Conway 1995). This is because positional errors produce residual phase shifts which cannot be perfectly modeled as a position shift alone when applied to the quasar, and can result in severe image degradation in the weak quasar sources (Reid et al. 2009a).

6.3.8 Parallax

We used the algorithm employed by Reid et al. (2014) to determine the parallax from the astrometric measurements of the phase–referenced quasars.

Taking the longitude of the Sun as 0° at the vernal equinox[2] on 21 March (0.220 years), we calculated the Solar longitude $\mathscr{L}_\odot$ corresponding to each epoch T (in decimal format) of observation as

$$\mathscr{L}_\odot = 2\pi(T - 0.220) \text{ radians} \tag{6.7}$$

The obliquity of the ecliptic is the angle between the plane of Earth's orbit and the equator and is given by $\Theta = 0.408$ radians. We then represent the Sun's position in 3D Cartesian coordinates as

$$X_\odot = \cos\Theta \tag{6.8}$$
$$Y_\odot = \sin\mathscr{L}_\odot \cos\Theta \tag{6.9}$$
$$Z_\odot = \sin\mathscr{L}_\odot \sin\Theta \tag{6.10}$$

[2] http://aa.usno.navy.mil/data/docs/EarthSeasons.php

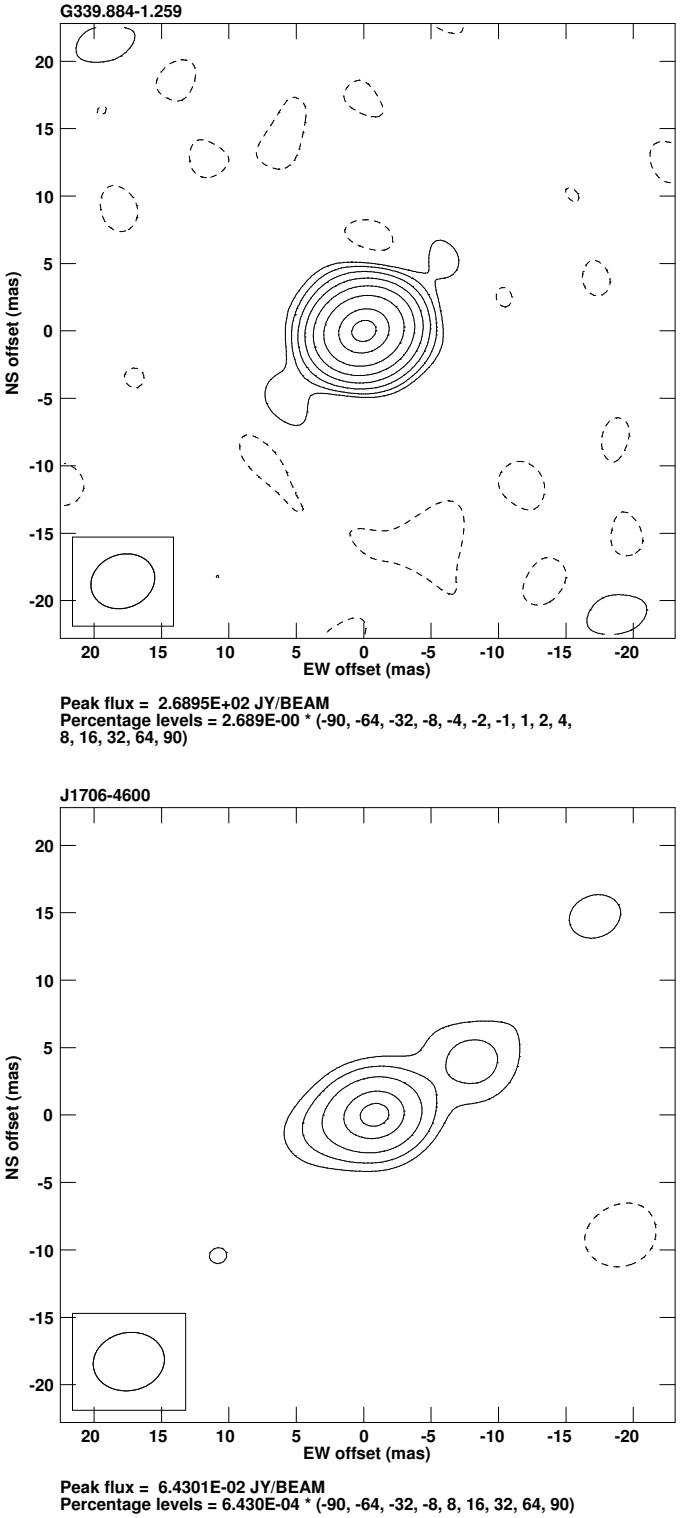

Figure 6.5: Emission from the phase–reference channel corresponding to $v_{\rm lsr} = -35.6$ km s^{-1} in G 339.884−1.259 (top) that was strong and showed compact structure. J 1706−4600 (bottom) showed consistent centroid structure dominated by a single peak throughout all epochs.

During its orbit, the Earth is at a distance of 1 AU from the Sun[3] on approximately 04 April (0.257 years). A correction for the longitudinal projection ϵ resulting from the elliptical orbit with eccentricity[4] $e = 0.0167$ is

$$\epsilon = 1.0 + 0.0167 \sin 2\pi(T - 0.257) \tag{6.11}$$

The change in the position of the phase–reference feature in the maser with respect to the quasar was modelled independently in right ascension and declination. We allowed for systematic sources of uncertainty in each coordinate $(\Delta\alpha_\pi, \Delta\delta_\pi)$ in the parallax model and added these in quadrature to the formal errors in the measured x and y offset positions from JMFIT* (e.g. columns 2 and 4 of Table 7.2). The resulting parallax (π — in milliarcseconds) for a source with coordinates $(\alpha\,, \delta)$ is then

$$\alpha_\pi = x \times \epsilon\,(Y_\odot \cos\alpha - X_\odot \sin\alpha) \tag{6.12}$$

$$\delta_\pi = y \times \epsilon\,(Z_\odot \cos\delta - X_\odot \cos\alpha \sin\delta - Y_\odot \sin\alpha \sin\delta) \tag{6.13}$$

A χ^2_ν (per degree of freedom) for the α_π and δ_π residuals was determined and we iteratively adjusted the estimated errors in $\Delta\alpha_\pi$ and $\Delta\delta_\pi$ in the parallax model until $\chi^2_\nu \approx 1$.

6.4 Conclusion

The correlated data from our observations in Chapter 5 is reduced using AIPS following the procedures for maser astrometry as described in Reid et al. (2009a). In Section 6.2 we describe the steps in calibrating the geodetic mode ICRF observations prior to obtaining the multiband delays to determine $\tau_{\rm tropo}$ and the non–dispersive clock delays for the phase–referenced data. In Section 6.3, we detail the steps which were used to prepare the 6.7 GHz methanol maser and quasar phase–referenced data, prior to obtaining the parallax. A graphical representation of these steps is shown in Figure 6.6. The AIPS runfiles which were used for data reduction in the 2012 March epoch is provided in Appendix A. In Chapters 7 and 8 we present the first parallax results from the LBA maser astrometry program.

[3] http://aa.usno.navy.mil/data/docs/geocentric.php
[4] http://aa.usno.navy.mil/faq/docs/eqtime.php

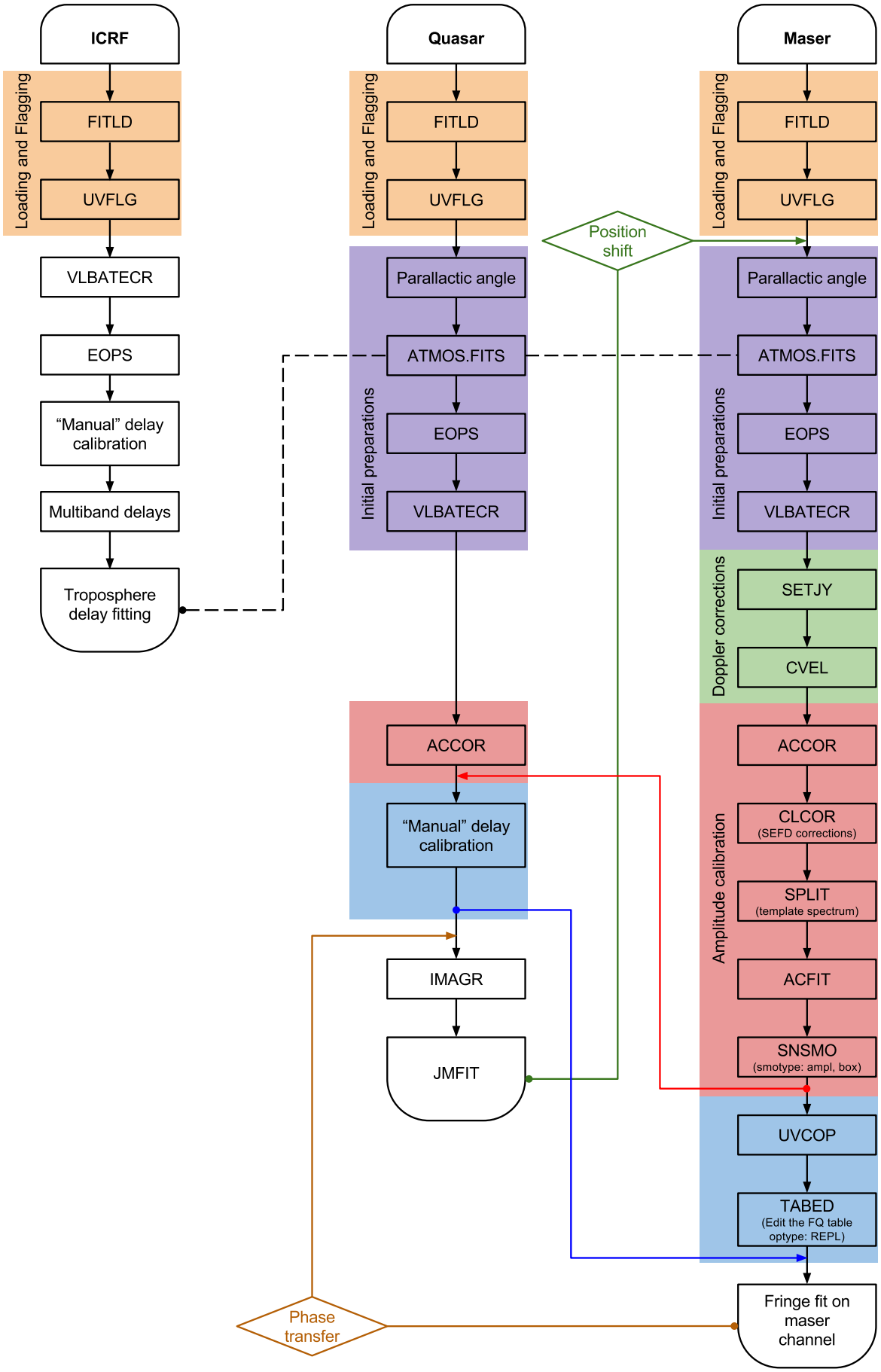

Figure 6.6: A graphical representation of the data reduction pathway in this chapter. The coloured arrows represent instances when SN tables are transferred from the quasar to the maser dataset or vice versa.

Chapter 7

A 6.7 GHz Methanol Maser Parallax with the LBA

G 339.884−1.259 is one of the strongest (1520 Jy at −38.7 km s^{-1} (Caswell et al. 2011c)) 6.7 GHz methanol masers and has been well studied in a range of maser and thermal molecular transitions (e.g. Norris et al. 1993; De Buizer et al. 2002; Ellingsen et al. 2004, 2011) and in continuum emission at a range of wavelengths (e.g. Ellingsen et al. 1996b; Walsh et al. 1998; Ellingsen et al. 2005). The autocorrelation spectrum of the 6.7 GHz methanol maser emission of this source from the 2013 June epoch of observation is shown in Figure 7.1. Its peak flux density and spectral profile has been relatively stable over the last 20 years, and interferometric observations of the masers indicate several compact features (Norris et al. 1993; Ellingsen et al. 1996b; Caswell et al. 2011c), making it a suitable candidate for phase–referenced astrometry. Previous estimates of the distance to G 339.884−1.259 have utilised the kinematic distance method (e.g. Caswell & Haynes 1983; Green & McClure-Griffiths 2011) which yields a kinematic heliocentric distance of between 2.5 to 3.0 kpc (depending on the assumed Galactic parameters). The coordinates used for G 339.884−1.259 in the current observations are given in Section 7.1.3 with updated coordinates presented in Table 7.1.

Methanol masers in G 339.884−1.259 were first observed by Norris et al. (1987) at 12.2 GHz and high resolution synthesis images were made of the emission at 6.7, and 12.2 GHz by Norris et al. (1993). Interestingly, the maser emission was found to have a linear spatial distribution and had a corresponding monotonic velocity gradient. In light of this, G 339.884−1.259 became a prime candidate for astronomers to model the conditions for HMSF (Ellingsen et al. 1996b; Norris et al. 1998; Phillips et al. 1998b; Walsh et al. 1998; De Buizer et al. 2002; Dodson 2008). Ellingsen et al. (1996b) proposed that the masers are located within a cicrumstellar disk, and Norris et al. (1998) showed that the emission fit a model of a Keplerian disk around an OB type star. However, these claims were disputed by De Buizer et al. (2002) who demonstrated that what was initially thought to be a single circumstellar disk could be resolved into three mid–infrared sources near the location of the methanol masers. Dodson (2008) attempted to test the hypothesis of a circumstellar disk in G 339.884−1.259 by making polarization measurements of the magnetic fields associated with this source. From their images, they report a primarily disordered field accompanying much of the emission, and proposed that this matches the expectations for the masers being associated with an

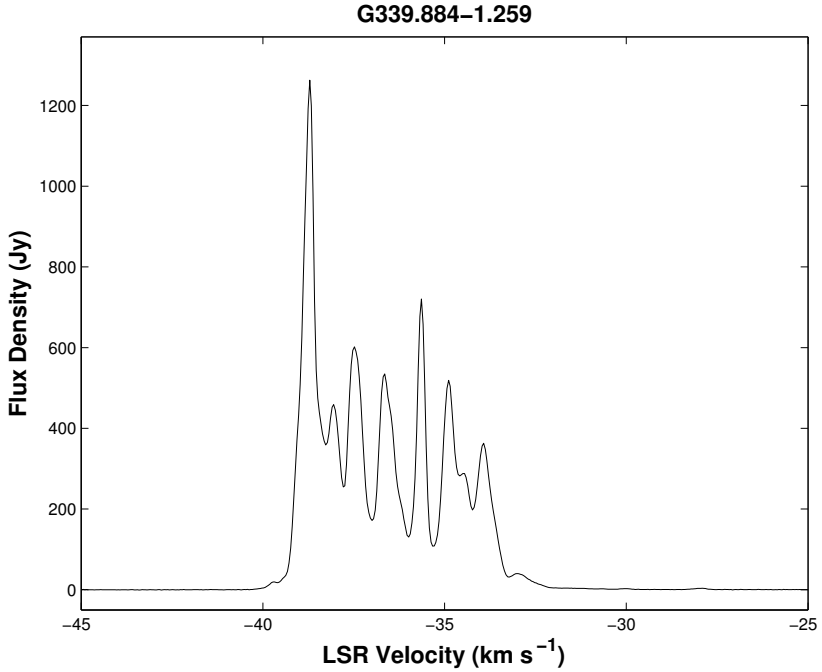

Figure 7.1: The autocorrelation spectrum of G 339.884−1.259 using all antennas except HartRAO from 2013 June.

outflow–related shock. One small region of methanol maser emission does show a magnetic field direction perpendicular to the elongation of the maser emission, suggestive of a disk (Dodson 2008). However, the mass of the enclosed object (assuming Keplarian rotation) is of magnitude of only 0.03 $M_{\odot}$ (assuming a distance of 3 kpc to G 339.884−1.259).

	Source	Correlated flux (mJy)	Separation (°)	Position angle (°)	RA (h m s)	Dec (° ′ ″)
Masers:						
	G 339.884−1.259	–	–	–	16 52 04.6776	−46 08 34.404
Detected quasars:						
	J 1706−4600	131.1	2.48	88.1	17 06 22.0503	−46 00 17.824
	J 1654−4812	3.8	2.11	169.9	16 54 18.2448	−48 13 03.756
Non–detected quasars:						
	J 1648−4826	<0.5	2.36	193.3	16 48 47.9200	−48 26 18.800
	J 1644−4559	<0.5	1.27	276.5	16 44 49.2856	−45 59 09.646
	J 1648−4521	<0.9	1.03	319.1	16 48 14.2110	−45 21 38.090
	J 1649−4536	<0.4	0.72	317.1	16 49 14.7810	−45 36 31.190
Masers:						
	G 305.200+0.019	–	–	–	13 11 16.8912	−62 45 55.008
	G 305.202+0.208	–	0.19	356.24	13 11 10.4904	−62 34 38.856
	G 305.208+0.206	–	0.19	358.12	13 11 13.6992	−62 34 41.412
Detected quasars:						
	J 1254−6111	389.0	2.50	307.21	12 54 46.5768	−61 11 34.969
	J 1256−6449	131.4	2.65	217.58	12 56 03.4030	−64 49 14.817
	J 1312−6035	10.2	2.17	2.99	13 12 12.2928	−60 35 38.220
Non–detected quasar:						
	J 1259−6519		2.88	205.54	12 59 23.9000	−65 19 53.200

Table 7.1: Coordinates of the observed sources between 2012 – 2015 March, which are analyzed in this thesis. The separation and position angle columns describe the offset in the sky between the respective quasar and the 6.7 GHz methanol masers in G 339.884−1.259 and G 305.200+0.019. The offset and separation of the methanol masers in G 305.202+0.208 and G 305.208+0.206 with respect to G 305.200+0.019 is also listed. The reported positions of G 339.884−1.259 and J 1654−4812 have been revised (see Section 7.1.3) based on the 2013 March epoch. The reported positions for G 305.200+0.019, G 305.202+0.208 and G 305.208+0.206 are revised based on the 2013 June epoch (see Section 8.2). We failed to detect the quasars J 1648−4826, J 1644−4559, J 1648−4521, J 1649−4536 and J 1259−6519 in our observations. The upper limits for detection is 5 times the image RMS (from a box of size 1.5×1.5 arcsec).

Table 7.2: Measured flux densities and differential fitted positions between the −35.6 km s^{-1} feature in G 339.884−1.259 and J 1706−4600 across all epochs after phase–referencing. The formal errors in each coordinate are determined from the output of IMFIT.

					J 1706−4600		G339.884-1.259	
Epoch	**x Offset**	**Error**	**y Offset**	**Error**	**Flux**	**RMS**	**Flux**	**RMS**
2012 March	4.177	0.056	2.998	0.098	30.29	0.55	413.07	0.03
2013 March	2.667	0.026	1.085	0.023	28.98	0.36	418.17	0.02
2013 June	1.654	0.003	0.464	0.002	114.84	0.15	427.49	0.02
2013 August	1.031	0.021	0.208	0.017	61.06	0.65	462.02	0.02
2013 November	0.727	0.016	0.006	0.012	62.25	0.38	268.95	0.02

A large number of additional class II methanol maser transitions have been detected towards G 339.884−1.259. Observations of multiple maser transitions are required to place constrains on the environmental conditions in the region surrounding the young high–mass star where the masers arise. This is because any model will need to account for the specific conditions required for the observed transition (Cragg et al. 1992; Sobolev et al. 1997). Norris et al. (1993) made high–resolution maps of the 6.7 and 12.2 GHz maser spots in G 339.884−1.259 and found little evidence for spatial coincidence with the spots at different frequencies. Caswell et al. (2000) made observations of 107.0 and 156.6 GHz methanol masers in G 339.884−1.259 and found the emission peak at these frequencies coincided with the 6.7 GHz maser site to within 5″. These are relatively rare transitions, with only 22 and 4 detections respectively from a pool of 80 sources. Ellingsen et al. (2004) discovered emission from the 19.9 GHz transition in G 339.884−1.259, and in Krishnan et al. (2013) it was shown that there was little evidence for spatial or velocity coincidence between the masers at 6.7 and 19.9 GHz, with only 2 maser components identified at 19.9 GHz as opposed to ∼10 components in 6.7 and 12.2 GHz observations with similar angular resolution (Norris et al. 1993).

UCHII regions are bubbles of ionized gas associated with newly formed massive stars, and the first detection of such a region in G 339.884−1.259 was by Ellingsen et al. (1996b). The emission was measured at 8.5 GHz and had a peak brightness of 6.1 mJy beam^{-1}. The peak of the methanol emission at −38.7 km s^{-1} was offset from the continuum peak by 0.6″, with the methanol masers lying in a line approximately across the centre of the continuum emission and in an orientation which is perpendicular to the direction of extension of the UCHII region. De Buizer et al. (2002) interpret the radio continuum emission is being due to an ionized outflow along the axis of extension.

7.1 Astrometry, parallax and proper motion

Figure 7.1 shows that there are multiple strong (>100 Jy) 6.7 GHz methanol maser components in G 339.884−1.259 which offer potential spectral channels for astrometry. We examined the cross correlation spectra to find the spectral features which showed the smallest relative flux density variations across all baselines for the duration of the observations, taking this to be an indication that it was an unresolved point source, which would enable an accurate

Table 7.3: Parallax distance and proper motion of G 339.884−1.259.

Maser feature (km s^{-1})	**Parallax** (mas)	**Distance** (kpc)	μ_x (mas y^{-1})	μ_y (mas y^{-1})
−35.6	0.48±0.08	$2.1^{+0.4}_{-0.3}$	−1.6±0.1	−1.9±0.1

position determination. We found the spectral feature at −35.6 km s^{-1} (see Figure 6.5) to be clearly the best choice for G 339.884−1.259. All the other peaks exhibited substantial variability across individual baselines suggesting that emission is not point–like on milliarcsecond scales, or that there is a blend of emission from different locations. We then fringe fit on the maser spectral channel associated with this feature before transferring the phase solutions to J 1706−4600. Figure 6.4 shows a typical plot of phase versus time from the 2013 August observations.

After transferring the phase corrections, we averaged all channels in the quasar dataset and then imaged the emission using a Gaussian beam of 5.9×4.2 mas. We report detections for J 1706−4600 and J 1654−4812 on VLBI baselines, and only the first of these was suitable for astrometry. J 1706−4600 was observed in all epochs and appears to be dominated by a single component with no jets. J 1654−4812 was observed in all epochs except 2012 March and showed variable source structure which made it unsuitable for parallax determination. J 1706−4600 has a positional accuracy of 2.10 mas (Petrov et al. 2011) and shows deviation from point–like structure at levels <10% of the peak flux density (Figure 6.5). J 1654−4812 had an estimated positional accuracy of 0.4″ (McConnell et al. 2012) and from our phase–referenced images, we are able to present updated coordinates for J 1654−4812 to an uncertainty of 2.1 mas in Table 7.1. We located the centroid position of the quasar by fitting a 2D Gaussian to the deconvolved J 1706−4600 emission. The offset of the emission peak from the centre of the image field was recorded for all epochs and we present these data in Table 7.2.

The change in the position of the −35.6 km s^{-1} feature in G 339.884−1.259 with respect to J 1706−4600 was modelled using the procedure in Section 6.3.8.The parallax was measured to be 0.48±0.08 mas corresponding to a distance of $2.1^{+0.4}_{-0.3}$ kpc to G 339.884−1.259. The proper motion was $\mu_x = -1.6\pm0.1$ mas y^{-1} and $\mu_y = -1.9\pm0.1$ mas y^{-1} (Figure 7.2 and Table 7.3). In order to constrain errors in the measured proper motion, we made image cubes of the maser emission for all epochs, and analyzed the changes in the distribution from 2012 March to 2014 November. We found that internal motions in G 339.884−1.259 can be up to ∼0.4 mas y^{-1} in right ascension and declination. These motions dominate over the formal errors in (μ_x, μ_y) when added in quadrature, and we report the measured proper motion with errors as $\mu_x = -1.6\pm0.4$ mas y^{-1} and $\mu_y = -1.9\pm0.4$ mas y^{-1}. This measured uncertainty corresponds to internal motions of ∼2 km s^{-1} in the maser emission and is consistent with proper motion estimates of 6.7 GHz methanol masers in HMSFRs (e.g. Goddi et al. 2011; Moscadelli & Goddi 2014; Sugiyama et al. 2014). A more detailed analysis of the internal motions of the 6.7 GHz emission in G 339.884−1.259 is beyond the scope of the current text and will be presented in future publications.

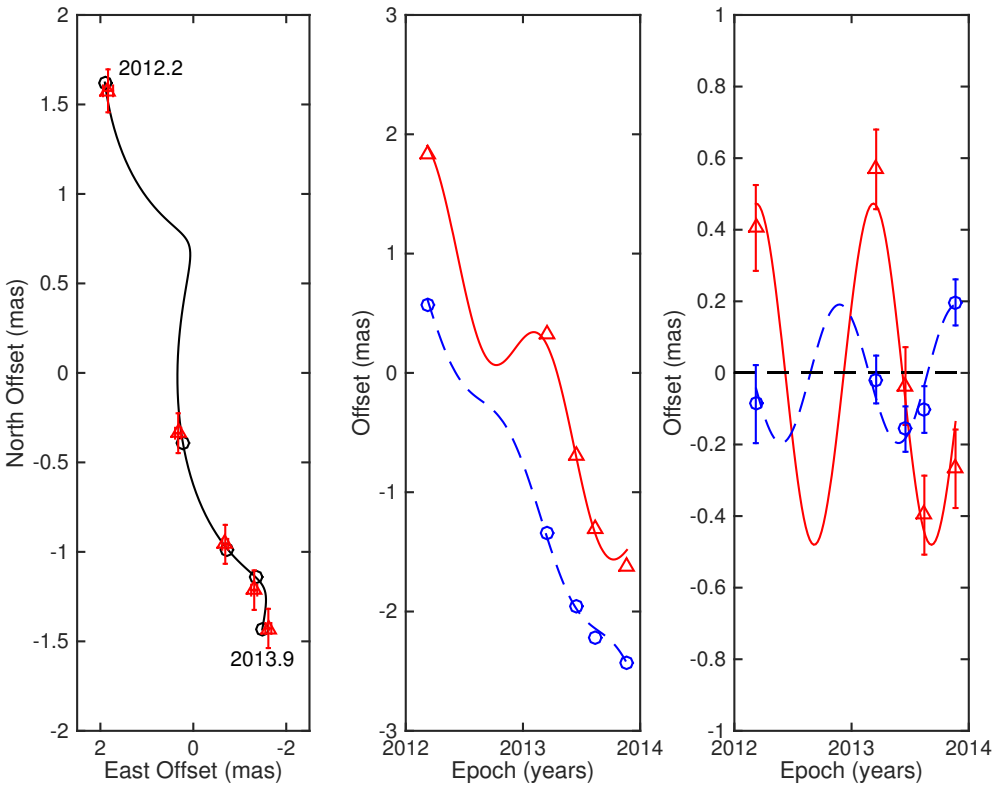

Figure 7.2: Parallax and proper motion of the -35.6 km s^{-1} reference feature in G 339.884−1.259. The expected positions from the fits are indicated with triangular and circular markers. Left panel: the sky positions with the first and last epochs labeled. Middle panel: East–West (triangles) and North–South (circles) motion of the position offsets and best combined parallax and proper motions fits versus time. The models are offset along the y–axis for clarity. Right panel: the parallax signature with the best fit proper motions removed.

We excluded data from the 2014 March observations in our parallax and proper motion analysis as there were significant technical difficulties during that session which prevented us from obtaining accurate measurements of the maser–quasar separation for that epoch.

The LBA has previously been used to measure distances to a number of pulsars at 1.6 GHz using trigonometric parallax (Dodson et al. 2003; Deller et al. 2009b,a). The uncertainty in our LBA parallax measurement to G 339.884−1.259 is estimated to be 80 μas and is equivalent to the errors of the best LBA Southern pulsar parallax measurement (Deller et al. 2009a). The uncertainty from our observations is a factor of 2 poorer than the parallax of 6.7 GHz methanol masers in ON 1 (0.389 ± 0.045 mas) measured by Rygl et al. (2010) using the EVN. The LBA (when operating without HartRAO; see Section 7.3) and the EVN configuration in Rygl et al. (2010) both have a maximum East–West baseline separation of ∼2000 km, giving them similar resolution capabilities for parallax determination (Reid et al. 2009a). Rygl et al. (2010) reduced random errors in their measurements by modelling parallaxes determined from the averaged positions of several maser spots. However, given the strong and compact nature of the maser spot at -35.6 km s^{-1}, we are not able to reduce our astrometric errors using this method as these will be dominated by systemics from the uncompensated atmosphere. Additionally, the the EVN observations of ON1 utilise background quasars with separation angles of 1.71° and 0.73°, and in comparison J 1706−4600 is separated by 2.48° from G 339.884−1.259 (Table 7.1). This would have adversely affected the interpolated phase transfer solutions and contributed to the larger uncertainty estimate presented here (see Section 7.3). In considering these factors, we assess that with better atmospheric calibration and smaller separation between the maser and quasar, it will be possible to attain parallax accuracies of ∼20 μas using the LBA.

7.1.1 Kinematic distance to G339.884-1.259

The kinematic distance to sources in the Galactic Plane can be determined from a model which describes the rotational speed of the disk at the Sun Θ_0, distance of the Sun from the Galactic Centre R_0, and the measured $v_{\rm lsr}$. Green & McClure-Griffiths (2011) report a kinematic distance to G 339.884−1.259 of 2.6±0.4 kpc using $\Theta_0 = 246$ km s^{-1}, $R_0 = 8.4$ kpc (Reid et al. 2009b) and $v_{\rm lsr} = -34.3$ km s^{-1} (the mid–point of the 6.7 GHz methanol maser emission range Figure 7.1). Previous studies of the HMSFR associated with G 339.884−1.259 (e.g. Ellingsen et al. 1996b; De Buizer et al. 2002; Dodson 2008) have used a kinematic distance of ∼3 kpc to this source. This value was determined using earlier models with Galactic rotation speeds of $\Theta_0 \simeq 220$ km s^{-1} (see Section 7.2.2 for further comments).

Using updated Galactic parameters of $\Theta_0 = 240$ km s^{-1}, $R_0 = 8.34$ kpc and solar motion parameters of $U_\odot = 10.70$ km s^{-1} (towards the Galactic Centre), $V_\odot = 15.60$ km s^{-1} (clockwise and in the direction of Galactic rotation as viewed from the North Galactic Pole) and $W_\odot = 8.90$ km s^{-1} (towards the North Galactic Pole; Reid et al. 2014), we report the kinematic distance to the associated CS(2–1) cloud with $v_{\rm lsr} = -31.6$ km s^{-1} (Bronfman et al. 1996) to be 2.5±0.5 kpc. This result is comparable to the parallax distance in Section 7.1 but with a large estimated error. Given an uncertainty of ∼8 km s^{-1} in Θ_0 (Reid et al. 2014), the estimated error in the quoted kinematic distance of 2.5 kpc is doubled to ∼1 kpc.

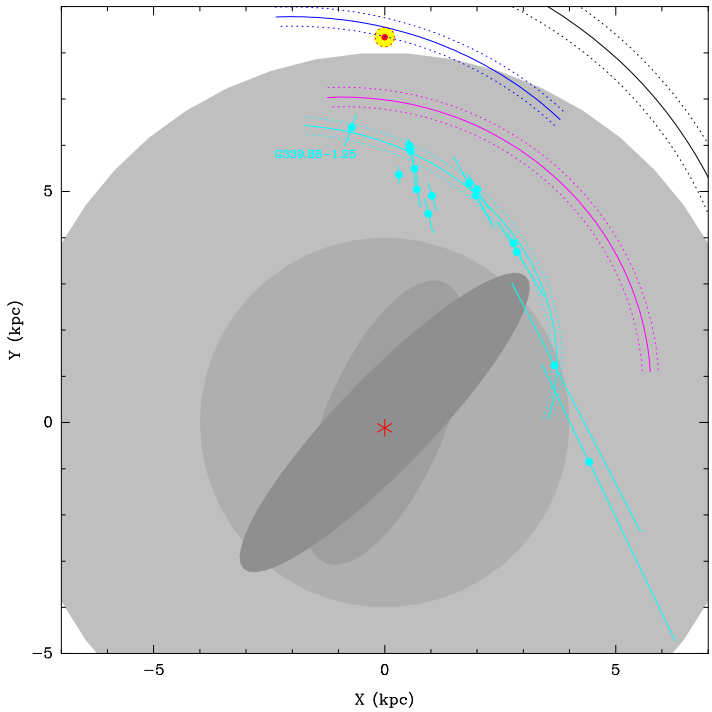

Figure 7.3: A face–on view of the Milky Way galaxy showing G 339.884−1.259 in relation to other HMSFRs in the Scutum arm (Sato et al. 2014). Sections of arcs of the Perseus (top right), Local (top centre with Solar position) and Sagittarius arms are also shown. The background circular disks are scaled to approximate the Galactic bar region (∼4 kpc) and the solar circle (∼8 kpc; Reid et al. 2014).

7.1.2 Association of G339.884-1.259 HMSFR with Scutum arm

Our ability to precisely determine the structure of the Milky Way is hampered by our location in the midst of its spiral arms. Jones et al. (2013); Dame et al. (2001); Cohen et al. (1980); Westerhout (1957); and others have used surveys of HI and CO molecular clouds to identify the Galaxy's spiral arms from the ensuing longitude–velocity ($\ell - V$) diagrams. This method of spiral arm modelling has been used by Xu et al. (2013); Zhang et al. (2013); Choi et al. (2014); Reid et al. (2014); Sanna et al. (2014); Sato et al. (2014); Wu et al. (2014) to assign HMSFRs to spiral arms, by associating them with molecular clouds in our Galaxy.

Based on the $v_{\rm lsr}$ of the CO spectrum in the region (T. Dame 2014, private communication) and the parallax distance in Table 7.3, we suggest that G 339.884−1.259 is located in the near edge of the Scutum spiral arm as shown in Figure 7.3. Sato et al. (2014) modeled the Scutum arm based on measurements of 16 HMSFRs, and we show the position of G 339.884−1.259 with relation to these in Figure 7.3. It can be seen that at the longitude of G 339.884−1.259, the Sagittarius and Scutum arms are in close proximity, and extrapolating the best information currently available suggests that these two arms may merge at lower longitudes.

Using a log–periodic spiral model, Sato et al. (2014) measured a pitch angle of $\psi = 19.8^\circ \pm 3.1^\circ$ for the Scutum arm. We have now included G 339.884−1.259 into this model, using a source which extends the Galactocentric azimuth by about 10°, giving an updated value of $\psi = 19.2^\circ \pm 4.1^\circ$.

7.1.3 Updated coordinates for G339.884-1.259 and J1654-4812

During the observations we used $\alpha = 16^h52^m04.6700^s$, $\delta = -46°08'34.200''$ as the coordinates for G 339.884−1.259 (Caswell et al. 2011c). This is the position of the maser spectral peak at −38.7 km s^{-1} (Figure 7.1). When applying phase corrections from the −35.6 km s^{-1} feature to J 1706−4600, we can assume that any offset of the quasar image from the centre of the field is due to the offset of the phase–referenced position with respect to the true maser position. We iteratively corrected the maser coordinates in the AIPS source table using CLCOR until there was no further improvement in the quasar position from the image centre in the 2013 March epoch of observations. It is important to use accurate maser coordinates in the data reduction process, to minimize errors in determining the quasar position during phase–referencing (Reid et al. 2009a). The position corrections from the March 2013 epoch of observations were then applied to G 339.884−1.259 for all epochs, and we present the updated coordinates corresponding to the −38.7 km s^{-1} feature in Table 7.1. We find that there is a difference of 0.219″ between our measured position and that reported by Caswell et al. (2011c). The formal errors in the fitted position for J 1706−4600 were <0.1 mas (Table 7.2). As this is an order of magnitude smaller than the known positional error of this source (see Section 7.1), the resultant uncertainty in the updated maser position remains as 2.1 mas when error contributions are added in quadrature.

Observations of J 1654−4812 were made using the coordinates $\alpha = 16^h54^m18.24^s$, $\delta = -48°13'03.7''$ from McConnell et al. (2012). The updated position of this source when measured relative to the corrected G 339.884−1.259 position is also presented in Table 7.1 to an accuracy of 2.1 mas. There is a separation difference of 0.074″ between the original and updated positions.

7.2 Properties of associated HMSFRs

7.2.1 Peculiar motion

The proper motions $\mu_x = -1.6\pm0.4$ mas y^{-1}, $\mu_y = -1.9\pm0.4$ mas y^{-1} and of $v_{\rm lsr} = -31.6$ km s^{-1} of the CS(2–1) cloud associated with this source (Bronfman et al. 1996), make it possible to determine the full 3D motion of G 339.884−1.259 with respect to the Galactic Centre. The dynamical model of the Galaxy we use assumes a flat rotation curve of the disk with a speed of $\Theta_0 = 240$ km s^{-1}. This is a reasonable assumption based on the recent analysis in Reid et al. (2014). The distance of the Sun to the Galactic Centre is taken to be $R_0 = 8.34$ kpc, and assumed to have peculiar motion components $U_\odot = 10.70$ km s^{-1}, $V_\odot = 15.60$ km s^{-1} and $W_\odot = 8.90$ km s^{-1} (Reid et al. 2014). When using this model, we find the peculiar motion for G 339.884−1.259 to be $U = -4.0\pm5.9$ km s^{-1}, $V = 6.47\pm4.6$ km s^{-1} and $W = 10.0\pm1.2$ km s^{-1}, in a reference frame that is rotating with the Galaxy. Hence all components of peculiar velocity are consistent (within estimated uncertainty) with the bulk of HMSFRs in the Milky Way. In Reid et al. (2014) there is a good fit to the model of spiral arm motions when a RMS of about 5 – 7 km s^{-1} is assumed for each velocity component of HMSFR. This is reasonable for Virial motions of stars in giant molecular clouds and so there may not be much evidence for large (>10 km s^{-1}) streaming motions in general.

Table 7.4: Physical parameters of G 339.884−1.259 as described in Section 7.2.2 and adjusted to a preferred distance of 2.1 kpc.

n_e (cm^{-3})	M_{HII} ($M_\odot$)	U (pc cm^{-2})	log N_L (s^{-1})	Spectral type
3.1×10^4	6×10^{-4}	5.7	45.6	B1

7.2.2 Physical constraints on the ionizing star

HMSF is still not well understood, and there is a vibrant debate regarding the processes which result in their formation (e.g. McKee & Tan 2003; Bonnell et al. 1998; Garay & Lizano 1999). Accurate distances to star formation regions help to put tight constraints on the physical environments from which young high–mass stars are born. This includes fundamental attributes such as size, enclosed mass and luminosity. Therefore, any accurate model describing the star formation process must also be governed by the limits of these physical constraints.

Previous groups have determined the properties of G 339.884−1.259 based on kinematic distance (see Section 7.1.1). Using values from Ellingsen et al. (1996b) and the equations from Panagia & Walmsley (1978), we present updated estimates for the electron density n_e, mass of ionized hydrogen M_{HII}, excitation parameter U and the Lyman continuum photon flux N_L in Table 7.4. Based on $\log N_L = 45.6$ s^{-1} in Table 7.4, we find that the radio continuum emission is consistent for a core object to be a B1 type star (Panagia 1973). This classification implies that G 339.884−1.259 is relatively small for a young high–mass star. It has been proposed that the luminosity of 6.7 GHz methanol masers increases as the associated young stellar object evolves (e.g. Breen et al. 2010b). In this scenario sources such as G 339.884−1.259, which is amongst the most luminous 6.7 GHz methanol masers in the galaxy and is associated with a number of rare class II methanol transitions (Krishnan et al. 2013; Ellingsen et al. 2013), are close to the end of the methanol–maser phase of HMSF. Recently, Urquhart et al. (2015) have put forward an alternative interpretation, that the methanol maser luminosity has a closer dependence on the bolometric luminosity of the associated high–mass star than its evolutionary phase. In this case, we would expect G 339.884−1.259 to be associated with a high–mass young stellar object towards the upper end of the mass–range. However, this is not the case and demonstrates that high luminosity, multiple transition methanol maser emission need not be associated with the most massive O–type young stars. A single example is insufficient to resolve the issue of whether evolutionary stage or stellar mass plays the primary role in determining class II methanol maser luminosity, however, G 339.884−1.259 shows greater consistency with the expectations of the Breen et al. (2010b) evolutionary hypothesis.

7.3 Atmospheric contributions to astrometric accuracy

We found that the parallax measurement with the smallest error floors was obtained when troposphere corrections were applied to the 2013 March and 2013 August epochs only. When the corrections were incorporated for all epochs, the parallax was measured to be 0.58±0.11 mas.

When we excluded the tropospheric corrections for all epochs the measured trigonometric parallax was 0.50±0.13 mas. We attribute the effectiveness of applying this calibration in each epoch to limitations that we encountered in applying the tropospheric and ionospheric delays for the phase–referenced data in Section 6.3.1.

7.3.1 Troposphere calibration

The red graph in Figure 5.1 models the theoretical delay from the 6300 and 6316 MHz IF configuration which was used to determine the multiband delays in Section 6.2.4. In Honma et al. (2008), the tropospheric excess Δl is approximated as

$$\Delta l = c\,\tau_{\rm tropo}\,\sec\overline{Z}\,\tan\overline{Z}\,\Delta Z \tag{7.1}$$

Assuming a mean zenith angle $\overline{Z} = 45^\circ$ for the phase–referenced maser and quasar, a source separation of $\Delta\overline{Z} = 2^\circ$ and $\tau_{\rm tropo} \simeq 0.1$ nsec (the reported RMS in the multiband delay from FRING* in Section 6.2.4), gives $\Delta l = 0.015$ m for the tropospheric excess. Considering that the longest baseline between Ceduna – Hobart is $B = 1700$ km, the astrometric uncertainty is $\frac{\Delta l}{B} = 0.17$ mas. The magnitude of this error is consistent with Pradel et al. (2006) who demonstrate that the tropospheric zenith delay can be the dominant source of error in VLBI (at 8.4 GHz), and in agreement with the errors reported at the beginning of Section 7.3. This is a factor of $\lesssim$9 poorer than the estimated astrometric capability of the LBA as assessed at the end of Section 7.1. There is therefore a need to reduce the errors from our multiband delay solutions from about 0.1 nsec, which corresponds to ∼3 cm, to about 0.03 nsec, corresponding to the 1 cm level (Honma et al. 2008), which could allow us to meet the estimated astrometric capability of the LBA.

In addition to the ICRF sources in Section 5.2 having point–like structure and well known positions, and accurate station coordinates for the VLBI array, obtaining reliable $\tau_{\rm tropo}$ is dependant on having a favourable ICRF mode set–up (e.g. the *Golomb ruler* in Figure 5.1) and accurate $\tau_{\rm iono}$ corrections (see Section 7.3.2). Until these issues are sufficiently well addressed for the LBA, it is recommended that the tropospheric path length corrections from Section 6.2.5 be excluded. The clock drift over the course of the observations was also resolved from the multiband delays in Section 6.2.5 and must still be modeled. Figure 6.3 shows the residual differences between the measured clock and modeled offsets for the duration of an observation. The squares, circles and crosses represent (respectively) the data, the model and residuals between the two. The near zero scatter of the residuals indicates that a linear model for the clock drift at each station was successful. The RMS noise of the residuals were between 0.03 to 0.3 nsec across all baselines and epochs.

The hetrogeneous nature of the array means that some antennas were able to participate in a relatively small number of ICRF scans, Parkes due to a combination of slow slew rates, limited elevation coverage and HartRAO due to its distance from the rest of the LBA antennas. We were not able to include HartRAO in the majority of the ICRF observations as the quasars which had risen at the Australian stations were often set here. As a result, we were unable to determine the clock drift for HartRAO and have not included observations from this station to determine the results given in Table 7.3. We are currently investigating

alternative methods to determine the clock drift rate from HartRAO for inclusion in the future.

7.3.2 Ionosphere calibration

Given the observing parameters (6.7 GHz, 4 minute cycle time, 2.48° separation between the calibrator and the target, 3 cm residual zenith path length (Reid et al. 1999) and residual ionospheric content of 6 TECU (Ho et al. 1997)) we can estimate the expected error contributions from static and dynamic components of the troposphere and the ionosphere using the formulae in Asaki et al. (2007). This predicts a dynamic tropospheric phase error of 28°, a static tropospheric phase error of 15°, a dynamic ionospheric phase error of 5° and a static ionospheric phase error of 21°. The geodetic blocks typically reduce the residual zenith path length to about 1 cm, which would decrease the static tropospheric phase error to 5°. Dynamic errors, because of the short timescale on which these operate, reduce the measured flux density of the targeted source without having a large effect on the positional centroid. This clearly leaves the residual static ionosphere as the largest uncorrected effect. Static residuals will introduce a shift in the observed position, as measured on any single baseline. For arrays with 10 or so antennas these shifts average out somewhat, but the LBA with 5 to 6 antennas is more vulnerable to this effect.

Tuning the observational parameters, such as the cycle time and the separation between sources, is the most effective method to reduce these error contributions. For example, reducing the cycle time to 60 seconds would diminish the dynamic phase errors to less than 10° and decreasing the separation between the calibrator and the target to 1° would cut back the static phase errors to less than 10°. However, the array sensitivity places limits the minimum useful scan duration and the separation of the closest suitable phase calibrator. In this case we were not able to have shorter scans or closer calibrators.

For observations at higher frequencies, such as 22 GHz, the contribution of the residual zenith path length dominates. Therefore the geodetic blocks are absolutely essential for the measurements in Reid et al. (2014); Honma et al. (2012) as they reduce the typical errors from 3 cm to about 1 cm. However at 6.7 GHz the residual ionospheric contribution of 6 TECU is equivalent to 5.3 cm, as opposed to 0.5 cm at 22 GHz, and there is currently no established strategy for minimizing these contributions.

Deller et al. (2009a) explain that the available TEC models for ionosphere delay correction in the Southern Hemisphere are sometimes in error due to the lower density of GPS stations in this region. Hence at 6.7 GHz, even after removing the effects of the ionosphere by using TEC maps, there is about 5 cm of residual dispersive delay in the data. This is comparable to the expected residual (non–dispersive) delay from the wet troposphere (Brunthaler et al. 2011). Both dispersive and non–dispersive delays contribute to the measured group delays in equation (5.2) and there is a crucial need to separate the contributions. This is because for the dispersive case, the phase correction is $\phi = -\nu\tau_{\rm iono}$ whereas for non–dispersive delay it is $\phi = \nu\tau_{\rm tropo}$. Hence, any treatment of dispersive delays as non–dispersive will result in erroneous phase corrections. This condition creates some uncertainty over the effectiveness of the ICRF block calibrations for our 6.7 GHz observations, and could be the reason why the search for multiband delays over the more sensitive 390 MHz range was noisy (see Section 6.2.4

and Figure 6.2).

7.3.3 Multi-view VLBI

High–accuracy, sub–milliarcsecond astrometry with the LBA will only be possible if error contributions from tropospheric and ionospheric effects are well constrained. In order to improve the astrometric accuracy of the LBA, we are investigating the use of the *multi–view* (or *Cluster–Cluster*) VLBI technique (Sasao & Morimoto 1991), which corrects for distortions in ϕ arising from the spatial and temporal structure in the troposphere and ionosphere (Rioja et al. 2009). Multi–view VLBI observations are similar to the phase–referencing observations detailed in Section 5.3, except that the observing cycle incorporates several calibrator sources (instead of just a single calibrator) surrounding a central target source (e.g. Porcas et al. 2003; Fomalont & Kopeikin 2002). The spatial and temporal structure in both the troposphere and ionosphere are then modelled as a 2D delay and phase surface plane in the direction of the sources. The interpolated phase solutions which are applied to the target are accurate for the line–of–sight direction to the sources, and low–frequency (where the ionospheric effects dominate) simulations by Jimenez-Monferrer et al. (2010) show improvements of an order of magnitude from $\sim$1 – 0.1 mas in the astrometric precision of the LBA at $\leq$ 1.4 GHz when this technique is employed.

7.4 Conclusion

We are currently conducting a large project using the LBA to measure the positions of thirty, 6.7 GHz methanol masers relative to background quasars, in the Southern Hemisphere to sub-milliarcsecond accuracy. These measurements will be used to determine their distances using trigonometric parallax. The source list contains many prominent HMSFRs in the 3$^{\rm rd}$ and 4$^{\rm th}$ quadrants of the Milky Way galaxy, where the LBA's performance is unmatched in its astrometric capabilities as a VLBI instrument. In this paper, we have shown the potential of this project by successfully making the first parallax measurements to a Southern 6.7 GHz methanol maser source. The parallax of 0.48$\pm$0.08 mas to G 339.884$-$1.259 corresponds to a distance of $2.1^{+0.4}_{-0.3}$ kpc. In combining this result with measurements of other HMSFRs in Sato et al. (2014), we place G 339.884$-$1.259 at the near edge of the Scutum spiral arm of the Milky Way, and determine an updated pitch angle of $\psi = 19.2^{\circ}\pm4.1^{\circ}$ for this arm.

We have used the parallax distance to update the estimated physical parameters for the G339.884$-$1.259 star formation region and now classify it to be of spectral type B1. The young stellar object associated with G 339.884$-$1.259 is relatively small for a "high–mass" object and is a strong example of the uncorrelated nature between stellar mass and intensity of 6.7 GHz maser emission.

Chapter 8

Parallaxes to the G305 Region

8.1 Introduction

The G 305 region is a vast HMSFR in the Southern Galactic Plane (Hindson et al. 2013, 2012, 2010) with numerous sources exhibiting 6.7 GHz methanol masers, including emission associated with G 305.200+0.019, G 305.202+0.208 and G 305.208+0.206 (see Figure 8.1). Phillips et al. (1998b) published the 6.7 GHz methanol maser spectrum and component map for G 305.202+0.208 (as G 305.202+0.207) and report a curved distribution of maser emission with a peak of 92.00 Jy at -44.0 km s^{-1}. ATCA observations by Norris et al. (1993) show G 305.208+0.206 to also have a linear distribution of 6.7 GHz methanol masers but with a monotonic velocity gradient and a peak of 447 Jy at -33.1 km s^{-1}. The G 305.208+0.206 site contains both OH and methanol masers (Caswell et al. 1995c), and is located only 22″ to the East of G 305.202+0.208. The 6.7 GHz methanol maser emission in G 305.200+0.019 is weaker than the emission associated with either G 305.202+0.208 and G 305.208+0.206, with a peak flux of 46 Jy at -33.1 km s^{-1} (Green et al. 2012b).

Walsh et al. (2007) confirm the hot core nature of G 305.208+0.206 through their molecular observations of CH_3OH, CH_3N, NH_3, OCS and H_2O, and estimate the age of the core to be between 2×10^4 – 1.5×10^5 yr. In contrast there is a lack of molecular emission surrounding G 305.202+0.208, suggesting that it is an older source which has had time to disperse much of the surrounding material. Unlike G 305.202+0.208 (referred to as G 305B by Walsh et al. 2001) which is associated with a very bright and reddened IR source (De Buizer 2003), there is little evidence to suggest coincident IR emission associated with G 305.208+0.206 (referred to as G 305A by Walsh et al. 2001). Even though G 305.208+0.206 is not associated with a bright IR source it is known to be a strong source of continuum emission (see Table 8.7).

Walsh et al. (1997) find that the single–star luminosity for G 305.208+0.206 is between 2.1 – 4.7×10^5 $L_\odot$ and classify it as an O5.5 – O6 star for a source at a near/far kinematic distance of 4.6/6.9 kpc. Assuming a distance of 6.2 kpc, Phillips et al. (1998b) propose upper–limit spectral types of <B1 and <B0.5 for G 305.208+0.206 and G 305.202+0.208, based on the absence of associated UC HII regions. In addition to the different distances which have been adopted, the discrepancy in spectral types can be attributed to the 3.3′ resolution of the Walsh et al. (1997) observations which measure the luminosity of the extended region, rather than individual objects. Hill et al. (2005) calculate a core mass of 2.7×10^3 $M_\odot$ for the 1.2 mm

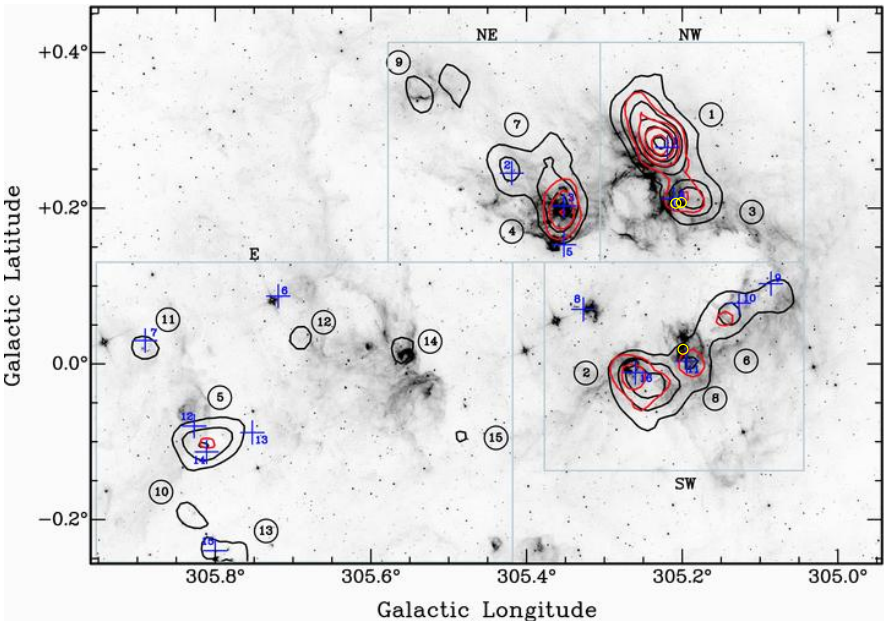

Figure 8.1: Contour map of the peak temperature $NH_3(1,1)$ and (2,2) emission from Hindson et al. (2010) showing 15 clumps divided into four regions: NE, NW, SW and E. $NH_3(1,1)$ and (2,2) emission are shown as black and red contours respectively. Water maser emission is shown as blue crosses. The yellow circles indicate 6.7 GHz methanol maser emission associated with G 305.202+0.208 and G 305.208+0.206 found in the NW region, and 6.7 GHz methanol maser emission associated with G 305.200+0.019 in the SW region.

continuum peak centred on G 305.208+0.206, assuming a distance of 3.9 kpc. Based on a distance of 3.9 kpc, Walsh et al. (2007) conclude that the powering high–mass source is between spectral type O9.5 – B0 and O8 – B0 for G 305.208+0.206 and G 305.202+0.208 respectively. This demonstrates that the large uncertainty in the adopted distance by various authors affects any constraints on the physical parameters that are determined for the young high–mass stars in the G 305 region. In this chapter, we provide trigonometrical parallax distances to two of the 6.7 GHz methanol maser sources in this region, and provide updated physical parameters of the young high–mass sources.

8.2 Observations

Five epochs of observations were made of the 6.7 GHz methanol masers in G 305.200+0.019, G 305.202+0.208 and G 305.208+0.206, as well of the background quasars J 1312−6035, J 1254−6111 and J 1256−6449 (see Table 7.1) during the 2013 March, June, August, November and 2015 March epochs (see Table 5.1). The J 2000 coordinates which were used for the maser observations were from the MMB catalogue by Green et al. (2012b): G 305.200+0.019 at $\alpha = 13^h11^m16.93^s$, $\delta = 62°45' 55.1''$, G 305.202+0.208 at $\alpha = 13^h11^m10.49^s$, $\delta = -62°34' 38.8''$ and G 305.208+0.206 at $\alpha = 13^h11^m13.71^s$, $\delta = -62°\ 34'\ 41.4''$. The latter two sources are separated by $22''$ and we pointed the telescopes mid–way between these two positions, prior to correlating the individual sources at the MMB positions.

From our phase–referenced observations we present updated coordinates (using the procedure described in Section 7.1.3) for G 305.200+0.019, G 305.202+0.208 and G 305.208+0.206

Quasar	Epoch	x Offset (mas)	Error	y Offset (mas)	Error	Flux (mJy)	Parallax (mas)
J 1254−6111	2013.210	2.711	0.102	−0.362	0.063	561.408	0.30±0.08
	2013.460	0.332	0.008	−0.252	0.010	311.139	
	2013.621	−0.500	0.017	−0.157	0.015	159.655	
	2013.887	−2.101	0.017	0.047	0.016	132.474	
	2015.236	−11.350	0.019	−0.706	0.014	178.399	
J 1312−6035	2013.210	1.267	0.101	0.536	0.057	66.405	0.35±0.19
	2013.460	−0.736	0.082	0.008	0.055	7.797	
	2013.621	−2.020	0.041	−0.275	0.028	13.888	
	2013.887	−3.648	0.057	−0.622	0.049	12.584	
	2015.236	−12.050	0.041	−1.338	0.029	17.397	

Table 8.1: Measured flux densities and differential fitted positions between the −33.1 km s^{-1} feature in G 305.200+0.019 and background quasars J 1254−6111 and J 1312−6035.

in Table 7.1 with respect to J 1254−6111 from the 2013 June epoch. The offset between the source coordinates in Table 7.1 and Green et al. (2012b) for G 305.200+0.019 is 0.282″, G 305.202+0.208 is 0.056″ and G 305.208+0.206 is 0.076″.

The coordinates for J 1254−6111 and J 1256−6449 in Table 7.1 are from Petrov et al. (2011) with uncertainties of 1.49 mas and 1.26 mas respectively. The coordinates which were used for J 1312−6035 were $\alpha = 13^h12^m12.34$, $\delta = -60^\circ\ 35'\ 38.1''$ (Murphy et al. 2010b) are accurate to $\lesssim 1''$. From our phase–referenced images, we present updated coordinates for this source with an error of 1.49 mas in Table 7.1, with an offset of 0.368″ from the Murphy et al. (2010b) position. We also observed J 1259−6519 (McConnell et al. 2012) for ∼6 mins to test its suitability as background quasar in the 2013 March epoch, but failed to detect it.

8.3 Data reduction

We followed the data reduction procedure which was described in Chapter 6 but omitted the tropospheric path length corrections (in light of our findings in Section 7.3). We analyzed the cross correlation spectra of each maser shown in Figure 8.2 in search of the feature(s) which exhibited the smallest relative flux density variations across all baselines for the duration of the observations, taking this to be an indication that it was an unresolved point source, which would enable an accurate position determination. We fringe fit on the maser spectral channel associated with this feature before transferring the phase solutions to the quasars which were observed in conjunction with this source. We used the −33.1 km s^{-1} feature for G 305.200+0.019, the −44.0 km s^{-1} feature for G 305.202+0.208 and the −38.3 km s^{-1} feature for G 305.208+0.206 for astrometry.

After transferring the phase corrections from the maser channel, we averaged all channels in the quasar dataset and imaged the emission using a Gaussian beam of 5.28×4.00 mas (averaged over all epochs). We report detections for J 1254−6111, J 1256−6035 and J 1312−6035 on VLBI baselines. The quasars appear to be dominated by single components, and show

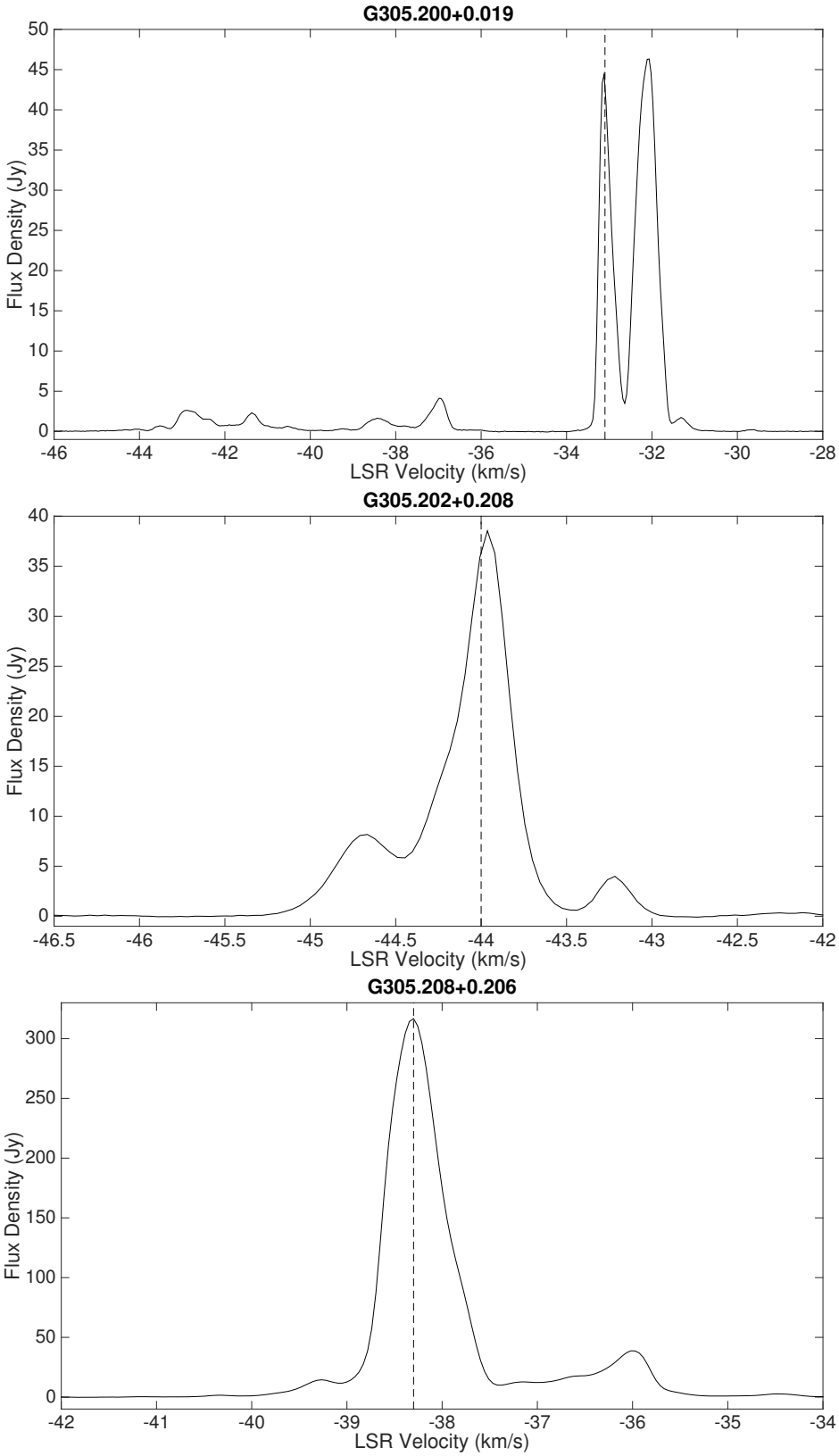

Figure 8.2: The autocorrelation spectra using all antennas from 2013 November of TOP: G 305.200+0.019 (-38.0 to -29.5 km s^{-1}) and G 305.199+0.005 (-45.0 to -40.0 km s^{-1}); the emission in the region with peak at -38.5 km s^{-1} was not not detected in Green et al. (2012b), MIDDLE: G 305.202+0.208 and BOTTOM: G 305.208+0.206. The dashed vertical lines indicate the maser spectral feature which we deemed to be most suitable for astrometry (see Section 8.3).

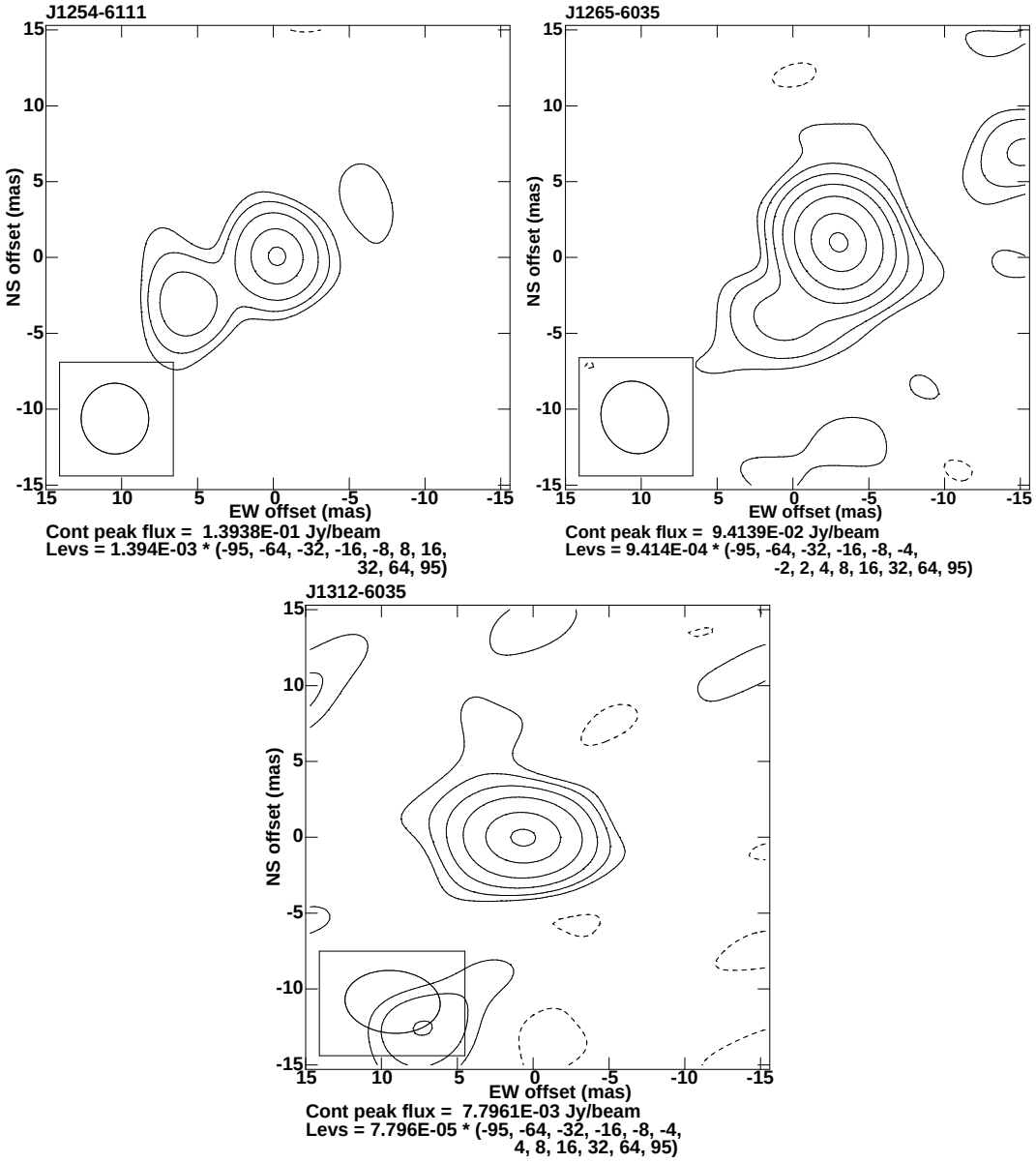

Figure 8.3: J 1254−6111 (top left), J 1256−6035 (top right) and J 1312−6035 (bottom) from the 2013 June session and are typical of the images which we obtained from our analysis. The quasars showed consistent centroid structure dominated by a single peak throughout all epochs. There was some variability in the quality of the images from one epoch to another, with image distortions resulting from phase errors. The extension in the quasar image for J 1254−6111 shows that the phase transfer from the maser to the quasar is especially poor for this epoch (but not others), and does not prevent us from accurately measuring the position of the core.

Quasar	Epoch	x Offset (mas)	Error	y Offset (mas)	Error	Flux (mJy)	Parallax (mas)
J 1254−6111	2013.210	3.240	0.034	0.583	0.023	195.085	0.58±0.16
	2013.460	0.863	0.024	0.204	0.022	283.989	
	2013.621	−0.604	0.024	0.478	0.021	174.741	
	2013.887	−1.343	0.160	−0.385	0.148	91.500	
	2015.236	−10.907	0.292	−0.791	0.354	44.120	
J 1256−6449	2013.210	6.775	0.082	−0.291	0.046	39.475	0.54±0.30
	2013.460	3.611	0.018	−0.620	0.016	128.405	
	2013.621	2.352	0.040	−0.487	0.036	54.085	
	2013.887	2.078	0.200	−0.555	0.154	30.149	
	2015.236	−8.571	0.479	−0.856	0.426	120.373	
J 1312−6035	2013.210	2.508	0.029	0.959	0.021	16.702	0.44±0.24
	2013.460	−0.253	0.021	0.124	0.018	19.745	
	2013.621	−1.529	0.051	0.259	0.048	10.974	
	2013.887	−2.740	0.038	−0.368	0.033	10.797	
	2015.236	−12.117	0.143	−1.320	0.141	11.113	

Table 8.2: Measured flux densities and differential fitted positions between the −44.0 km s^{-1} feature in G 305.202+0.208 and background quasars J 1254−6111, J 1256−6449 and J 1312−6035.

deviation from point–like structure at levels <10% of the peak flux density as show in Figure 8.3. Phase errors contribute to the distortions in the final images and indicate the need to refine the tropospheric calibration step which has been omitted here. We located the centroid position of the quasar by fitting a 2D Gaussian to the deconvolved quasar emission. The offset of the emission peak from the centre of the image field was recorded for all epochs and we present these data for G 305.200+0.019 in Table 8.1 and for G 305.202+0.208 in Table 8.2. The change in the position of the maser feature used for astrometry was modelled using the procedure outlined in Section 6.3.8.

8.4 Results

The parallax and proper motion results are summarised in Table 8.3 and described in Figure 8.4. The parallax to G 305.200+0.019 was measured to be 0.30±0.08 mas with respect to J 1254−6111, corresponding to a distance of $3.3^{+1.2}_{-0.7}$ kpc. The proper motion was $\mu_x = -6.9\pm0.1$ mas y^{-1} and $\mu_y = -0.1\pm0.1$ mas y^{-1}. In order to constrain errors in the measured proper motion, we made image cubes of the maser emission for all epochs, and analyzed the changes in the distribution from 2012 to 2015 March. We found that internal motions in G 305.200+0.019 can be up to ∼0.2 mas y^{-1} in right ascension and were an order of magnitude greater than the internal motions in declination. We added these in quadrature to the formal errors in (μ_x, μ_y) and report the measured proper motion with errors as $\mu_x = -6.9\pm0.3$ mas y^{-1} and $\mu_y = -0.1\pm0.2$ mas y^{-1}.

The parallax to G 305.202+0.208 was measured to be 0.58±0.16 mas with respect to J 1254−6111 corresponding to a distance of $1.7^{+0.7}_{-0.4}$ kpc. The proper motion is $\mu_x = -6.9\pm0.2$ mas y^{-1} and $\mu_y = -0.5\pm0.5$ mas y^{-1} (Table 8.3 and Figure 8.5). We found that internal motions

Source name	Maser feature (km s^{-1})	Parallax (mas)	Distance (kpc)	μ_x (mas y^{-1})	μ_y (mas y^{-1})
G 305.200+0.019	−33.1	0.30±0.08	$3.3^{+1.2}_{-0.7}$	−6.9±0.3	−0.1±0.2
G 305.202+0.208	−44.0	0.58±0.16	$1.7^{+0.7}_{-0.4}$	−6.9±0.3	−0.5±0.5

Table 8.3: Parallax distance and proper motion of G 305.200+0.019 and G 305.202+0.208 with respect to J 1254−6111.

(from 2012 to 2015 March) in G 305.202+0.208 can be up to ∼0.3 mas y^{-1} in right ascension and were an order of magnitude greater than the internal motions in declination. We added these in quadrature to the formal errors in (μ_x, μ_y) and report the measured proper motion with errors as $\mu_x = -6.9\pm0.3$ mas y^{-1} and $\mu_y = -0.5\pm0.5$ mas y^{-1}.

These measured uncertainties correspond to internal motions of $\lesssim$5 km s^{-1} in the maser emission and are consistent with proper motion estimates of 6.7 GHz methanol masers in HMSFRs (e.g. Goddi et al. 2011; Moscadelli & Goddi 2014; Sugiyama et al. 2014). A more detailed analysis of the internal motions of the 6.7 GHz emission in the G 305 sources is beyond the scope of the current text and will be the subject of future analysis.

We were unable to model the parallax signature of G 305.208+0.206 from our observations. We suspect this may be a source which is unsuitable for astrometry as there was evidence for blending in the −38.3 km s^{-1} main peak of the maser spectrum, and the secondary peaks showed greater variation in flux intensity over the different baseline than the −38.3 km s^{-1} peak. However, due to its angular proximity with G 305.202+0.208 (see Section 8.2), we propose that the masers belong to the same region and attribute a distance of $1.7^{+0.7}_{-0.4}$ kpc to G 305.208+0.206 as well.

8.4.1 Parallaxes with secondary quasars

Tables 8.1 and 8.2 show that we successfully managed to extract parallaxes to G 305.200+0.019 and G 305.202+0.208 from J 1254−6111, J 1312−6035 and J 1256−6449. The parallax measurements to all quasars are consistent, although there is greater uncertainty in the measurement for J 1312−6035 and J 1256−6449.

As described in Section 6.3.8, we allow for *a priori* astrometric uncertainties in right ascension and declination in computing the parallax. These estimates are iteratively adjusted until $\chi^2_\nu \approx 1$ is obtained for the parallax model. We found that the parallax results obtained with J 1254−6111 required smaller *a priori* uncertainties (between ∼0.1 – 0.6 mas). We took this to indicate structural changes or extended sizes for J 1312−6111 and J 1256−6449, which adversely affect the parallax measurement and could explain our failure to model the parallax of G 305.200+.0.019 with respect to J 1256−6449. We therefore quote the measured parallax and proper motions with respect to J 1254−6111 as the preferred result.

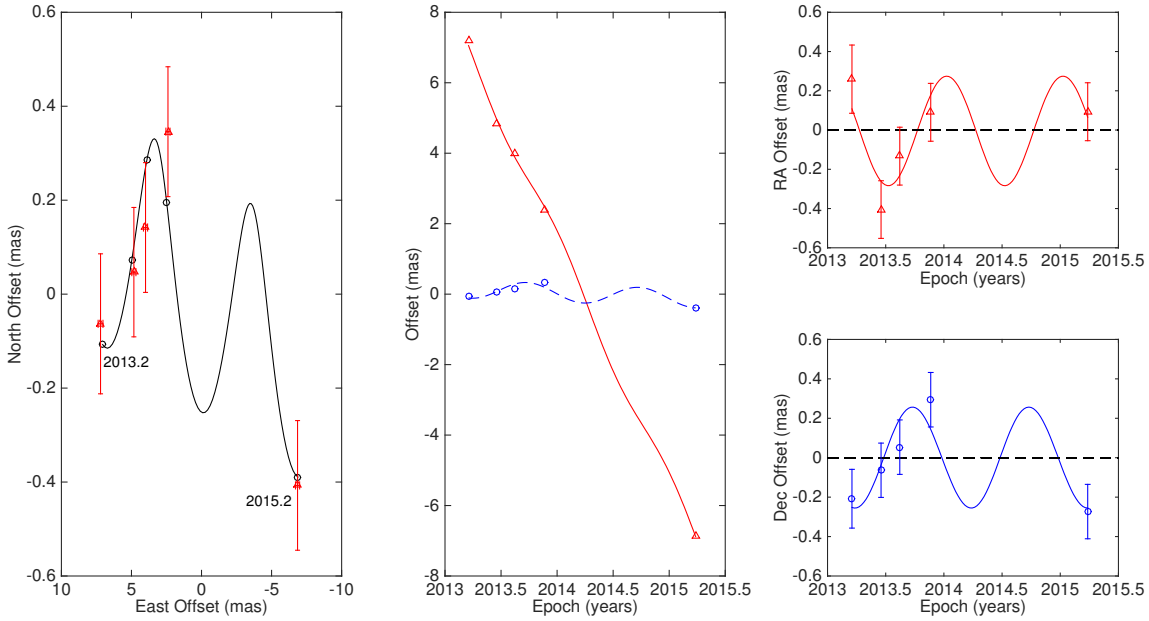

Figure 8.4: Parallax and proper motion of the −33.1 km s^{-1} reference feature in G 305.200+0.019 with respect to J 1254−6111. Left panel: the sky positions with the first and last epochs labeled. The expected positions from the fits are indicated with circular markers. Middle panel: East–West (triangles) and North–South (circles) motion of the position offsets and best combined parallax and proper motions fits versus time. Right panels: the RA (top) and Dec (bottom) parallax signature with the best fit proper motions removed.

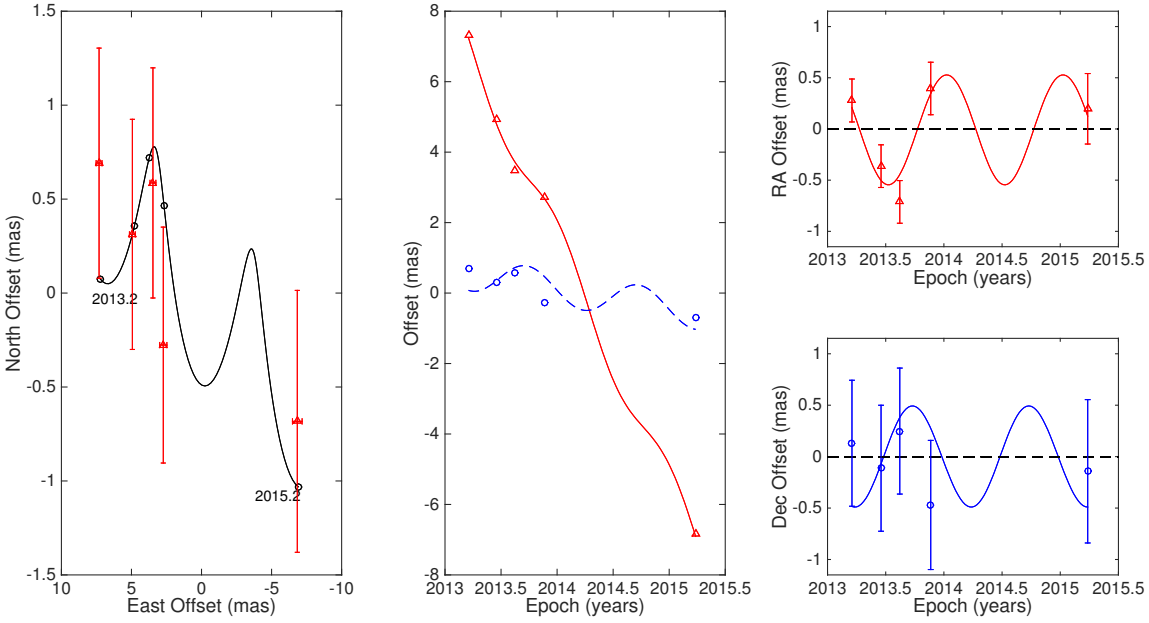

Figure 8.5: Parallax and proper motion of the −44.0 km s^{-1} reference feature in G 305.202+0.208 with respect to J 1254−6111. Left panel: the sky positions with the first and last epochs labeled. The expected positions from the fits are indicated with circular markers. Middle panel: East–West (triangles) and North–South (circles) motion of the position offsets and best combined parallax and proper motions fits versus time. Right panels: the RA (top) and Dec (bottom) parallax signature with the best fit proper motions removed.

6.7 GHz maser	^{13}CO clump	Clump $v_{\rm lsr}$ (km s^{-1})	ΔV (km s^{-1})	MMB $v_{\rm lsr}$ (km s^{-1})	Separation (°)
G 305.200+0.019	G 305.19+0.01	−31.8	3.49	−33.1	0.01
G 305.202+0.208	G 305.21+0.21	−43.3	1.35	−44.0	0.01
G 305.208+0.206	–	–	–	−38.3	0.004

Table 8.4: A comparison of the ^{13}CO molecular clumps from Hindson et al. (2013) and the associated 6.7 GHz methanol masers in G 305.200+0.019, G 305.202+0.208 and G 305.208+0.206. The 6.7 GHz methanol maser MMB peak velocity from Green et al. (2012b) is also listed. ΔV is the spread in the observed $v_{\rm lsr}$ of the ^{13}CO clumps. We classify both G 305.202+0.208 and G 305.208+0.206 to be associated with the clump G 305.21+0.21. The separation column describes the angular distance between the 6.7 GHz methanol maser and corresponding ^{13}CO molecular clump.

8.5 Discussion of the parallax distance

Since the 1980s there have been numerous attempts to determine the distance to the G 305 complex. Using optical–near IR colours, Danks et al. (1983) suggest a distance of 3.7 – 4.5 kpc to the WR 48a region containing the G 305 complex. Caswell & Haynes (1987) find the near/far kinematic distance using $R_0 = 10$ km s^{-1} and $\Theta_0 = 250$ km s^{-1} (Schmidt 1965) to G 305.202+0.022 to be 3.5/8.0 kpc. Norris et al. (1993) present a kinematic heliocentric distance of 8.0 kpc to G 305.208+0.206. Phillips et al. (1998b) used the Brand & Blitz (1993) model with $R_0 = 8.5$ kpc and $\Theta_0 = 220$ km s^{-1} to update this to 6.2 kpc for G 305.208+0.206 and 4.8 kpc for G 305.202+0.208 (no ambiguity). The authors explain that it is likely that both sources are associated with the same region, and adopt a combined distance of 6.2 kpc. Using the same kinematic distance model, Russeil et al. (1998) find from radio and Hα observations with $V_{syst} = -38$ km s^{-1} that G 305 at a distance of 3.5 kpc, cautioning that large velocity dispersions are present in the the Hα data. Green & McClure-Griffiths (2011) do not provide kinematic distances for G 305.208+0.206 and G 305.202+0.208 using the Reid et al. (2009b) model, as they are not able to determine HISA due to no HI data, or because of the absence of an associated continuum source.

Hindson et al. (2013) measured the $v_{\rm lsr}$ velocities of ^{13}CO molecular clumps associated with the G 305 region (see Table 8.4), and we have used these velocities to determine the kinetic distances to G 305.200+0.019, G 305.202+0.208 and G 305.208+0.206. Using the latest Galactic parameters of $\Theta_0 = 240$ km s^{-1}, $R_0 = 8.34$ kpc (including an uncertainty of 8 km s^{-1} in Θ_0; Reid et al. 2014), the (near) kinematic distance to G 305.200+0.019 is $2.6^{+0.8}_{-0.7}$ kpc, which is closer than the parallax distance of $3.3^{+1.2}_{-0.7}$. The (near) kinematic distance to G 305.202+0.208 and G 305.208+0.206 is $4.3^{+2.2}_{-0.4}$ kpc, which is more than twice as far as the parallax distance of $1.7^{+0.7}_{-0.4}$ kpc to G 305.202+0.208.

8.5.1 Uncertainty in the kinematic distances

As discussed in Section 1.1.2, the kinematic distance technique is susceptible to large errors if the sources exhibit large peculiar motions or broad spectral line profiles. Table 8.4 shows

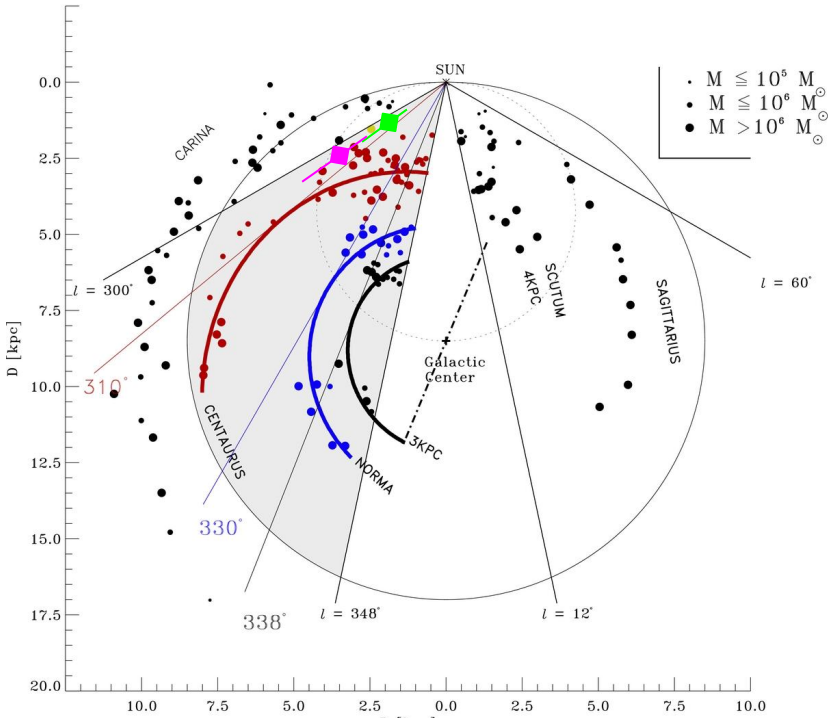

Figure 8.6: A plan view of the distributions of the spiral arms in the 4$^{\text{th}}$ quadrant of the Milky Way galaxy from García et al. (2014). The 6.7 GHz methanol masers associated with G 305.202+0.208 and G 305.200+0.019 are plotted as green and pink diamonds respectively. Based on the (l, b, V) diagrams in García et al. (2014), the masers are either associated with the Carina (black circles) or Centaurus (red circles) spiral arms.

that the spread in the $v_{\rm lsr}$ in the ^{13}CO molecular clumps associated with the 6.7 GHz maser sources is between 1 – 3.5 km s^{-1}, and in the case of G 305.208+0.206, there is a difference of 5 km s^{-1} between the MMB peak velocity of the 6.7 GHz methanol maser emission and the associated ^{13}CO clump G 305.21+0.21. In considering these uncertainties, we find that the (near) kinematic distance to G 305.200+0.019 can range between 1.8 and 3.6 kpc, G 305.202+0.208 between 2.8 and 6.6 kpc and G 305.208+0.206 between 2.4 and 6.5 kpc. This indicates that using the kinematic distance technique on these sources can produce extremely erroneous results.

8.6 Properties of associated HMSFRs

8.6.1 Peculiar motion

In using the measured proper motions (Table 8.3) in conjunction with the $v_{\rm lsr}$ of the associated ^{13}CO molecular clumps (Table 8.4), we have determined the full 3D motion of G 305.200+0.019, G 305.202+0.208 and G 305.208+0.206 in Table 8.5. The dynamical model of the Galaxy we use assumes a flat rotation curve of the disk with a speed of $\Theta_0 = 240$ km s^{-1}, based on the analysis in Reid et al. (2014). The distance of the Sun to the Galactic Centre is taken to be $R_0 = 8.34$ kpc, and is modelled to have peculiar motion components $U_\odot = 10.70$ km s^{-1}, $V_\odot = 15.60$ km s^{-1} and $W_\odot = 8.90$ km s^{-1} (Reid et al. 2014). In Reid et al. (2014) there is a good fit to the model of spiral arm motions when a RMS of

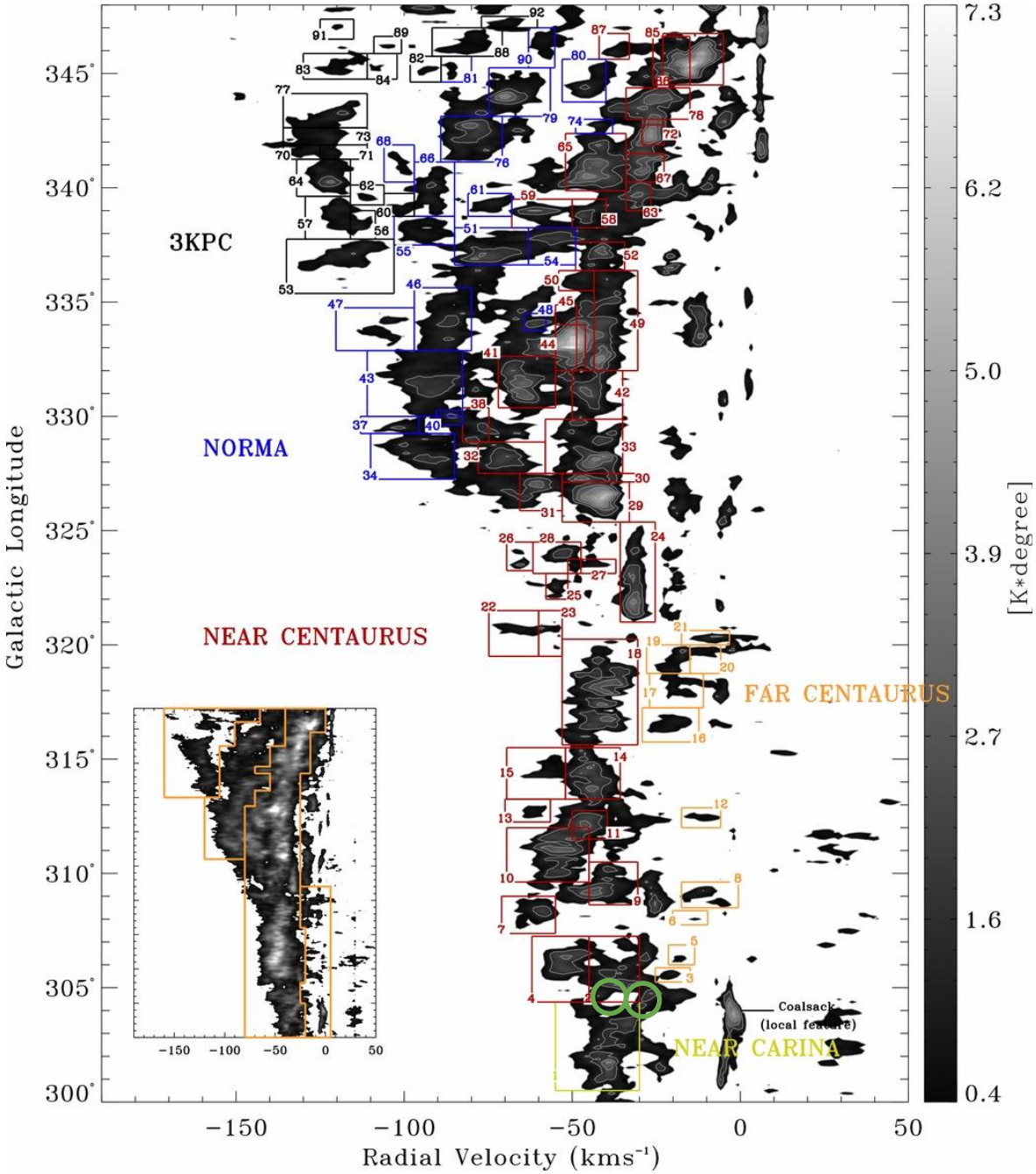

Figure 8.7: The $(\ell - V)$ diagram from García et al. (2014) shows the Carina, Centaurus and 3 kpc spiral arms of the Milky Way galaxy. G 305.202+0.208 and G 305.208+0.206 (green circles) are likely to be associated with either the Centaurus or Carina arms, or a spur extending between the two (see Section 8.6.3).

Source name	**D (kpc)**	U (km s^{-1})	V (km s^{-1})	W (km s^{-1})
G 305.200+0.019	3.3	−2.00±4.90	−7.26±13.40	15.70±3.70
G 305.202+0.207	1.7	−8.33±3.49	19.02±9.01	8.71±5.48
G 305.208+0.206	1.7	−7.79±3.19	19.27±8.40	12.28±2.24

Table 8.5: Peculiar motions for G 305.200+0.019, G 305.202+0.208 and G 305.208+0.206 in a reference frame that is rotating with the Galaxy. The components of peculiar velocity seem to be large compared with the bulk of HMSFRs (∼10 km s^{-1}) in the Milky Way.

n_e (cm^{-3})	$M_{\rm HII}$ ($M_\odot$)	log N_L (s^{-1})	M_* ($M_\odot$)	Spectral type
0.62×10^4	25.9×10^{-4}	46.04	11.3	B1

Table 8.6: Physical parameters of G 305.200+0.019 from Hindson et al. (2012) adjusted to a preferred distance of 3.3 kpc.

about 5 – 7 km s^{-1} is assumed for each velocity component of HMSFR. This is reasonable for Virial motions of stars in giant molecular clouds and so there may not be much evidence for large (>10 km s^{-1}) streaming motions in general. While G 305.200+0.019 follows this trend for the tangential (V) component, G 305.202+0.208 and G 305.208+0.206 do not. Interestingly, all three sources exhibit large ($\gtrsim$10 km s^{-1}) peculiar motions out of the Galactic Plane (compared to the sources in Reid et al. 2009b).

8.6.2 Physical constraints on the ionizing star

Assuming a distance of 3.8±0.6 kpc, Hindson et al. (2012) derive the properties of the embedded high–mass star for the candidate UC HII region associated with G 305.200+0.019. Using their results along with the equations from Panagia & Walmsley (1978) we estimate the electron density n_e, mass of ionized hydrogen $M_{\rm HII}$, the Lyman continuum photon flux N_L in Table 8.6. From this we find the (lower limit) mass of the ionizing source responsible for the observed Lyman flux to be a B1 type[1] star, and consistent with Hindson et al. (2012). This is expected as the change in the adopted distance is only by a factor of ∼0.1.

G 305.202+0.208 is associated with a bright IR source (De Buizer 2003; Walsh et al. 1999) but not any radio continuum emission (Hindson et al. 2012; Phillips et al. 1998b). G 305.208+0.206 is neither associated with a bright IR source (De Buizer 2003) nor any detectable radio continuum emission (Hindson et al. 2012; Phillips et al. 1998b). Based on the absence of HII regions Walsh & Burton (2006) propose that G 305.202+0.208 and G 305.208+0.206 are at early stages of stellar evolution, with G 305.208+0.206 likely to be at an earlier stage, as it shows strong mm continuum emission (Table 8.7) and no detectable IR emission. Walsh et al. (1997) find that the near kinematic distances to G 305.202+0.019 (G 305.200+0.019) and G 305.208+0.206 are 2.8 and 4.6 kpc, and derive luminosities of 13.2×10^4 $L_\odot$ and 20.9×10^4 $L_\odot$ for the associated IRAS sources. (Note that

[1]In Section 7.2.2 we found that G 339.884−1.259 has log N_L = 45.6 s^{-1} which is similar to G 305.200+0.019 and so it is unsurprising that both sources have the same spectral classification.

Walsh et al. (1999) show that the IR emission is in fact associated with G 305.202+0.208 and not G 305.208+0.206.) Using the updated distances to these sources, we find that the luminosities of G 305.200+0.019 and G 305.208+0.206 are $18.3{\times}10^4$ $L_\odot$ and $2.9{\times}10^4$ $L_\odot$, corresponding to O6.5 and B0.5 spectral sources (Panagia 1973). As described in Section 8.1, the arcminute resolution in Walsh et al. (1997) means that these results are susceptible to diffuse emission surrounding the IRAS sources, resulting in the higher derived spectral type for G 305.200+0.019 compared to Table 8.6.

The estimated masses from 870 μm observations associated with quiescent and star–forming clumps from Csengeri et al. (2014) and 1.2 mm observations from Hill et al. (2005) are shown in Table 8.7. The masses (M) have been determined from the following equation assuming the emission (at 870 μm and 1.2 mm) is from optically thin cold dust (Hildebrand 1983),

$$M = \frac{S_\nu \, R \, d^2}{B_\nu(T_d) \, \kappa_\nu} \tag{8.1}$$

where S_ν is the integrated flux, R is the gas–to–dust mass ratio of 100 (Csengeri et al. 2014; Hill et al. 2005), d is the distance to the source, κ_ν is the mass absorption coefficient (0.185 and 0.1 $\mathrm{m^2\,kg^{-1}}$ for the 870 μm and 1.2 mm observations by Csengeri et al. (2014) and Hill et al. (2005) respectively) and $B_\nu(T_d)$ is the Planck blackbody function at 20 K (Hill et al. 2005).

6.7 GHz maser	Distance (kpc)	Compact source	RA (h m s)	Dec (° ′ ″)	Separation	Integrated Flux (Jy)	Mass ($M_\odot$)
G 305.200+0.019	3.3	G 305.1996+0.0194[a]	13 11 16.728	−62 45 54.00	1.51″	1.89	115
		G 305.200+0.02[b]	13 11 17.0	−62 45 53	2.14″	0.7	130
G 305.202+0.208	1.7	G 305.1997+0.2067[a]	13 11 9.2400	−62 34 41.88	9.15″	3.88	62
		G 305.202+0.230[b]	13 11 09.4	−62 33 17	1.37′	1.4	69
G 305.208+0.206	1.7	G 305.2083+0.2063[a]	13 11 13.704	−62 34 40.80	0.61″	26.12	417
		G 305.21+0.21[b]	13 11 14.1	−62 34 45	4.53″	10.6	524

Table 8.7: Estimated masses of compact quiescent and star–forming clumps from the 870 μm observations by Csengeri et al. (2014)[a] and 1.2 mm observations by Hill et al. (2005)[b], associated with the 6.7 GHz methanol maser emission in G 305.200+0.019, G 305.202+0.208 and G 305.208+0.206. The masses have been determined from equation 8.1 for dust temperature at 20 K. The masses determined for the Hill et al. (2005) sources have been updated for the preferred distances of 3.3 kpc to G 305.200+0.019 and 1.7 kpc to G 305.202+0.208 and G 305.208+0.206. The separation is between the 6.7 GHz masers and associated compact source.

8.6.3 Spiral arm allocation

While spiral arms of the Milky Way have been identified from over 100 parallaxes to Northern Hemisphere HMSFRs (Reid et al. 2014), there have been insufficient parallaxes to Southern HMSFRs to trace the spiral arms in the 3$^{\rm rd}$ and 4$^{\rm th}$ quadrants using this method (see Figure 4.3).

Recently García et al. (2014) have measured CO(1–0) emission in the 4$^{\rm th}$ quadrant of the Galaxy to separate the components into spiral arms (see Figure 8.6). Based on their (ℓ−V) diagrams G 305.200+0.019, G 305.202+0.208 and G 305.208+0.206 are associated with either the Centaurus or Carina arms (see Figure 8.7). The CO spectrum toward the sources has $v_{\rm lsr}$ velocity of −39.3km s^{-1} (T. Dame 2015, private communication), and is almost exactly between the velocities of G 305.200+0.019 and G 305.202+0.208. Based on the 6.7 GHz methanol maser $v_{\rm lsr}$ (see Table 8.4), G 305.202+0.208 would seem to favor the Centaurus arm, whereas G 305.200+0.019 has a $v_{\rm lsr}$ about half way between the Centaurus and Carina arms. If these sources are associated with the Centaurus arm, they would be a few degrees outside the tangent point of ∼310° (see Figure 8.7) and at a distance of ∼5.2 kpc. However, if they are associated with the Carina arm at a longitude of 305°, we would expect them to have a $v_{\rm lsr} = -17$km s^{-1} at a distance of ∼3.2 kpc.

While the masers are associated with CO emission that is unusually strong not to be associated with an arm, the emission is near the terminal velocity locus where velocity crowding tends to enhance the CO emission (T. Dame 2015, private communication). While we are currently unable to associate the masers with either the Centaurus or Carina spiral arms without more parallaxes to HMRFRs in the region, it is possible that the sources are in a spur that extends between them.

8.7 Summary of findings

We have successfully obtained a further two parallaxes to prominent Southern HMSFRs in the Milky Way galaxy with the LBA. The parallax to G 305.200+0.019 is measured to be 0.30±0.08 mas, corresponding to a distance of $3.3^{+1.2}_{-0.7}$ kpc. The parallax to G 305.202+0.208 is measured to be 0.58±0.16 mas, corresponding to a distance of $1.7^{+0.7}_{-0.4}$ kpc. We also made astrometric observations of the 6.7 GHz methanol masers in G 305.208+0.206 (in conjunction with G 305.200+0.019 and G 305.202+0.208) but were unable to model its parallax signature. We associate the distance to G 305.208+0.206 with that of G 305.202+0.208 as both sources are separated by 22″ in the sky. The parallax distances are different from the derived kinematic distances to G 305.200+0.019 of $2.6^{+0.8}_{-0.7}$ and to G 305.202+0.208 and G 305.208+0.206 of $4.3^{+2.2}_{-0.4}$ kpc, when using the latest Galactic parameters from Reid et al. (2014), in conjunction with the $v_{\rm lsr}$ of associated ^{13}CO molecular clumps from Hindson et al. (2013). These results provide further evidence (e.g. Xu et al. 2006) on the unreliability of model dependent techniques for providing reliable distances for the study of HMSF.

Using the distances from our parallax measurements together with the measured fluxes of the compact sub–millimetre sources identified by Csengeri et al. (2014), we have determined the masses of the high–density objects associated with G 305.200+0.019, G 305.202+0.208 and G 305.208+0.206 in Table 8.7. G 305.200+0.019 is the only object from our pool of

sources to be associated with an UC HII region, and from the observed Lyman flux we derive the spectral type of the ionizing source to be consistent with a B1 star.

Reid et al. (2014) show from over 100 proper motion measurements that the majority of HMSFRs in our Galaxy have peculiar components which deviate by less than $\sim$10 km s^{-1} from spiral arm motions. However, we find that G 305.200+0.019, G 305.202+0.207 and G 305.208+0.206 seem to deviate with large tangential (V) and perpendicular (W) components from the circular and planar orbits of typical Galactic spiral arm motions.

Based on the ($\ell - V$) diagrams of García et al. (2014), we propose that G 305.200+0.019 and G 305.202+0.207 are associated with either the Centaurus or Carina spiral arms in the 4$^{\rm th}$ quadrant of the Galaxy. There is currently some uncertainty as to which arm to assign these sources to as the Galactic Longitude of the masers suggests that they would be associated with the Carina arm. However, the observed $v_{\rm lsr}$ of the 6.7 GHz masers is consistent with the $v_{\rm lsr}$ of the CO emission in the Centaurus spiral arm instead. It is therefore possible that the HMSFRs associated with the masers are in a spur between Carina and Centaurus. We anticipate that further parallaxes to Southern HMSFR masers will build a more complete picture of the spiral structure of in the 3$^{\rm rd}$ and 4$^{\rm th}$ quadrants to remove the ambiguity.

Chapter 9

Final Remarks

Distance is fundamental to astronomy and governs our ability to estimate important properties such as the luminosity, size and mass of celestial objects. Because of the immense range of scales involved, no one method of distance measurement is valid across the entire field of astronomy. Trigonometric stellar parallax remains the most direct and accurate method to determine distances to objects beyond our Solar System. This is a model independent technique which relies on the change in perspective of foreground sources against distant background ones as the Earth orbits the Sun, making it robust to systematic errors. It therefore forms the fundamental rung of the cosmic distance ladder system by providing reliable distances to objects in the Milky Way.

9.1 Overview of results in this thesis

Interstellar masers are bright point–like radio sources, which makes them ideal candidates for VLBI parallax measurements. The objective of the ongoing BeSSeL survey is to obtain the parallax and proper motion to methanol and water masers associated with HMSFRs. As the masers are deeply embedded in dense molecular clouds within HMSFRs, which trace the spiral arms of the Milky Way galaxy, the results from BeSSeL are being used to determine the latest structural and dynamical properties of the Milky Way.

In using over 100 parallax and proper motion measurements, Reid et al. (2014) report a distance to the Galactic Centre of $R_0 = 8.3 \pm 0.16$ kpc, circular rotation speed of the spiral arms of $\Theta_0 = 240 \pm 8$ km s^{-1} and a flat rotation curve between radii of $\sim$5 – 16 kpc from the Galactic Centre. The IAU recommended value for Θ_0 is 220 km s^{-1}, and has not been updated for almost 30 years. All the results in Reid et al. (2014) have been obtained from Northern Hemisphere VLBI instruments, and the data is concentrated towards the 1$^{\rm st}$ and 2$^{\rm nd}$ quadrants of the Galaxy. Southern sources are beyond the reach of Northern VLBI telescopes for the purposes of accurate astrometry, and there is a corresponding paucity of data in the 3$^{\rm rd}$ and 4$^{\rm th}$ quadrants for spiral arm assignment. In order to ensure that these latest models of the Milky Way's structure and rotational properties are reliable, they must be derived from a more uniformly sampled distribution, including sources from the 3$^{\rm rd}$ and 4$^{\rm th}$ quadrants.

My collaborators and I have made the first parallax and proper motion measurements of Southern 6.7 GHz methanol masers using the LBA as part of the astrometry program.

This program was initiated in 2008, with the aim of contributing vital Southern Hemisphere LBA data to the BeSSeL project. The parallax of G 339.8841.259 measured from five epochs of observations is 0.48±0.08 mas, corresponding to a distance of $2.1^{+0.4}_{-0.3}$ kpc. The proper motion is measured to be $\mu_x = -1.6\pm0.4$ mas y^{-1}, $\mu_y = -1.9\pm0.4$ mas y^{-1}. Our results place G 339.884−1.259 in the near edge of the Scutum spiral arm of the Milky Way. This extends the Galactocentric azimuth of the Scutum arm by about 10°, giving an updated value of $\psi = 19.2°\pm4.1°$ for the chirality of the arm. We also measured the parallax of G 305.200+0.019 to be 0.30±0.08 mas, corresponding to a distance of $3.3^{+1.2}_{-0.7}$ kpc, with $\mu_x = -6.9\pm0.3$ mas y^{-1} and $\mu_y = -0.1\pm0.2$ mas y^{-1}. The parallax of G 305.202+0.208 is measured to be 0.58±0.16 mas, corresponding to a distance of $1.7^{+0.7}_{-0.4}$ kpc, with $\mu_x = -6.9\pm0.3$ mas y^{-1} and $\mu_y = -0.5\pm0.5$ mas y^{-1}. G 305.200+0.019 and G 305.202+0.207 are likely to be associated with either the Centaurus or Carina spiral arms of the Galaxy, although it is possible that the sources are in a spur between them. Assigning G 305.200+0.019 and G 305.202+0.207 to a spiral arm is not straightforward, because of the paucity of parallax distances to HMSFRs in this area and highlights the need for more data from this region.

9.2 Future considerations

In the course of conducting the 6.7 GHz observations, and through the data calibration process, my collaborators and I have identified several elements of the LBA astrometry program which can be refined in order to obtain more accurate results. These are:

1. Improved ionosphere calibration.
2. Improved troposphere calibration.
3. Inclusion of the HartRAO and Wark30m antennas.
4. Observations to coincide with the maximum amplitude in the parallax signature.
5. Availability of Southern Hemisphere calibrators.

9.2.1 Improved ionosphere calibration

Deller et al. (2009a) explain that the available TEC models for ionosphere delay correction in the Southern Hemisphere are sometimes in error due to the lower density of GPS stations in this region. This results in dispersive ionospheric delays being treated as non–dispersive delays during the subsequent tropospheric calibration step, leading to erroneous phase corrections. In Section 7.3.2 my co–authors and I find that at 6.7 GHz the residual ionospheric contribution can be as great as ∼5.3 cm, and would dominate over tropospheric effects. In order to improve the astrometric accuracy of the LBA, we are investigating the use of the multi–view VLBI technique (Sasao & Morimoto 1991) in future LBA maser astrometry observations. This technique will allow us to model the 2D delay and phase surface plane in the direction of the maser and quasar, in order to constrain the spatial and temporal structure in the ionosphere. Simulations of this technique show improvements of an order of magnitude in the astrometric accuracy of the LBA at ≤1.4 GHz, and a proposal has been submitted

to the LBA time allocation committee to trial the effectiveness of the multi–view technique at 6.7 GHz.

9.2.2 Improved tropospheric calibration

An excess in the tropospheric delay limits the relative positional accuracy between the methanol maser and quasar sources. Following the calibration procedure in Reid et al. (2009a), we aimed to reduce this source of error by conducting ICRF mode observations. In Section 7.3.1, I find that the astrometric uncertainty from our observations is $\sim$0.17 mas when an RMS of $\sim$0.1 nsec (the mean in the solutions from FRING*) is assumed for the multiband delay solutions. However in Section 7.1, we estimate that the astrometric capability of the LBA can be as good as $\sim$20 μas, should tropospheric delay calibration be satisfactorily performed. In order to maximize the effectiveness of the ICRF mode observations, there is a need to set–up the IFs in a way which minimizes the ambiguity in finding the delay solutions. This can be achieved by including both narrow and wide margins between consecutive IFs in order to rule out very large and small delays. However, the LBA is a heterogeneous instrument, and we compromised on the frequency setup so that it could be adopted by all antennas, thereby affecting the quality of the multiband delay solutions (see Figure 5.1). This was further compounded by imperfections in the ionospheric calibration stage, resulting in dispersive delays being treated as non–dispersive (see Section 9.2.1). While the current hardware for the LBA will not allow us to adopt an ideal IF set–up configuration, we highlight upcoming developments in Section 9.3 that will address this issue.

9.2.3 Inclusion of the HartRAO and Wark30m antennas

VLBI telescopes are successful tools for astrometry because the effective diameters of the synthesized apertures can span thousands of kilometers, thereby giving excellent resolution because $\theta_d \approx \lambda/D$. There were between 5 – 7 antennas participating the LBA observations reported in this thesis (see Table 5.2.1). For the results presented here, the longest baseline joins Ceduna – Hobart (1,702 km). Including Wark30m would increase the maximum baseline to Ceduna – Wark30m (3,718 km), and including HartRAO would extend this further to HartRAO – Wark30m (10,481 km).

HartRAO was not able to participate in the majority of the ICRF observations as the quasars which had risen at the Australian stations were often set here. This prevented us from modelling the clock drift, leading to its exclusion from the results presented in this thesis. For the upcoming observations, we recommend including HartRAO in at least three ICRF sessions, by choosing between 5 – 10 sources (per session) which can be observed by all the antennas in the array, thereby providing sufficient data to model the clock drift at HartRAO.

The Wark30m antenna only participated in the 2014 November and 2015 March epochs. The sources which were observed during these epochs will need to be scheduled in at least two more sessions with the LBA in a similar configuration before parallax results that include the Wark30m antenna can be obtained.

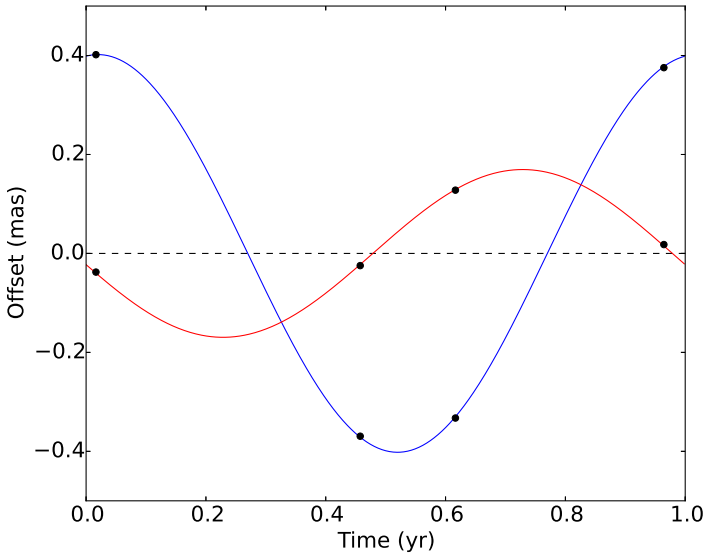

Figure 9.1: The parallax signature in right ascension (blue) and declination (red) for an imaginary source at a distance of 5 kpc from the Sun, with peaks in the right ascension amplitude in January, June and December. The black dots depict the best case scenario where the observation times coincide with these peaks to sample the maximum offsets. Conversely, observations which coincide near the zero offsets are not as advantageous for parallax measurement.

9.2.4 Observations to coincide with the maximum amplitude in the parallax signature

The peak in amplitude in the parallax signature of a Galactic source is dependent on its longitude. Figure 9.1 shows the parallax signature of an imaginary source at a distance of 5 kpc, with maximum offsets in amplitude in right ascension in January, June and December. The black dots depict the best case scenario where the observation times coincide with these peaks to sample the maximum offsets. Conversely, observations which coincide near the zero offsets are not as advantageous for parallax measurement. Figures 7.2, 8.4 and 8.5 show that the observing epochs for the sources in this thesis coincide near the peaks as well as near the zero offsets in the sinusoidal amplitude. The reason is that the LBA is operated by several independent organisations, with VLBI observations for each year being scheduled in advance. These VLBI sessions do not necessarily coincide with epochs that allow the peaks in the parallax signature (as described in the idealized case) to be sampled, and I examine how this issue will be addressed in Section 9.3.

9.2.5 Availability of Southern Hemisphere calibrators

During phase–referencing observations the tropospheric and ionospheric effects create a phase gradient over each antenna. This results in errors in the relative positional accuracy between the maser and quasar that scales with the separation of the sources in the sky, making it necessary to choose background quasars which are as close to the maser source as possible. There currently exist numerous catalogues of compact radio sources with sub–milliarcsecond positional accuracies. However, these are predominantly Northern Hemisphere databases and

there is a paucity of known calibrators in Southern regions with accurately known positions.

Figure 5.2 shows that the concentration of sources in the ICRF2 catalogue is lower in the Southern Hemisphere as compared to the North. In Malkin et al. (2015) the authors report on the progress being made towards developing the ICRF3 catalogue to be made available in 2018. The report contains strategies to improve the coverage of known ICRF sources in the Southern Hemisphere, in terms of both the number of sources as well as their positional accuracy. This will be accomplished by incorporating additional antennas from the Southern Hemisphere (as compared to previously), including three 12 m geodetic antennas from Australia (in Hobart, Katherine and Yarragadee), the Warkworth 12 m antenna from New Zealand and the 15 m antenna in Hartebeesthoek, South Africa. Larger telescopes including HartRAO, Hobart, Parkes and the 34 m (DSS45) antenna in Tidbinbilla will be included for high sensitivity observations. These improvements will lead to a more comprehensive coverage of sources in the ICRF3 catalogue for use with the Southern Hemisphere maser astrometry program.

9.3 Forward planning

At the beginning of 2015, the Australian Research Council (ARC) awarded a Linkage Infrastructure, Equipment and Facilities (LIEF) grant, to upgrade the University of Tasmania's 12 m AuScope VLBI antennas at Hobart, Katherine and Yarragadee. The new receivers will have bandwidths spanning between 2 and 14 GHz, and the digital base band converters (DBBCs) can be configured to allow both broad and narrow spacings between consecutive IFs. This will address the issue raised in Section 9.2.2 to improve the tropospheric calibration procedure. The prototype receiver has undergone initial testing on the Hobart12m antenna site, and parallax observations are expected to commence in the second half of 2016. In addition to the three AuScope antennas, the Ceduna (and possibly the Wark30m) antenna will also be available for observations. This will be a dedicated array for the Southern Hemisphere maser astrometry program, and we anticipate significant expansion of the results presented here. Thousands of hours worth of observations are expected corresponding to $\sim$100 southern HMSFR parallaxes.

An important aspect of the Southern astrometry program is to identify suitable 6.7 GHz methanol maser sources for parallax determination. Experience from the BeSSeL survey has shown that some methanol masers are significantly affected by interstellar scattering, or have emission which is insufficiently compact for parallax measurements. In light of this, we have also submitted a proposal to use the LBA to survey potential maser sites for sources best suited as parallax targets.

9.4 Conclusion

All the VLBI telescopes in operation today are involved in extensive observation programs to determine parallax distances to maser sources associated with HMSFRs throughout the Milky Way galaxy. Requirements for accurate parallaxes are stringent and the astrometric capability of the Australian LBA is unsurpassed for sources at declinations South of -20°.

This is because these sources only rise to low elevations in the Northern Hemisphere, resulting in irreversible distortion of the incoming radiation by the atmosphere. In 2008 the 6.7 GHz maser astrometry program was initialized to measure the parallax distances to ∼30 methanol masers in the Southern Hemisphere with the LBA. I have presented parallaxes of the first three sources in this thesis, thereby establishing the data reduction pathway for the remaining sources in the program.

Results from VLBI astrometric observations including the BeSSeL survey are continuing to shape the way we view our Galaxy by clearly revealing its spiral arm structure, rotational properties and mass. These results are based on observations which are concentrated in the 1st and 2nd quadrants of the Milky Way, and the inclusion of results from the LBA is vital to ensure that sources are sampled from across a broad range of longitudes in order for a complete picture of the Galaxy to emerge.

Acknowledgements

The research in Chapter 3 was undertaken using the Australia Telescope Compact Array which is part of the Australia Telescope, funded by the Commonwealth of Australia for operation as a National Facility managed by CSIRO. The research in Chapter 7 was undertaken using the Long Baseline Array which is funded by the Commonwealth of Australia for operation as a National Facility managed by CSIRO and the University of Tasmania. Funding assistance for the research in this chapter was provided in part by Sigma Xi Grants–in–Aid of research and the Deutscher Akademischer Austauschdienst (DAAD). The research for this thesis has made use of NASA's Astrophysics Data System Abstract Service.

Appendices

Appendix A

AIPS Runfiles

The data reduction pipeline described in Chapter 6 and Figure 6.6 was standardized using a series of AIPS runfiles. Here I present the annotated scripts which were used for the 2012 March epoch of observations for the results in Chapter 7. Lines starting with the * character are comments which are ignored by AIPS.

```
*** Runfile: Q1_LOAD.0BQ
*** This is a preliminary runfile to load the data into AIPS.
*** Before running the command "run Q_LOAD", make sure that the raw data
*** files are in the listed directory in 'fitld'.
*** v255q observed 7th March 2012. AIPS user 502.

* For ICRF dataset 4 IFs at 16-MHz bandwidth: 0, 16, 342 and 358 MHz.
* IFs 1 & 2 are observed in stokes RR and 3 & 4 in LL.
* For LINE dataset 1 IF at 2-MHz bandwidth:
* (start: 0 Hz, step: 976.56 Hz, count: 2048) LL and RR.
* For CONT dataset 2 IFs at 16-MHz bandwidth:
* 0, 16 (start: 0 Hz, step: 0.5 MHz, count: 32) LL and RR.

*=====================================================================
*       Load the data.
*
task 'fitld'
     default
     outclass   'uvdata'
     outseq      1
     outdisk     1
     douvcomp    1
     digicor     1
     timerang    0

     datain     'V255Q.ICRF.FITS
```

```
     outname    'v255q_icrf'
     go ; wait

     datain     'V255Q.CAL.FITS
     outname    'v255q_cont'
     go ; wait

     datain     'V255Q.LINE2.FITS
     outname    'v255q_line2'
     go ; wait

recat

*=====================================================================
*       Save tables of loaded data.
*
task 'tasav'
     default
     inname     'v255q_cont' ; inclass  'uvdata' ; inseq  1 ; indisk 1
     outname    'v255q_cont' ; outclass 'tasav'  ; outseq 1 ; outdisk 1

     go ; wait

     inname     'v255q_line2' ; inclass  'uvdata' ; inseq  1 ; indisk 1
     outname    'v255q_line2' ; outclass 'tasav'  ; outseq 1 ; outdisk 1

     go ; wait
```

```
*** Runfile: Q2_FLAG.0BQ
*** Flags are applied here.
*** v255q observed 7th March 2012. AIPS user 502.

*=====================================================================
*       Flag each antenna when it is off source using the automatic flags
*       generated by each antenna.
*
task 'uvflg'
     default
     inname 'v255q_icrf' ; inclass 'uvdata' ; inseq 1 ; indisk 1
     intext 'v255qho.uvflg
     go ; wait
     intext 'v255qcd.uvflg
     go ; wait
     intext 'v255qpk.uvflg
     go ; wait
     intext 'v255qmp.uvflg
     go ; wait

     default
     inname 'v255q_cont' ; inclass 'uvdata' ; inseq 1 ; indisk 1
     intext 'v255qho.uvflg
     go ; wait
     intext 'v255qcd.uvflg
     go ; wait
     intext 'v255qpk.uvflg
     go ; wait
     intext 'v255qmp.uvflg
     go ; wait

     default
     inname 'v255q_line2' ; inclass 'uvdata' ; inseq 1 ; indisk 1
     intext 'v255qho.uvflg
     go ; wait
     intext 'v255qcd.uvflg
     go ; wait
     intext 'v255qpk.uvflg
     go ; wait
     intext 'v255qmp.uvflg
     go ; wait
```

```
*** Runfile: Q3_ICRF.0BQ
*** Geodetic block preparation.
*** v255q observed 7th March 2012. AIPS user 502.

*=====================================================================
*       Correct for the ionosphere.
*       CL2 created.
*       WARNING: The following commands need to be issued by hand.

*    restore 0
*    run newparms
*    run vlbautil
*    inname 'v255q_icrf' ; inclass 'uvdata' ; inseq 1 ; indisk 1
*    vlbatecr

*=====================================================================
*       Correct the data for latest EOP values.
*       CL3 created.
*
task 'clcor'
     default
     inname     'v255q_icrf' ; inclass 'uvdata' ; inseq 1 ; indisk 1
     gainver     2
     gainuse     3
     opcode     'eops'

*    Following file needs to be obtained from:
*    http://gemini.gsfc.nasa.gov/solve_save/usno_finals.erp
*    Do not use an old copy as the latest values are needed.

     infile     'usno_finals.erp

     go ; wait

*=====================================================================
*       Make a copy of the flag tables to flag out IF 3 & 4 (LL)
*       polarization.
*       FG1 --> FG2
*
task 'tacop'
     default
     inname     'v255q_icrf' ; inclass  'uvdata' ; inseq  1 ; indisk 1
```

```
     outname    'v255q_icrf' ; outclass 'uvdata' ; outseq 1 ; outdisk 1
     inext      'fg'
     invers      1
     outvers     2
     ncount      1

     go ; wait

*=============================================================================
*       Now do the flagging of the IFs 3 & 4 as FRING is having
*       difficulty finding a "manual" phase cal solution on these two IFs
*       based on LL polarization.
*
task 'uvflg'
     default
     inname     'v255q_icrf' ; inclass 'uvdata' ; inseq 1 ; indisk 1
     bif         3
     eif         4
     opcode     'flag'
     outfgver    2

     go ; wait

*=============================================================================
*       "Manual" phase calibration on ICRF source in 5th block.
*       CL3 to create SN1.
*
task 'fring'
     default
     inname     'v255q_icrf' ; inclass 'uvdata' ; inseq 1 ; indisk 1
     flagver     1
     docalib     1
     gainuse     3
     snver       0
     solint      2
     aparm       0
*    aparm(6) is print level
     aparm(6)    3
*    Don't solve for fringe rates. zero RATES: YES, zero DELAYS: NO,
*    zero PHASE: NO
     dparm(8)    1
     dparm(1)    1
*                              ************************
```

```
*                               *
                                CALSOUR   ''1349-439''
                                TIMER      0 21 35 15 0 21 36 15
                                REFANT     2
*                               *
*                               ************************
     go ; wait

*=========================================================================
*       Apply the solution.
*       SN1 + CL3 --> CL4.
*
task 'clcal'
     default
     inname     'v255q_icrf' ; inclass 'uvdata' ; inseq 1 ; indisk 1
     snver       1
     inver       1
     gainver     3
     gainuse     4

     go ; wait

*=========================================================================
*       Now do the multiband delay by including all the ICRF sources.
*       CL4 to create SN2.
*
task 'fring'
     default
     inname     'v255q_icrf' ; inclass 'uvdata' ; inseq 1 ; indisk 1
     flagver     1
     docalib     1
     gainuse     4
     solint      2

*     FRING parms from definitions_bessel_current.py:
*     fringe.aparm[1:]   = [2, 0, 0, 0, 1]
*     fringe.dparm[1:]   = [1, 20, 50, 0]
*     fringe.dparm[4]    = 0
*     fringe.dparm[8]    = 0

     aparm(1)    2
     aparm(4)    0
     aparm(5)    1
```

```
     aparm(6)    2
     snver       0
     dparm       0
     dparm(1)    1
     dparm(2)    20
     dparm(3)    50
     refant      2
*                              ************************
*                              *
*                              Exclude the "manual" phase calibrator
                               CALSOUR    ’-1349-439’’
*                              *
*                              ************************
     go ; wait

*=============================================================================
*       Now print out the sources and rates to fit with Mark’s
*       fit_geoblocks.f script.
*
task ’prtab’
     default
     inname     ’v255q_icrf’ ; inclass ’uvdata’ ; inseq 1 ; indisk 1
     inext      ’sn’
     invers      0
     docrt      -1
     ndig        1
     box         1 3 4 9 13 15
     dohms      -1
     outprint   ’2012MAR08_RATE_MDEL.DAT’

     go ; wait

     inext      ’su’
     box         1 2 11 12 13 14 15
     outprint   ’2012MAR08_SU_TABLE.PRTAB’

     go ; wait
```

```
*** Runfile: Q4_CONT.0BQ
*** Apply various preliminary as well as position shifts.
*** v255q observed 7th March 2012. AIPS user 502.

*=====================================================================
*       Correct for CONT source position.
*       CL2 created.
*
task 'clcor'
     default
     inname     'v255q_cont' ; inclass 'uvdata' ; inseq 1 ; indisk 1
     gainver     1
     gainuse     2
     opcode     'antp'

*    The corrections to be added to the source position at the picture
*    plane are given in sec of arc as CLCORPRM(5) for RA direction and
*    as CLCORPRM(6) for declination. OPCODE 'ANTP' adds the corrections
*    to the apparent positions and recomputes the positions of epoch,
*    'ANTC' does the reverse.
*                                ************************
*                                *
                                 SOURCE        'J1706-4600''
                                 CLCORPRM(5) =  0.031
                                 CLCORPRM(6) = -0.026
*                                *
*                                ************************
     go ; wait

     gainver     2
     gainuse     2

*    The maser is correlated to the CONT resolution, and not used for
*    astrometry. Position shift applied for consistency.

*                                ************************
*                                *
                                 SOURCE        'G339.884-1.2''
                                 CLCORPRM(5) = -0.021
                                 CLCORPRM(6) = -0.023
*                                *
v*                                ************************
```

```
     go ; wait

*=====================================================================
*       Correct for feed rotation effects.
*       CL3 created.
*
task 'clcor'
     default
     inname     'v255q_cont' ; inclass 'uvdata' ; inseq 1 ; indisk 1
     gainver     2
     gainuse     3
     opcode     'pang'

*    'PANG' => Add or remove parallactic angle
*    corrections from CL table entries.
*    CLCORPRM(1) >  0 => Add corrections
*    CLCORPRM(1) =< 0 => Remove corrections

     clcorprm    1 0

     go ; wait

*=====================================================================
*       Correct for zenith atmospheric delays.
*       CL4 created.
*
task 'clcor'
     default
     inname     'v255q_cont' ; inclass 'uvdata' ; inseq 1 ; indisk 1
     gainver     3
     gainuse     4
     opcode     'atmo'

*    CLCORPRM(1): Correction to make to the CL table.
*    0 => only atmosphere
*    1 => atmosphere + clocks

     clcorprm    1 0

*    ATMOS.FITS contains zenith delays, clock drifts and clock rates,
*    produced using M. Reid's fit_geoblocks.f script.

     infile     'V255Q_AT.FITS'
```

```
     go ; wait

*=====================================================================
*       Correct the data for latest EOP values.
*       CL5 created.
*
task 'clcor'
     default
     inname     'v255q_cont' ; inclass 'uvdata' ; inseq 1 ; indisk 1
     gainver     4
     gainuse     5
     opcode     'eops'

*    Following file needs to be obtained from:
*    http://gemini.gsfc.nasa.gov/solve_save/usno_finals.erp
*    Do not use an old copy as the latest values are needed.

     infile     'usno_finals.erp

     go ; wait

*=====================================================================
*       Correct for the ionosphere.
*       CL6 created.
*       WARNING: The following commands need to be issued by hand.

*    restore 0
*    run newparms
*    run vlbautil
*    inname 'v255q_cont' ; inclass 'uvdata' ; inseq 1 ; indisk 1
*    vlbatecr
```

```
*** Runfile: Q5_LINE2.0BQ
*** Apply various preliminary corrections as well as position shifts.
*** v255q observed 7th March 2012. AIPS user 502.

*=====================================================================
*       Correct for LINE2 source position.
*       CL2 created.
*
task 'clcor'
     default
     inname     'v255q_line2' ; inclass 'uvdata' ; inseq 1 ; indisk 1
     gainver     1
     gainuse     2
     opcode     'antp'

*    The corrections to be added to the source position at the picture
*    plane are given in sec of arc as CLCORPRM(5) for RA direction and
*    as CLCORPRM(6) for declination. OPCODE 'ANTP' adds the corrections
*    to the apparent positions and recomputes the positions of epoch,
*    'ANTC' does the reverse.
*                               ************************
*                               *
                                SOURCE        'G339.884-1.2''
                                CLCORPRM(5) = -0.021
                                CLCORPRM(6) = -0.023
*                               *
*                               ************************
     go ; wait


*=====================================================================
*       Correct for feed rotation effects.
*       CL3 created.
*
task 'clcor'
     default
     inname     'v255q_line2' ; inclass 'uvdata' ; inseq 1 ; indisk 1
     gainver     2
     gainuse     3
     opcode     'pang'

*    'PANG' => Add or remove parallactic angle
```

```
*    corrections from CL table entries.
*    CLCORPRM(1) >  0 => Add corrections
*    CLCORPRM(1) =< 0 => Remove corrections

     clcorprm    1 0

     go ; wait

*=======================================================================
*       Correct for zenith atmospheric delays.
*       CL4 created.
*
task 'clcor'
     default
     inname     'v255q_line2' ; inclass 'uvdata' ; inseq 1 ; indisk 1
     gainver     3
     gainuse     4
     opcode     'atmo'

*    CLCORPRM(1): Correction to make to the CL table.
*    0 => only atmosphere
*    1 => atmosphere + clocks

     clcorprm    1 0

*    ATMOS.FITS contains zenith delays, clock drifts and clock rates,
*    produced using M. Reid's fit_geoblocks.f script.

     infile     'V255Q_AT.FITS'

     go ; wait

*=======================================================================
*       Correct the data for latest EOP values.
*       CL5 created.
*
task 'clcor'
     default
     inname     'v255q_line2' ; inclass 'uvdata' ; inseq 1 ; indisk 1
     gainver     4
     gainuse     5
     opcode     'eops'
```

```
*    Following file needs to be obtained from:
*    http://gemini.gsfc.nasa.gov/solve_save/usno_finals.erp
*    Do not use an old copy as the latest values are needed.

     infile     'usno_finals.erp

     go ; wait

*=====================================================================
*       Correct for the ionosphere.
*       CL6 created.
*       WARNING: The following commands need to be issued by hand.

*    inname 'v255q_line2' ; inclass 'uvdata' ; inseq 1 ; indisk 1
*    vlbatecr
```

```
*** Runfile: Q6_CVEL.0BQ
*** Channel velocity calibration.
*** v255q observed 7th March 2012. AIPS user 502.

*=====================================================================
*       Set the velocity channel information.
*
task 'setjy'
     default
     inname     'v255q_line2' ; inclass 'uvdata' ; inseq 1 ; indisk 1
     veltyp     'lsr'
     veldef     'radio'

*    The rest frequency is taken to be RESTFREQ(1) + RESTFREQ(2) with
*    both values converted to double precision before adding.  For
*    example, the frequency 1420.405752E6 is too precise for a single
*    adverb.  However, RESTFREQ = 1420.4E6, 5752. will convey the
*    desired value correctly.

     restfreq    6668e6 519.2e3
*                               ************************
*                               *
                                APARM(1)         1025
                                SYSVEL  =       -21.5
*                               *
*                               ************************
     go ; wait

*=====================================================================
*       Shift spectrum to correct for Doppler effects.
*       All CL tables propagated into new dataset.
*       LINE2 ; seq 2 created. CL6 retained.
*
task 'cvel'
     default
     inname     'v255q_line2' ; inclass  'uvdata' ; inseq  1 ; indisk 1
     outname    'v255q_line2' ; outclass 'uvdata' ; outseq 2 ; outdisk 1
     doband     -1
     freqid      1
     aparm(10)   1
     flagver     1
     gainuse     6
```

```
*                              ************************
*                              *
*                              vpk = -38.7 km/s (MMB) verified in POSSM
                               SOURCE 'G339.884-1.2''
*                              *
*                              ************************
     go ; wait
```

```
*** Runfile: Q7_AMP.0BQ
*** Amplitude calibration is done by fitting a split maser spectrum to
*** the LINE2 dataset and applying some scaling. The scaling factor is
*** transferred to the CONT dataset. A couple of mock SN tables need
*** to be created in the CONT dataset to ensure that SN table
*** propagation is consistent with the LINE2 SN table propagation.
*** v255q observed 7th March 2012. AIPS user 502.

*=====================================================================
*       Run ACCOR.
*       SN1 created here for both LINE2 ; seq 2 and CONT.
*
task 'accor'
     default
     inname     'v255q_line2' ; inclass 'uvdata' ; inseq 2 ; indisk 1
     solint      4

     go ; wait

     inname     'v255q_cont'  ; inclass 'uvdata' ; inseq 1 ; indisk 1

     go ; wait

*=====================================================================
*       Apply the ACCOR corrections to LINE2 ; seq 2 and CONT.
*       SN1 + CL6 --> CL7.
*
task 'clcal'
     default
     inname     'v255q_line2' ; inclass 'uvdata' ; inseq 2 ; indisk 1
     gainver     6
     gainuse     7
     snver       1
     invers      1

     go ; wait

     inname     'v255q_cont'  ; inclass 'uvdata' ; inseq 1 ; indisk 1

     go ; wait

*=====================================================================
```

```
*       Input the SEFD values for each antenna independently for
*       LINE2 ; seq 2 and CONT datasets.
*       CL7 --> CL8.
*
task 'clcor'
     default
     inname     'v255q_line2' ; inclass 'uvdata' ; inseq 2 ; indisk 1
     opcode     'gain'
     gainver     7
     gainuse     8

*    ATCA
     antenna     1
     clcorprm(1) = 11.83
     go ; wait

     gainver     8

*    Ceduna
     antenna     2
     clcorprm(1) = 23.45
     go ; wait

*    Hobart
     antenna     3
     clcorprm(1) = 26.46
     go ; wait

*    Mopra
     antenna     4
     clcorprm(1) = 24.50
     go ; wait

*    Parkes
     antenna     5
     clcorprm(1) = 10.49
     go ; wait

     default

     inname     'v255q_cont'  ; inclass 'uvdata' ; inseq 1 ; indisk 1
     opcode     'gain'
     gainver     7
```

```
     gainuse     8

*    ATCA
     antenna     1
     clcorprm(1) = 11.83
     go ; wait

     gainver     8

*    Ceduna
     antenna     2
     clcorprm(1) = 23.45
     go ; wait

*    Hobart
     antenna     3
     clcorprm(1) = 26.46
     go ; wait

*    Mopra
     antenna     4
     clcorprm(1) = 24.50
     go ; wait

*    Parkes
     antenna     5
     clcorprm(1) = 10.49
     go ; wait

*=======================================================================
*       Split off a single scan of maser data for a template spectrum.
*
task 'split'
     default
     inname     'v255q_line2' ; inclass 'uvdata' ; inseq 2 ; indisk 1
     docalib     1
     doband     -1
*    aparm(5) = 2 => pass only autocorrelation spectra
     aparm       0 0 0 0 2 0
     flagver     1
     gainuse     8
*                               ************************
*                               *
```

```
                                SOURCE  'G339.884-1.2''
                                TIMER    0 18 10 0 0 18 15 0
*                               *
*                               ************************
     go ; wait

*=======================================================================
*       Now perform amplitude calibration.
*       CL8 to create SN2.
*
task 'acfit'
     default
     inname     'v255q_line2' ; inclass 'uvdata' ; inseq 2 ; indisk 1
     in2class   'split' ; in2seq 1 ; in2disk 1
     gainuse     8
     docalib     1
     doband     -1
     solint      3
     snver       0
     bchan       1250
     echan       1450

*    aparms 1 & 2 => Order of polynomial baseline
*    aparms 3 & 4 => Sensitivity of template antenna Jy/K
*    aparms 5 & 6 => minimum & maximum gains allowed
*    aparm  7 => maximum allowed gain error
*    aparm  8 => print level
*    aparm  9 = 0 => fits done after baseline subtraction
*    aparm 10 = => don't write baseline subtracted spectra to file

     aparm       1 1 0 0 0 10 0 3 0

*    pairs of baseline channels in the source spectra

     bparm       500 1000 1500 2000

*    pairs of baseline channels in the template spectra

     cparm       500 1000 1500 2000

*    The Tsys (in K) of the template antenna polarizations
*    setting these to values other than 0 seems to scale the
*    output by this factor.
```

```
*                               ************************
*                               *
                                XPARM     0
                                YPARM     0
                                IN2NAME  'G339.884-1.2'
                                CALSOUR  'G339.884-1.2''
                                REFANT    5
*                               *
*                               ************************
     go ; wait

*=====================================================================
*       Apply some smoothing.
*       First median window filter out outliers: SN2 to create SN3.
*       Then apply a 30 min boxcar: SN3 to create SN4.
*
task 'snsmo'
     default
     inname     'v255q_line2' ; inclass 'uvdata' ; inseq 2 ; indisk 1
     samptype   'mwf'
     bparm       0.25 0
     smotype    'ampl'
     doblank    -1
     invers      2
     outvers     0
*                               ************************
*                               *
                                REFANT   5
*                               *
*                               ************************
     go ; wait

     samptype   'box'
     bparm       0.5 0
     invers      3

     go ; wait

*=====================================================================
*       Apply the amplitude calibration to LINE2 ; seq 2 dataset.
*       SN4 + CL8 --> CL9.
*
task 'clcal'
```

```
     default
     inname     'v255q_line2' ; inclass 'uvdata' ; inseq 2 ; indisk 1
     gainver     8
     gainuse     9
     snver       4
     invers      4

     go ; wait

*=====================================================================
*       Copy amplitude calibration over to CONT dataset.
*       SN4 in LINE2 ; seq 2 --> SN2 in CONT.
*
task 'sncop'
     default
     inname     'v255q_line2' ; inclass  'uvdata' ; inseq  2 ; indisk 1
     outname    'v255q_cont'  ; outclass 'uvdata' ; outseq 1 ; outdisk 1
     inext      'sn'
     invers      4
     box         1 1

     go ; wait

*=====================================================================
*       Apply the amplitude calibration to CONT dataset.
*       SN2 + CL8 --> CL9.
*
task 'clcal'
     default
     inname     'v255q_cont' ; inclass 'uvdata' ; inseq 1 ; indisk 1
     gainver     8
     gainuse     9
     snver       2
     invers      2

     go ; wait


*=====================================================================
*      Create mock SN tables in CONT to align tables with LINE2 ; seq 2.
*      SN2 --> SN3 --> SN4.
*
task 'tacop'
```

```
default
inname     'v255q_cont' ; inclass  'uvdata' ; inseq  1 ; indisk 1
inext      'sn'
invers      2
outname    'v255q_cont' ; outclass 'uvdata' ; outseq 1 ; outdisk 1
outvers     3

go ; wait

invers      3
outvers     4

go ; wait
```

```
*** Runfile: Q8_PHAS.0BQ
*** Now do "manual" phase calibration.
*** Phase calibration is done N times based on N number of ICRF runs
*** before each phase-referenced observation.
*** v255q observed 7th March 2012. AIPS user 502.

*=====================================================================
*       "Manual" phase calibration.
*       CL9 to create SN5.
*
task 'fring'
     default
     inname     'v255q_cont' ; inclass 'uvdata' ; inseq 1 ; indisk 1
     flagver     1
     docalib     1
     gainuse     9
     snver       0
     solint      2
     aparm       0
*    aparm(6) is print level
     aparm(6)    3
*    Don't solve for fringe rates. zero RATES: YES, zero DELAYS: NO,
*    zero PHASE: NO
     dparm(8)    1
     dparm(1)    1
*                               ************************
*                               *
                                SOURCE  'J1706-4600''
                                TIMER    0 15 25 45 0 15 27 0
                                REFANT   1
*                               *
*                               ************************
     go ; wait

*=====================================================================
*       "Manual" phase calibration.
*       CL9 to create SN6.
*
task 'fring'
     default
     inname     'v255q_cont' ; inclass 'uvdata' ; inseq 1 ; indisk 1
     flagver     1
```

```
     docalib     1
     gainuse     9
     snver       0
     solint      3
     aparm       0
*    aparm(6) is print level
     aparm(6)    3
*    Don't solve for fringe rates. zero RATES: YES, zero DELAYS: NO,
*    zero PHASE: NO
     dparm(8)    1
     dparm(1)    1
*                              ************************
*                              *
                               SOURCE  'J1706-4600''
                               TIMER    0 16 42 45 0 16 45 0
                               REFANT   1
*                              *
*                              ************************
     go ; wait

*=========================================================================
*       "Manual" phase calibration.
*       CL9 to create SN7.
*
task 'fring'
     default
     inname     'v255q_cont' ; inclass 'uvdata' ; inseq 1 ; indisk 1
     flagver     1
     docalib     1
     gainuse     9
     snver       0
     solint      2
     aparm       0
*    aparm(6) is print level
     aparm(6)    3
*    Don't solve for fringe rates. zero RATES: YES, zero DELAYS: NO,
*    zero PHASE: NO
     dparm(8)    1
     dparm(1)    1
*                              ************************
*                              *
                               SOURCE  'J1706-4600''
                               TIMER    0 18 24 45 0 18 26 0
```

```
                                REFANT   1
*                               *
*                               ************************
     go ; wait

*=======================================================================
*       "Manual" phase calibration.
*       CL9 to create SN8.
*
task 'fring'
     default
     inname     'v255q_cont' ; inclass 'uvdata' ; inseq 1 ; indisk 1
     flagver     1
     docalib     1
     gainuse     9
     snver       0
     solint      2
     aparm       0
*    aparm(6) is print level
     aparm(6)    3
*    Don't solve for fringe rates. zero RATES: YES, zero DELAYS: NO,
*    zero PHASE: NO
     dparm(8)    1
     dparm(1)    1
*                               ************************
*                               *
                                SOURCE  'J1706-4600''
                                TIMER    0 20 10 50 0 20 12 0
                                REFANT   1
*                               *
*                               ************************
     go ; wait

*=======================================================================
*       Apply the solution for CONT between 4th, 5th and 6th ICRF blocks.
*       SN5 + SN6 + SN7 + SN8 + CL9 --> CL10.
*       NOTE: I've checked the POSSM plots for this method of processing
*       multiple SN tables in a single CLCAL step. The phases are at
*       intercept = slope = 0 at the particular timeranges of the
*       "manual" phase cal source observations.
*
task 'clcal'
     default
```

```
     inname     'v255q_cont' ; inclass 'uvdata' ; inseq 1 ; indisk 1
     snver       5
     inver       8
     gainver     9
     gainuse     10

     go ; wait

*=======================================================================
*       Make a copy of the LINE2 ; seq 2 dataset and
*       call it LINE2 ; seq 3.
*
task 'uvcop'
     default
     inname     'v255q_line2' ; inclass  'uvdata' ; inseq  2 ; indisk 1
     outname    'v255q_line2' ; outclass 'uvdata' ; outseq 3 ; outdisk 1

*                               ************************
*                               *
                                TIMER   0 13 0 0 0 21 0 0
*                               *
*                               ************************
     go ; wait

*=======================================================================
*
*       Edit the frequency channel width and bandpass width information
*       in LINE2 ; seq 3.
*
task 'tabed'
     default
     inname     'v255q_line2' ; inclass  'uvdata' ; inseq  3 ; indisk 1
     outname    'v255q_line2' ; outclass 'uvdata' ; outseq 3 ; outdisk 1
     inext      'fq'
     invers      1
     optype     'REPL'
*    Column 3 parameter is channel width
     aparm(1)    3
*                               ************************
*                               *
*                               * G339.884-1.259, -35.6 km/s feature
                                KEYVALUE   9.142858E+03 0
*                               *
```

```
*                               ************************
     go ; wait

*    Column 4 parameter is total bandwidth
     aparm(1)   4
     keyvalue   1.6e7 0

     go ; wait

*=====================================================================
*       Copy "manual" phase calibration solutions from CONT over to
*       LINE2 ; seq 3 dataset.
*       SN5/6/7/8 in CONT --> SN5/6/7/8 in LINE2 ; seq 3.
*
task 'sncop'
     default
     inname     'v255q_cont'  ; inclass  'uvdata' ; inseq  1 ; indisk 1
     outname    'v255q_line2' ; outclass 'uvdata' ; outseq 3 ; outdisk 1
     inext      'sn'
     invers      5
*    Only copy solutions from 2nd IF which is shared with LINE2 ; seq 3.
     box         2 2

     go ; wait

     invers      6

     go ; wait

     invers      7

     go ; wait

     invers      8

     go ; wait

*=====================================================================
*       Apply the solution for LINE2 ; seq 3, between the relevant
*       ICRF blocks using the updated FQ table.
*       FQ1 + SN5 + SN6 + CL9 --> CL10.
*
task 'clcal'
```

```
default
inname     'v255q_line2' ; inclass 'uvdata' ; inseq 3 ; indisk 1
snver       5
inver       8
gainver     9
gainuse     10

go ; wait
```

```
*** Runfile: Q9_PR.0BQ
*** Now there is a need to fringe fit on the maser channel in LINE2 ;
*** seq 3 and transfer the solutions to the CONT dataset.
*** v255q observed 7th March 2012. AIPS user 502.

*=====================================================================
*       Fringe fit on the maser peak channel of choice in the
*       LINE2 ; seq 3 dataset.
*       CL10 to create SN9.
*
task 'fring'
     default
     inname     'v255q_line2' ; inclass 'uvdata' ; inseq 3 ; indisk 1
     docalib     1
     gainuse     10
     aparm       2 0
     snver       0
*    dparm(4)=2 is 2 seconds as the correlator
     dparm       1 0 0 2 0
     dparm(2)=  -1
     flagver     1
*    M. Reid doubles the solint from the phase-referenced observations.
     solint      3
*    aparm(6) = print level
     aparm(6)    3
*                               ************************
*                               *
                                CALSOUR  'G339.884-1.2''
                                BCHAN     1347
                                ECHAN     1347
                                REFANT    2
*                               *
*                               ************************
      go ; wait

*=====================================================================
*       Apply the solution to LINE2 ; seq 3.
*       SN9 + CL10 --> CL11.
*
task 'clcal'
     default
     inname     'v255q_line2' ; inclass 'uvdata' ; inseq 3 ; indisk 1
```

```
     snver       9
     inver       9
     gainver     10
     gainuse     11

     go ; wait

*=====================================================================
*       Copy phase calibration from LINE2 ; seq 3 over to CONT dataset.
*       SN9 in LINE2 ; seq 3 --> SN9 in CONT.
*
task 'sncop'
     default
     inname     'v255q_line2' ; inclass  'uvdata' ; inseq  3 ; indisk 1
     outname    'v255q_cont'  ; outclass 'uvdata' ; outseq 1 ; outdisk 1
     inext      'sn'
     invers      9
*    Only copy solutions from 1st IF as this is shared with CONT.
     box         1 1

     go ; wait

*=====================================================================
*       Apply the solution to CONT.
*       SN9 + CL10 --> CL11.
*
task 'clcal'
     default
     inname     'v255q_cont' ; inclass 'uvdata' ; inseq 1 ; indisk 1
     snver       9
     inver       9
     gainver     10
     gainuse     11

     go ; wait
```

```
*** Runfile: Q_J1706.0BQ
*** Runfile to image the background QSO after phase-referencing.
*** v255q observed 7th March 2012. AIPS user 502.

*=====================================================================
*       Flag some poor data
*
task 'tacop'
     default
     inname     'v255q_cont' ; inclass  'uvdata' ; inseq  1 ; indisk 1
     outname    'v255q_cont' ; outclass 'uvdata' ; outseq 1 ; outdisk 1
     inext      'fg'
     invers      1
     outvers     2

     go ; wait

task 'uvflg'
     default
     inname     'v255q_cont' ; inclass 'uvdata' ; inseq 1 ; indisk 1
     outfgver    2
     opcode     'flag'
*                               ************************
*                               *
                                TIMER   0 0 0 0 0 15 0 0
*                               *
*                               ************************
     go ; wait
*                               ************************
*                               *
                                TIMER   0 17 0 0 0 18 0 0
*                               *
*                               ************************
     go ; wait

     antenna     5
     baseline    0

*                               ************************
*                               *
                                TIMER   0 19 0 0 0 19 30 0
*                               *
```

```
*                               ************************
     go ; wait

*=====================================================================
*       Split the background source from CONT to average all
*       frequencies before imaging.
*       The timerange is chosen to limit imaging to when the "manual"
*       phase calibration solution is valid (i.e. in between adjacent
*       ICRF block observations from when calibration was performed).
*
task 'split'
     default
     inname     'v255q_cont' ; inclass 'uvdata' ; inseq 1 ; indisk 1
     gainuse     11
     docalib     1
     doband     -1
     flagver     2

*    aparm(1) = 2 => average freqs in IF

     aparm       2 0
     bif         2
     eif         2

*                               ************************
*                               *
                                SOURCE          'J1706-4600''
*                               *
*                               ************************
     go ; wait

*=====================================================================
*
*       Image
*
task 'imagr'
     default
     inname     'J1706-4600' ; inclass 'split' ; inseq 1 ; indisk 1
     nfield      1
     dotv       -1

     nfield      1
     dotv       -1
```

```
     stokes     'i'

*    UVWTFN   = 'CS' => take 1 / square root of weight_in
*    UVWTFN   = 'CV' => take 1 / fourth root of weight_in
     uvwtfn     'cv'
*                              ************************
*                              *
                               ANTEN           1 2 4 5
                               BASELINE        ANTEN
                               NITER           1000
                               CELLSIZE        0.0003
                               IMSIZE          2048
                               MINPATCH        201
                               GAIN            0.1
                               ROBUST          2
*                              *
*                              ************************
     go ; wait
```

Bibliography

Ade, P. A. R., Aghanim, N., Alves, M. I. R., et al. 2014, A&A, 571, A13

Amigo, P., Stetson, P. B., Catelan, M., Zoccali, M., & Smith, H. A. 2013, AJ, 146, 130

An, D., Terndrup, D. M., & Pinsonneault, M. H. 2007a, ApJ, 671, 1640

An, D., Terndrup, D. M., Pinsonneault, M. H., et al. 2007b, ApJ, 655, 233

Anderson, L. D., Bania, T. M., Balser, D. S., et al. 2014, ApJS, 212, 1

Anderson, L. D., Bania, T. M., Balser, D. S., & Rood, R. T. 2011, ApJS, 194, 32

Araya, E., Hofner, P., Churchwell, E., & Kurtz, S. 2002, ApJS, 138, 63

Argon, A. L., Reid, M. J., & Menten, K. M. 2000, ApJS, 129, 159

Arthur, S. J., & Hoare, M. G. 2006, ApJS, 165, 283

Asaki, Y., Deguchi, S., Imai, H., et al. 2010, ApJ, 721, 267

Asaki, Y., Imai, H., Sobolev, A. M., & Parfenov, S. Y. 2014, ApJ, 787, 54

Asaki, Y., Sudou, H., Kono, Y., et al. 2007, PASJ, 59, 397

Bania, T. M., Anderson, L. D., Balser, D. S., & Rood, R. T. 2010, ApJ, 718, L106

Barrett, A. H., Schwartz, P. R., & Waters, J. W. 1971, ApJ, 168, L101

Bartkiewicz, A., Sanna, A., Szymczak, M., & Moscadelli, L. 2014, in Proceedings of the 12th European VLBI Network Symposium and Users Meeting (EVN 2014). 7-10 October 2014. Cagliari, Italy., 39

Bartkiewicz, A., Szymczak, M., van Langevelde, H. J., Richards, A. M. S., & Pihlström, Y. M. 2009, A&A, 502, 155

Batchelor, R. A., Caswell, J. L., Haynes, R. F., et al. 1980, Australian Journal of Physics, 33, 139

Batrla, W., Matthews, H. E., Menten, K. M., & Walmsley, C. M. 1987, Nat, 326, 49

Battersby, C., Ginsburg, A., Bally, J., et al. 2014, ApJ, 787, 113

Beasley, A. J., & Conway, J. E. 1995, in Astronomical Society of the Pacific Conference Series, Vol. 82, Very Long Baseline Interferometry and the VLBA, ed. J. A. Zensus, P. J. Diamond, & P. J. Napier, 327

Beltrán, M. T., Cesaroni, R., Neri, R., & Codella, C. 2011, A&A, 525, A151

Beltrán, M. T., Sánchez-Monge, Á., Cesaroni, R., et al. 2014, A&A, 571, A52

Benedict, G. F., McArthur, B. E., Feast, M. W., et al. 2007, AJ, 133, 1810

Benjamin, R. A., Churchwell, E., Babler, B. L., et al. 2003, PASP, 115, 953

Bernasconi, P. A., & Maeder, A. 1996, A&A, 307, 829

Beuther, H., Linz, H., & Henning, T. 2013a, A&A, 558, A81

Beuther, H., Schilke, P., Menten, K. M., et al. 2002, ApJ, 566, 945

Beuther, H., Linz, H., Tackenberg, J., et al. 2013b, A&A, 553, A115

Bird, J. C., Stanek, K. Z., & Prieto, J. L. 2009, ApJ, 695, 874

Boehm, J., Niell, A., Tregoning, P., & Schuh, H. 2006, GeoRL, 33, 7304

Bondi, H., & Hoyle, F. 1944, MNRAS, 104, 273

Bonnell, I. A., & Bate, M. R. 2006, MNRAS, 370, 488

Bonnell, I. A., Bate, M. R., Clarke, C. J., & Pringle, J. E. 1997, MNRAS, 285, 201

—. 2001, MNRAS, 323, 785

Bonnell, I. A., Bate, M. R., & Zinnecker, H. 1998, MNRAS, 298, 93

Bourke, T. L., Myers, P. C., Robinson, G., & Hyland, A. R. 2001, ApJ, 554, 916

Bovy, J., Allende Prieto, C., Beers, T. C., et al. 2012, ApJ, 759, 131

Braga, V. F., Dall'Ora, M., Bono, G., et al. 2015, ApJ, 799, 165

Brand, J. 2008, in Star Formation Across the Milky Way Galaxy, 20

Brand, J., & Blitz, L. 1993, A&A, 275, 67

Brand, J., Cesaroni, R., Comoretto, G., et al. 2003, A&A, 407, 573

Breen, S., Ellingsen, S., Caswell, J., et al. 2012a, MNRAS, 426, 2189

Breen, S. L., Caswell, J. L., Ellingsen, S. P., & Phillips, C. J. 2010a, MNRAS, 406, 1487

Breen, S. L., & Ellingsen, S. P. 2011, MNRAS, 416, 178

Breen, S. L., & Ellingsen, S. P. 2012, in IAU Symposium, Vol. 287, IAU Symposium, ed. R. S. Booth, W. H. T. Vlemmings, & E. M. L. Humphreys, 156–160

Breen, S. L., Ellingsen, S. P., Caswell, J. L., et al. 2011, ApJ, 733, 80

—. 2012b, MNRAS, 421, 1703

Breen, S. L., Ellingsen, S. P., Caswell, J. L., & Lewis, B. E. 2010b, MNRAS, 401, 2219

Breen, S. L., Ellingsen, S. P., Contreras, Y., et al. 2013, MNRAS, 435, 524

Breen, S. L., Ellingsen, S. P., Johnston-Hollitt, M., et al. 2007, MNRAS, 377, 491

Breen, S. L., Ellingsen, S. P., Caswell, J. L., et al. 2014, MNRAS, 438, 3368

Breen, S. L., Fuller, G. A., Caswell, J. L., et al. 2015, MNRAS, 450, 4109

Brisken, W. F. 2014, A Guide to the DiFX Software Correlator Version 2.2, Tech. rep., National Radio Astronomy Observatory

Brogan, C. L., Goss, W. M., Hunter, T. R., et al. 2013, ApJ, 771, 91

Bronfman, L., Nyman, L.-A., & May, J. 1996, A&AS, 115, 81

Brown, C., Dickey, J. M., Dawson, J. R., & McClure-Griffiths, N. M. 2014, ApJS, 211, 29

Brunthaler, A., Reid, M. J., Menten, K. M., et al. 2009, ApJ, 693, 424

—. 2011, Astronomische Nachrichten, 332, 461

Burton, W. B., Gordon, M. A., Bania, T. M., & Lockman, F. J. 1975, ApJ, 202, 30

Busfield, A. L., Purcell, C. R., Hoare, M. G., et al. 2006, MNRAS, 366, 1096

Cacciari, C. 2013, in IAU Symposium, Vol. 289, IAU Symposium, ed. R. de Grijs, 101–108

Cacciari, C., Corwin, T. M., & Carney, B. W. 2005, AJ, 129, 267

Calcutt, H., Viti, S., Codella, C., et al. 2014, MNRAS, 443, 3157

Carey, S. J., Feldman, P. A., Redman, R. O., et al. 2000, ApJ, 543, L157

Cassisi, S., Castellani, M., Caputo, F., & Castellani, V. 2004, A&A, 426, 641

Caswell, J. L. 1996, MNRAS, 279, 79

—. 1997, MNRAS, 289, 203

—. 1998, MNRAS, 297, 215

—. 2001, MNRAS, 326, 805

—. 2003, MNRAS, 341, 551

Caswell, J. L., Batchelor, R. A., Forster, J. R., & Wellington, K. J. 1983, Australian Journal of Physics, 36, 401

—. 1989, Australian Journal of Physics, 42, 331

Caswell, J. L., & Breen, S. L. 2010, MNRAS, 407, 2599

Caswell, J. L., Breen, S. L., & Ellingsen, S. P. 2011a, MNRAS, 410, 1283

Caswell, J. L., Green, J. A., & Phillips, C. J. 2013, MNRAS, 431, 1180

—. 2014, MNRAS, 439, 1680

Caswell, J. L., & Haynes, R. F. 1983, Australian Journal of Physics, 36, 361

—. 1987, A&A, 171, 261

Caswell, J. L., Kramer, B. H., & Reynolds, J. E. 2009, MNRAS, 398, 528

—. 2011b, MNRAS, 414, 1914

Caswell, J. L., Murray, J. D., Roger, R. S., Cole, D. J., & Cooke, D. J. 1975, A&A, 45, 239

Caswell, J. L., & Phillips, C. J. 2008, MNRAS, 386, 1521

Caswell, J. L., Vaile, R. A., Ellingsen, S. P., & Norris, R. P. 1995a, MNRAS, 274, 1126

Caswell, J. L., Vaile, R. A., Ellingsen, S. P., Whiteoak, J. B., & Norris, R. P. 1995b, MNRAS, 272, 96

Caswell, J. L., Vaile, R. A., & Forster, J. R. 1995c, MNRAS, 277, 210

Caswell, J. L., Yi, J., Booth, R. S., & Cragg, D. M. 2000, MNRAS, 313, 599

Caswell, J. L., Fuller, G. A., Green, J. A., et al. 2010, MNRAS, 404, 1029

—. 2011c, MNRAS, 417, 1964

Cesaroni, R. 2005, in IAU Symposium, Vol. 227, Massive Star Birth: A Crossroads of Astrophysics, ed. R. Cesaroni, M. Felli, E. Churchwell, & M. Walmsley, 59–69

Cesaroni, R., Hofner, P., Walmsley, C. M., & Churchwell, E. 1998, A&A, 331, 709

Cesaroni, R., Pestalozzi, M., Beltrán, M. T., et al. 2015, A&A, 579, A71

Chen, X., de Grijs, R., & Deng, L. 2015, MNRAS, 446, 1268

Chen, X., Ellingsen, S. P., & Shen, Z.-Q. 2009, MNRAS, 396, 1603

Chen, X., Ellingsen, S. P., Shen, Z.-Q., Titmarsh, A., & Gan, C.-G. 2011, ApJS, 196, 9

Cheung, A. C., Rank, D. M., Townes, C. H., Thornton, D. D., & Welch, W. J. 1969, Nat, 221, 626

Chibueze, J. O., Omodaka, T., Handa, T., et al. 2014, ApJ, 784, 114

Chiosi, C., Wood, P. R., & Capitanio, N. 1993, ApJS, 86, 541

Choi, M., Lee, J.-E., & Kang, M. 2012, ApJ, 747, 112

Choi, Y. K., Hachisuka, K., Reid, M. J., et al. 2014, ApJ, 790, 99

Choudhury, R., Schilke, P., Stéphan, G., et al. 2015, A&A, 575, A68

Churchwell, E. 2002, ARA&A, 40, 27

Clemens, D. P. 1985, ApJ, 295, 422

Clement, C. M., Muzzin, A., Dufton, Q., et al. 2001, AJ, 122, 2587

Clementini, G., Bragaglia, A., di Fabrizio, L., et al. 2002, in Astronomical Society of the Pacific Conference Series, Vol. 259, IAU Colloq. 185: Radial and Nonradial Pulsationsn as Probes of Stellar Physics, ed. C. Aerts, T. R. Bedding, & J. Christensen-Dalsgaard, 124

Cohen, R. E., Sarajedini, A., Kinemuchi, K., & Leiton, R. 2011, ApJ, 727, 9

Cohen, R. S., Cong, H., Dame, T. M., & Thaddeus, P. 1980, ApJ, 239, L53

Colom, P., Lekht, E. E., Pashchenko, M. I., & Rudnitskij, G. M. 2015, A&A, 575, A49

Comeron, F., & Torra, J. 1996, A&A, 314, 776

Cook, A. H. 1968, Nat, 220, 44

Cosmovici, C., Pluchino, S., Pogrebenko, S., et al. 2010, in European Planetary Science Congress 2010, 269

Cosmovici, C. B., Montebugnoli, S., Orfei, A., Pogrebenko, S., & Colom, P. 1996, P&SS, 44, 735

Cosmovici, C. B., Pluchino, S., Montebugnoli, S., & Pogrebenko, S. 2014, P&SS, 96, 22

Cotton, W. D. 1995, in Astronomical Society of the Pacific Conference Series, Vol. 82, Very Long Baseline Interferometry and the VLBA, ed. J. A. Zensus, P. J. Diamond, & P. J. Napier, 189

Cragg, D. M., Johns, K. P., Godfrey, P. D., & Brown, R. D. 1992, MNRAS, 259, 203

Cragg, D. M., Sobolev, A. M., Caswell, J. L., Ellingsen, S. P., & Godfrey, P. D. 2004, MNRAS, 351, 1327

Cragg, D. M., Sobolev, A. M., Ellingsen, S. P., et al. 2001, MNRAS, 323, 939

Cragg, D. M., Sobolev, A. M., & Godfrey, P. D. 2002, MNRAS, 331, 521

—. 2005, MNRAS, 360, 533

Crowther, P. A. 2007, ARA&A, 45, 177

Csengeri, T., Bontemps, S., Schneider, N., Motte, F., & Dib, S. 2011, A&A, 527, A135

Csengeri, T., Urquhart, J. S., Schuller, F., et al. 2014, A&A, 565, A75

Cyganowski, C. J., Brogan, C. L., Hunter, T. R., & Churchwell, E. 2009, ApJ, 702, 1615

—. 2011, ApJ, 743, 56

Cyganowski, C. J., Brogan, C. L., Hunter, T. R., et al. 2012, ApJ, 760, L20

Cyganowski, C. J., Whitney, B. A., Holden, E., et al. 2008, AJ, 136, 2391

Dambis, A. K., Berdnikov, L. N., Kniazev, A. Y., et al. 2013, MNRAS, 435, 3206

Dame, T. M., Hartmann, D., & Thaddeus, P. 2001, ApJ, 547, 792

Dame, T. M., & Thaddeus, P. 2008, ApJ, 683, L143

Dame, T. M., Ungerechts, H., Cohen, R. S., et al. 1987, ApJ, 322, 706

Danks, A. C., Dennefeld, M., Wamsteker, W., & Shaver, P. A. 1983, A&A, 118, 301

Davies, B., Hoare, M. G., Lumsden, S. L., et al. 2011, MNRAS, 416, 972

De Buizer, J. M. 2003, MNRAS, 341, 277

De Buizer, J. M., Bartkiewicz, A., & Szymczak, M. 2012, ApJ, 754, 149

De Buizer, J. M., & Vacca, W. D. 2010, AJ, 140, 196

De Buizer, J. M., Walsh, A. J., Piña, R. K., Phillips, C. J., & Telesco, C. M. 2002, ApJ, 564, 327

de Villiers, H. M., Chrysostomou, A., Thompson, M. A., et al. 2014, MNRAS, 444, 566

—. 2015, MNRAS, 449, 119

de Wit, W. J., Testi, L., Palla, F., & Zinnecker, H. 2005, A&A, 437, 247

Deb, S., & Singh, H. P. 2010, MNRAS, 402, 691

Deller, A. T., Tingay, S. J., Bailes, M., & Reynolds, J. E. 2009a, ApJ, 701, 1243

Deller, A. T., Tingay, S. J., & Brisken, W. 2009b, ApJ, 690, 198

Deller, A. T., Brisken, W. F., Phillips, C. J., et al. 2011, PASP, 123, 275

Di Benedetto, G. P. 2002, AJ, 124, 1213

Dodson, R. 2008, A&A, 480, 767

Dodson, R., Legge, D., Reynolds, J. E., & McCulloch, P. M. 2003, ApJ, 596, 1137

Dodson, R., Rioja, M. J., Jung, T.-H., et al. 2014, AJ, 148, 97

Egan, M. P., Shipman, R. F., Price, S. D., et al. 1998, ApJ, 494, L199

Elitzur, M. 1976, A&A, 52, 213

—. 1992, ARA&A, 30, 75

Elitzur, M., Hollenbach, D. J., & McKee, C. F. 1989, ApJ, 346, 983

Ellingsen, S. P. 2006, ApJ, 638, 241

Ellingsen, S. P., Breen, S. L., Sobolev, A. M., et al. 2011, ApJ, 742, 109

Ellingsen, S. P., Breen, S. L., Voronkov, M. A., & Dawson, J. R. 2013, MNRAS, 429, 3501

Ellingsen, S. P., Cragg, D. M., Lovell, J. E. J., et al. 2004, MNRAS, 354, 401

Ellingsen, S. P., Cragg, D. M., Minier, V., Muller, E., & Godfrey, P. D. 2003, MNRAS, 344, 73

Ellingsen, S. P., Norris, R. P., & McCulloch, P. M. 1996a, MNRAS, 279, 101

—. 1996b, MNRAS, 279, 101

Ellingsen, S. P., Shabala, S. S., & Kurtz, S. E. 2005, MNRAS, 357, 1003

Ellingsen, S. P., Sobolev, A. M., Cragg, D. M., & Godfrey, P. D. 2012, ApJ, 759, L5

Ellingsen, S. P., Voronkov, M. A., Cragg, D. M., et al. 2007, in IAU Symposium, Vol. 242, IAU Symposium, ed. J. M. Chapman & W. A. Baan, 213–217

Ellsworth-Bowers, T. P., Glenn, J., Rosolowsky, E., et al. 2013, ApJ, 770, 39

Engels, D., Winnberg, A., Brand, J., & Walmsley, C. M. 1999, in IAU Symposium, Vol. 191, Asymptotic Giant Branch Stars, ed. T. Le Bertre, A. Lebre, & C. Waelkens, 373

Fedele, D., van den Ancker, M. E., Henning, T., Jayawardhana, R., & Oliveira, J. M. 2010, A&A, 510, A72

Federrath, C., & Klessen, R. S. 2013, ApJ, 763, 51

Federrath, C., Klessen, R. S., & Schmidt, W. 2008, ApJ, 688, L79

Felli, M., Brand, J., Cesaroni, R., et al. 2007, A&A, 476, 373

Fiorentino, G., Clementini, G., Marconi, M., et al. 2012, Astrophys. Space. Sci., 341, 143

Fish, V. L., & Reid, M. J. 2006, ApJS, 164, 99

—. 2007, ApJ, 670, 1159

Fish, V. L., Reid, M. J., Argon, A. L., & Menten, K. M. 2003, ApJ, 596, 328

Fomalont, E. 1995, in Astronomical Society of the Pacific Conference Series, Vol. 82, Very Long Baseline Interferometry and the VLBA, ed. J. A. Zensus, P. J. Diamond, & P. J. Napier, 363

Fomalont, E., Johnston, K., Fey, A., et al. 2010, in Sixth International VLBI Service for Geodesy and Astronomy. Proceedings from the 2010 General Meeting, "VLBI2010: From Vision to Reality". Held 7-13 February, 2010 in Hobart, Tasmania, Australia. Edited by D. Behrend and K.D. Baver. NASA/CP 2010-215864., p.300-304, ed. S. Rogstad, C. E. Goodhart, J. E. Clark, S. Finley, G. E. Lanyi, L. A. White, & C. S. Jacobs, 300–304

Fomalont, E. B. 2013, Astrometry for Astrophysics: Methods, Models, and Applications (Cambridge University Press), 175–198

Fomalont, E. B., & Kopeikin, S. 2002, in Proceedings of the 6th EVN Symposium, ed. E. Ros, R. W. Porcas, A. P. Lobanov, & J. A. Zensus, 53

Fontani, F., Cesaroni, R., & Furuya, R. S. 2010, A&A, 517, A56

Forster, J. R., & Caswell, J. L. 1989, A&A, 213, 339

—. 1999, A&AS, 137, 43

—. 2000, ApJ, 530, 371

Freedman, W. L., Madore, B. F., Gibson, B. K., et al. 2001, ApJ, 553, 47

Froebrich, D., & Rowles, J. 2010, MNRAS, 406, 1350

Fujisawa, K., Takase, G., Kimura, S., et al. 2014, PASJ, 66, 78

Galt, J. 1998, AJ, 115, 1200

Galván-Madrid, R., Keto, E., Zhang, Q., et al. 2009, ApJ, 706, 1036

Garay, G., & Lizano, S. 1999, PASP, 111, 1049

García, P., Bronfman, L., Nyman, L.-Å., Dame, T. M., & Luna, A. 2014, ApJS, 212, 2

Garcia-Segura, G., & Franco, J. 1996, ApJ, 469, 171

Gerner, T., Beuther, H., Semenov, D., et al. 2014, A&A, 563, A97

Gerner, T., Shirley, Y. L., Beuther, H., et al. 2015, A&A, 579, A80

Girichidis, P., Konstandin, L., Whitworth, A. P., & Klessen, R. S. 2014, ApJ, 781, 91

Giveon, U., Becker, R. H., Helfand, D. J., & White, R. L. 2005, AJ, 130, 156

Goddi, C., Moscadelli, L., & Sanna, A. 2011, A&A, 535, L8

Gómez, L., Wyrowski, F., Schuller, F., Menten, K. M., & Ballesteros-Paredes, J. 2014, A&A, 561, A148

Gonidakis, I., Chapman, J. M., Deacon, R. M., & Green, A. J. 2014, MNRAS, 443, 3819

Greco, C., Clementini, G., Catelan, M., et al. 2007, ApJ, 670, 332

—. 2009, ApJ, 701, 1323

Green, J. A., Caswell, J. L., & McClure-Griffiths, N. M. 2015, MNRAS, 451, 4593

Green, J. A., & McClure-Griffiths, N. M. 2011, MNRAS, 417, 2500

Green, J. A., McClure-Griffiths, N. M., Caswell, J. L., Robishaw, T., & Harvey-Smith, L. 2012a, MNRAS, 425, 2530

Green, J. A., Caswell, J. L., Fuller, G. A., et al. 2010, MNRAS, 409, 913

—. 2012b, MNRAS, 420, 3108

Greisen, E. W. 2003, 2003iha book, 285, 109

Hachisuka, K., Brunthaler, A., Menten, K. M., et al. 2006, ApJ, 645, 337

Hancock, P. J., Roberts, P., Kesteven, M. J., et al. 2011, Experimental Astronomy, 32, 147

Haschick, A. D., Menten, K. M., & Baan, W. A. 1990, ApJ, 354, 556

Haverkorn, M., Gaensler, B. M., McClure-Griffiths, N. M., Dickey, J. M., & Green, A. J. 2006, ApJS, 167, 230

Heckman, T. M., Sembach, K. R., Meurer, G. R., et al. 2001, ApJ, 558, 56

Hernández-Hernández, V., Zapata, L., Kurtz, S., & Garay, G. 2014, ApJ, 786, 38

Higuchi, A. E., Chibueze, J. O., Habe, A., Takahira, K., & Takano, S. 2014, AJ, 147, 141

Higuchi, A. E., Kurono, Y., Naoi, T., et al. 2013, ApJ, 765, 101

Hildebrand, R. H. 1983, QJRAS, 24, 267

Hill, T., Burton, M. G., Minier, V., et al. 2005, MNRAS, 363, 405

Hindson, L., Thompson, M. A., Urquhart, J. S., Clark, J. S., & Davies, B. 2010, MNRAS, 408, 1438

Hindson, L., Thompson, M. A., Urquhart, J. S., et al. 2012, MNRAS, 421, 3418

—. 2013, MNRAS, 435, 2003

Hinkle, K. H., & Barnes, T. G. 1979, ApJ, 227, 923

Hirabayashi, H., Fomalont, E. B., Horiuchi, S., et al. 2000, PASJ, 52, 997

Ho, C. M., Wilson, B. D., Mannucci, A. J., Lindqwister, U. J., & Yuan, D. N. 1997, Radio Science, 32, 1499

Hoare, M. G., Kurtz, S. E., Lizano, S., Keto, E., & Hofner, P. 2007, Protostars and Planets V, 181

Hofner, P., & Churchwell, E. 1996, A&AS, 120, 283

Hofner, P., Wyrowski, F., Walmsley, C. M., & Churchwell, E. 2000, ApJ, 536, 393

Hollenbach, D., Elitzur, M., & McKee, C. F. 2013, ApJ, 773, 70

Hollenbach, D., Johnstone, D., Lizano, S., & Shu, F. 1994, ApJ, 428, 654

Honma, M., Tamura, Y., & Reid, M. J. 2008, PASJ, 60, 951

Honma, M., Bushimata, T., Choi, Y. K., et al. 2004, in 2004evn conf, ed. R. Bachiller, F. Colomer, J.-F. Desmurs, & P. de Vicente, 203–204

Honma, M., Bushimata, T., Choi, Y. K., et al. 2007, PASJ, 59, 889

Honma, M., Nagayama, T., Ando, K., et al. 2012, PASJ, 64, 136

Horiuchi, S., Fomalont, E. B., Taylor, W. K., et al. 2004, ApJ, 616, 110

Hubble, E. P. 1925, The Observatory, 48, 139

Hutawarakorn, B., & Cohen, R. J. 2003, MNRAS, 345, 175

—. 2005, MNRAS, 357, 338

Imai, H., Kurayama, T., Honma, M., & Miyaji, T. 2013, PASJ, 65, 28

Jimenez-Monferrer, S., Rioja, M. J., Dodson, R., Smirnov, O., & Guirado, J. C. 2010, in 10th European VLBI Network Symposium and EVN Users Meeting: VLBI and the New Generation of Radio Arrays, 84

Jones, C., & Dickey, J. M. 2012, ApJ, 753, 62

Jones, C., Dickey, J. M., Dawson, J. R., et al. 2013, ApJ, 774, 117

Jordan, C. H., Walsh, A. J., Lowe, V., et al. 2015, MNRAS, 448, 2344

Jurcsik, J., Smitola, P., Hajdu, G., & Nuspl, J. 2014, ApJ, 797, L3

Kalenskii, S. V., Johansson, L. E. B., Bergman, P., et al. 2010, MNRAS, 405, 613

Kauffmann, J., & Pillai, T. 2010, ApJ, 723, L7

Kennicutt, R. C. 2005, in IAU Symposium, Vol. 227, Massive Star Birth: A Crossroads of Astrophysics, ed. R. Cesaroni, M. Felli, E. Churchwell, & M. Walmsley, 3–11

Kerr, F. J., Hindman, J. V., & Gum, C. S. 1959, Australian Journal of Physics, 12, 270

Kerr, F. J., & Lynden-Bell, D. 1986, MNRAS, 221, 1023

Keto, E. 2003, ApJ, 599, 1196

—. 2007, ApJ, 666, 976

Krishnan, V., Ellingsen, S. P., Voronkov, M. A., & Breen, S. L. 2013, MNRAS, 433, 3346

Kritsuk, A. G., Norman, M. L., & Wagner, R. 2011, ApJ, 727, L20

Kudritzki, R. P. 2002, ApJ, 577, 389

Kunder, A., Salaris, M., Cassisi, S., et al. 2013, AJ, 145, 25

Kurtz, S., Cesaroni, R., Churchwell, E., Hofner, P., & Walmsley, C. M. 2000, Protostars and Planets IV, 299

Kurtz, S., Churchwell, E., & Wood, D. O. S. 1994, ApJS, 91, 659

Kurtz, S., Hofner, P., & Álvarez, C. V. 2004, ApJS, 155, 149

Kusuno, K., Asaki, Y., Imai, H., & Oyama, T. 2013, ApJ, 774, 107

Lada, C. J., & Lada, E. A. 2003, ARA&A, 41, 57

Lambert, S. 2014, A&A, 570, A108

Larson, R. B., & Starrfield, S. 1971, A&A, 13, 190

Layden, A. C., Hanson, R. B., Hawley, S. L., Klemola, A. R., & Hanley, C. J. 1996, AJ, 112, 2110

Leavitt, H. S., & Pickering, E. C. 1912, Harvard College Observatory Circular, 173, 1

Lee, K., Looney, L. W., Schnee, S., & Li, Z.-Y. 2013, ApJ, 772, 100

Lekht, E. E., Rudnitskij, G. M., Mendoza-Torres, J. E., & Tolmachev, A. M. 2005, A&A, 437, 127

Lizano, S., Canto, J., Garay, G., & Hollenbach, D. 1996, ApJ, 468, 739

Lockman, F. J. 1989, ApJS, 71, 469

Longmore, S. N., Burton, M. G., Minier, V., & Walsh, A. J. 2006, MNRAS, 369, 1196

Lyo, A.-R., Kim, J., Byun, D.-Y., & Lee, H.-G. 2014, AJ, 148, 80

Ma, C., Arias, E. F., Eubanks, T. M., et al. 1998, AJ, 116, 516

Ma, C., Arias, E. F., Bianco, G., et al. 2009, The Second Realization of the International Celestial Reference Frame by Very Long Baseline Interferometry, IERS Technical Note 35, International Earth Rotation and Reference System Service (IERS), International VLBI Service for Geodesy and Astrometry (IVS)

Malkin, Z., Jacobs, C., Arias, F., et al. 2015, in Journées 2014 "Systèmes de référence spatio-temporels", ed. Z. Malkin & N. Capitaine, 3–8

Marconi, G., Andreuzzi, G., Pulone, L., et al. 2001, A&A, 380, 478

Marconi, M., Nordgren, T., Bono, G., Schnider, G., & Caputo, F. 2005, ApJ, 623, L133

Martínez-González, S., Silich, S., & Tenorio-Tagle, G. 2014, ApJ, 785, 164

Matsumoto, N., Hirota, T., Sugiyama, K., et al. 2014, ApJ, 789, L1

McCarthy, D. D., & Petit, G. 2004, IERS Technical Note, 32, 1

McConnell, D., Sadler, E. M., Murphy, T., & Ekers, R. D. 2012, MNRAS, 422, 1527

McKee, C. F., & Ostriker, E. C. 2007, ARA&A, 45, 565

McKee, C. F., & Tan, J. C. 2003, ApJ, 585, 850

McNamara, D. H., & Barnes, J. 2014, AJ, 147, 31

Mehringer, D. M., & Snyder, L. E. 1996, ApJ, 471, 897

Melis, C., Reid, M. J., Mioduszewski, A. J., Stauffer, J. R., & Bower, G. C. 2014, Science, 345, 1029

Menten, K. 1991a, in Astronomical Society of the Pacific Conference Series, Vol. 16, Atoms, Ions and Molecules: New Results in Spectral Line Astrophysics, ed. A. D. Haschick & P. T. P. Ho, 119

Menten, K. 1991b, in Astronomical Society of the Pacific Conference Series, Vol. 16, Atoms, Ions and Molecules: New Results in Spectral Line Astrophysics, ed. A. D. Haschick & P. T. P. Ho, 119

Menten, K. M., & Batrla, W. 1989, ApJ, 341, 839

Menten, K. M., Reid, M. J., Pratap, P., Moran, J. M., & Wilson, T. L. 1992, ApJ, 401, L39

Migenes, V., Coziol, R., Cooprider, K., et al. 2011, MNRAS, 416, 1267

Minier, V., & Booth, R. S. 2002, A&A, 387, 179

Minier, V., Booth, R. S., & Conway, J. E. 2000, A&A, 362, 1093

—. 2002, A&A, 383, 614

Minier, V., Burton, M. G., Hill, T., et al. 2005, A&A, 429, 945

Minier, V., Conway, J. E., & Booth, R. S. 2001, A&A, 369, 278

Minier, V., & Lineweaver, C. 2006, A&A, 449, 805

Mioduszewski, A. J., & Kogan, L. 2009, Strategy for Removing Tropospheric and Clock Errors using DELZN Version 2.0, AIPS Memo 110, National Radio Astronomy Observatory and Cornell University

Miranda, L. F., Gómez, Y., Anglada, G., & Torrelles, J. M. 2001, Nat, 414, 284

Moran, J. M., Reid, M. J., Lada, C. J., et al. 1978, ApJ, 224, L67

Moscadelli, L., & Goddi, C. 2014, A&A, 566, A150

Moscadelli, L., Menten, K. M., Walmsley, C. M., & Reid, M. J. 2002, ApJ, 564, 813

Moscadelli, L., Reid, M. J., Menten, K. M., et al. 2009, ApJ, 693, 406

Moscadelli, L., Sanna, a., & Goddi, C. 2011, A&A, 536, A38

Mottram, J. C., Hoare, M. G., Davies, B., et al. 2011, ApJ, 730, L33

Müller, H. S. P., Menten, K. M., & Mäder, H. 2004, A&A, 428, 1019

Murphy, T., Cohen, M., Ekers, R. D., et al. 2010a, MNRAS, 405, 1560

Murphy, T., Sadler, E. M., Ekers, R. D., et al. 2010b, MNRAS, 402, 2403

Navarrete, C., Contreras Ramos, R., Catelan, M., et al. 2015, ArXiv e-prints, arXiv:1501.02286

Ngeow, C.-C., Lee, C.-H., Yang, Michael, M. T.-C., et al. 2015, AJ, 149, 66

Niell, A. E. 1996, JGR, 101, 3227

Norberg, P., & Maeder, A. 2000, A&A, 359, 1025

Norris, R. P., Caswell, J. L., Gardner, F. F., & Wellington, K. J. 1987, ApJ, 321, L159

Norris, R. P., Whiteoak, J. B., Caswell, J. L., Wieringa, M. H., & Gough, R. G. 1993, ApJ, 412, 222

Norris, R. P., Byleveld, S. E., Diamond, P. J., et al. 1998, ApJ, 508, 275

Osorio, M., Anglada, G., Lizano, S., & D'Alessio, P. 2009, ApJ, 694, 29

Panagia, N. 1973, AJ, 78, 929

Panagia, N., & Walmsley, C. M. 1978, A&A, 70, 411

Pandian, J. D., Menten, K. M., & Goldsmith, P. F. 2009, ApJ, 706, 1609

Pandian, J. D., Momjian, E., Xu, Y., Menten, K. M., & Goldsmith, P. F. 2010, A&A, 522, A8

Paron, S., Ortega, M. E., Dubner, G., et al. 2015, AJ, 149, 193

Pavlakis, K. G., & Kylafis, N. D. 2000, ApJ, 534, 770

Pejcha, O., & Kochanek, C. S. 2012, ApJ, 748, 107

Perault, M., Omont, A., Simon, G., et al. 1996, A&A, 315, L165

Percival, S. M., Salaris, M., & Groenewegen, M. A. T. 2005, A&A, 429, 887

Peretto, N., & Fuller, G. A. 2009, A&A, 505, 405

Perryman, M. A. C., Lindegren, L., Kovalevsky, J., et al. 1995, A&A, 304, 69

Perryman, M. A. C., de Boer, K. S., Gilmore, G., et al. 2001, A&A, 369, 339

Persic, M., Salucci, P., & Stel, F. 1996, MNRAS, 283, 1102

Pestalozzi, M. R., Elitzur, M., Conway, J. E., & Booth, R. S. 2004, ApJ, 603, L113

Peters, T., Banerjee, R., Klessen, R. S., et al. 2010, ApJ, 711, 1017

Petrov, L., Natusch, T., Weston, S., et al. 2015, PASP, 127, 516

Petrov, L., Phillips, C., Bertarini, A., Murphy, T., & Sadler, E. M. 2011, MNRAS, 414, 2528

Phillips, C. J., Norris, R. P., Ellingsen, S. P., & McCulloch, P. M. 1998a, MNRAS, 300, 1131

—. 1998b, MNRAS, 300, 1131

Pihlström, Y. M., Sjouwerman, L. O., Frail, D. A., et al. 2014, AJ, 147, 73

Plunkett, A. L., Arce, H. G., Corder, S. A., et al. 2015, ApJ, 803, 22

Pon, A., Johnstone, D., Bally, J., & Heiles, C. 2014, MNRAS, 441, 1095

Porcas, R. W., Alef, W., Rioja, M.-J., et al. 2003, in Astronomical Society of the Pacific Conference Series, Vol. 306, New technologies in VLBI, ed. Y. C. Minh, 39

Poretti, E., Clementini, G., Held, E. V., et al. 2008, ApJ, 685, 947

Pradel, N., Charlot, P., & Lestrade, J.-F. 2006, A&A, 452, 1099

Pritzl, B. J., Smith, H. A., Catelan, M., & Sweigart, A. V. 2001, AJ, 122, 2600

Purcell, C. R., Balasubramanyam, R., Burton, M. G., et al. 2006, MNRAS, 367, 553

Purcell, C. R., Longmore, S. N., Walsh, A. J., et al. 2012, MNRAS, 426, 1972

Purcell, C. W., Bullock, J. S., Tollerud, E. J., Rocha, M., & Chakrabarti, S. 2011, Nat, 477, 301

Qiao, H., Li, J., Shen, Z., Chen, X., & Zheng, X. 2014, ArXiv e-prints, arXiv:1404.4677

Ragan, S., Henning, T., Krause, O., et al. 2012, A&A, 547, A49

Rathborne, J. M., Garay, G., Jackson, J. M., et al. 2011, ApJ, 741, 120

Rathborne, J. M., Jackson, J. M., Chambers, E. T., et al. 2010, ApJ, 715, 310

Rathborne, J. M., Jackson, J. M., Zhang, Q., & Simon, R. 2008, ApJ, 689, 1141

Rathborne, J. M., Johnson, A. M., Jackson, J. M., Shah, R. Y., & Simon, R. 2009, ApJS, 182, 131

Rathborne, J. M., Simon, R., & Jackson, J. M. 2007, ApJ, 662, 1082

Reid, I. N. 1999, ARA&A, 37, 191

Reid, M. J. 1995, in Astronomical Society of the Pacific Conference Series, Vol. 82, Very Long Baseline Interferometry and the VLBA, ed. J. A. Zensus, P. J. Diamond, & P. J. Napier, 209

Reid, M. J., & Brunthaler, A. 2004, ApJ, 616, 872

Reid, M. J., & Honma, M. 2014, ARA&A, 52, 339

Reid, M. J., Menten, K. M., Brunthaler, A., et al. 2009a, ApJ, 693, 397

Reid, M. J., & Moran, J. M. 1981, ARA&A, 19, 231

Reid, M. J., Readhead, A. C. S., Vermeulen, R. C., & Treuhaft, R. N. 1999, ApJ, 524, 816

Reid, M. J., Menten, K. M., Zheng, X. W., et al. 2009b, ApJ, 700, 137

Reid, M. J., Menten, K. M., Brunthaler, A., et al. 2014, ApJ, 783, 130

Reynolds, J. 1994, A Revised Flux Scale for the AT Compact Array, Tech. Rep. 39.3/040, ATNF, http://www.atnf.csiro.au/observers/memos/d96783~1.pdf

Ridge, N. A., & Moore, T. J. T. 2001, A&A, 378, 495

Riess, A. G., Casertano, S., Anderson, J., MacKenty, J., & Filippenko, A. V. 2014, ApJ, 785, 161

Riess, A. G., Li, W., Stetson, P. B., et al. 2004, in Bulletin of the American Astronomical Society, Vol. 36, American Astronomical Society Meeting Abstracts, 1460

Rioja, M., Dodson, R., Porcas, R. W., et al. 2009, in 8th International e-VLBI Workshop, 14

Rioja, M. J., Dodson, R., Kamohara, R., et al. 2008, PASJ, 60, 1031

Roman-Duval, J., Jackson, J. M., Heyer, M., et al. 2009, ApJ, 699, 1153

Russeil, D., Georgelin, Y. M., Amram, P., et al. 1998, A&AS, 130, 119

Rygl, K. L. J., Brunthaler, A., Menten, K. M., Reid, M. J., & van Langevelde, H. J. 2008, in 2008evn conf

Rygl, K. L. J., Brunthaler, A., Reid, M. J., et al. 2010, A&A, 511, A2

Sakai, N., Honma, M., Nakanishi, H., et al. 2012, PASJ, 64, 108

Sakai, T., Sakai, N., Foster, J. B., et al. 2013, ApJ, 775, L31

Sánchez-Monge, Á., Beltrán, M. T., Cesaroni, R., et al. 2014, A&A, 569, A11

Sandage, A., & Tammann, G. A. 2006, ARA&A, 44, 93

Sanna, A., Reid, M. J., Carrasco-González, C., et al. 2012, ApJ, 745, 191

Sanna, A., Reid, M. J., Moscadelli, L., et al. 2009, ApJ, 706, 464

Sanna, A., Reid, M. J., Menten, K. M., et al. 2014, ApJ, 781, 108

Sasao, T., & Morimoto, M. 1991, in Geodetic VLBI: Monitoring Global Change, 48

Sato, M., Wu, Y. W., Immer, K., et al. 2014, ApJ, 793, 72

Sault, R. J. 2003, ATCA flux density scale at 12mm, Technical Memos 39.3/124, ATNF, http://www.atnf.csiro.au/observers/memos/AT39.3_124.pdf

Schmeja, S., & Klessen, R. S. 2004, A&A, 419, 405

Schmidt, M. 1965, in Galactic Structure, ed. A. Blaauw & M. Schmidt, 513

Schneider, N., André, P., Könyves, V., et al. 2013, ApJ, 766, L17

Schneider, N., Csengeri, T., Klessen, R. S., et al. 2015, A&A, 578, A29

Schönrich, R., Binney, J., & Dehnen, W. 2010, MNRAS, 403, 1829

Schwab, F. R., & Cotton, W. D. 1983, AJ, 88, 688

Schwartz, P. R., Wilson, W. J., & Epstein, E. E. 1973, ApJ, 186, 529

Shipman, R. F., van der Tak, F. F. S., Wyrowski, F., Herpin, F., & Frieswijk, W. 2014, A&A, 570, A51

Shu, F. H. 1977, ApJ, 214, 488

Siegel, M. H., Majewski, S. R., Reid, I. N., & Thompson, I. B. 2002, ApJ, 578, 151

Simon, R., Rathborne, J. M., Shah, R. Y., Jackson, J. M., & Chambers, E. T. 2006, ApJ, 653, 1325

Simon, R., Shah, R. Y., Rathborne, J., et al. 2004, in Astronomical Society of the Pacific Conference Series, Vol. 317, Milky Way Surveys: The Structure and Evolution of our Galaxy, ed. D. Clemens, R. Shah, & T. Brainerd, 159

Skarka, M. 2014, MNRAS, 445, 1584

Slysh, V. I., Kalenskii, S. V., Valtts, I. E., & Otrupcek, R. 1994, MNRAS, 268, 464

Sobolev, A. M., Cragg, D. M., & Godfrey, P. D. 1997, A&A, 324, 211

Sobolev, A. M., & Deguchi, S. 1994, A&A, 291, 569

Sowell, J. R., Trippe, M., Caballero-Nieves, S. M., & Houk, N. 2007, AJ, 134, 1089

Stahler, S. W., Palla, F., & Ho, P. T. P. 2000, Protostars and Planets IV, 327

Stark, D. P., Goss, W. M., Churchwell, E., Fish, V. L., & Hoffman, I. M. 2007, ApJ, 656, 943

Steinbring, E. 2014, AJ, 148, 10

Straižys, V., Milašius, K., Boyle, R. P., et al. 2014, AJ, 148, 89

Sugitani, K., Fukui, Y., & Ogura, K. 1991, ApJS, 77, 59

Sugiyama, K., Fujisawa, K., Doi, A., et al. 2014, A&A, 562, A82

Sullivan, III, W. T. 1971, ApJ, 166, 321

Sunada, K., Nakazato, T., Ikeda, N., et al. 2007, PASJ, 59, 1185

Sutton, E. C., Sobolev, A. M., Ellingsen, S. P., et al. 2001, ApJ, 554, 173

Szymczak, M., Bartkiewicz, A., & Richards, A. M. S. 2007, A&A, 468, 617

Szymczak, M., Pillai, T., & Menten, K. M. 2005, A&A, 434, 613

Tackenberg, J., Beuther, H., Henning, T., et al. 2012, A&A, 540, A113

Tanvir, N. R., Hendry, M. A., Watkins, A., et al. 2005, MNRAS, 363, 749

te Lintel Hekkert, P. T. L., Chapman, J. M., & Zijlstra, A. A. 1992, ApJ, 390, L23

Teixeira, G. D. C., Kumar, M. S. N., Bachiller, R., & Grave, J. M. C. 2012, A&A, 543, A51

Titmarsh, A. M., Ellingsen, S. P., Breen, S. L., Caswell, J. L., & Voronkov, M. A. 2013, ApJ, 775, L12

—. 2014, MNRAS, 443, 2923

Torrelles, J. M., Gómez, J. F., Rodríguez, L. F., et al. 1998, ApJ, 505, 756

Torrelles, J. M., Patel, N. A., Anglada, G., et al. 2003, ApJ, 598, L115

Traficante, A., Fuller, G. A., Peretto, N., Pineda, J. E., & Molinari, S. 2015, MNRAS, 451, 3089

Trinidad, M. A., Curiel, S., Cantó, J., et al. 2003, ApJ, 589, 386

Urquhart, J. S., Figura, C. C., Moore, T. J. T., et al. 2014a, MNRAS, 437, 1791

Urquhart, J. S., Hoare, M. G., Lumsden, S. L., et al. 2012, MNRAS, 420, 1656

Urquhart, J. S., Thompson, M. A., Moore, T. J. T., et al. 2013, MNRAS, 435, 400

Urquhart, J. S., Moore, T. J. T., Csengeri, T., et al. 2014b, MNRAS, 443, 1555

Urquhart, J. S., Moore, T. J. T., Menten, K. M., et al. 2015, MNRAS, 446, 3461

Valdettaro, R., Palla, F., Brand, J., & Cesaroni, R. 2005, A&A, 443, 535

Valdettaro, R., Palla, F., Brand, J., et al. 2002, A&A, 383, 244

Val'tts, I. E., Dzura, A. M., Kalenskii, S. V., et al. 1995, A&A, 294, 825

Val'tts, I. E., Ellingsen, S. P., Slysh, V. I., et al. 2000, MNRAS, 317, 315

—. 1999, MNRAS, 310, 1077

van der Tak, F. F. S., van Dishoeck, E. F., & Caselli, P. 2000, A&A, 361, 327

Varney, R. H., Hysell, D. L., & Huba, J. D. 2011, Journal of Geophysical Research (Space Physics), 116, 6321

Viti, S. 2005, in IAU Symposium, Vol. 231, Astrochemistry: Recent Successes and Current Challenges, ed. D. C. Lis, G. A. Blake, & E. Herbst, 67–76

Voronkov, M. A. 1999, Astronomy Letters, 25, 149

Voronkov, M. A., Brooks, K. J., Sobolev, A. M., et al. 2006, MNRAS, 373, 411

Voronkov, M. A., Caswell, J. L., Britton, T. R., et al. 2010a, MNRAS, 408, 133

Voronkov, M. A., Caswell, J. L., Ellingsen, S. P., et al. 2012, in IAU Symposium, Vol. 287, IAU Symposium, ed. R. S. Booth, W. H. T. Vlemmings, & E. M. L. Humphreys, 433–440

Voronkov, M. A., Caswell, J. L., Ellingsen, S. P., Green, J. A., & Breen, S. L. 2014, MNRAS, 439, 2584

Voronkov, M. A., Caswell, J. L., Ellingsen, S. P., & Sobolev, A. M. 2010b, MNRAS, 405, 2471

Voronkov, M. A., Sobolev, A. M., Ellingsen, S. P., & Ostrovskii, A. B. 2005, MNRAS, 362, 995

Walborn, N. R., Howarth, I. D., Lennon, D. J., et al. 2002, AJ, 123, 2754

Walker, R. C., Matsakis, D. N., & Garcia-Barreto, J. A. 1982, ApJ, 255, 128

Walmsley, M. 1995, in Revista Mexicana de Astronomia y Astrofisica Conference Series, Vol. 1, Revista Mexicana de Astronomia y Astrofisica Conference Series, ed. S. Lizano & J. M. Torrelles, 137

Walsh, A. J., Bertoldi, F., Burton, M. G., & Nikola, T. 2001, MNRAS, 326, 36

Walsh, A. J., Breen, S. L., Bains, I., & Vlemmings, W. H. T. 2009, MNRAS, 394, L70

Walsh, A. J., & Burton, M. G. 2006, MNRAS, 365, 321

Walsh, A. J., Burton, M. G., Hyland, A. R., & Robinson, G. 1998, MNRAS, 301, 640

—. 1999, MNRAS, 309, 905

Walsh, A. J., Chapman, J. F., Burton, M. G., Wardle, M., & Millar, T. J. 2007, MNRAS, 380, 1703

Walsh, A. J., Hyland, A. R., Robinson, G., & Burton, M. G. 1997, MNRAS, 291, 261

Walsh, A. J., Lee, J.-K., & Burton, M. G. 2002, MNRAS, 329, 475

Walsh, A. J., Purcell, C. R., Longmore, S. N., et al. 2014, MNRAS, 442, 2240

Walsh, A. J., Breen, S. L., Britton, T., et al. 2011, MNRAS, 416, 1764

Wang, K.-S., van der Tak, F. F. S., & Hogerheijde, M. R. 2012, A&A, 543, A22

Weaver, H., Williams, D. R. W., & Dieter, N. H. andLum, W. T. 1965, Nat, 208, 29

Webb, S. 1999, Measuring the Universe: The Cosmological Distance Ladder, Springer Praxis Books / Space Exploration (Springer)

Westerhout, G. 1957, BAN, 13, 201

Wilson, T. L., Walmsley, C. M., Menten, K. M., & Hermsen, W. 1985, A&A, 147, L19

Wood, D. O. S., & Churchwell, E. 1989a, ApJ, 340, 265

—. 1989b, ApJS, 69, 831

Woosley, S. E., Heger, A., & Weaver, T. A. 2002, Reviews of Modern Physics, 74, 1015

Wu, Y. W., Sato, M., Reid, M. J., et al. 2014, A&A, 566, A17

Xu, Y., Reid, M. J., Menten, K. M., et al. 2009, ApJ, 693, 413

Xu, Y., Reid, M. J., Zheng, X. W., & Menten, K. M. 2006, Science, 311, 54

Xu, Y., Li, J. J., Reid, M. J., et al. 2013, ApJ, 769, 15

Zhang, B., Reid, M. J., Menten, K. M., et al. 2013, ApJ, 775, 79

Zhang, B., Zheng, X. W., Reid, M. J., et al. 2009, ApJ, 693, 419

Zhang, C.-P., Wang, J.-J., Xu, J.-L., Wyrowski, F., & Menten, K. M. 2014, ApJ, 784, 107

Zhang, Q., Ho, P. T. P., & Ohashi, N. 1998, ApJ, 494, 636

Zhu, G., Zaw, I., Blanton, M. R., & Greenhill, L. J. 2011, ApJ, 742, 73

Zinnecker, H., & Yorke, H. W. 2007, ARA&A, 45, 481